DRAFT

DRAFT

Unsaturated Flow and Transport Through Fractured Rock - Related to High-Level Waste Repositories - Phase II

VOLUME 1

Compiled and Written By

Todd C. Rasmussen and Daniel D. Evans
Department of Hydrology and Water Resources
University of Arizona
Tucson, AZ 85721

DRAFT

Prepared For

Division of Radiation Programs and Earth Sciences
U.S. Nuclear Regulatory Commission
Washington, D.C. 20555

Under Contract No. NRC-04-81-224

April 30, 1986

DRAFT

DRAFT

OFFICIAL USE ONLY

ABSTRACT

In response to high-level radioactive waste repository licensing needs of the U.S. Nuclear Regulatory Commission, this report examines and provides insights into physical characteristics and methodologies for performance assessment of candidate sites in unsaturated fractured rock. The focus is on the ability of the geologic medium surrounding an underground repository to isolate radionuclides from the accessible environment. Media of interest are consolidated rocks with variable fracturing, rock matrix permeabilities, contained water under negative pressure, and air-filled voids. Temperature gradients are also of interest. Studies present conceptual and theoretical considerations, physical and geochemical characterization, computer modeling techniques, and parameter estimation procedures. Radionuclide transport pathways are as solutes in ground water and as vapor through air-filled voids. The latter may be important near a heat source. Water flow and solute transport properties of a rock matrix may be quantified using rock core analyses. Natural spatial variation dictates many samples. Observed fractures can be characterized and combined to form a fracture network for hydraulic and transport assessments. Unresolved problems include the relation of network hydraulic conductivity to fluid pressure and to scale. Once characterized, the matrix and fracture network can be coupled. Reliable performance assessment requires additional studies.

ACKNOWLEDGEMENTS

This report was compiled and written by Todd C. Rasmussen and Daniel D. Evans. Drafting and technical editing was performed by Marie Engle. Contributions from the following individuals are acknowledged:

Dr. James G. McCray	Dept of Nuclear and Energy Engineering
Dr. Eugene S. Simpson	Dept of Hydrology and Water Resources
Dr. Shlomo P. Neuman	Dept of Hydrology and Water Resources
Dr. Arthur W. Warrick	Dept of Soils and Water Science
Dr. Chi-Hua Huang	Dept of Hydrology and Water Resources

In addition, the following graduate students within the Department of Hydrology and Water Resources substantially contributed to the material presented:

Steve Amter	Bill Davies	Andy Messer
Rikki Amutis	Douglas Earp	Khayyun Rahi
Ingrid Anderson	Tim Goering	Mary Roberts
John Andrews	Ron Green	Todd Shrauf
Steve Brown	Richard Kilbury	Robert Trautz
Steve Cullinan	Dan Mathews	Dan Weber

The NRC project technical monitor was Mr. Thomas J. Nicholson, Division of Radiation Programs and Earth Sciences, U.S. Nuclear Regulatory Commission, 7915 Eastern Avenue, Silver Spring, MD, 20910, phone (301)-427-4585.

TABLE OF CONTENTS

TABLE OF CONTENTS (Continued)

TABLE OF CONTENTS (Continued)

TABLE OF CONTENTS (Continued)

TABLE OF CONTENTS (Continued)

VOLUME 2

TABLE OF CONTENTS (Continued)

TABLE OF CONTENTS (Continued)

LIST OF APPENDICES

LIST OF APPENDICES (Continued)

LIST OF TABLES

LIST OF TABLES (Continued)

LIST OF TABLES (Continued)

LIST OF FIGURES

LIST OF FIGURES

LIST OF FIGURES

LIST OF FIGURES

LIST OF FIGURES

LIST OF FIGURES

LIST OF FIGURES

LIST OF FIGURES

LIST OF FIGURES

LIST OF FIGURES

LIST OF FIGURES

LIST OF FIGURES

LIST OF FIGURES

LIST OF FIGURES

EXECUTIVE SUMMARY

0.0 General

In response to the need of the U.S. Nuclear Regulatory Commission (NRC) to review characterizations of candidate sites for the ability of geologic media to isolate high-level nuclear waste (HLW), this report provides elements of the conceptual, theoretical, methodological and technological tools which are appropriate for use at sites located in unsaturated fractured rock. The ability to characterize fluid flow and solute transport in the medium surrounding a repository stems from a number of legislative acts, in particular 10CFR60.

This report documents work performed for the NRC by the Department of Hydrology and Water Resources of the University of Arizona in Tucson. Provided in this report are methods to characterize physical properties of geologic media, including the porosity, pore-size distribution, specific sufaces, as well as fracture characteristics, such as densities, orientations, apertures, lengths and centers. Also provided are techniques for characterizing hydraulic and pneumatic properties of geologic media. The measurement of moisture potential and water release curves are two important parameters necessary for the determination of the direction and magnitude of groundwater flow. Downhole, as well as surface, testing techniques are presented which are used to estimate hydraulic and pneumatic conductivities of rock masses.

The influence of heat on fluid flow may be appreciable in the vicinity of a high-level waste repository. This influence results in two-phase flow, i.e., simultaneous liquid and vapor flow. Laboratory and field evidence of counter-current flow is presented. Counter-current flow may result in the formation of a natural barrier to the movment of soluble contaminants in the event of a failure of the waste package and engineered barriers in the near-field.

Tools useful for the characterization of solute transport in unsaturated, isothermal media environment are also presented. Because removing a liquid sample in the unsaturated zone is restricted to only the wet range, the development of effective tracers and recovery techniques is paramount. Presented methods include the use of both volatile and flourescent tracers. Recovery techniques using thermoelectric cooling elements and vacuum lysimeters are presented.

Movement of contaminants in the vapor phase is a secondary pathway for radionuclide escape. Governing equations describing the forces which

influence the movement of wastes away from a repository in unsaturated fractured media are presented.

In summary, this report summarizes knowledge gained during the four previous years with regard to the physical and chemical properties of unsaturated, fractured rock. The knowledge was obtained using theoretical investigations, computer simulations, laboratory experiments, and field observations. In addition, professional meetings and special symposiums were conducted to evaluate and disseminate conclusions and observations.

0.1 Measurement of Radionuclide Transport

The assessment of the potential of a geologic medium to transmit HLW from a repository constructed for the permanent storage of those wastes is an important component of site characterization. Hydrogeologic and hydrogeochemical studies of the unsaturated zone are used to interpret rates and magnitudes of ground-water flow and the ability of ground water to transport HLW over time periods of thousands of years.

The transport of HLW may occur in the liquid phase as a solute, or in the vapor phase as a gas or aerosol. The relative importance of transport rates in each phase is largely dependent upon the degree of saturation of the medium. It is also dependent upon the size and degree of connection between voids such as fractures, pores, and shafts.

0.1.1 Conduction in the Liquid Phase

Water flow in the liquid phase through unsaturated rock may be the dominant mechanism for the transport of contaminants from a repository to the biosphere. The characterization of flow through an unsaturated formation requires the understanding of liquid flow through the pores and micro-fractures within the rock mass, as well as the movement through larger fractures.

Fluid flow is site and depth dependent. Important determinants of the water intake at the upper surface of the lithosphere include:

- o Surface properties, such as depressions, fracture densities, etc.;
- o Climatic properties, such as evaporation rates, surface temperatures, relative humidity, and rainfall duration and intensity; and
- o Vegetation properties, such as canopy coverage, plant densities, and rooting depth.

In addition, the subsequent redistribution of water originating at the atmosphere-earth interface is strongly dependent upon percolation characteristics, including:

- o Stratification of geologic materials;
- o The relative permeabilities of the rock matrix and fractures; and
- o The abilitiy of the rock matrix to act as a buffer for fracture flow.

Near the atmosphere-earth interface, ground water will move primarily through fractures as discrete pulses. This plug flow will be damped out with depth, however. Depending upon the degree of saturation of the geologic media, part of the fracture flow will either move into the rock matrix, into smaller, drained fractures, or drain into lower fractures.

0.1.1.1 Matrix Transport

Within the matrix of unfractured geologic material, existing soil physics techniques, with modifications as described in this report, can be used to estimate the following parameters from drilled core samples:

- o Moisture release curves;
- o Hydraulic diffusivity;
- o Total and effective porosities;
- o Pore size distributions;
- o Air entry potentials; and
- o Geochemical and thermal properties.

In situ techniques can also be used to obtain parameters important for the characterization of the rock matrix. These parameters include:

- o Air permeabilities; and
- o Water contents, using the neutron method.

Determination of Moisture Release Curves

Moisture release curves relate the unsaturated matrix hydraulic conductivity to the water content and/or the potential at which water is held within the porous medium. Parameters such as total and effective porosities, and the pore size distribution are important determinants of the moisture release curve. Several equations have been proposed to calculate moisture release curves from experiments performed on drilled core samples. These equations have primarily been used to estimate the hydraulic conductivity of unconsolidated materials. The application to consolidated and/or fractured media have not been widely tested.

A recent study (Peters et al., 1984) applied the Mualem model (1976) to tuff samples, but because of the difficulty in obtaining field estimates

of the conductivity, the models could not be validated. Direct measurement of the unsaturated hydraulic conductivity in situ is a difficult and inexact task because of long measurement times and the spatial variability of the parameter.

Determination of Water Potentials

In addition to unsaturated hydraulic conductivity, water potentials in the geologic media are required. This need is twofold. Spatial changes in the total water potential drive fluid movement. Also, the rock water content, an important parameter for determining the unsaturated hydraulic conductivity, is a direct function of the water potential.

In the zone above the region water table, water potentials are generally negative. Water moves from areas where the potential is higher (less negative) to areas of lower potential (more negative). Various field methods have been developed for measuring rock water potentials in situ. The methods include an osmotic tensiometer and filter papers used in conjunction with a thermocouple psychrometer.

The osmotic tensiometer is composed of a steel cylinder core on which a semi-permeable membrane is sealed. The osmotic tensiometer is designed for emplacement in a borehole. When in place, the annular space between the core and the membrane is filled with an osmotic solution. The rock-water flows into or out of the device in response to relative changes in the total potential on either side of the membrane.

The osmotic tensiometer works on the principle that osmotic pressures and hydraulic pressure differences are equally effective in moving water through a membrane when the solutes are completely restricted. Thus, a proper combination of solute and membrane is essential for obtaining data about the rock-water potential.

The filter paper method in conjunction with a thermocouple psychrometer has been evaluated as a method for measuring in situ rock-water potential. Use of the method assumes that a filter paper in liquid or vapor contact with fractured rock will exchange moisture until equilibrium is achieved.

0.1.1.2 Fracture Transport

At high suctions, fluid flow and solute transport through the rock matrix will be more significant than fracture flow, resulting from the size difference between fracture apertures and matrix pores. Vugs and

larger apertures will drain first, followed by smaller fractures, and then micro-fractures and pores. In highly-fractured geologic media, drained fractures may impede flow from matrix block to matrix block. Flow from block to block will occur at fracture asperities and in zones where pendular water is present within a fracture.

In highly-fractured geologic media at low suctions, fractures may provide the principal pathway for fluid flow and solute transport. Film flow will also become important at lower suctions, yet the magnitude of film flow is small relative to flow through saturated fractures.

Flow and solute transport through fractures requires the determination of rock-fracture parameters, such as:

- o Fracture densities, from spacing data along boreholes or from surface exposures;
- o Fracture orientations, also from borehole and surface exposure data;
- o Fracture lengths, using connections between boreholes and surface exposure data;
- o Fracture apertures, using apparent hydraulic or pneumatic aperture for existing water contents; and
- o Fracture shapes, using surface exposures.

A direct means for estimating flow through saturated fractures is to use a relation which combines Poiseuille's law with Darcy's law. This relation can be applied to unsaturated fractures by including capillary theory, which relates the aperture of the fracture to the potential at which the fracture will drain (or fill). Pneumatic and hydraulic methods to estimate the fracture aperture are presented.

0.1.1.3 Determination of Liquid Velocities

A major difficulty associated with monitoring the velocity of water and solutes in unsaturated porous media is the necessity of removing samples of the rock water at different times for analysis. Several solutions are proposed. One is to use a tracer which is transported in a soluble form, and can also be measured in a gaseous state. The advantage of measuring the tracer in the gaseous state is that gas samples can be easily obtained. The suitability of using volatile fluorocarbons for this purpose is currently under investigation.

Gaseous sampling of a fluorocarbon tracer in equilibrium with the liquid phase can be used to predict the rate of liquid redistribution, thus eliminating the need for direct sampling of the liquid phase. Gas

monitoring offers a low cost, reliable method for monitoring travel times of soluble constituents at sites located in the unsaturated zone.

To determine travel times of water within unsaturated geologic media, laboratory soil column studies have been conducted to test the suitability of fluorocarbon tracers. Modeling of the fluorocarbon tracer in both the gaseous and liquid phases has been performed using computer simulations. Results from laboratory column tests have been used to test the accuracy and validity of the computer model. The experimental approach and computer simulation have also been extended to a fractured rock field setting.

A second technique for determining travel times in unsaturated media is to modify vacuum lysimeter use. The modification is composed of:

- o An injection phase, in which a known quantity of fluid is injected into the media surrounding a lysimeter to provide sufficient fluids to bring the potential of the water in the media to near saturation;
- o A redistribution phase, in which the injected fluids mix with the native fluids; and
- o A recovery phase, in which injected and native fluids are recovered by applying a partial vacuum within the lysimeter.

A third technique uses fluorescent tracers to identify visually the arrival of a tracer front. Various tracers are evaluated and the suitability of these tracers is discussed.

Finally, a technique which uses Peltier cooling of a thermopile is used to recover samples from the gas phase. The method uses an electric current to provide a cooling surface upon which water vapor condenses and is collected. The objectives of this investigation have been:

- o The assessement of a laboratory procedure making use of the Peltier effect, which once established could be adapted into an <u>in situ</u> field method; and
- o The evaluation of the usefulness of tritium in its vapor state as a tracer, and other possible tracers should tritium prove ineffective or impractical.

The Peltier effect is produced when a current is passed through a junction of two different metals of a thermopile, resulting in a rising or lowering of temperature depending on current direction. If a current is induced in the direction such that the temperature is reduced, and the thermopile is placed in a humid environment, continuation of cooling to the dewpoint will result in condensation of water vapor onto the

thermopile. The condensate, which initially might consist of tritium enriched water, can then be collected for analysis.

0.1.1.4 Geochemical Factors

Identifying mineralogic changes and measuring isotopic variations may help establish the history of climatic and geomorphologic processes that might affect the isolation properties of a repository site. Previous work in this area for unsaturated fractured rock is sparse. Field work has been performed to assess mineralogic and isotopic techniques for obtaining information on flow regimes in unsaturated rock of low permeability.

Careful selection of the particular hydrogeochemical parameters and interpretation of the data can help characterize a representative site's unsaturated zone hydrology. Mineralogic and isotopic analyses can yield important information on how the system has behaved in the past and predict how it will behave in the future.

A field site near Superior, Arizona, where the predominant geologic material is a partially welded tuff (or, quartz latite), has been selected to conduct this assessment. The information that has been targeted for mineralogic and isotopic analysis includes:

- o Origins of pore waters;
- o Distinction of flow paths, mixing, and variability;
- o Age and age gradients of bound water;
- o Paleoclimatic information; and
- o Natural water-rock interactions.

Understanding site-specific parameters is important for proper selection and interpretation of the hydrogeochemical data. A program has been performed for evaluating existing techniques for fracture-filling mineral assemblages with regard to:

- o Sampling;
- o Initial treatment (e.g., filtration, nonfiltration, acidification, addition of precipitating salts); and
- o Preservation (e.g., isolation, temperature control).

Analysis and influence of drilling methods and drilling fluids will also be important.

Mineralogical indicators that are the most important to distinguish in fracture zones are the silica and clay assemblages. The key isotopes to be determined include ^{3}H, ^{14}C, ^{2}H, ^{18}O, ^{13}C, ^{36}Cl, and $^{87}Sr/^{86}Sr$. A

high concentration of tritium (^3H) is an indication of recent water either by contamination or infiltration. The carbon, oxygen, and strontium isotopes are useful for dating and for inferring the origins of pore and bound waters. Disequilibrium of uranium and radium isotopes can provide information on age and natural interactions. Isotopic analysis of uranium and thorium of fracture fillings can be used to date those minerals.

0.1.2 Conduction in the Vapor Phase

Vapor phase transport may be significant when large driving forces are present and suitable voids exist within the geologic media. The voids may be open shafts, or drained fractures and pores. The movement of gas in an unsaturated, non-isothermal, fractured medium which is located near a radioactive source can take place as a result of several different driving forces. The driving forces present in this setting include those resulting from:

- o A concentration or partial pressure gradient;
- o A total pressure gradient; or
- o A liquid or surface concentration gradient;

Each driving force results in an associated transport mechanism. A concentration gradient can cause ordinary diffusion. Diffusion includes Knudsen flow, self-diffusion, binary diffusion and surface flow. A gradient in the total pressure can result in viscous flow which includes Poiseuille (or Couette) and slip flow. An electric field can result in forced diffusion. And finally, a thermal gradient can cause a mechanism called thermal diffusion. A brief review of the equations governing gas movement in a fractured medium are presented.

Possible pathways for migration include direct transport in the vapor phase to the accessible environment, or to a zone of higher saturation where the contaminant is further transported in the liquid phase. An important conclusion drawn from this analysis is that because the potential influence of the driving forces are strongly dependent upon parameters unique to each application, the importance of vapor transport must be assessed for each site and engineering design.

0.2 Influence of Thermal Loading on Solute Transport

Heat released by the radioactive decay of HLNW in an underground repository will cause a long-term thermal disturbance in the host rock containing it (Wang et al., 1979). Therefore, non-isothermal moisture flow must be considered. Experiments have shown that a counter-current

is established when a thermal gradient is applied to a sealed rock core. The counter-current is composed of movement in the vapor phase away from the heat source, and a compensating movement in the liquid phase toward the heat source.

To date, little research has been conducted with regard to non-isothermal unsaturated water transport through fractured media. If, however, an unsaturated fracture can be considered to be analogous to a single pore, having both an air phase and a water film, then a significant amount of literature on non-isothermal moisture movement in unsaturated porous media (i.e. the air-filled volume of the granular media and the associated film absorbed to the pore forming particles) can be applied.

Philip and de Vries (1957) provided the first comprehensive work dealing with moisture movement in granular materials under temperature gradients. Their work is a water content formulation and took into account both liquid and vapor flowing response to both soil-water pressure and thermal gradients.

Taylor and Cary (1964) developed flow equations which were based on the laws of irreversible thermodynamics, and considers the heat flux. Both the Philip-de Vries and the Taylor-Cary theories involve the use of soil-water diffusivities. Milly (1982) developed a matric head, as opposed to water content, model of moisture and heat flow in a porous media. This change in dependent variable made possible the incorporation of hysteresis and soil heterogeneities.

All of the mathematical models proposed consider simultaneous heat, liquid water, and water vapor transfer. At the elevated temperatures expected in the vicinity of the HLNW repository, vapor transfer will presumably be greater than liquid water transfer. In addition, the resulting latent heat storage and advection of sensible heat by the vapor phase will be small when compared to heat conduction through the rock matrix. This fact allows for indirect coupling of heat and mass transfer rather than direct coupling.

Heating experiments have been performed to establish a vapor liquid counter-current in a sealed rock core. After a temperature gradient is established along the rock core, the core is monitored to determine changes in water content, temperature, and electrical resistivity. With this information, the ion movement caused by the counter-current is determined. Water soluble ions will move with liquid water toward the heat source but will not move away in the water vapor.

In fractured media, fracture flow may dominate in the zone of condensation around the repository. The lower suction in the zone of condensation will allow larger fractures to saturate, establishing a zone of higher fluid conductivity.

0.3 Limitations and Recommendation for Further Research

Limitations with current theories and techniques include the inadequate testing of measurement techniques over a wide range of suctions, especially the dry range which may be of particular interest. Also, accurate methods for measuring matrix suction, or the hydraulic head, are not currently available.

The sampling of pore or fracture fluids is difficult at high suctions. Thus, samples for examining travel times of tracers or for investigating geochemical processes are difficult to obtain.

The conductivity of fractures as a function of fluid suction is an area for additional research. Little empirical evidence has been obtained with regard to the moisture release curve for an individual fracture. Also, the lack of data has impeded the calibration of conceptual and computer models.

It is recommended that further research be performed, specifically with regard to large-scale field facility for testing of a well-instrumented heating experiment. In addition, it is recommended that a natural analog be identified for use in model calibration and validation.

CHAPTER 1
INTRODUCTION

This document describes field, laboratory and numerical methodologies for judging the contaminant isolation capabilities of unsaturated fractured rock. The focuses are on the hydrologic and transport issues stated in the revisions to 10 CFR 60 formulated to include unsaturated media as potential repository sites for high level waste disposal (Hackbarth, Nicholson and Evans, 1985). The research which this document summarizes is generic in nature, having application to the characterization of specific unsaturated fractured rock sites.

1.1 Scope

Of primary interest to regulatory reviewers will be the ability to demonstrate the potential for a geologic setting to isolate a wide assortment of nuclear wastes from the accessible environment. Of primary interest is high-level radioactive waste from commercial sources. By showing that the geologic media, in conjunction with engineered barriers, adequately prevents harmful levels of radioactive materials from reaching the biosphere, the regulators and general public can be more assured of the safety of nuclear waste disposal. The scope, therefore, is the ability to accurately determine fluid and solute movement within the zone around the waste canisters, and also at greater distances.

To provide a quantitative understanding of the rate and amount of fluid and solute transport through the geologic media surrounding proposed repositories within unsaturated zones, an integrated package of research topics has been undertaken. The research topics have provided new, substantial information which is critical to the successful design and understanding of the hydrogeologic environment at a proposed repository site.

The research topics are of interest because of the potential difficulty of quantifying fluid and solute movement through unsaturated fractured rocks of low permeability. Previous to the current research, the understanding of movement of fluids and solutes was limited to saturated and unsaturated media composed of uniformly porous material with moderate to high permeability, or to saturated rock of low permeability.

Thus, the topics of interest incorporate theory, experimental and statistical methods, and laboratory and field data, which differ from classical studies on several points. In particular, transport through

discrete fractures, as opposed to continuous porous media transport, requires new sampling techniques and procedures. The interpretation of data from discrete points is more difficult when averaging over space. Also, there is a major difficulty associated with the application of fluid and vapor transport theories in the unsaturated zone. This results from the paucity of empirical support to provide a consistent and universally acceptable basis for consensus.

To overcome these and other difficulties, the present program has generated data, information, and techniques which are useful for resolving issues central to successful site characterization for the isolation of nuclear waste materials.

The research has been conducted by the Department of Hydrology and Water Resources, College of Engineering and Mines, University of Arizona. The program has been closely coordinated with a parallel, NRC-funded project at the University of Arizona focused on contaminant transport through saturated fractured rock, with Drs. S. P. Neuman and E. S. Simpson as co-principal investigators. The methods and results obtained for saturated conditions are directly applicable to the special case of a combined unsaturated-saturated system.

1.2 Organization

A general overview of the project is presented in this first chapter, along with a description of the field sites and available computer and laboratory resources. Following this introductory chapter, an assessment of the information required to describe the physical and chemical nature of the rock matrix and fractures located within a rock matrix is presented. The chapter focuses on techniques to describe the physical properties of both the rock matrix and fracture systems within the rock body. Methods to determine the porosity, pore size distribution and fracture parameters such as density, orientation, etc., are also presented.

Chapter 3 describes the current status of the ability to provide data about the energy distribution of fluids within geologic media. Because fluids flow from regions of higher energy potential to regions of lower potential, the knowledge of energy levels will indicate the direction of fluid flow. Also necessary is the rate at which fluid flow occurs. By knowing the potential distribution and estimating the hydraulic conductivity of each medium, one may obtain an estimation of the flux and velocity of the fluid. A technique which is useful for determining the conductivity as a function of the energy potential is described.

Stored high-level waste will generate heat and cause a thermal gradient to develop in the media surrounding the waste. The determination of fluid flow and solute transport through geologic media where non-isothermal conditions are present requires the application of coupled process analysis. A coupled approach for simultaneous fluid, vapor, solute, and heat is presented in Chapter 4. Numerical, laboratory and field experiments are presented which support the hypothesis that a counter-current flow regime may develop near the heat source.

A counter-current flow regime will result in liquid and solutes moving toward the heat source while vapor and heat are transported away from the heat source. It is possible that heat generated by a repository will result in the net migration of dissolved constituents back to the repository. If this process is confirmed, then even if radionuclides escape engineered structures, then natural mechanisms will prevent the migration of the soluble nuclides away from the repository. This fail-safe mechanism has been demonstrated.

Chapter 5 presents solute transport research which is useful for confirming calculated velocities. Sampling the rock water for chemical analysis is a major difficulty associated with solute transport assessment. Several approaches have been explored and preliminary results are presented.

A field technique is described which utilizes a volatile tracer (i.e., a chemical compound which vaporizes easily) to monitor the progress of a fluid as it moves through the unsaturated zone. This technique is useful because obtaining a gas sample from unsaturated rock with low water content and with the liquid under negative pressure is easier than obtaining a liquid sample.

Another technique to examine fluid and solute movement through unsaturated media considers the possibility of recovering water vapor which would be in equilibrium with liquid water within the rock. The testing of water vapor for the presence of an isotope of water can indicate the source and/or age of the water. This may lead to an understanding of the past and present movement of the water.

The total flux and solute movement through unsaturated media might be estimated by utilizing geo-chemical mixing at or near the water-table. By identifying the reaction kinetics and the mixing process of two dissimilar water components, a more accurate assessment of the through-flow of solutes and fluids can be made. In addition, the reaction

kinetics will provide a more detailed understanding of the migration of escaped radionuclides.

Chapter 6 investigates the potential influence nuclear materials will have on liquid, vapor and solutes in the zone immediately surrounding a repository. This analysis explores the possibility that gamma radiation may provide a mechanism for the dispersal of positively-charged ions away from a repository. The mechanism is considered to be near-field effect resulting from the decay of nuclear materials in the repository.

A final, summary chapter reviews the procedures presented in this report for evaluating the capacity of unsaturated media to isolate wastes. Appendices are also included which more specifically describe laboratory and field procedures described in this report.

1.3 Field Study Areas

Two field study areas have been developed for the assessment of methods to measure fluid flow and solute transport in unsaturated geologic media. Both study areas (Figure 1.1) are located in unsaturated, fractured rock. One study area is located near Patagonia, Arizona, in the region surrounding the Patagonia Mountains in southeast Arizona. The other study area is located near Superior, Arizona, on the western edge of the Pinal Mountains in central Arizona.

The climate at the study areas is semi-arid, receiving less than 510 mm of rain per year. Rainfall varies seasonally, with the majority occurring during two periods, July through September, and December through March. Thunderstorms produce localized, high-intensity precipitation events during the summer months, and frontal storms produce widespread, but low-intensity, precipitation during the winter months. Summer temperatures typically range from 10 to 40°C, while winter temperatures range from -5 to 15°C.

1.3.1 Patagonia Mountains Study Area

The Patagonia Mountains are a north-northwesterly trending range lying east of Nogales and south of Patagonia in southeastern Arizona. The mountains consist in large part of Mesozoic volcanic and sedimentary rocks. The layered rocks comprise six stratigraphic units of known or strongly inferred Mesozoic age and two units of uncertain but probable Late Cretaceous or early Tertiary age. The aggregate total thickness is unknown, but may be as much as 4500 m. Volcanic rocks of silicic to intermediate composition make up 75 percent or more of the Mesozoic

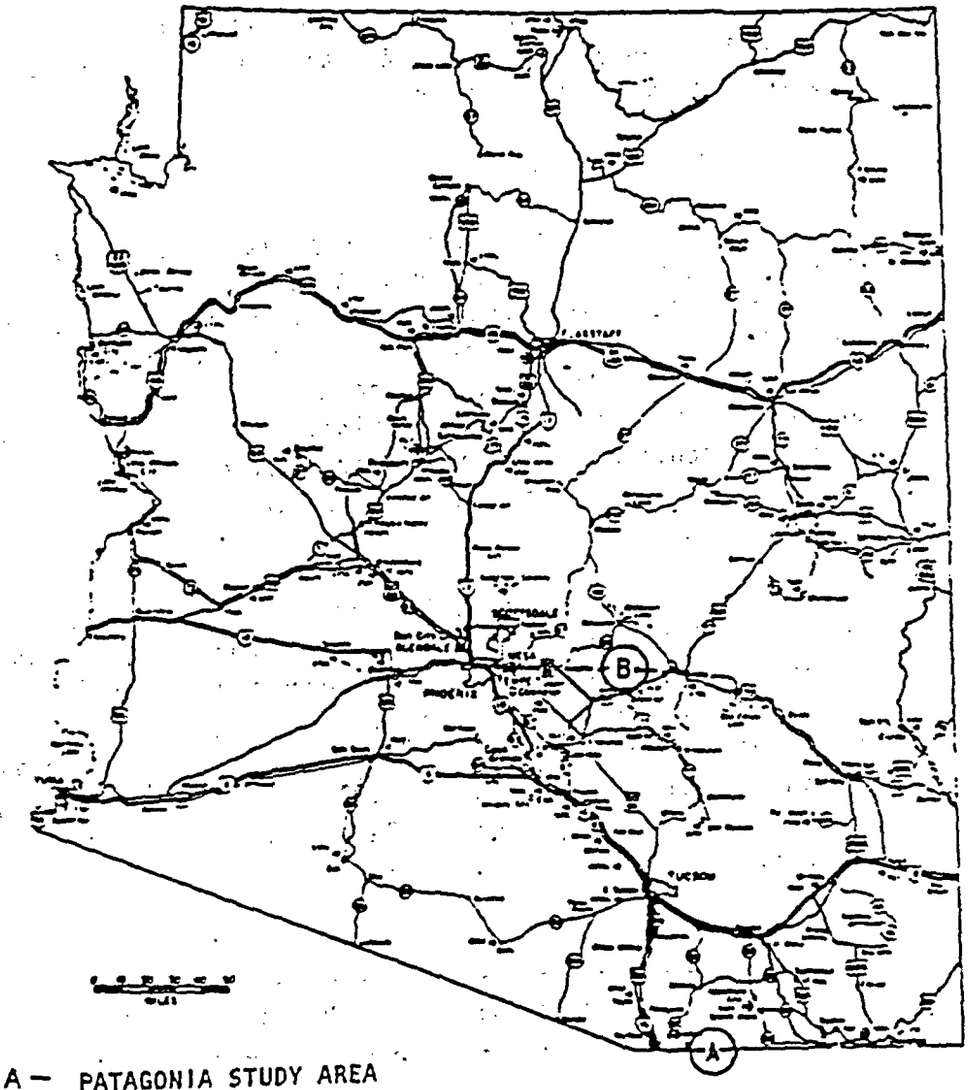

Figure 1.1 Location map of the Patagonia and Superior study areas.

stratigraphic column; the remainder is sedimentary rocks and some interlayered volcanic beds.

Three field sites have been developed in the Patagonia Mountains. The locations of sites are presented in Figure 1.2. One site, the Santo Nino mine, is located in quartz diorite. A second site, the Patagonia field site, is located in bedded, welded tuff. The third site, at the Pride-of-the-West Mine, is not described. A description of the other two sites is summarized below.

1.3.1.1 Santo Nino Mine Site

The Santo Nino mine site lies at an elevation of approximately 1800 m in the extreme southern section of Arizona, 3 km directly north of the Mexican border. The mine is located in section 9, township 24 south, range 16 east on the eastern slope of the Patagonia Mountains. The mine penetrates the Patagonia range batholith, a tertiary intrusive underlying the Patagonia mountains. The rock is described as a gray quartz monzonite. The principal ore-bearing formation was described by Kirkemo et al. (1965) as a pink feldspar-rich medium-grained granitic rock.

The contact between the pink feldspar rock and the granitic monzonite is gradational and irregular, suggesting the ore body has replaced the surrounding country rock. Copper and molybdenite disseminated throughout the ore body were the principal ores mined. Specific mineralogy is presented in Table 1.1 (Baker, 1962). The bulk density of the quartz monzonite matrix is 2.63 ± 0.06 g/cm^3 and the grain density is 2.67 ± 0.04 g/cm^3 (Evans, 1983a). Thus, the matrix porosity is 1.7 ± 0.8 percent.

Table 1.1 Mineralogy of Santo Nino Quartz Monzonite, after Baker (1962).

Mineral	Percent
Albite-orthoclase	32 - 38
Potassium feldspar	26 - 29
Quartz	20 - 33
Biotite	6 - 8
Hornblend	0 - 3

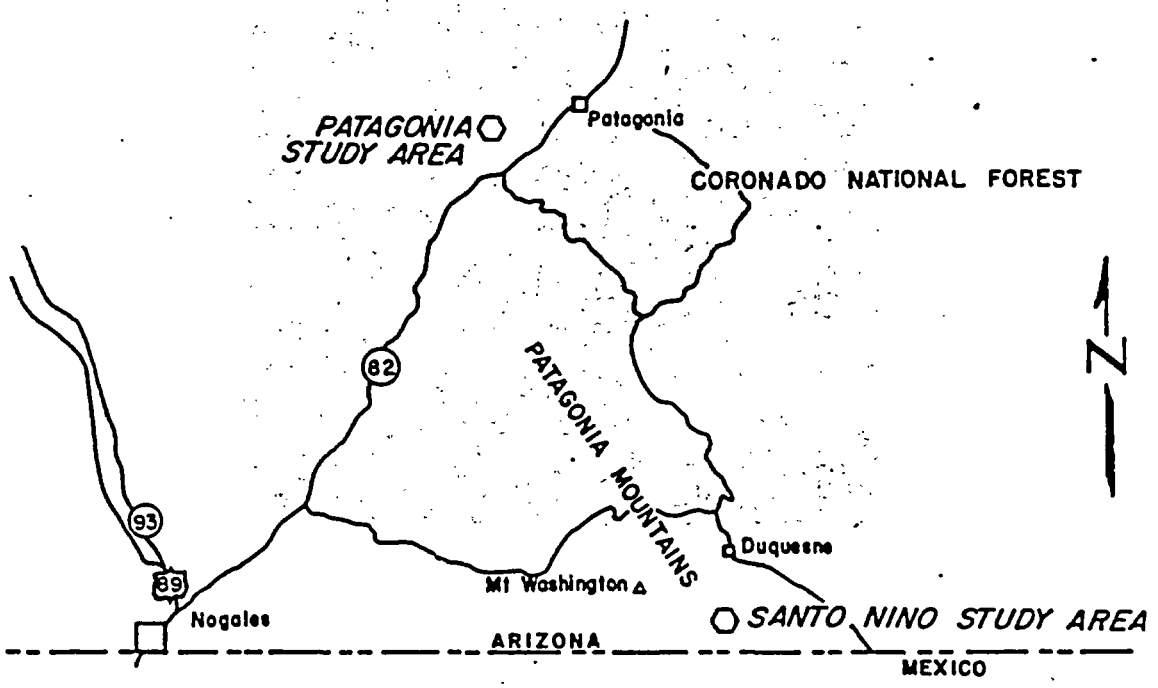

Figure 1.2 Location map of the Santo Nino mine, the Pride-of-the-West mine and the Patagonia field sites.

Figure 1.3 Photograph of entrance to the Santo Nino mine.

Three prominent fracture sets, both mineralized and unmineralized, are found inside the mine and at the surface (Figure 1.3). These three joint sets are nearly perpendicular to one another, thus forming an orthogonal fractured rock system. Even though conventional blasting techniques were employed in constructing the drift, all three sets can be still be distinguished from the fractures caused by blast damage.

A fracture survey was conducted along the first 100 m of the adit (Figure 1.4). Sampling was conducted along a scanline taken at approximately 1.2 m above the floor and along the western rib of the adit. All fractures which had a regular trace and intercepted the scanline were noted. Fracture data recorded included:

(1) orientation;
(2) spacing;
(3) length of trace;
(4) surface regularity;
(5) fracture filling;
(6) weathering;
(7) seepage characteristics; and
(8) shear displacement.

The fracture orientation data were plotted on a Schmidt stereonet and contoured for fracture density (Figure 1.5). The data indicate that two prominent fracture sets were present. The most pervasive set runs parallel to several major faults and gouge zones. Its apparent dominance is primarily due to the near perpendicular orientation of the fracture relative to the axis of the adit. The third fracture set is not evident because it lies parallel to the adit and is difficult, if not impossible, to sample.

The poles of the second fracture set almost plot in the center of the Schmit net, thus indicating this set is nearly horizontal. The density is slightly diminished in comparison to the first set because the second set is parallel to the survey scanline. A third, less-pronounced set also runs parallel to the survey scanline. The existence of the third set is made evident by the large exposures of these fracture planes along the adit walls.

Eight holes, each with a diameter of 4.75 cm were drilled into the walls of the Santo Nino mine. Of these, two horizontal holes in the east wall were logged for this study. They are located 5.2 and 5.8 m from the portal and six meters below the surface. Borehole 5.2 is 5.6 m long and Borehole 5.8 is 6.4 m long. The spatial location of fractures detected using a video logger in Boreholes 5.2 and 5.8 are presented in Figure 1.6. The fracture density calculated from the core data is three fractures per meter.

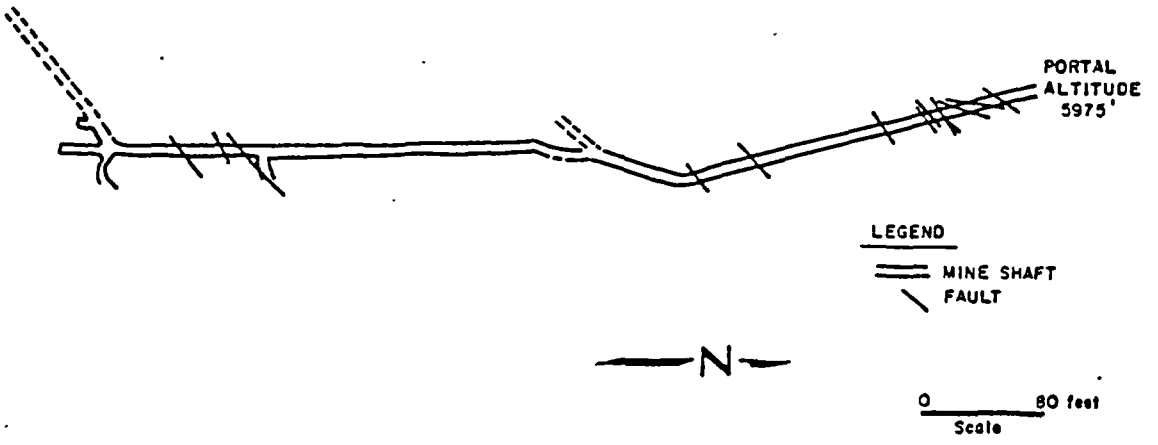

Figure 1.4 Plan view of Santo Nino mine adit (after Baker, 1962).

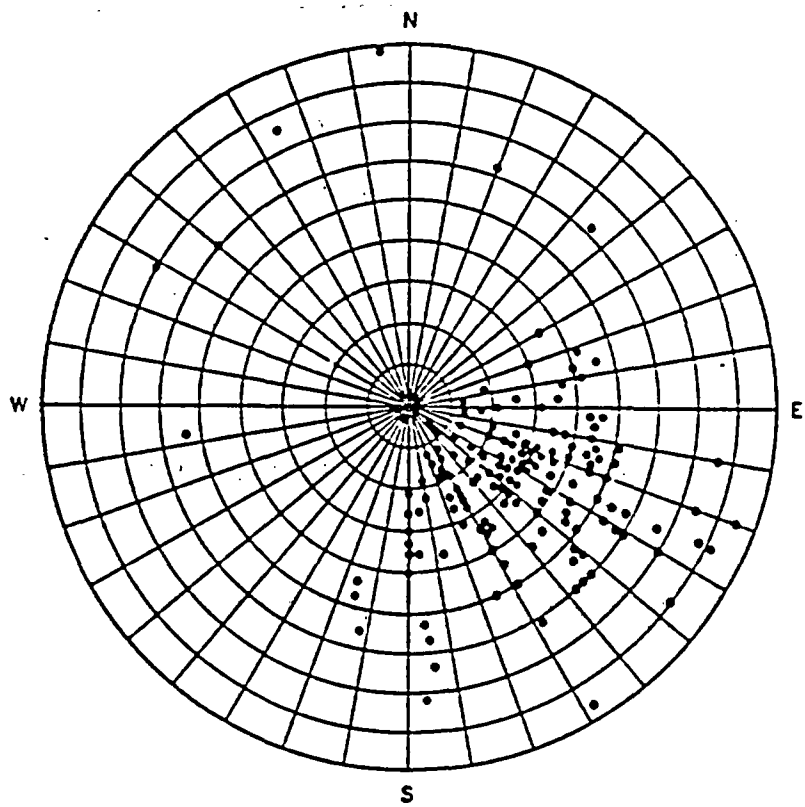

Figure 1.5 Schmidt stereonet of fracture orientation.

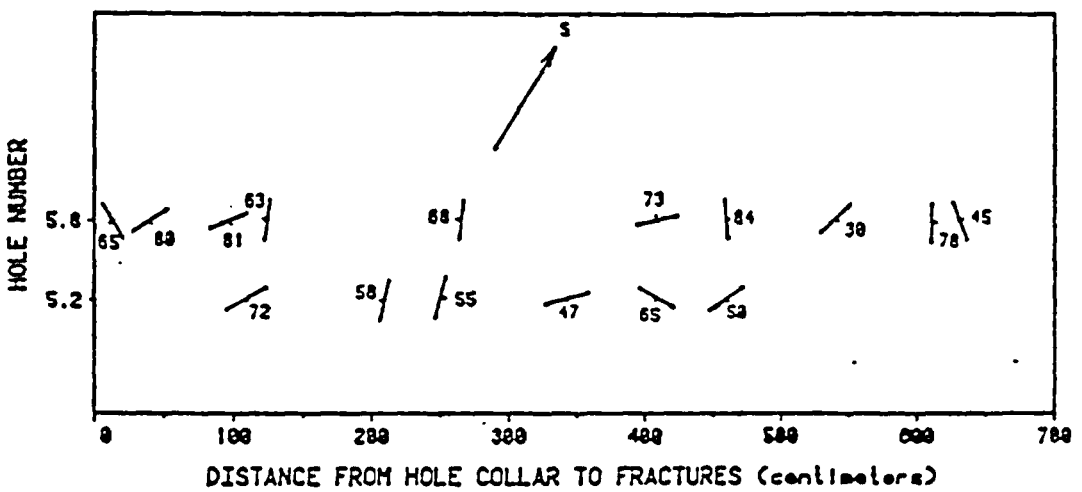

Figure 1.6 Plan view location, strike and dip for each fracture detected on the video log.

Figure 1.7 provides a cross-section of the Santo Nino mine. Two slightly inclined holes (10° below horizontal) in the west wall six meters from the portal have standing water. Water levels in the upper hole (Borehole 6.0a) measured between October 1982, and August 1983, are presented in Figure 1.8 (Evans, 1983c). Precipitation data collected in the Patagonia Mountains between September 1982 and August 1983 from a rain gage situated above the Santa Nino mine are also presented in Figure 1.8. Mean monthly surface and recorded borehole temperatures for the Santo Nino mine are presented in Figure 1.9. The mean monthly data, from the Nogales weather station, have been corrected for an elevation difference of 640 m using an adiabatic lapse rate of 2°C per 300 m.

By comparing the precipitation histogram with the the borehole water level profile, it appears that the response time between the surface and Borehole 6.0a is approximately eight weeks when the overburden is initially dry, and less than four weeks when the overburden is nearly saturated. The water levels for Borehole 6.0b are not included because the standing water on the mine floor flooded this hole in February and again in July. Although a drain was installed at the portal, flow into the mine exceeded the capacity of this pipe. Unexpectedly, standing water above the pipe level remained through the dry spring months. A diagram of the location of these boreholes and the standing water levels is presented in Figure 1.10.

1.3.1.2 Patagonia Field Site

The Patagonia field site (Figure 1.11) is located approximately two miles southwest of the town of Patagonia, 1.2 km north of Sonoita Creek, between Goat Canyon to the west and Temporal Canyon to the east, Santa Cruz County, Arizona. Its formal location description is Patagonia, Arizona, U.S. Geological Survey 17-minute quadrangle. The study area lies on the privately-owned land bounded on the south by the Patagonia Bird Sanctuary and the north by the Coronado National Forest. Across Sonoita Creek to the southeast are Alum and Flux Mountains. The Santa Rita Mountains are approximately eight kilometers to the north.

The Patagonia study area is a flat-topped butte approximately 1.4 hectares in area, at an approximate elevation of 1,280 m above sea level. Geology of the local area has been studied in detail by Drewes (1972). The butte which comprises the study area is capped by a Paleocene aged (60 to 65 million years) welded ash-flow tuff. This rhyolitic tuff, described as the basal unit of the upper member of the Gringo Gulch Volcanics, is the unit characterized by this investigation. It was deposited largely by airfall and fluvial processes. The welded

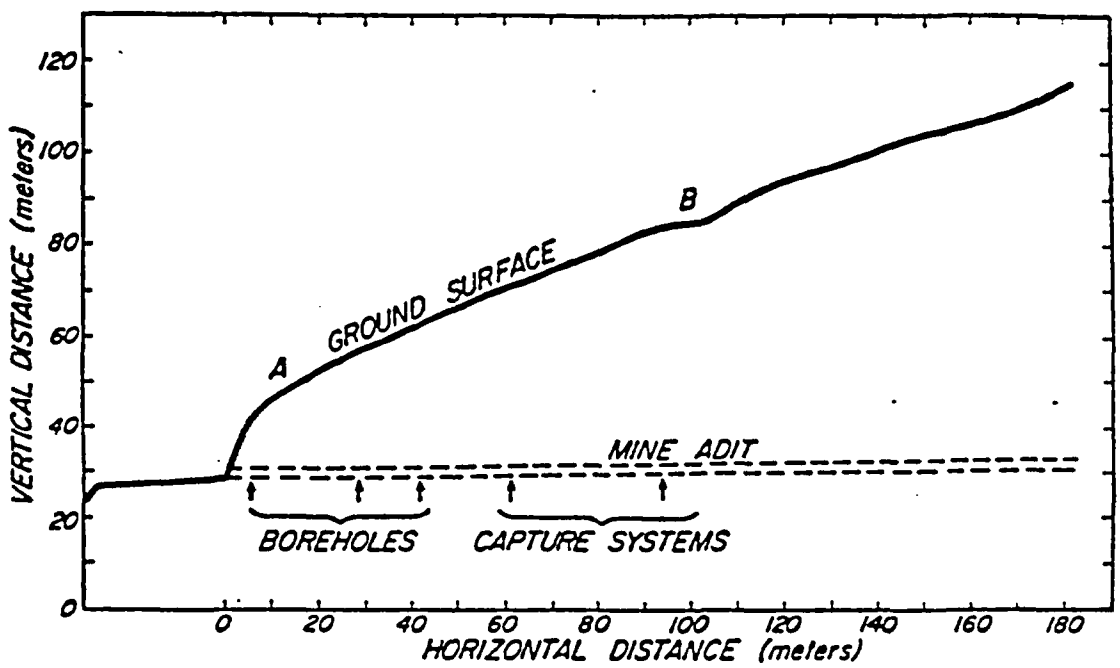

Figure 1.7 Cross-section of the Santo Nino mine.

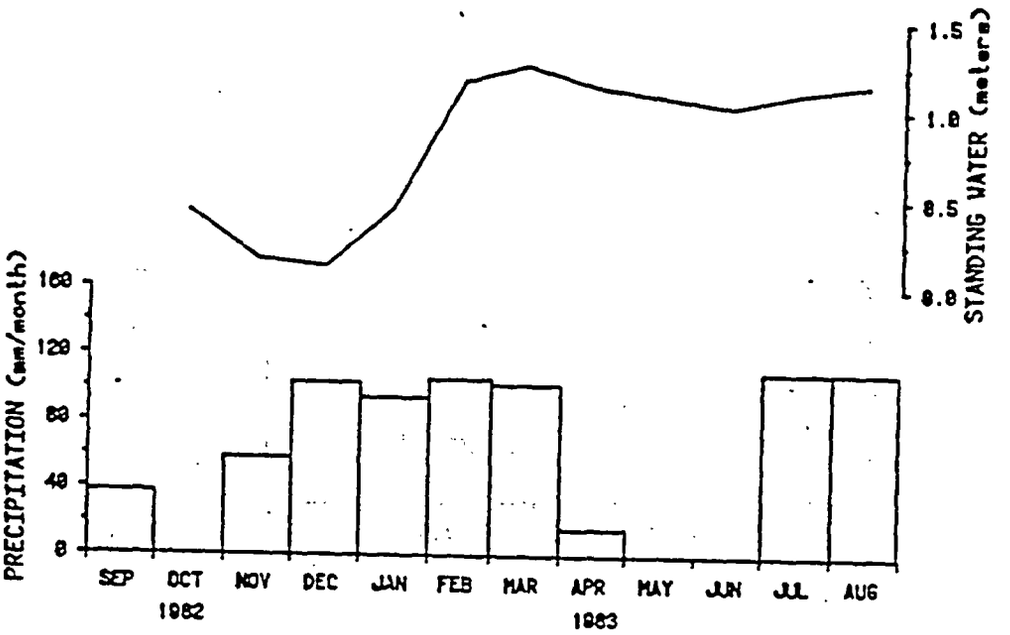

Figure 1.8 Relative water levels in Borehole 6.0a.

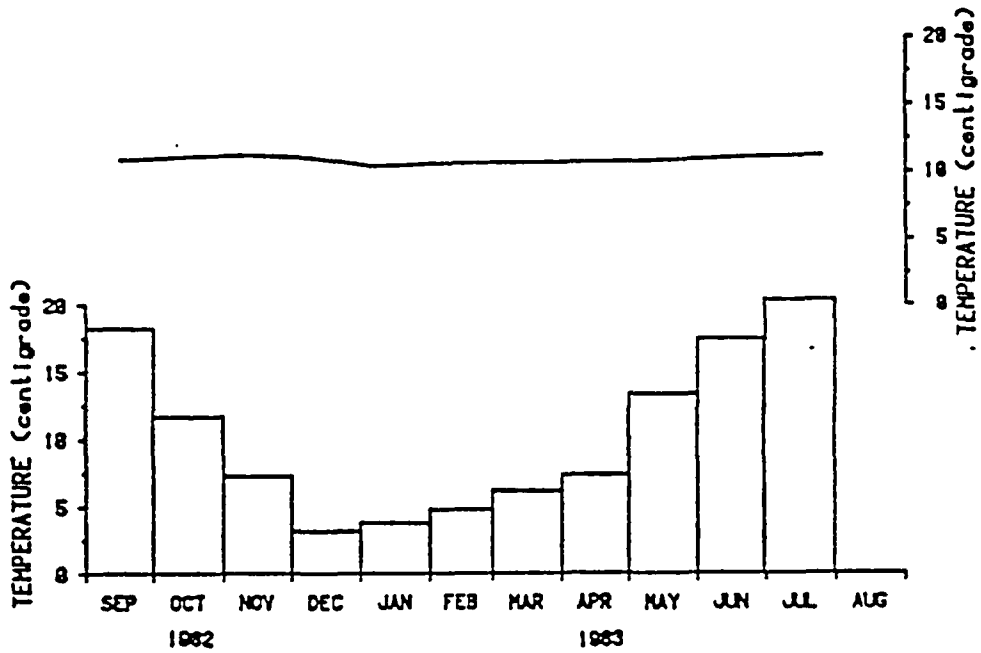

Figure 1.9 Borehole temperatures (line graph) and mean monthly surface temperatures (bar graph) at the Santo Nino field site.

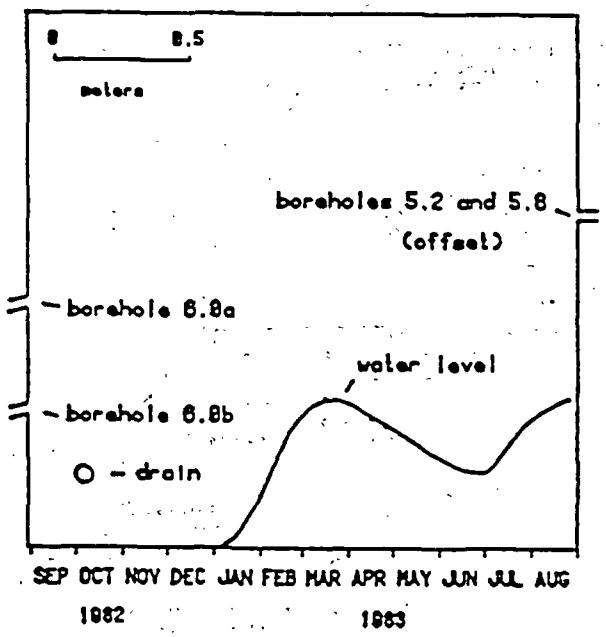

Figure 1.10 Cross-section perpendicular to the Santo Nino mine adit showing the location of boreholes and ponded water levels.

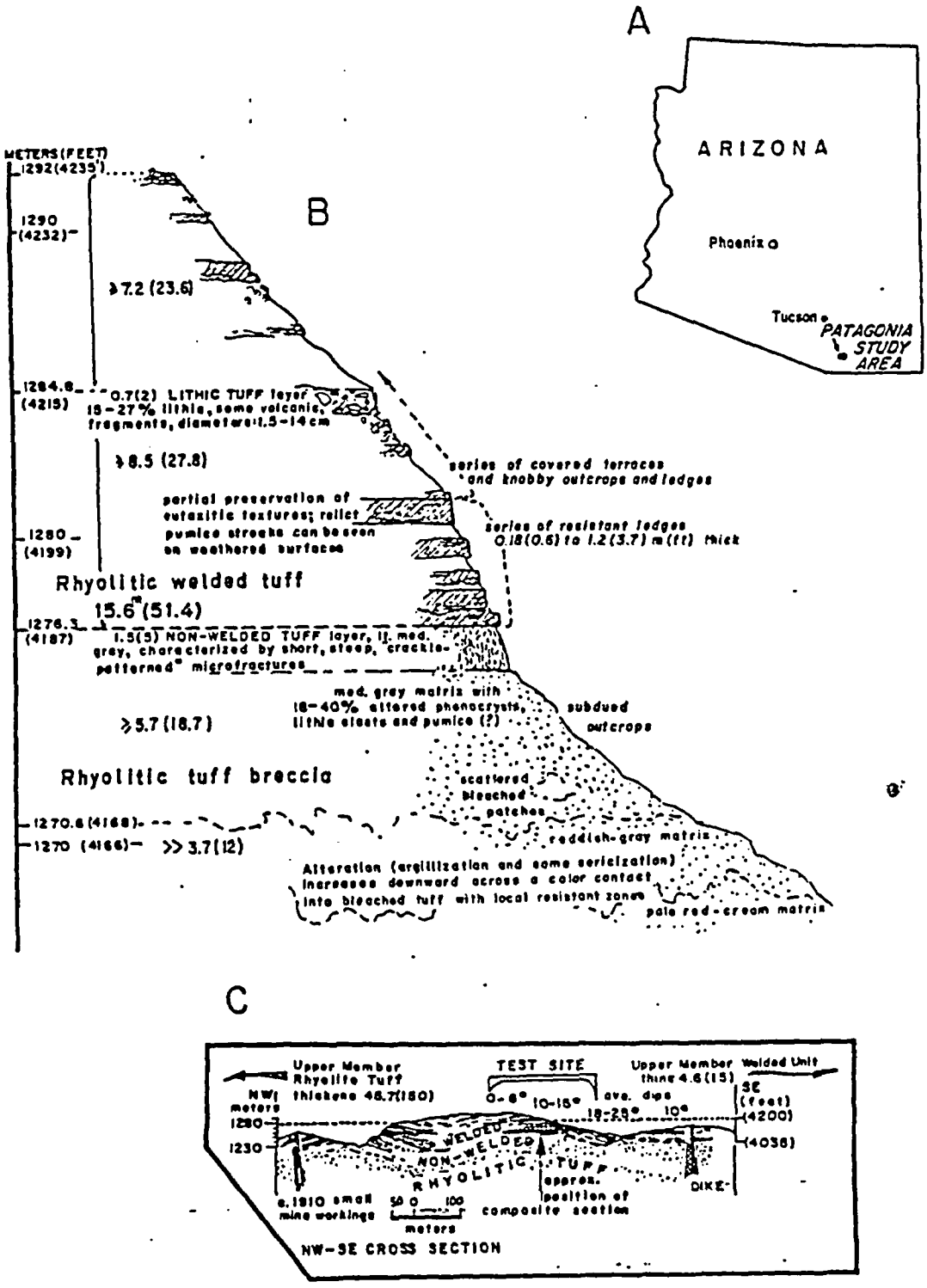

Figure 1.11 Site location map (A), partial stratigraphic section (B), and structural cross-section (C) of Patagonia study area.

tuff is approximately 15 m thick (Figure 1.12). It overlies the lower member of the Gringo Gulch Volcanics, a non-trending undifferentiated rhyolitic tuff, and is dissected by a northwest-trending fault (Drewes, 1971). The Gringo Gulch Volcanics lies unconformably upon the upper Cretaceous Josephine Canyon Diorite, whose youngest member is 65 million years old (Drewes, 1972).

The welded tuff at the Patagonia study area is relatively flat. Dips range from 5 to 9° striking an approximate north to northwest direction. Horizontal fractures in the tuff are evidenced by a series of terraces and ledges (Figure 1.13) which produce an obvious bedded appearance. The tuff matrix is microcrystalline, dark blue-gray in color, and contains less than 10 to 20 percent phenocrysts of altered biotite and plagioclase. Flattened, subparallel, aligned pumic fragments, with an estimated 15:1 length-width ratio, are evidence of a high degree of welding.

Vertical fractures in the tuff are considered to be the major form of recharge through the unsaturated zone. The large number of fractures present in the tuff is likely the result of the brittle nature of the rock. No single dominant vertical fracture strike pattern is apparent. It is likely that a combination of fracture-inducing events, such as contraction due to cooling and tectonic events, produced the random strike pattern at the Patagonia study area. Near the perimeter of the study area large blocks break off the ledges revealing the nature of the vertical fracture planes at depth. The planes are surprisingly smooth, free of fracture waviness and abnormalities (Figure 1.14).

1.3.2 Superior Study Area

The Superior study area is located near the extreme western edge of the Pinal mountains of central Arizona. Elevations rising above 2100 m are found in the Mazatzal Mountains, 50 km to the north-northwest, in the Sierra Ancha Mountains, 56 km to the north-northwest, and in the Pinal Mountains, 25 km to the east (Sellers, 1974).

Dacitic ash-flow deposits at one time covered an area of approximately 1000 km^2 in the region. Presently, this area has been reduced by erosion to 250 km^2. Although the average thickness of the ash flow is about 150 m, its thickness exceeds 600 m east of Superior (Peterson, 1961). Ash-flow tuffs are consolidated deposits of volcanic ash (diameter less than 0.4 mm) resulting from a turbulent mixture of gas and pyroclastic materials of high temperature, ejected from a crater, that have traveled rapidly down the slope of a volcano. The beds

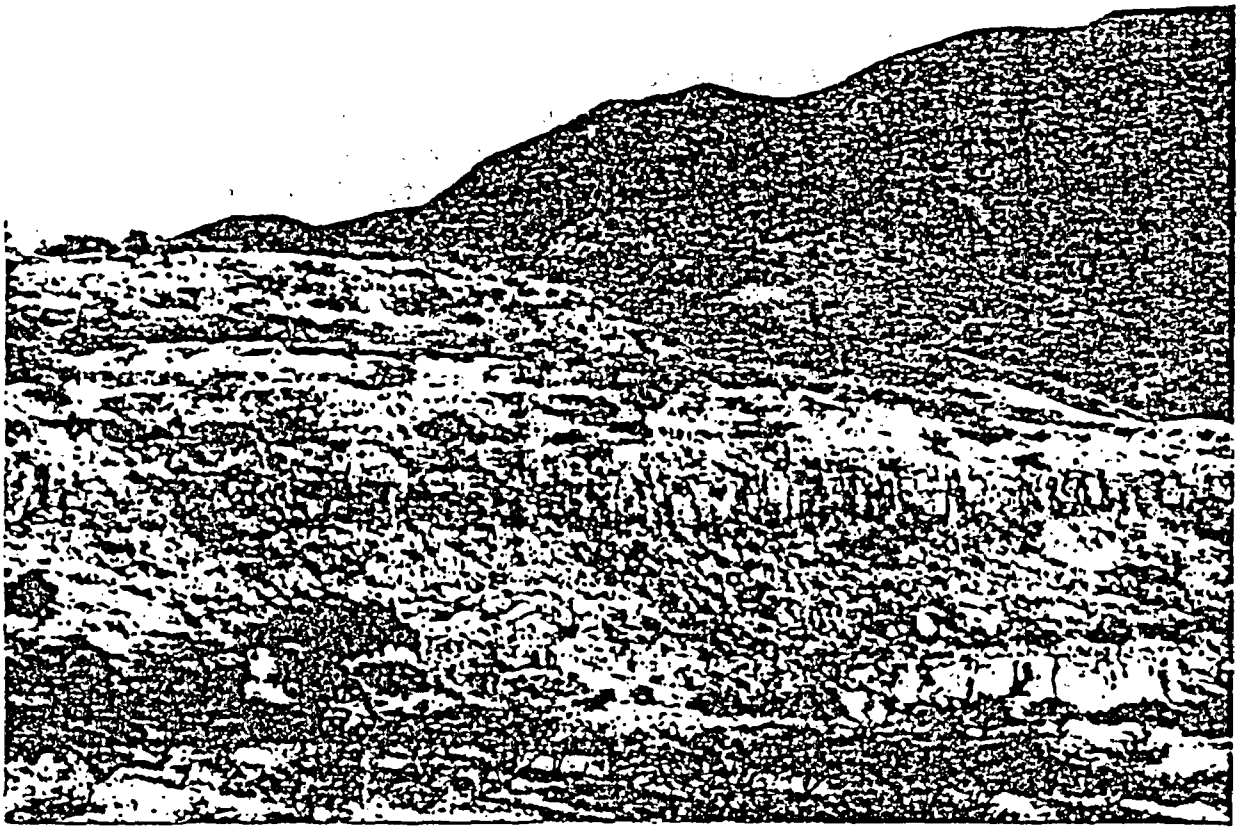

Figure 1.12 Photograph of the Patagonia study area welded tuff outcrop.

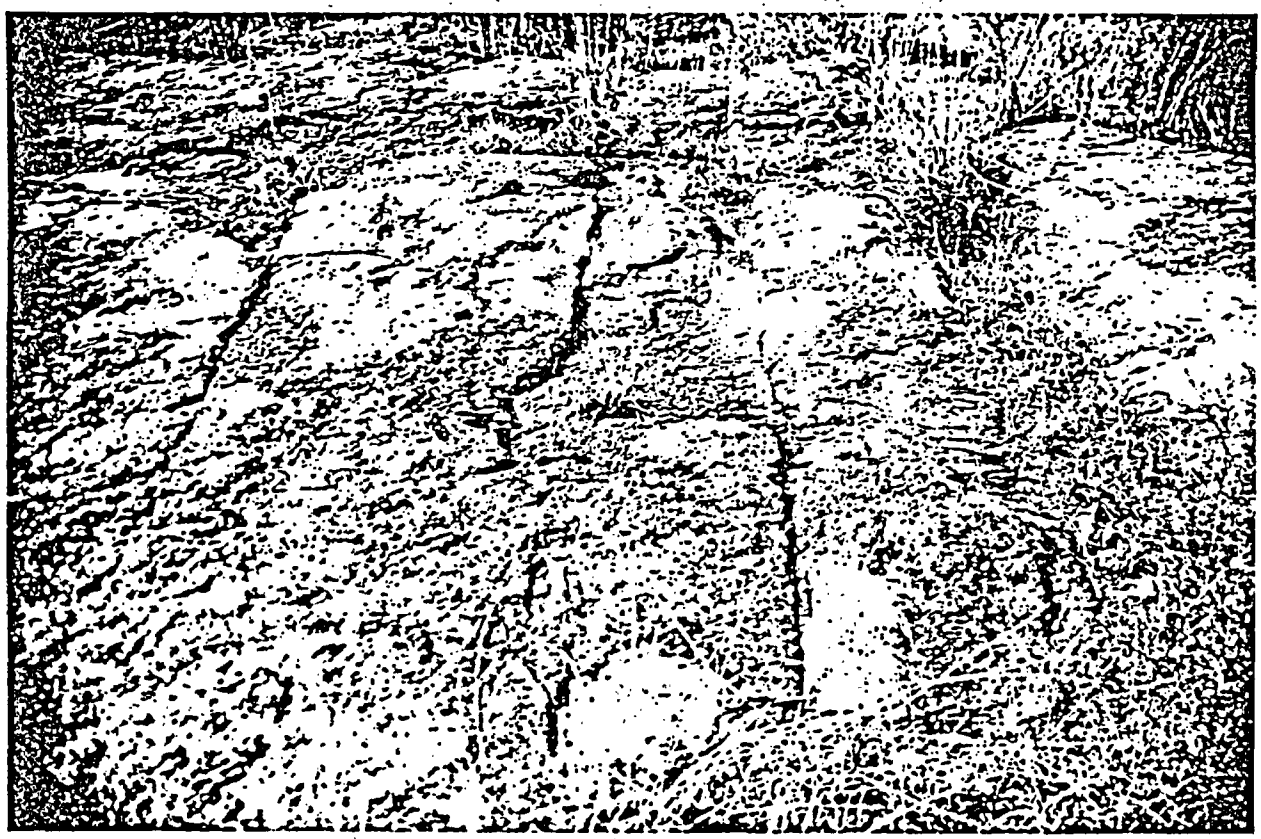

Figure 1.13 Photograph of the Patagonia study area surface.

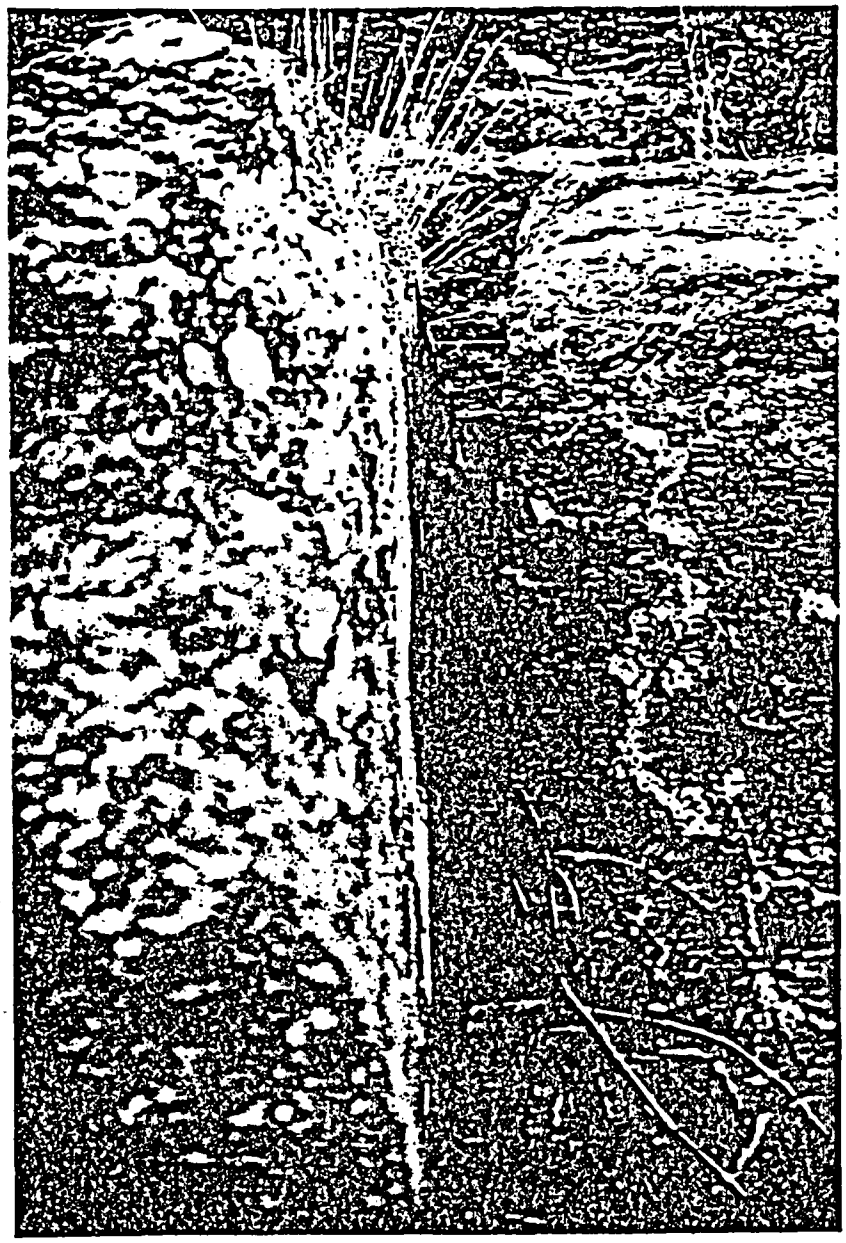

Figure 1.14 Photograph showing a vertical fracture plane area at the Patagonia study area.

resulting from this flow mechanism may or may not be completely or partially welded (Ross, 1961).

The geologic deposit in the which the Superior study area is located is a dacitic ash-flow sheet made up of an undeterminated number of separate ash flows. The ash flows have been dated to 19.9 ± 0.9 million years (middle Miocene age). It is believed they were erupted in rapid succession to form a single ash-flow sheet, which represents a single cooling unit. In places, the individual units cannot be recognized.

Part of the ash flow is composed of densely-welded tuff, other parts are slightly-welded. Peterson (1968) divided the ash-flow sheet into five different units based upon the degree of welding (Figure 1.15). Peterson also determined, on the basis of chemical composition, that the volcanic ash-flow sheet is a quartz latite. Although classified as a quartz latite, dacite is a genetically more descriptive term because the tuff units consist of large phenocrysts embedded in a groundmass. The mineralogy of the phenocrysts (ranging in diameter from 0.5 to 3.0 mm) and the crypto- and micro-crystalline groundmass is presented in Table 1.2 for the brown zone.

Table 1.2 Mineralogy of the Magma Quartz Latite, after Peterson (1961).

Phenocrysts (0.5 - 3 mm)		Groundmass (< 0.5 mm)	
Plagioclase	75 %	Cristobalite	-
Quartz	10 %	Potassium feldspar	-
Biotite	10 %	Quartz	-
Sanidine	-	Plagioclase	-
Magnetite	< 5 %		
TOTAL	35 - 45 %	TOTAL	55 - 65 %

Three test sites have been developed in the tuff deposit. The highest site both stratigraphically and elevationally is the Apache Leap site, located in slightly-welded tuff. Lower in the column are two densely-welded tuff sites. The Queen Creek road tunnel site is located approximately 200 m below the Apache Leap site in an abandoned road tunnel on U.S. Route 60, below the new road tunnel. The main haulage tunnel in the Magma Mine is the third site, located approximately 200 m below the Queen Creek road tunnel site.

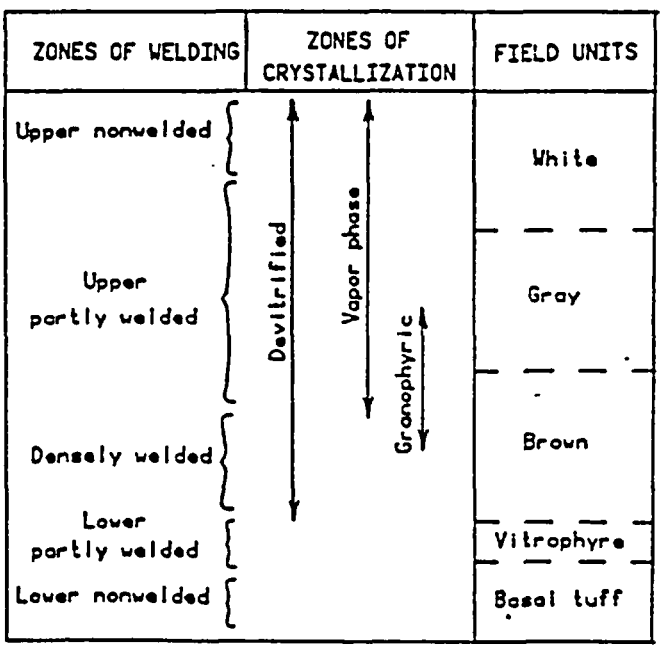

Figure 1.15 Physical characteristics of the dacitic ash-flow sheet.

1.3.2.1 Apache Leap Field Site

Three boreholes have been placed in slightly-welded volcanic tuff at the Apache Leap site near Superior, Arizona (Figure 1.16). The 10-cm diameter boreholes are inclined at an angle of 45° from the vertical and are offset from each other by a vertical distance of 10 m (Figure 1.17). The boreholes vary in length from 18.3 m for the uppermost (X-1), to 46.6 m for the lowermost (X-3), with the intermediate borehole (X-2) having a length of 32.6 m. This design allows for the monitoring of fluid and solute flow in both the horizontal and vertical directions.

Scribed cores with a diameter of 6.35 cm were also obtained from the borehole. The scribing tool provided an orientation mark every 3.05 m. The cores have been logged to provide information regarding the location and orientation of fractures within the boreholes, and the composition and occurrence of fracture fillings. This information is presented in Table 1.3. X-ray diffraction and thin sections of the host rock and the fracture fillings are also being made.

To determine the alignment of the boreholes, photographs of a downhole gyroscope have been obtained. The photographs indicate that the total displacement of the boreholes from design specifications amounted to less than 1.5°. Additionally, downhole televiewer images have been obtained. Due to instrument difficulties only one borehole was viewed.

1.3.2.2 Queen Creek Road Tunnel Site

The Queen Creek road tunnel site is located in the unit with the highest degree of welding. Because the unit is noticably darker than the overlying unit, the unit is also referred to as the brown unit. The site is developed in an abandoned road tunnel on U.S. Route 60, below the new road tunnel.

The bulk density of the brown zone, calculated from core samples, is approximately 2.41 grams per cubic centimeter, and the matrix porosity is about 9.0 percent. The fracture density, also from core data, is three fractures per meter. Estimating an average aperture of 300 micrometers, a crack porosity of 0.1 can be calculated. An estimate of total porosity for the Magma brown zone is, therefore, 9.1 percent.

Jointing at the Queen Creek road tunnel site is not as conspicuous in the dacite as it is in the quartz monzonite at the Santo Nino mine site. Blast damage resulting from the construction of the road tunnel helped to mask natural fractures in the dacite, making mapping difficult.

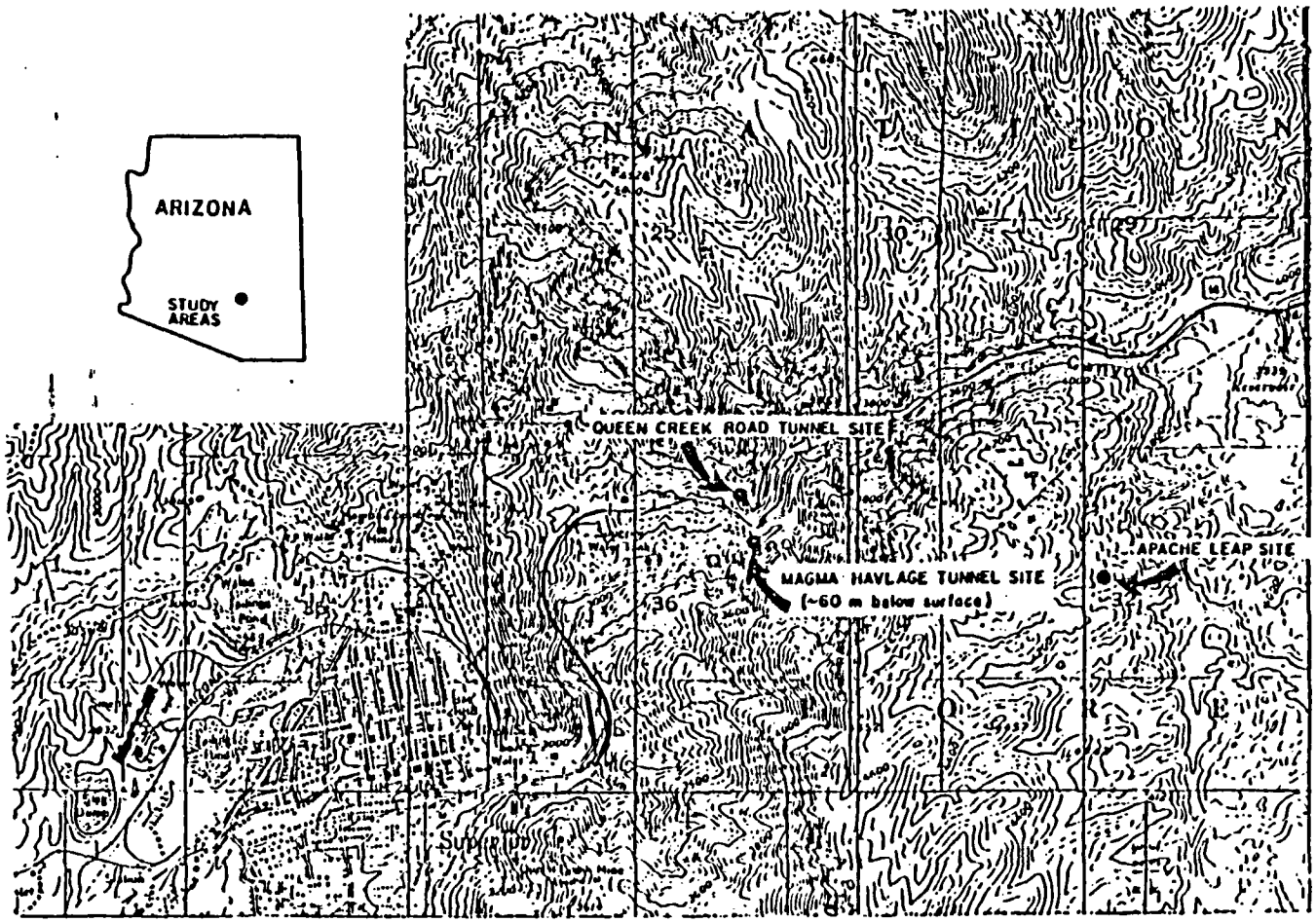

Figure 1.16 Location map of Superior field sites.

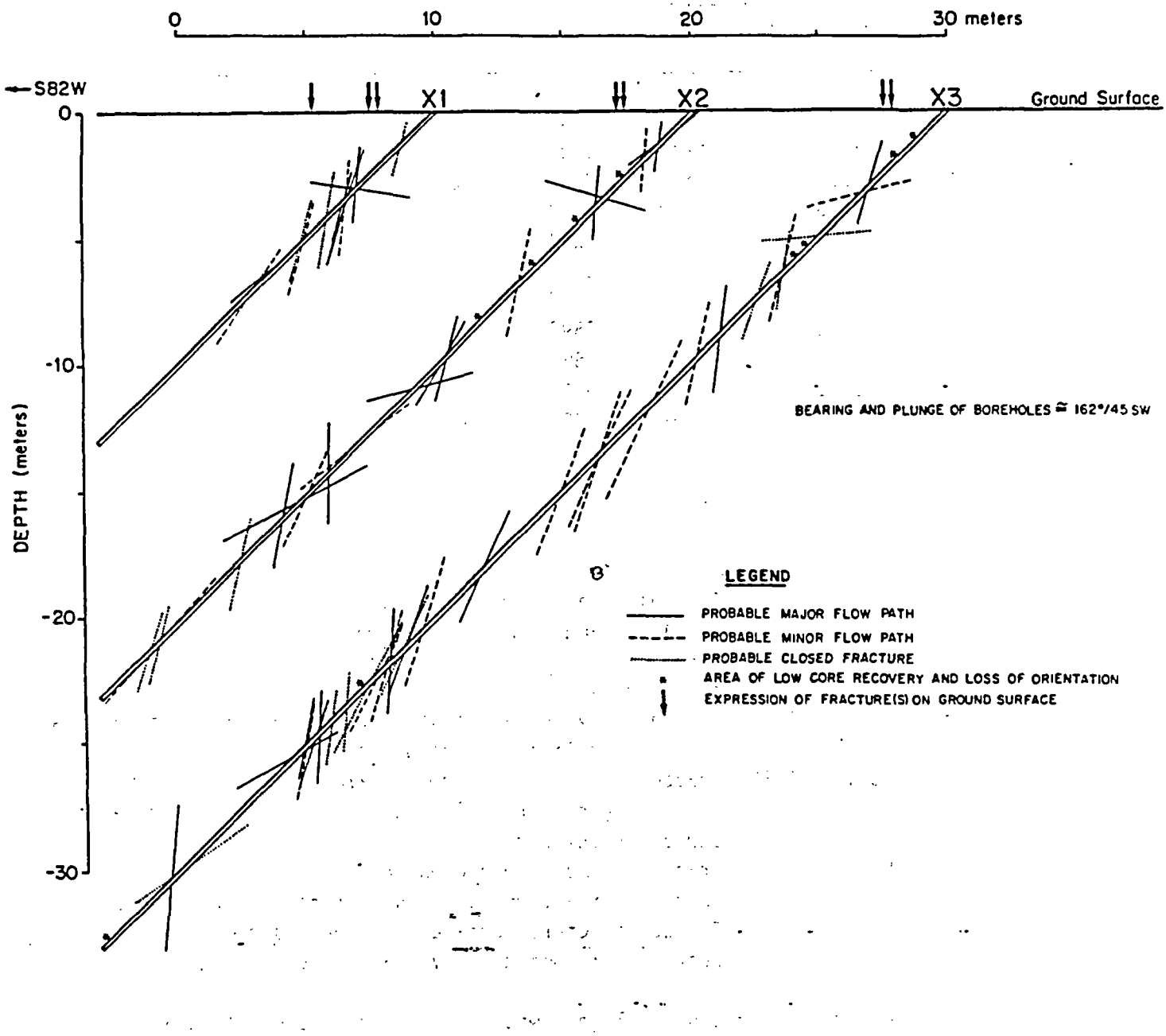

Figure 1.17 Borehole diagram, Apache Leap field site.

Table 1.3 Results of fracture survey at Apache Leap tuff site.

Borehole X-1 (Total Borehole Length 18.44 m)

Distance from Surface (m)	Class[1]	Strike	Dip ---- True	Dip ---- Apparent[2]
1.77	*	345°	75°	75°
4.15	****	352°	85°	85°
4.33	****	215°	12°	171°
4.36	****	346°	73°	73°
4.63	****	329°	76°	75°
4.79	***	336°	84°	84°
5.73	*	326°	82°	81°
6.92	***	359°	75°	75°
7.13	*	358°	69°	69°
8.93	****	031°	48°	40°
9.78	***	035°	64°	56°

[1] Class:

**** OPEN	Probable major flow channel, fracture surfaces separate easily upon removal from core barrel and wasclearly open when in situ. Fracture surfaces highly weathered and friable.
*** PARTLY OPEN	Same as above except that exposed fracture surface shows portions of little to no weathering.
** POSSIBLY OPEN	Fracture aperture filled or nearly filled with minerals indicating historic flow but limited flow at present. Surface subplanar.
* CLOSED	Fracture remains unbroken when core is removed from core barrel or fracture surfaces mesh tightly together. Exposed fracture surfaces show no visible sign of weathering; some display trace minerals.

[2] Apparent dip of fractures aligned with bearing of borehole (262°)

Table 1.3 (Continued)

Borehole X-2 (Total Borehole Length 32.61 m)

Distance from Surface (m)	Class[1]	Strike	Dip ---- True	Dip ---- Apparent[2]
1.77	****	359°	82°	82°
2.32	****	300°	56°	42°
2.38	***[3]	-	-	-
2.47	-	359°	85°	85°
3.63	** [3]	-	-	-
3.69	** [3]	-	-	-
3.75	** [3]	-	-	-
4.85	***	191°	17°	164°
5.18	****	354°	84°	84°
6.07	**[3]	-	-	-
8.50	** [3]	-	-	-
9.14	***	347°	78°	78°
10.67 to 12.19	----	low core recovery		----
13.38	****	331°	75°	74°
13.56	****	342°	59°	59°
15.49	****	20°	17°	15°
15.51	****	20°	17°	15°
18.68	***	032°	47°	39°
20.27	***	327°	89°	89°
21.03	***	334°	67°	66°
21.67	****	16°	30°	28°
22.49	****	347°	79°	79°
24.78	*	339°	76°	76°
28.47	***	303°	60°	49°
28.56	* [3]	-	-	-
28.65	***	44°	63°	50°
29.23	*	318°	78°	76°
29.38	*	3°	72°	72°

1 See note on initial page of table.
2 See note on initial page of table.
3 No orientation possible either due to very subplanar fracture, high degree of mineralization closing fracture, or loss of orientation during drilling.

Table 1.3 (Continued)

Borehole X-3 (Total Borehole Length 46.64 m)

Distance from Surface (m)	Class[1]	Strike	Dip ---- True	Dip ---- Apparent[2]
1.62	****[3]	-	-	-
2.74	** [3]	-	-	-
4.15	****	356°	74°	74°
4.60	***	338°	14°	14°
5.52	* [3]	-	-	-
7.01	***	19°	6°	5°
7.01 to 7.62	*	---- low core recovery ----		
7.62	* [3]	-	-	-
7.62 to 8.53	*	---- low core recovery ----		
8.83	**	5°	79°	79°
9.02	***	337°	76°	76°
10.12	*	20°	73°	71°
12.44	****	332	83°	82°
13.32	***	343°	76°	76°
15.85	***	336°	66°	65°
18.62	***	11°	67°	66°
18.90	***	6°	71°	71°
21.03	***	334°	71°	70°
25.60	***	10°	67°	66°
25.73	****	336°	66°	65°
28.68	***	8°	74°	73°
29.66	****	329°	72°	71°
29.81	**	11°	66°	65°
30.54	****	312°	87°	86°
30.60	***	336°	78°	76°
31.21	***	328°	66°	64°
31.58	**	336°	64°	63°
31.70 to 32.52	**	---- low core recovery ----		

(Borehole X-3 continued on next page)

1 See note on initial page of table.
2 See note on initial page of table.
3 See note on initial page of table.

Table 1.3 (Continued)

Borehole X-3 (Continued)

Distance from Surface (m)	Class[1]	Strike	Dip ---- True	Dip ---- Apparent[2]
32.64	*	332°	85°	85°
33.65	*	337°	82°	82°
34.47	****	339°	87°	87°
34.45	****	342°	72°	72°
35.14	***	324°	81°	80°
35.23	****	323°	80°	79°
35.97	****	316°	36°	29°
42.25	*	52°	55°	35°
42.55	****	309	86°	85°
46.30	* [3]	-	-	-

1 See note on initial page of table.
2 See note on initial page of table.
3 See note on initial page of table.

Moisture conditions in the dacite at the road tunnel site are measured using two sets of two boreholes drilled approximately 0.9 meters apart. In addition to measurements of moisture conditions, heater experiments have been performed to determine the movement of water in the presence of a strong thermal driving force.

1.3.2.3 Magma Site

The Magma field site is located inside Magma Copper Company's "Never Sweat" haulage tunnel in Superior, Arizona. Two horizontal holes were drilled where the densely-welded tuff intersects the "Never Sweat" haulage tunnel. These holes, 4.75 centimeters in diameter, are located 1800 meters from the portal and 80 meters below the surface (Figure 1.18). The 15-meter top hole was logged periodically with the resistivity and neutron probes between March an August 1983. Water did not stop flowing from the 22-meter bottom hole until June 1983. Therefore, this hole was not logged. Flowrates for the lower borehole are presented in Figure 1.19.

1.4 Laboratory Facilities

In addition to the field sites identified above, laboratories have been developed which provide facilities for the analysis of materials obtained from field sampling. These facilities include a constant temperature laboratory which is necessary for the isolation of samples from the effects of variable thermal influences. In addition, laboratory space is available for determining the porosity and moisture content of rock samples.

Available facilities also include four Tempe pressure cells, a rock-coring bit, a 5-bar and a 15-bar pressure plate extractor. This equipment is used for obtaining moisture release curves. Drilling equipment is also available to provide 5-cm rock cores. X-ray diffraction equipment is available for determining the composition of rock samples.

1.5 Computer Facilities

Simple numerical problems are solved using IBM-PC microcomputers equipped with 8087 numeric co-processors. For larger problems, a VAX 11/780 computer operating under VAX/VMS 4.1 is available. In applications where the VAX system is inadequate to arrive at a solution in a cost-effective manner, a CYBER 175 operating under NOS/BE 1.7 is used.

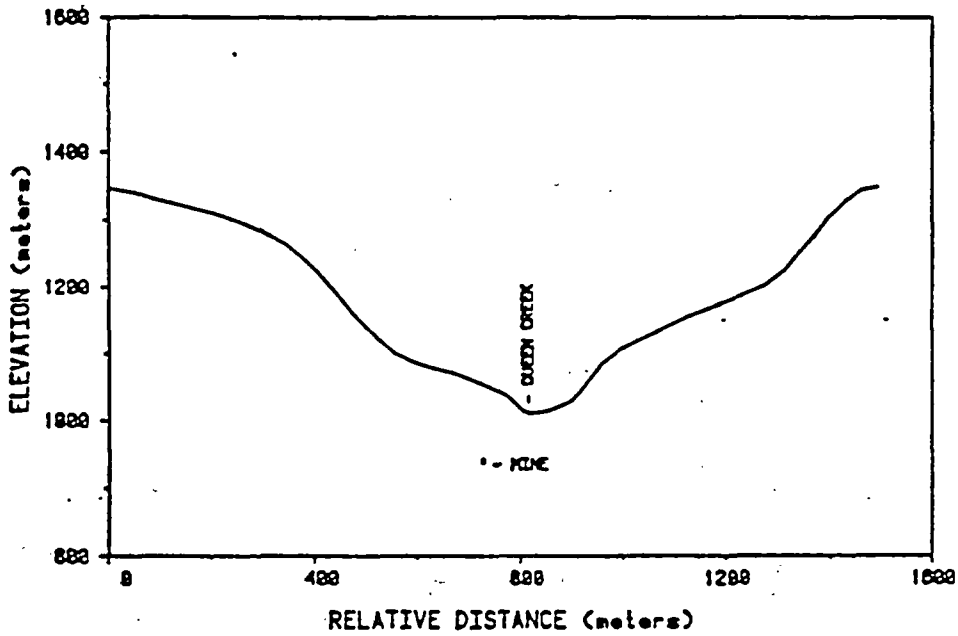

Figure 1.18 View perpendicular to the Magma haulage tunnel.

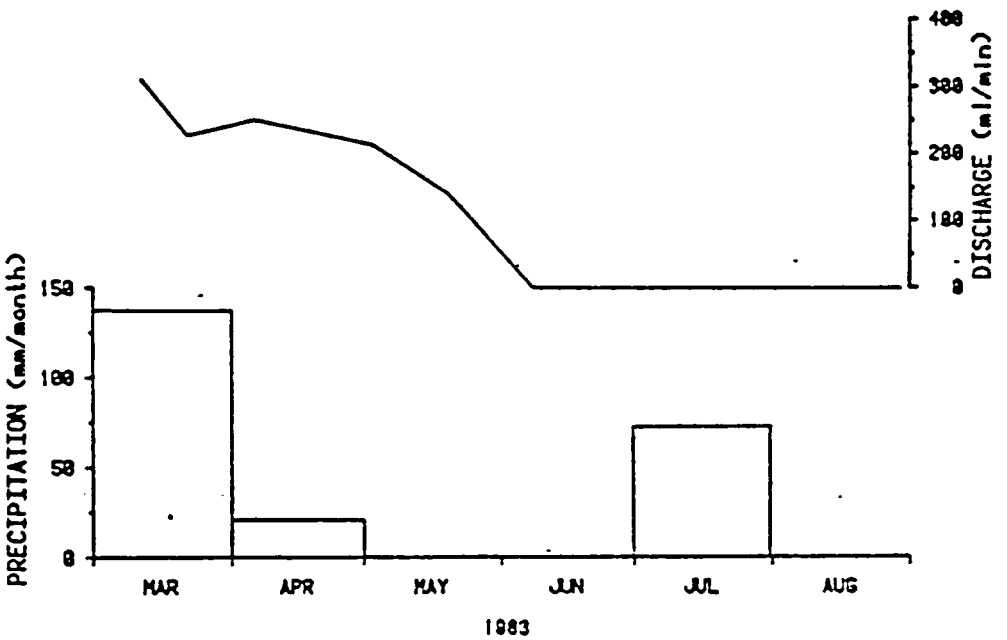

Figure 1.19 Flow rates from the lower borehole (line graph) and precipitation (bar graph) versus time at Magma field site.

CHAPTER 2
ROCK CHARACTERIZATION

Fluid fluxes and transport of solutes in geologic media are dependent on the physical and hydraulic properties of the media. The transport of solutes is also strongly dependent upon the degree of interaction between the medium and the solute. Of particular interest is the assessment of parameters which determine fluid and solute travel times and fluxes over space and time. By knowing the physical relations between measurable parameters, an improved understanding of factors which affect the travel times and fluxes are obtained, and quantification of processes are possible.

An important factor affecting ground-water travel times and fluxes is the hydraulic conductivity. At any point in the geologic media, the saturated hydraulic conductivity generally remains constant, only changing due to variable stress loading and temperatures. Unsaturated hydraulic conductivity, however, can vary with water content over time at a point, even at constant stress levels and temperatures.

Emphasis in this chapter is placed on the measurement techniques for physical parameters important in determining the unsaturated hydraulic conductivity, specifically in relation to the low permeability rocks in which a high-level nuclear waste repository site might be located. The use of these parameters for the purpose of determining the hydraulic conductivity is discussed in Chapter 3.

This chapter focuses on the characterization of rock-matrix properties, followed by a characterization of rock-fracture properties.

2.1 Rock Matrix Characterization

To characterize the capacity of a rock matrix for fluid fluxes and solute transport, several parameters must be evaluated:

(1) Total and matrix porosities, for determining total water holding capacity;
(2) Pore-size distribution, for determining the unsaturated hydraulic conductivity and the fluid content as a function of potential; and
(3) Matrix-specific surface areas, for determining sorption capacities.

2.1.1 Matrix Porosity Determination

The total porosity of a rock mass is the percentage of the total volume of a rock sample which is not occupied by the solid matrix. The matrix

porosity of a geologic medium is the amount of pore space within a rock mass, exclusive of fractures and sizable solution openings. The matrix porosity might include pores which are isolated from other pores or which dead-end. Both dead-end and isolated pores do not normally provide a conduit for the movement of fluids.

The effective matrix porosity refers specifically to interconnected pores, and is always less than the total matrix porosity. It is important to note that most techniques used to measure matrix porosity actually measure the total matrix porosity. Yet, the effective porosity is perhaps the more relevant parameter for predicting flow and diffusion rates within geologic media.

Porosities can be evaluated using four experimental techniques:
(1) Paraffin method;
(2) Water saturation method;
(3) Gravimetric method; and
(4) Gamma ray attenuation.
These techniques have been applied to rock samples obtained at the field study areas described in Chapter 1. A description of each technique is given in the following sections.

2.1.1.1 Paraffin Method

The paraffin method measures the total matrix porosity by weighing an oven-dried sample, then coating the sample with paraffin and measuring its buoyancy in water. The technique first requires that samples be oven-dried at 104°C and weighed daily to determine the total moisture loss. Once all interstitial moisture has evaporated, the samples are removed from the oven and cooled to room temperature. They are then dipped in molten paraffin heated to slightly above the melting temperature of the paraffin. After the paraffin coating solidifies and cools, the samples are weighed to determine the total amount of paraffin added to the sample. The volume of paraffin added can be calculated by dividing the weight of paraffin by the its density.

The samples are then suspended in water with thread, and reweighed to determine their buoyancy. The volume of rock plus paraffin can be calculated from the buoyancy, and from this, the bulk volume of sample can be determined. The bulk density can be calculated using:

$$(2.1) \qquad \rho_b = \rho_w W_d / (W_d - W_w + W_p(1-\rho_w/\rho_p))$$

where

ρ_b is the dry bulk density;
ρ_w is the density of water;
ρ_p is the density of paraffin, approximately 0.9;
W_d is the weight of the oven-dried sample;
W_w is the weight of the paraffin-coated sample in water; and
W_p is the weight of the paraffin coat.

The porosity is then determined by:

(2.2) $$n = 1 - \rho_b / \rho_s$$

where
n is the matrix porosity;
ρ_b is the dry bulk density; and
ρ_s is grain density.

An advantage of the paraffin method lies in the fact that any shaped sample may be used. A disadvantage of the technique is that foreknowledge of the grain density is required.

Four rock samples have been collected from the Magma Mine Number Nine Shaft vicinity, near Superior Arizona. These samples were of the slightly-welded unit of the Apache Leap tuff. Each rock was split into two sub-samples of approximately 5 cm diameter, and the paraffin technique was used to determine the total matrix porosity.

2.1.1.2 Water Saturation Method

The water saturation measures the effective matrix porosity by determining the volume of a regularly-shaped sample, such as a cylindrical core, then saturating the previously oven-dried sample under a vacuum and determining the saturated water content. The method yields the effective porosity,

(2.3) $$n_e = V_w / V_s$$

where
n_e is the effective matrix porosity;
V_w is the volume of water required to saturate the sample; and
V_s is the volume of the sample.

The porosity is determined by de-gassing the core samples in a vacuum and saturating them with water. Assuming full saturation, the volume of interconnected voids is calculated by weighing the water within the

cores. The difference between the matrix porosity and the effective porosity determined using this method is an indicator of the relative ratio of interconnected to isolated pores.

2.1.1.3 Gravimetric Method

The gravimetric method uses the same technique as the water saturation method, except the dry weight is used to calculate the bulk density and Equation (2.2) is used to calculate the total matrix porosity.

2.1.1.4 Gamma Ray Attenuation

A gamma ray attenuation method has also been used to determine the range of total matrix porosity of slightly-welded tuffs. The method is described in detail in Section 4.1. Briefly, the method employs a radiation beam which is attenuated as it passes through a sample. The magnitude of the attenuation is a direct function of the water content of the sample.

2.1.1.5 Comparison of Techniques

The porosity ranges of slightly-welded and densely-welded tuffs, and granodiorites have been measured and are presented as Figure 2.1. Table 2.1 contains data for the slightly-welded Apache Leap tuff obtained using the four methods described above. The water saturation results indicate an average effective matrix porosity of 18.1 percent for 6 samples obtained from cores removed from a tuff boulder. The paraffin technique was used on 7 rock chips with a resulting average total matrix porosity of 15.5 percent.

The results from the gamma-ray technique are from one core which measures 6.35 cm in diameter by 12.5 cm in length, with the measurement sites distributed 1 cm apart along the core. The range in total porosity over the core is 18.6 to 21.7 percent. The overall average for the twelve values is 20.0 percent. The same core was used to determine the total porosity using the gravimetric technique, which yielded an identical estimate of 20.0 percent. Table 2.2 presents results for densely-welded Apache Leap tuff. The results from two methods provide an average total porosity of approximately nine percent.

These preliminary results indicate a large spatial variation in the bulk density and porosity, as well as a sizable variation within a single core. A grain density of 2.65 g/cm^3 (used in the calculations) is tentative, based on the rock mineralogy. The density of rock powder can

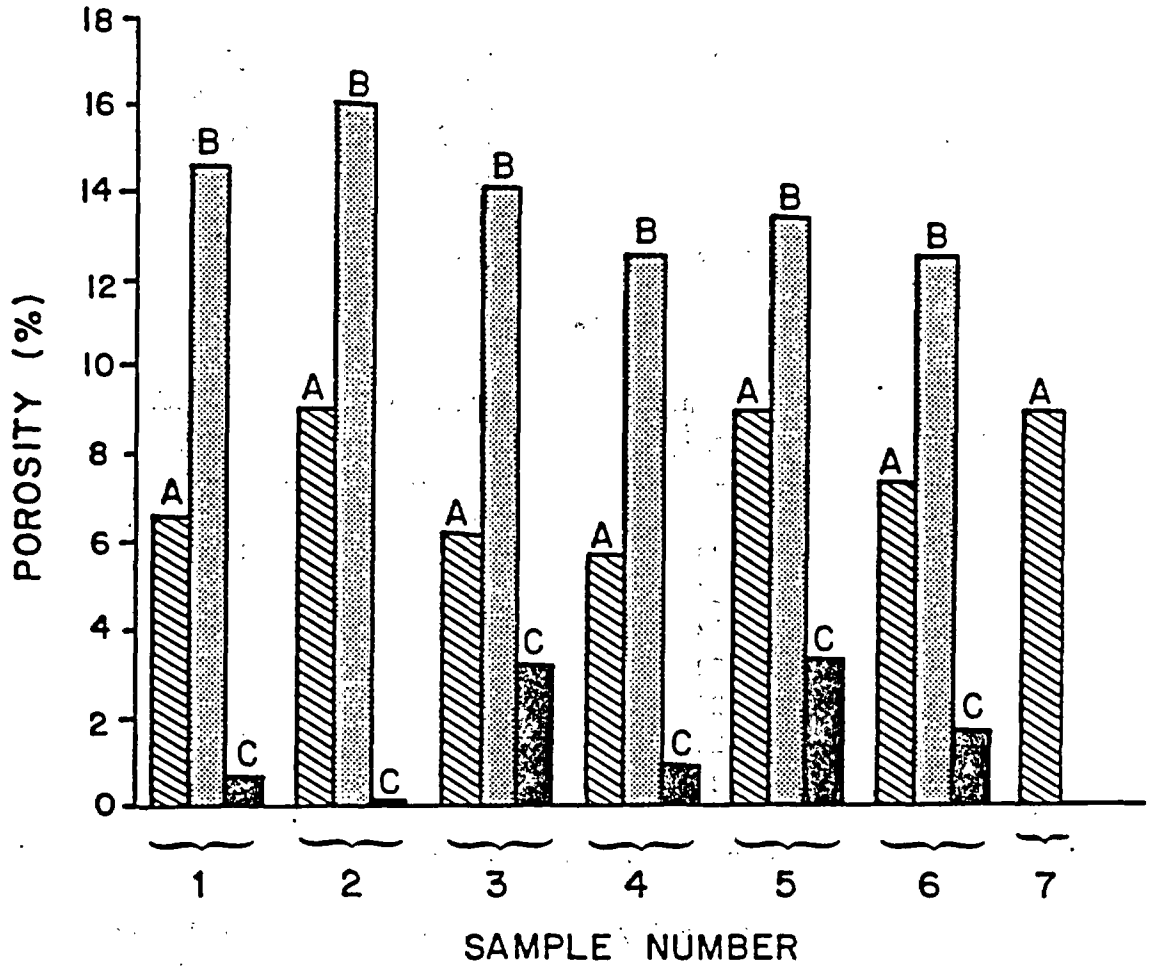

Figure 2.1 Range of primary porosities for samples of partially-welded tuff using the paraffin method (A), partially-welded tuff using the water saturation method (B), and granodiorite using the water-saturation method (C).

Table 2.1 Porosity measurements of the slightly-welded Apache Leap tuff.

Water Saturation Method

Sample Number	Bulk Density (g/cm^3)	Effective Porosity	Total Matrix * Porosity
1	2.07	17.3 %	21.9 %
2	2.03	19.1	23.4
3	2.08	17.8	21.5
4	2.11	17.8	20.4
5	2.09	18.6	21.1
6	2.12	17.8	20.0
Mean	2.08	18.1	21.4

Paraffin Method

Sample Number	Bulk Density (g/cm^3)	Effective Porosity	Total Matrix * Porosity
1	2.26	-	14.7 %
2	2.20	-	17.0
3	2.27	-	14.3
4	2.28	-	14.0
5	2.20	-	17.0
6	2.24	-	15.5
7	2.20	-	17.0
Mean	2.24	-	15.5

Gamma Ray Attenuation Method

Sample Number	Bulk Density (g/cm^3)	Effective Porosity	Total Matrix * Porosity
Range	-	-	18.5 to 21.7 %
Mean	-	-	20.0

* Using ρ_s of 2.65 g/cm^3

Table 2.2 Porosity measurements of the densely-welded Apache Leap tuff.

Paraffin Method

Sample Number	Bulk Density (g/cm^3)	Effective Porosity	Total Matrix Porosity *
1	2.42	-	8.75 %
2	2.43	-	8.49
3	2.41	-	9.02
4	2.41	-	8.94
5	2.40	-	9.55
Mean	2.41	-	8.95

Gravimetric Method

Sample Number	Bulk Density (g/cm^3)	Effective Porosity	Total Matrix Porosity *
1	2.41	-	9.06 %
2	2.41	-	9.06
Mean	2.41	-	9.06

* Using ρ_s of 2.65 g/cm^3

be used to determine the grain density, yet results for the tuff give unreasonably low values.

2.1.2 Pore-Size Distribution

Determination of the pore-size distribution is also critical to understanding unsaturated flow and solute transport. Mercury infusion (Gregg and Sing, 1967) and nitrogen gas adsorption (Norton and Knapp, 1977) are two commonly used techniques for determining the pore-size distribution of porous materials.

2.1.2.1 Mercury Infusion

A mercury porosimeter was constructed from a pycnometer and Ruska mercury pump, and a pore-size distribution for pores greater than 0.1 μm in radius was determined (Walter, 1982). The apparatus is comparable to available standardized mercury porosimeters, and is capable of supplying pressures of up to 140 bars. This enabled pores greater than 0.1 μm in radius to be mercury-intruded, as calculated by Washburn's equation:

$$r = 2\,T \cos \alpha \,/\, P \qquad (2.4)$$

where

r is the pore radius;
T is the surface tension;
α is the contact angle of mercury, equal to 140°; and
P is the applied pressure.

The mercury infusion method involved placing two to three grams of rock sample in a mercury-filled pycnometer, incrementally increasing the pressure within the chamber, and recording the volume of mercury intruded. Approximately 40 pressure intervals were used to establish the pressure/volume relationship, with readings taken every 0.14 bars for the range of 0 to 0.7 bars, every 0.7 bars from 0.7 to 7.0 bars, and every 7 bars from 7 to 140 bars.

The chamber expanded due to increasing pressures. This expansion was measured by repeating the experiment with an empty pycnometer. The blank run was used to calibrate the pressure/volume relationship of the system prior sample testing. Due to the extremely low porosities, a blank was also run using two silica marbles in the pycnometer.

Six granodiorite samples from the Santo Nino mine and two welded tuff samples from near Kingman, Arizona were analyzed using these techniques.

Each rock sample weighed 3 to 6 kg, and showed little apparent weathering. The samples were crushed using the U.A. Department of Mines ore crushing machines, and then sieved for ten minutes into five fractions ranging from less than 1 mm to greater than 9.4 mm in diameter. The four larger fractions were washed to remove smaller particulates and then oven dried at approximately 105 °C. The smallest fraction was used for grain density measurements, the 1 to 2 mm fraction was used for gas adsorption analysis, and the largest fraction was used for mercury infusion analysis.

2.1.2.2 Nitrogen Gas Adsorption

This method involves physically sorbing and then desorbing nitrogen gas at different pressure intervals onto a sample at the temperature of liquid nitrogen (76.8 °K). The total quantity of gas sorbed and desorbed onto the particle surfaces at various pressures is measured, and related to the pore radius through Kelvin's equation (Gregg and Sing, 1967):

$$(2.5) \qquad \ln(p/p_0) = - 2\ T\ V \cos \alpha\ /\ (r\ R\ t)$$

where

p_0 is the saturated vapor pressure;
p is the vapor pressure of the system;
T is the surface tension;
V is the molar volume of adsorbate;
α is the contact angle of liquid and solid;
r is the pore radius;
R is the gas constant; and
t is the temperature.

The sample is placed in a flask of known volume and weight, then weighed and degassed overnight to a pressure of about $1.33\ 10^{-7}$ bars. During the adsorption and desorption process the flask is submerged in a bath of liquid nitrogen to maintain a constant temperature of 76.8 °K. Using a manifold system of known volume (28.99 cm^3) and a second chamber (131.3 cm^3), the volumes and quantities of gas used in the experiment are measured using the equation of state for an ideal gas.

To determine the total volume of the sample, a known quantity of helium in the manifold is allowed to equilibrate with the sample in the flask. Helium is used because it is a non-adsorbing gas. After this determination is made, the flask is again degassed.

An adsorption isotherm is determined by sorbing nitrogen in a quasi-liquid state onto the surface of the material at different partial pressures. After complete saturation at one bar, a desorption isotherm is determined. The resulting complete adsorption-desorption isotherm with hysteresis is then known. The initial sorption curve up to 0.2 (p/p_o) can be used to determine the specific surface area of the sample using the BET equation (Gregg and Sing, 1967). The surface area determined in this manner is a summation of external surface areas plus surface areas on the interior of pores.

The specific surface area of the samples, while valuable information in itself, is not directly used in the determination of the pore-size distribution. The desorption portion of the isotherm (from 1.0 to about 0.5 P/P_o) is instead used for this analysis. The volume of nitrogen drained from the pores is measured for each decrement of pressure. The total pore volume of the samples with radii relating to the decremental pressures measured is determined using Kelvin's equation.

Desorption of the sample results in the determination of the pore-size distribution for the sample, as well as the specific surface area of the interiors. The adsorption-desorption isotherm has been determined for one sample of granodiorite and one sample of densely-welded tuff from near Kingman, Arizona. The 1- to 2-mm sieve fraction was used for these analyses. Analyses were performed on samples weighing 13 to 14 grams because a five gram sample failed to provide an accurate measurement.

2.1.2.3 Comparison of Methods

The two techniques were used to estimate the pore-size distribuion for granodiorite from the Santo Nino Mine. For the low porosity rock (less than 2 percent) and the equipment available, the techniques were applicable over different pore-size ranges. Consequently, an integrated procedure has been devised using mercury infusion for determining the size distribution of pores with radii greater than 0.1 μm and nitrogen gas adsorption for pores of radii between 0.1 and 0.0001 μm.

The pore-size distributions of seven granodiorite samples were determined using the mercury-infusion technique (Figure 2.2). The shape of the distributions are variable among samples, all samples indicating a range of pore-size distributions. Results in the range from 80 to 100 percent are inconclusive due to equipment limitations.

The results of mercury infusion experiments, as well as the bulk density and grain-density measurements for the seven granodiorite samples, are

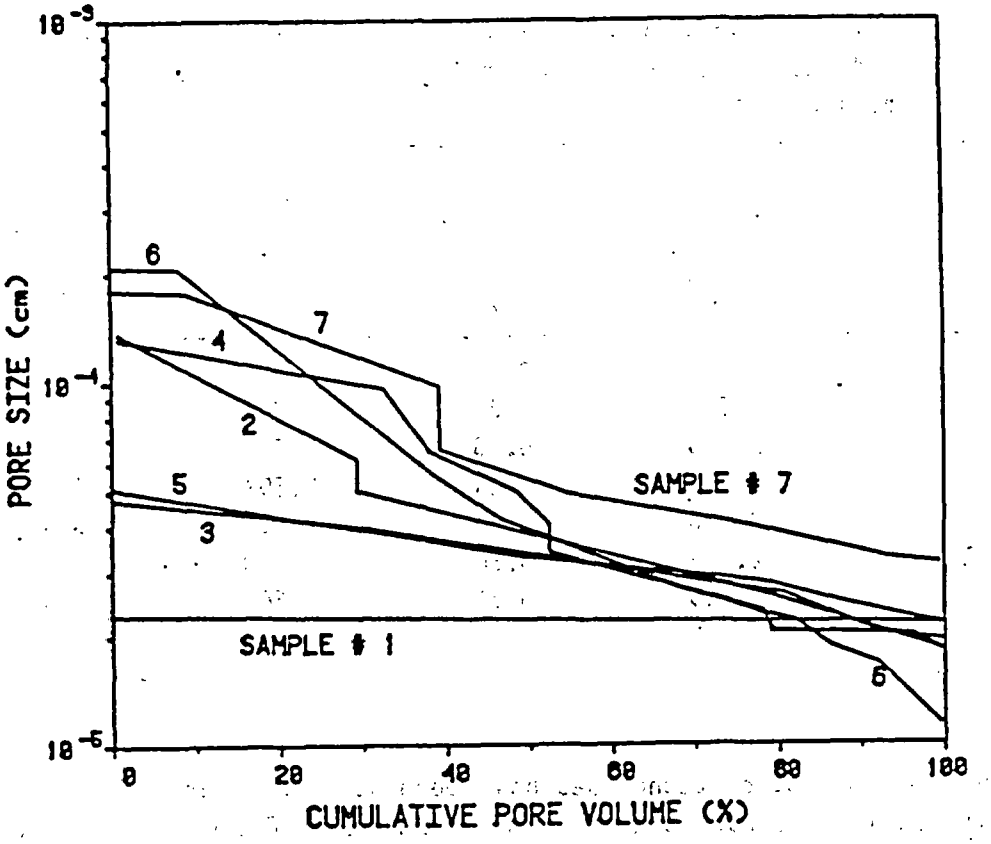

Figure 2.2 Pore-size distribution results from mercury infusion for granodiorite samples.

presented in Table 2.3. In general, the porosity values calculated with grain density measurements exceeded values determined by mercury infusion. This reflects the fact that mercury-infusion methods measure effective porosity, while grain-density calculations yield the total porosity. In addition, the mercury-infusion technique did not measure pores with radii smaller than 0.1 μm.

Table 2.3 Result of bulk density and grain density determinations of granodiorite samples. Percent porosity determination was made using mercury-infusion (Hg) and grain-density (ρ_g) measurements.

Sample	Bulk Density (g/cm^3)	Porosity (Hg) (%)	Grain Density (g/cm^3)	Porosity (ρ_g) (%)
1	2.665	0.05	-	-
2	2.636	0.29	2.654	0.68
3	2.696	0.43	2.697	0.04
4	2.609	1.44	2.697	3.26
5	2.676	0.84	2.703	1.01
6	2.522	4.50	2.610	3.37
7	2.615	0.81	2.663	1.83

Nitrogen gas adsorption techniques have been used to determine the pore-size distributions for pores ranging from 0.1 to 0.0001 μm in radius. Figure 2.3 presents the pore-size distributions determined with nitrogen gas adsorption methods for one of the granodiorite samples (Sample 5). The effective porosities determined by gas adsorption were 0.55 percent for the fraction between 0.1 and 0.0001 μm of the granodiorite samples. Pores with a radius greater than 0.1 μm are not measured by gas adsorption. As seen in Figure 2.3, only about 10 percent of the pore volume is composed of pores larger than 0.1 μm in radius. Figure 2.4 is a graph combining the mercury infusion and gas adsorption pore-size distribution results for a granodiorite sample from the study site at the Santo Nino mine.

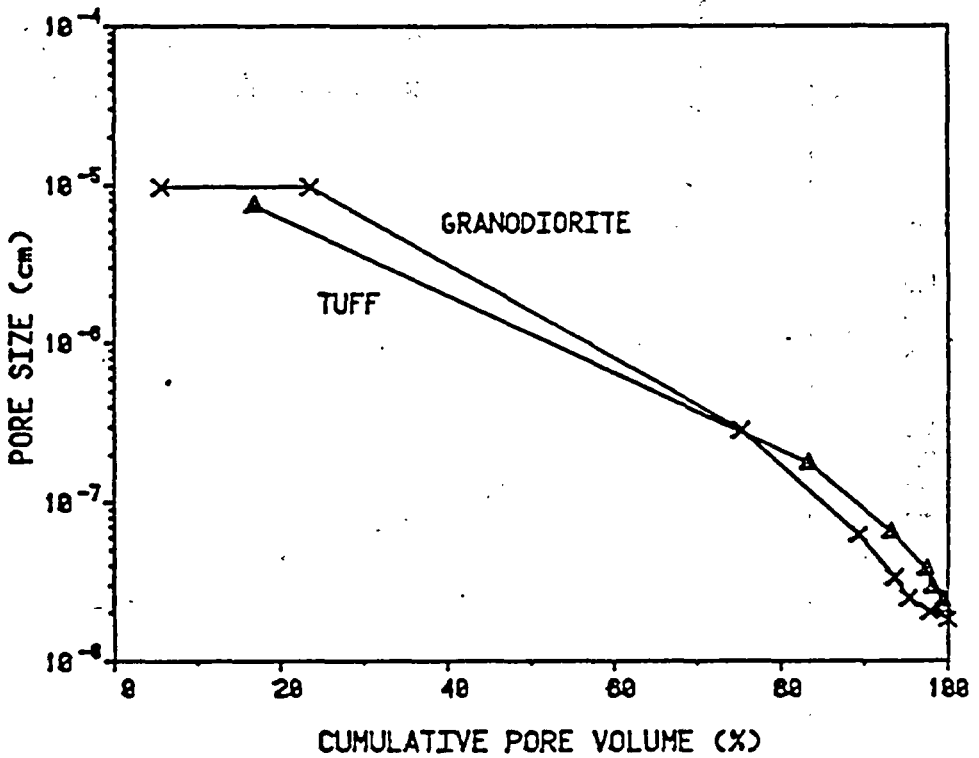

Figure 2.3 Pore-size distribution results from gas-adsorption for the same granodiorite sample shown in Figure 2.2.

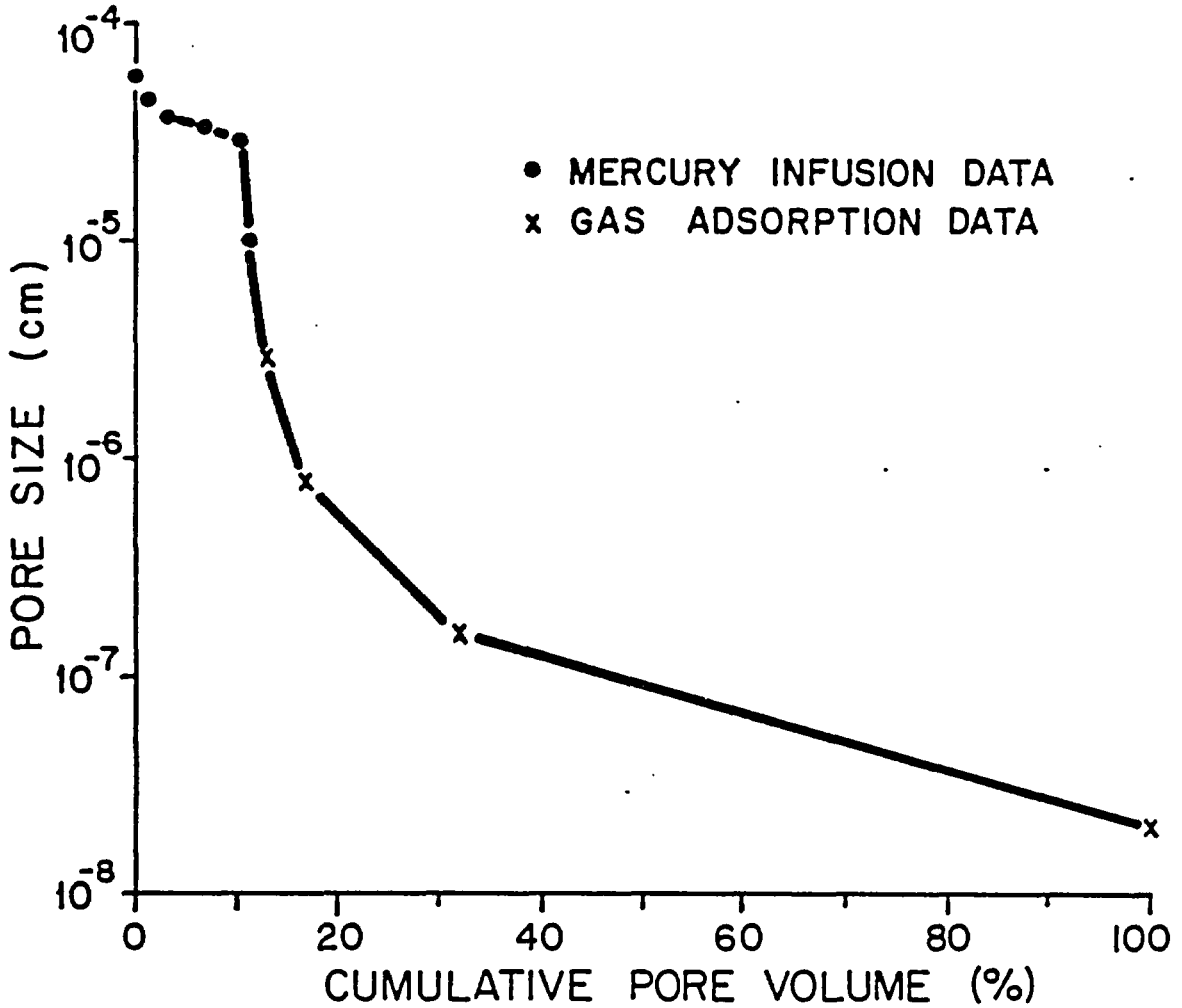

Figure 2.4 Pore-size distribution results combining two measurement techniques for a granodiorite sample obtained from the Santo Nino Mine.

2.1.2.4 Recommended Improvements

Three refinements are suggested to improve the mercury infusion and gas adsorption techniques:

(1) Krypton gas is better suited for gas adsorption on materials with low specific surface areas (due to the ability of Krypton gas to adsorb into smaller pores), and should be used in future tests on rocks of low porosity;
(2) More complete desorption isotherms should be used for determining pore-size distributions; and
(3) There is a gap between the effective range of pores measured by mercury infusion and that measured by gas adsorption. This could be eliminated by conducting mercury infusion at pressures greater than 138 bars, if possible. When continous porosity measurements are available, a comprehensive pore-size distribution from 10^{-4} to 10 μm can then be determined using a combined laboratory technique of mercury infusion and gas adsorption.

In conclusion, the mercury-infusion technique yields information on the pore-size distribution for pores of radii larger than 0.1 μm, while the nitrogen gas adsorption method provides information on the pore-size distribution for pores with radii ranging from 0.1 to 0.0001 μm. (Equipment is commercially available which extends this range.) These two methods can be combined to provide a more complete pore-size distribution diagram.

2.1.3 Specific Surface

Specific surface is another important measurement that aids in the hydrologic and geochemical characterization of a rock matrix. The matrix specific surface of a rock is defined as the total solid/pore surface area per unit, bulk, volume, or mass.

The standard procedure for determining the matrix specific-surface area is to measure the amount of gas or liquid required to form a monomolecular layer over the entire solid/pore surface area. Although a matrix specific-surface value may be measured using the nitrogen gas adsorption technique for a crushed rock sample, the resultant estimate may be higher than that for the uncrushed rock due to microfractures formed during the crushing operation. In order to obtain a more valid estimation of the matrix specific surface, the nitrogen gas adsorption method should be performed on larger sample fragments.

2.2 Fracture Characterization

In rocks of low matrix hydraulic conductivity, fracture systems may form the principal pathways for water and contaminant transport. Important fracture properties are fracture apertures, densities, and orientations. Specifically with regard to unsaturated flow, fracture system properties control:

(1) The relationship between water content and potential within the fractures;
(2) The preferred direction of flow pathway; and
(3) The corresponding rates of water or contaminant transport along these pathways.

The approaches to be discussed pertain to fracture systems which have sufficient regularity and continuity to be considered discrete systems. As fracturing increases in density and randomness, the individual fracture characteristics are masked by the averaged characteristics and an equivalent porous medium or continuum approach is applicable. While the contribution of the countless individual pores within a porous medium is physically averaged in a continuum sense, even on a very small scale, larger scale systems of discrete fractures are not so readily averaged. Even though it is not plausible to completely describe the geometry or hydrological behavior of an entire fracture system in a deterministic sense, a range of behaviors may be observed by using the statistical distributions of its parameters to obtain simulated behaviors.

Sources of data for analyzing rock masses are limited due to both the cost and destructive effects of sampling. As data sources are limited, selective sampling of fractures along cylinders (i.e., boreholes and mine shafts) and along planes (e.g., surface exposures) provide only a small base upon which to infer the total fracture system. Hence, additional information, such as that obtained from indirect measurements, must often be used to supplement data obtained by direct sampling.

While large geologic structures (dikes, faults, bedding planes, and large shear zones) can often be modeled individually using deterministic models because of their continuity and visibility, the minor structures (shrinkage joints, tectonic joints, stress-release joints, and cooling joints near margins of igneous bodies) usually cannot be mapped individually from one borehole or exposure to another. In the latter case, a statistical model must be developed which accurately simulates the fracture system and its response to some imposed condition.

To quantify a fracture system, particular attention must be placed on the types of data which can be obtained from the exposed rock mass. Such information would normally consist of (1) fracture strike and dip, (2) fracture spacing, (3) degree of fracture continuity (or areal extent), and (4) fracture aperture. In addition the presence of coatings and fillings within fractures can be noted.

Once the basic data have been obtained, statistical distributions can be developed which describe fracture characteristics. The following section discusses the measurement and statistical distribution of pertinent fracture parameters and the physical nature of fracture surfaces. The geochemistry of fracture surfaces is covered in Chapter 6.

2.2.1 Orientation

Fracture orientation is one of the more easily and widely measured fracture parameters. Spatial orientation of a fracture plane is characterized by two measurements; the dip direction and the dip angle (Figure 2.5). The dip direction is the azimuthal bearing of the line of steepest declination (as measured from the horizontal) in the plane of the fracture. The dip angle is the inclination of this line from the horizontal. Strike (dip direction plus or minus 90°) is sometimes used instead of dip direction since it is often measured directly; although a compass direction must then be specified with the dip angle.

Commonly, fracture strikes and dips are obtained from a large number of measurements of discontinuities. These features can be treated statistically and plotted on stereographic nets. Zanback (1977) has used the stereographic projections to develop two-dimensional normal distributions of fracture poles in a rock media. (A pole is the vector normal to the fracture plane surface). Because the poles of each fracture set tend to vary about some mean value, Zanback was able to obtain confidence intervals about the mean by assuming no correlation between the deviations in dip directions and dip angles.

Fracture orientations can be measured directly from surface exposures such as outcrops or mines using a compass and clinometer. Determination of fracture orientations from boreholes is also feasible using oriented core logging, borehole viewing, or acoustic-televiewer logging.

Oriented core is obtained from core-orientation devices which either mark the core at the end of each segment or scribe the core during drilling (Goodman, 1976). Determination of fracture orientation can then be analyzed by graphical or mathematical methods (McClellan, 1948).

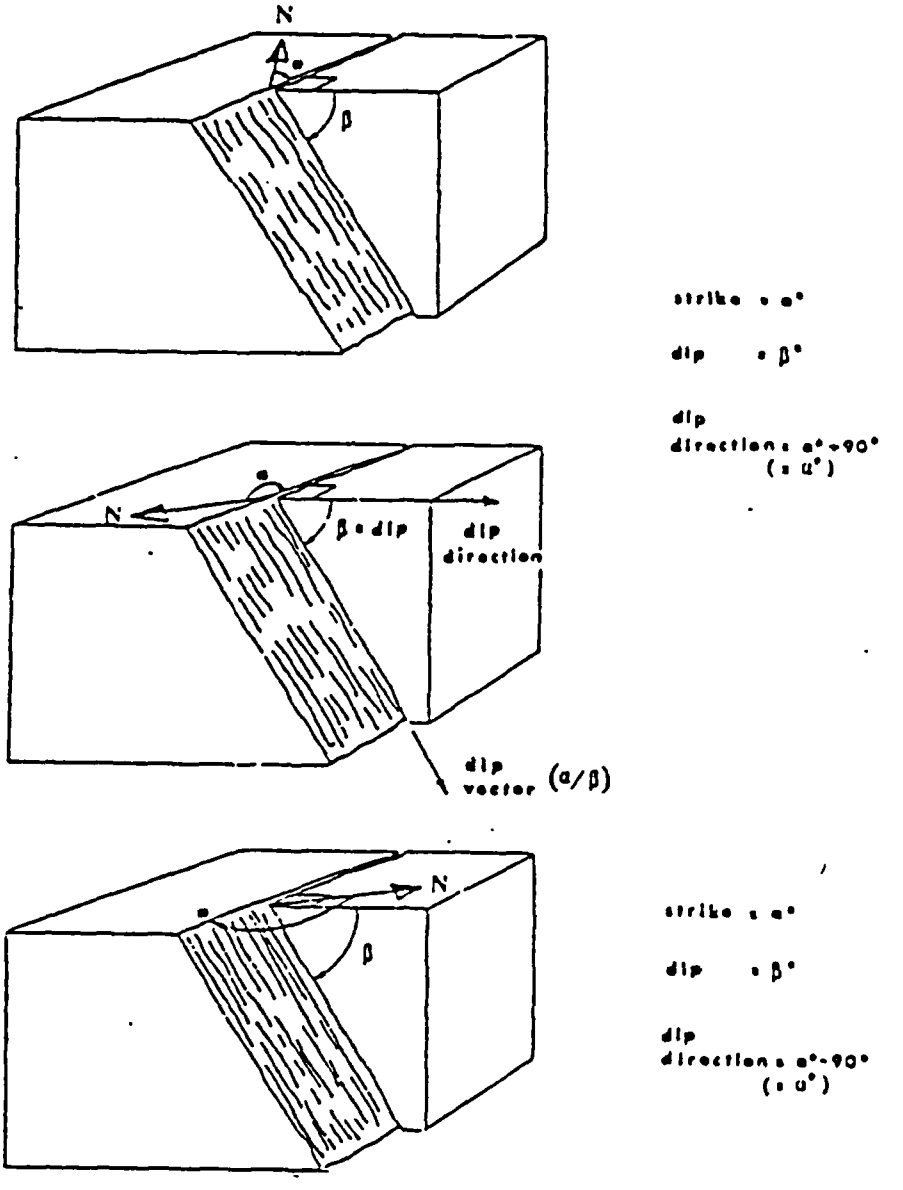

Figure 2.5 Diagrams showing strike, dip direction, and dip angle for three different fractures.

Direct viewing of the borehole wall is achieved using a borehole periscope (sometimes called borescope or stratascope) or a borehole television camera. Camera viewing is generally preferable as it can be used at greater depths, permits greater magnifications, and allows for video recording of the borehole surface for later viewing.

Fracture orientation is measured by either directly observing fracture dip and dip direction or by measuring intercept locations of the fracture trace at three locations along the borehole wall. Direct measurements of fracture dip and dip direction must be corrected for inclined boreholes.

The acoustic televiewer is a recently developed geophysical logging tool which delineates a fracture trace from seismic P-wave attenuation. Fracture dip and dip direction are measurable from these logs.

Fracture orientation data are commonly presented using a stereonet on which the poles (i.e., normals to fracture planes) are plotted (Figure 2.6). Generally, an equal area or Schmidt net is used to facilitate contour density plotting of the data (Figure 2.7). Contouring of the data aids in the identification of fracture sets or clusters (groupings of parallel fractures), while the peak contour densities are used to determine the density and mean orientation of each fracture set. An alternate means of identifying fracture sets is to cluster data points using specially designed computer programs (Shanley and Mahtab, 1974). The mean orientation of each cluster set is then computed as the vectorial sum of the cluster component orientations.

The spherical normal distribution has been applied to statistically characterize the variability of orientation within individual joint sets (Mahtab et al., 1972), but does not always accurately represent the variation which may be present. A bivariate normal distribution has also been suggested (Zanbak, 1977), which may be more appropriate due to the inclusion of an additional parameter. The bivariate normal distribution may be biased, however, due to two principal errors associated with contour diagrams. The errors are:

(1) Fracture surfaces which are perpendicular to the sampling surfaces (i.e., borehole or surface exposure) are more frequently encountered than those which are subparallel, thus biasing density contour plots. This bias can be removed by either sampling enough differently oriented surfaces or weighting the observed frequency by the sine of the angle between the observed feature and the orientation of the sampling line (Terzaghi, 1965).

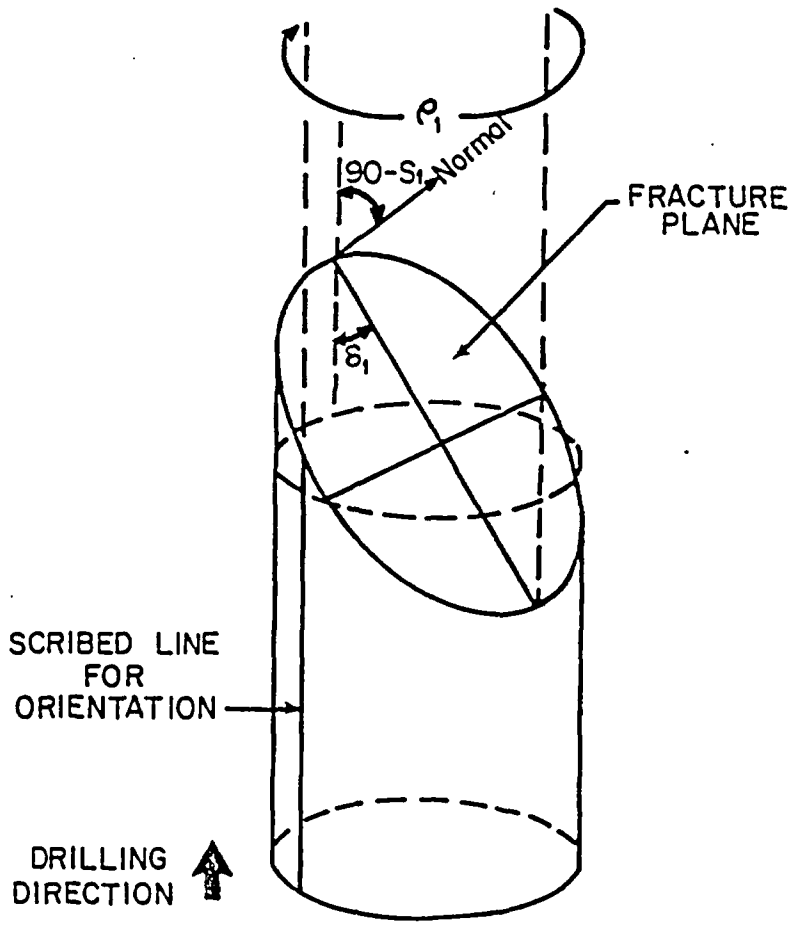

Figure 2.6 Measurements used to calculate strike, dip direction and dip angle of a fracture intersecting a borehole core.

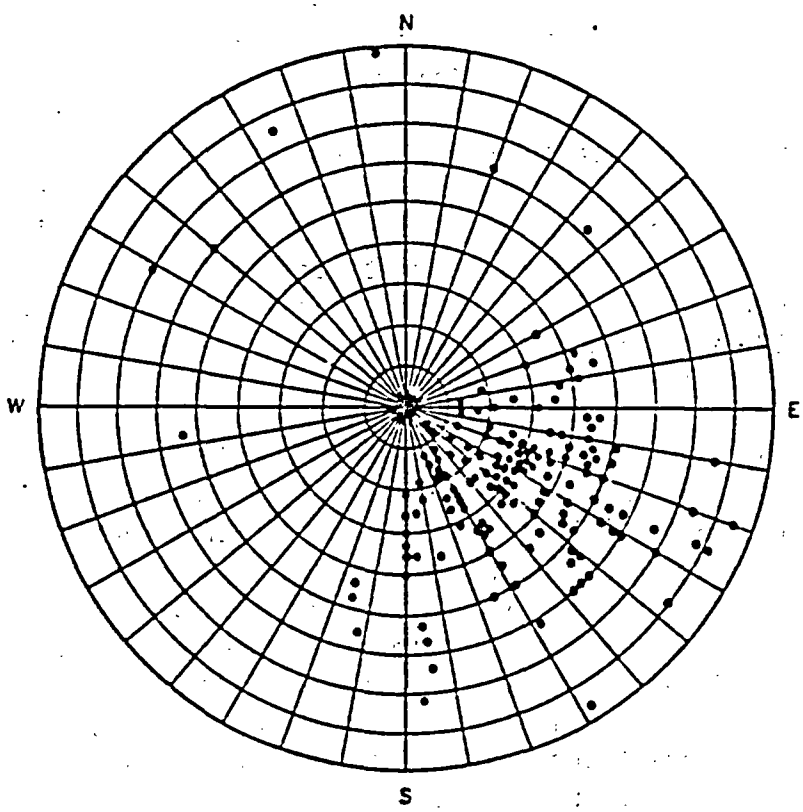

Figure 2.7 Plot of normals to discontinuities on a Schmidt polar equal area net.

(2) Individual poles may be double-counted if the same fracture is measured at two different boreholes, thereby violating the probability theory (ISRMC, 1978)

Despite these limitations, however, stereonet density contouring remains a valuable tool for the identification of joint sets and their mean orientation.

A fracture survey was made along the first 100 m of the main adit of the Santo Nino mine. Sampling was conducted along a scanline at midheight along the right (western) rib of the adit. All fractures with a regular trace intercepting the scan line were noted.

The orientation data taken have been plotted on a Schmidt net and contoured (Figure 2.8). These data indicate that the existence of two predominent fracture sets and suggest the existence of a third set as shown. Set number one is the most pervasive and parallels several faults and mineralized or altered zones. Its apparent dominance in Figure 2.8 is due partially to the fact that the set is nearly perpendicular to the main adit.

Set number two also appears to be a major fracture set, but is diminished slightly in the contour plot due to its near parallel orientation to the sampling line. Set number three appears to be more widely spaced than the other two fracture sets as it is only faintly suggested by the contour plot. This set also parallels the main adit, and therefore the number of intercepts are considerably fewer. The existence of this set, however, is supported by its large fracture surface exposures which define the adit walls along certain sections, and its numerous traces exposed in the bedrock surrounding the mine entrance (not included in the survey).

The data taken during this survey have been used to orient drillholes so as to perpendicularly intercept two of the major fracture sets. Unfortunately space and time constraints limited the number of drillholes. Only a few locations of overbreak along the adit provided the space required to drill. In all, a total of 18 holes were core drilled; 16 perpendicular to Fracture Set 3, and 2 perpendicular to Fracture Set 2. Although the holes were too small in diameter to permit the use of core-orientation devices, some oriented core was obtained by marking of the core stub at the start of each hole. This method provided 1.5 to 4.5 m of oriented core by matching successive pieces.

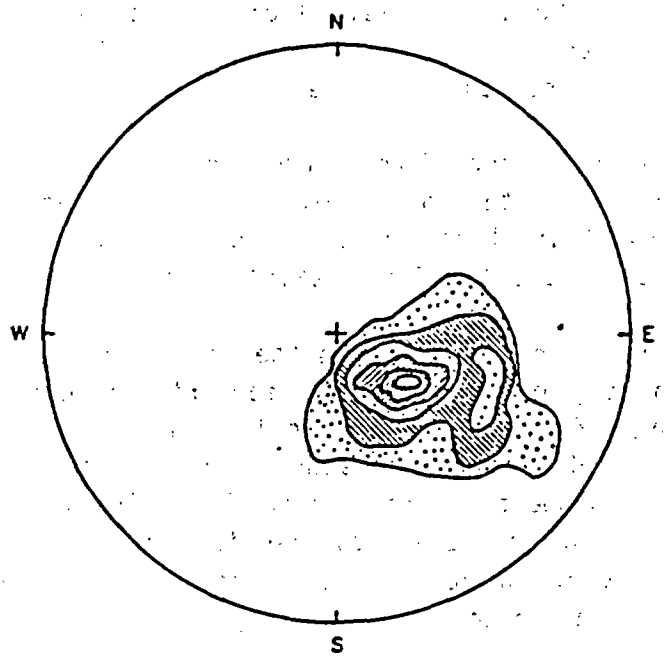

Figure 2.8 Contour plot of fracture data from Santo Nino mine.

A small diameter (32 mm) TV logging camera was used to measure sixteen of the eighteen drillholes to investigate nominal aperture widths. The method showed great potential although use of the camera for fracture orientation purposes was limited by lack of proper orientation rods and a measurement reference.

The field site in the slightly-welded unit of the Apache Leap tuff provides for many experiments that study how a fractured rock system controls unsaturated flow. Scribed cores with a diameter of 6.35 cm were obtained from each of the three inclined boreholes. The scribing tool provided an orientation mark every 3.05 meters. The cores have been logged in the laboratory regarding the location and orientation of fractures within the boreholes. A cross-sectional view along the bearing of the boreholes of these fractures and their intersection with the boreholes is presented as Figure 2.9.

To determine the alignment of the boreholes, photographs of a down-hole gyroscope were taken after the completion of drilling. The photographs indicated the total displacement of the boreholes deviate at the most 1° laterally and 3° vertically from design specifications.

The orientations of fractures within the boreholes have been determined with the aid of a goniometer designed for oriented core and a geometric solution given by Zimmer (1963) and McClellan (1948). These data, given in Figure 2.10, indicate the presence of many fracture sets that dip steeply to the southwest and northwest. The existence of these sets is supported by fracture surface exposures in surrounding outcrops of the study area. However, the apparent dominance of these trends is also due to the fact that the boreholes are nearly perpendicular to the fracture sets.

The orientation data in the fracture survey are used to identify fractures which are continuous between boreholes. This information is then used to help locate injection and monitoring equipment within the boreholes, which in turn provide data on such parameters as fluid and solute travel times, fracture apertures, rock moisture content, and chemistry of fracture-filling minerals.

2.2.2 Density and Spacing

An estimate of fracture spacing is dependent on two factors: the number of unique fractures per unit volume; and the mean area, or areal extent, of the fractures. Fracture spacing can be estimated by determining the number of fractures which intersect a line. If a line transect is used,

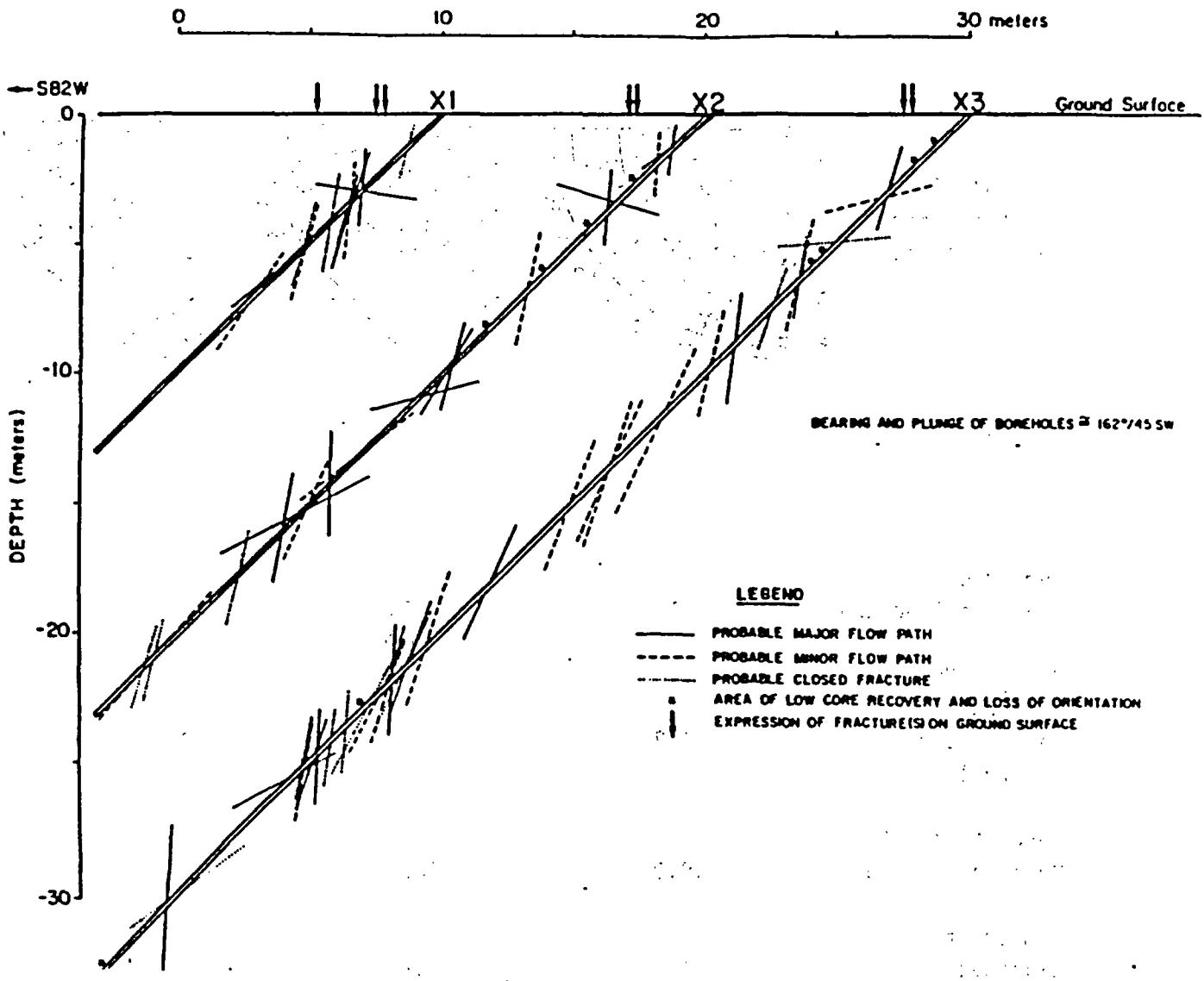

Figure 2.9 Map of fractures intersecting boreholes at the Apache Leap Tuff site.

Borehole Number	X-1	X-2	X-3
Interval (meter)	0.0-18.44	0.0-32.61	0.0-46.64

Percent of Fractures per 10° Increment

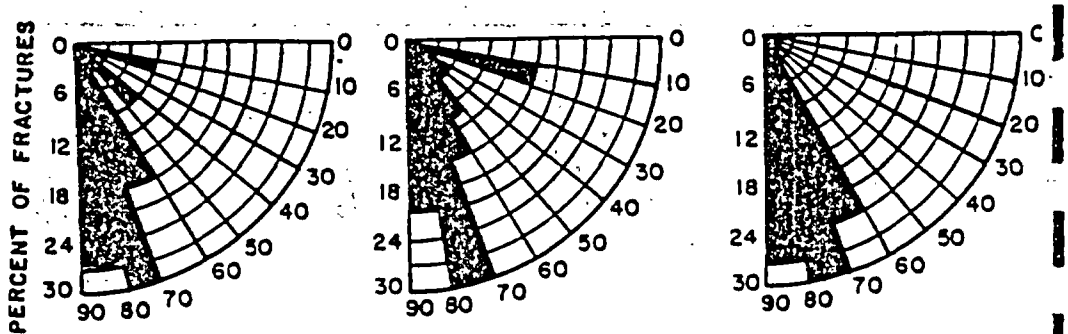

Number of Measured Fractures	11	20	30
Average Number of Measured Fractures per 3-Meter Interval	1.8	1.8	1.9
Percent of Total Measured Fractures	18.0	32.8	49.4
Number of Examined Fractures	11	27	38
Percent of Closed Fractures	27.3	14.8	23.7

Figure 2.10 Inclination of fractures intercepted by boreholes at the Apache Leap Tuff site.

then the average spacing is the length of the transect divided by the number of observed fractures. This technique is appropriate when no preferred fracture direction is present.

This technique is biased, however, if distinct fracture sets are present. To avoid the bias, transects are established normal to the preferred direction of each fracture set. Fracture spacing is obtained by dividing the transect length by the number of fractures belonging to the set of interest which intersect the transect. The scan line should be at least ten times the length of the average measured spacing. Spacing data are plotted on a histogram (Figure 2.11) from which the spacing frequency distribution can be estimated.

2.2.2.1 Fracture Centroids

The number of unique fractures per unit volume can be determined if the center of each fracture can be located. Ideally, the spacing of fracture centroids should follow some fixed rule; assuming a random distribution of centroids within a rock mass yields a Poisson rule for the density of the centroids. Without empirical evidence, such an assumption would seem untenable. Snow (1968) indicates that observed fracture spacings along a sample line can be found to belong to a negative exponential distribution. Such a distribution would be expected for a Poisson process. Baecher et al., (1977) supports this conclusion.

Other researchers (Priest and Hudson, 1976) have demonstrated that an evenly spaced set of centroids would result in a distribution which cannot be described by the negative exponential distribution. They observe, however, that a mix of random, clustered, and evenly-spaced centroids would tend to result in a distribution which can be statistically described by the negative exponential distribution.

2.2.2.2 Areal Extent

The areal extent of fractures is difficult to measure chiefly due to the limited rock surface exposures available. As a result, no standardized methods have been developed. In theory, fracture surfaces could be delineated from surface exposures or by correlation between borehole-fracture logs. In actuality, neither method is entirely successful. Most exposed rock surfaces are of limited extent and generally smaller than the linear fracture traces (intercept of the fracture surface with the exposed rock surface) being measured.

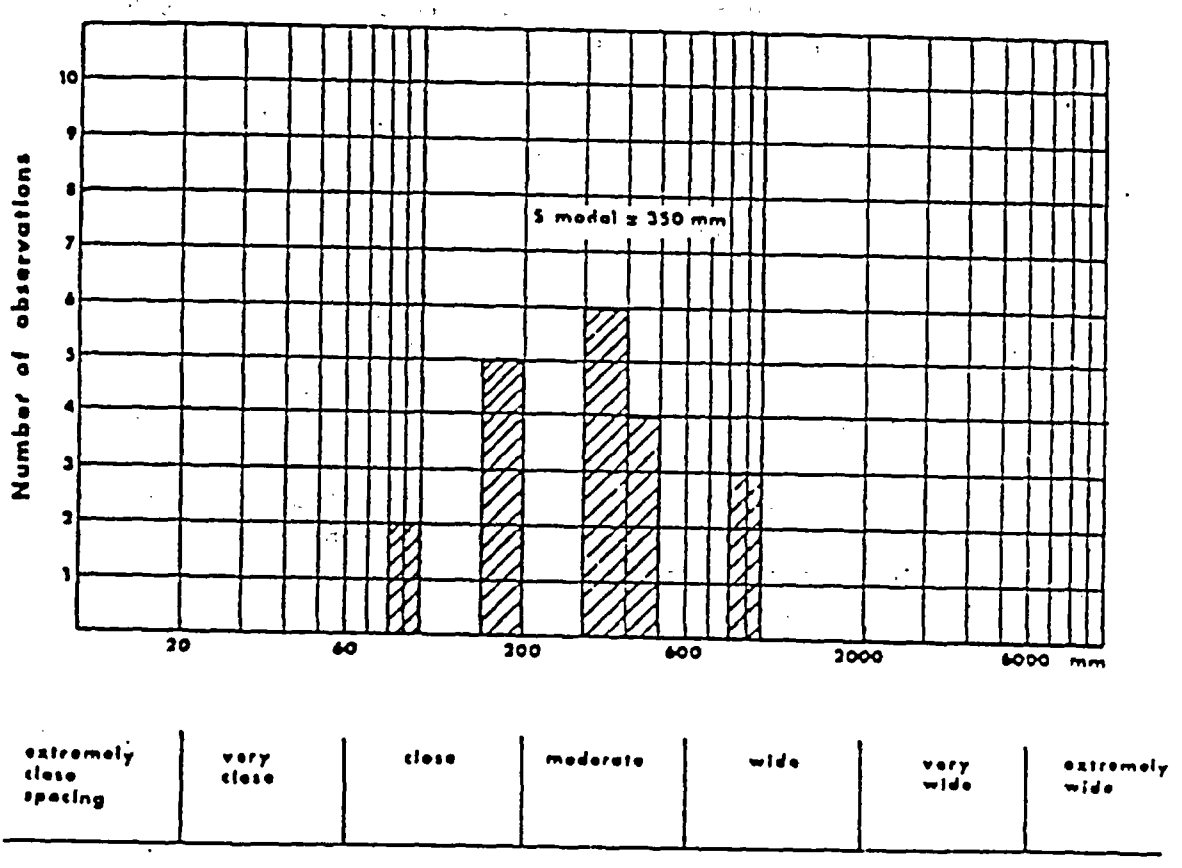

Figure 2.11 Fracture spacing histogram.

Additionally, only one chord across the fracture surface is generally measurable and this trace must be abstractly related to the dimensions of the entire fracture surface.

Use of borehole-fracture logs suffers from the limited ability to correlate fracture intercepts between all but closely-spaced boreholes. Hence, a large number of boreholes are required to delineate the areal extent of fractures. The analysis of fracture extent from fracture trace measurements is possible if certain simplifications can be made:

(1) The distribution of fracture centroids is assumed, usually random;
(2) Fractures have an assumed shape, usually circular; and
(3) The distribution of fracture lengths is assumed, usually lognormal or exponential.

While existing data cannot contradict these assumptions, only limited data are available to support the assumptions. In particular, the assumption of circular-fracture geometry is only an approximation.

If the validity of these simplifications is assumed, the distribution of trace lengths along any sampling line can be predicted. Field measurements of trace length represent a censored and truncated sample of this distribution, because larger trace lengths exceed the exposed measurement surface and very small trace lengths are often ignored during mapping. To account for the limited sample, the parameters of the complete trace distribution are first calculated. From this distribution, the parameters of the true-size distribution are obtained.

Robertson (1970) showed that fracture shape (plan view) is equi-dimensional (or the major axes are uncorrelated). Using this result, the effective centroid can be determined for each fracture. The centroid can then be used as a representative point which describes the position of a fracture in relation to the entire rock mass.

For assumed circular fractures, fracture lengths have been described by a lognormal distribution (Baecher et al., 1977) which was shown to pass the goodness-of-fit test. The gamma distribution did not provide as good a fit as the lognormal, while the exponential and normal distributions performed poorly. Baecher et al., (1977) cite MacMahon (1974), Bridges (1976), and Barton (1977) to support their observations. Other authors (Robertson, 1970; Stetten et al., 1970; Call et al., 1976), however, report obtaining better results using the exponential distribution.

2.2.3 Fracture Aperture

Aperture refers to the perpendicular distance between adjacent walls of a fracture in which the intervening space is air- or water-filled. This definition distinguishes fracture aperture from filled fracture widths. Fracture aperture is not a constant but varies from zero aperture at points of contact (which may exist to transmit stress), to some maximum value.

Apertures can be measured by direct and indirect methods. Larger apertures can be crudely measured along exposed rock surfaces using a millimeter scale while narrower apertures can be accurately measured with a feeler gauge. A very accurate method (<10 μm absolute error) has been developed (Snow, 1969) using a penetrant dye and camera. The difficulty with measurements at surface exposures is that stress relief, weathering, and blast damage tend to alter fracture apertures from those in undisturbed rock.

Boreholes provide another means of direct measurement. Under certain conditions a grouted rod may be overcored and removed to preserve fracture apertures in the core. More commonly, borehole surfaces are inspected directly using borescopes or borehole television cameras.

Indirect methods of measuring fracture apertures have been developed based on the hydraulic characteristics of fractures. Liquid- and gas-injection tests in both saturated and unsaturated rock have been used to measure changes in individual fracture apertures (Pratt et al., 1977; Hardin et al., 1981), to assess fracture aperture changes associated with blast damages (Montezer, 1982; Jakubick and Korompany, 1982), and to assess fracture porosity and aperture distribution (Snow, 1968, 1969).

The principal advantage of indirect methods is that the aperture over greater fracture surface areas are measured. The principal disadvantage is their reliance upon some physical relationship between the quantity being measured and the parameter of interest. In the case of fluid flow and a parallel plate-model, the physical relationship is the cubic law:

$$(2.6) \qquad -q = \rho g / 12\mu \, b^3 \, i$$

where

q is the volumetric flow rate per unit length of fracture;
ρ is the density of the fluid;
g is the gravitational constant;

μ is the dynamic viscosity of the fluid;
i is the hydraulic gradient; and
b is the aperture.

Equation (2.6) assumes that the fluid is incompressible and that flow is laminar. The law has been verified by several experimenters using glass plates (Lomize, 1951; Romm, 1966). If Equation (2.6) can be assumed to be valid, then measurements of the volumetric flow through individual fractures can be used to measure the mean fracture aperture with a high degree of accuracy. Yet the validity of the cubic law when applied to rough natural fractures remains an area of dispute. Experiments conducted by Sharp (1970) on rough, natural fractures suggest that the volumetric flow rate is approximately proportional to the square of the aperture, rather than to the cube.

Similar tests conducted by Iwai (1976), however, indicate the cubic law is valid even at aperture sizes as small as 10 μm. Gale (1975) re-evaluated Sharp's data and concluded that the cubic law is valid if the aperture measured from complete fracture closure is used instead of the aperture measured from maximum observed closure.

As rough fracture surfaces never completely close, even under very high stress, the measurement of absolute aperture has never been made. Instead, residual flows observed at maximum induced closure (minimum aperture) have been assumed to follow the cubic law in order to estimate the minimum absolute aperture. Hence, the value of aperture computed from the cubic law may differ from the mean aperture.

While the flow rate is generally the easiest flow parameter to measure, flow velocity is also measurable and provides a second method for determining the aperture of fractures. By noting that the velocity is the volumetric flow rate divided by cross-sectional area perpendicular to the flow, the velocity can also be related to the fracture aperture:

$$v = \rho g / 12\mu \, b^2 \, i \qquad (2.7)$$

where v is the average, true velocity of the fluid.

The velocity can be measured directly using a tracer and measuring transit times between the injection point and at least one observation point. Furthermore, because the velocity is an independent measurement of the volumetric flow rate, it provides a second estimate of the average fracture aperture.

A third measurable flow parameter which can be used to estimate fracture aperture is the transition between laminar and turbulent flow. Using the Reynolds' number concept, the upper limit of completely laminar flow is given by (Louis, 1969):

$$(2.8) \qquad R_e = 2b\ v/v_w \simeq 2300$$

where

R_e is Reynolds' number;
b is the aperture;
v is the velocity; and
v_w is the kinematic viscosity of the fluid.

The use of Equation (2.8) is limited to relatively smooth fractures with a surface roughness index (mean height of fracture asperities divided by twice the aperture) of less than 0.033 (Figure 2.12). Transition from laminar to turbulent flow is determined from a plot of the flow rate or flow velocity versus the hydraulic gradient (Figure 2.13) obtained from several measurements of the flow rate or flow velocity at several imposed gradients. Equation (2.8) is approximate and, therefore, apertures computed by this method are likely to be approximate in nature.

Pneumatic tests were used to measure fracture apertures and gas conductivities of fractures located at the Santo Nino mine and at the densely-welded tuff site, discussed in Chapter 3.

Fracture apertures have been shown to obey a lognormal distribution (Bianchi and Snow, 1969). The measurement of 256 such fractures on surface outcrops indicated that individual fracture apertures were lognormally distributed.

2.2.4 Fracture Porosity

In rocks of low permeability, the effective fracture porosity can be an important determinant of the overall hydraulic conductivity. The fracture porosity is the percentage volume of fracture openings. The effective fracture porosity is the percentage volume of fracture openings which are interconnected to each other and to an exterior surface. Fracture porosity is calculated from measurements of fracture apertures and fracture density. In many cases, the fracture porosity is a minor component of the total porosity, yet it can play an important role in determining the hydraulic conductivity of a geologic medium.

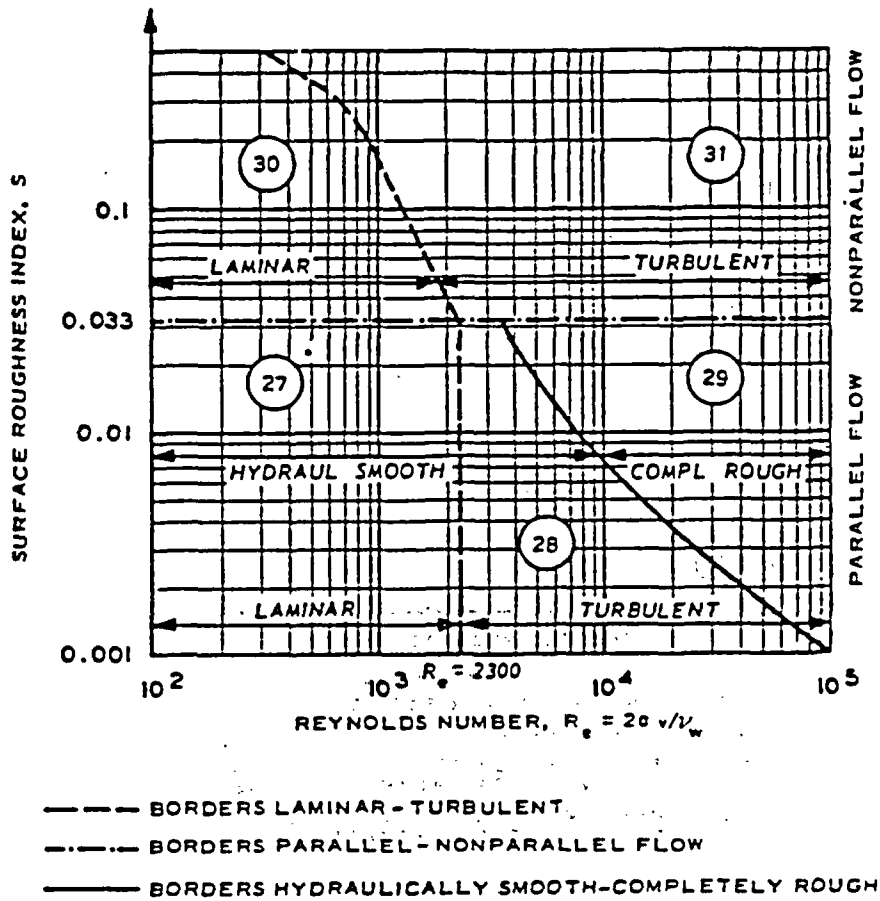

Figure 2.12 Reynolds number diagram for fracture flow.

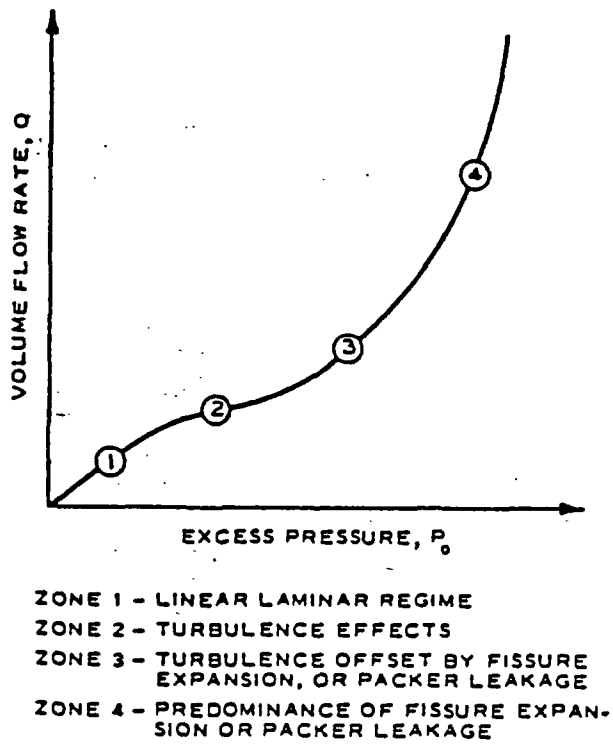

Figure 2.13 Typical curve of flow rate against hydraulic gradient.

To demonstrate that the fracture porosity is normally a minor percentage of the total porosity, the fracture density of a core taken from the densely-welded unit of the Apache Leap tuff is used as an example. The fracture density is estimated to be approximately three fractures per meter. By assuming an extreme mean aperture to be 300 μm, the fracture porosity is not more than 0.1 percent.

2.2.5 Fracture-Surface Characterization

As mentioned earlier, flow through rock fractures is often idealized as flow between smooth, parallel plates. Significant deviations of rough, natural fractures from an equivalent parallel plate model include:

(1) Deviation from a planar surface (fracture waviness);
(2) Deviation from parallel sides (aperture variation); and
(3) Reduction-of-flow cross section (increased contact area).

Schrauf (1984) shows that existing numerical and experimental data for fracture apertures under approximately 200 to 300 μm suggest that the magnitude of roughness and waviness effects of fracture surfaces are secondary in comparison with the effect of contact area between fracture surfaces. Iwai (1976), in a comprehensive study of water flow through a single fracture, demonstrated that the reduction of flow cross section as a result of increasing contact area was more significant. In fact, Iwai showed that the expected flow rate decreased hyperbolically as the fracture surface contact area increased. However, roughness and waviness of the fractures become more significant as apertures increase due to increased effects of turbulence and inertial forces.

2.2.5.1 Specific Surface

The fracture specific surface of a rock is defined as the total fracture surface area per bulk volume of rock. Specific surface resulting from fractures may be obtained by multiplying the number of fractures per square meter by two (the number of fracture sides), and dividing by a unit depth of one meter. For the densely-welded Apache Leap tuff site, the fracture specific surface may be obtained by using an average fracture density of three fractures per square meter. The fracture specific surface is calculated to be 60,000 cm^2 per cubic meter. Fracture density is a three-dimensional parameter, and cannot be accurately determined from two unidirectional cores.

2.2.5.2 Aperture Variability

The measurement of aperture variation has rarely been done. Field measurements have been limited to direct measurement (as discussed in the previous section) of fracture apertures along exposed rock surfaces where repeated measurements along a single fracture trace give an estimate of aperture variability. Unfortunately, it is difficult to extrapolate such results to deeper in situ fractures because of the complex relationship between stress and fracture aperture. Direct measurements of fracture aperture have also been made on large lab samples containing rough natural fractures (Sharp and Maini, 1972). Fracture contact areas as a function of stress were measured by Iwai (1976) using pressure sensitive plastic on lab samples containing rough, induced fractures.

Indirect methods of measuring fracture aperture variability can only be suggested at this point. Tracer dispersion may represent one possible method if diffusion and dispersion due to other factors can be separated or ignored. Another possible method is based on the relationship between stress and fracture aperture, which can be measured either in situ or on large laboratory samples. The required assumption is that the stiffness of a fracture loaded normally is strictly a function of the contact area between the opposing fracture surfaces. If this is true, then the change in average apertures with increasing stress can be related to the change in surface area of loading or, equivalently, the percentage of the surface area lying between the incremental values of absolute aperture. Difficulties with this approach include localized modulus variations due to fracture surface coatings, weathering, or crushing of asperities during loading; all of which influence fracture stiffness.

CHAPTER 3
ISOTHERMAL HYDROLOGIC CHARACTERIZATION

The *in situ* measurement of water potential in geologic media is essential for the determination of the magnitude and direction of ground-water flow. This is because the water potential is an expression of the free energy status of the water in the media. Changes in the free energy status are manifestations of the driving forces. The driving forces, in turn, are responsible for the magnitude and direction of the movement of ground water in geologic media.

In saturated geologic materials, water potentials, usually expressed in terms of potential (bars) or head (cm of water) are positive and liquid water moves from regions where the total potential is higher to regions where the total potential is lower. The measurement of fluid potential is obtained using water level elevations, and/or using pressure sensors. In unsaturated media, however, water potentials are negative and the use of standard measurement devices is inappropriate. It is the purpose of this chapter to review the determinants of the potential, and the means for measuring them.

3.1 Water Potential Measurement

Four components commonly contribute to the total moisture potential, ϕ_T, in ground-water systems:

(1) Elevation or gravitational potential, ϕ_G;
(2) Pressure potential, ϕ_P;
(3) Matric potential, ϕ_M, associated with capillary and adsorptive forces exerted by the rock matrix. The matric component of the total water potential determines which fractures and pores will be partially drained and also the thickness of water films along walls of drained fractures; and
(4) Osmotic potential, ϕ_O, associated with dissolved solute concentrations within the water.

Osmotic-potential gradients and matric potential gradients are not equally effective in inducing water flow in most hydrologic situations. It has been shown (Kemper and Evans, 1963; Kemper and Rollins, 1966; Letey et al., 1969) that the relative effectiveness of osmotic-pressure gradients depends on the solid medium, types of ions present in solution, size of solute molecules relative to pore-size, water-film thickness, and electrostatic interactions between solutes and the substrate.

Letey et al., (1969) and Kemper and Rollins (1966) demonstrated that solute concentration gradients are insignificant with regard to water flow at soil moisture potentials between 0 and 15 bars suction, and can therefore be neglected for practical purposes. Only when salt concentration gradients are large and water films are very thin (e.g., near evaporating surfaces) will osmotic potentials become significant in inducing fluid movement in soils (and presumably in fractured rock).

Osmotic potentials become increasingly significant when a concentration gradient exists across a semi-permeable membrane. Kemper and Evans (1963) demonstrated that the effectiveness of the osmotic potential increases as the degree of restriction of solute movement through the membrane increases, and that osmotic-pressure and hydraulic-pressure differences are equally effective in moving water through a membrane when the solutes are completely restricted. This principle has been applied in the present study in the selection of a solute and semi-permeable membrane for use in the prototype osmotic tensiometer.

Soil scientists employ various methods to measure water potential in situ. These methods include:

(1) Soil moisture blocks made of ceramic, gypsum or nylon (Marshall, 1959; Richards, 1949);
(2) Thermocouple psychrometers (Spanner, 1951; Richards and Ogata, 1958);
(3) Standard tensiometers (Richards and Gardner, 1936; Richards, 1965); and
(4) Osmotic tensiometers (Peck and Rabbidge, 1966, 1969).

Thermocouple psychrometers and osmotic tensiometers have been evaluated in this research program primarily because these devices appear to be most readily adaptable for use in fractured rocks of low permeablity. The thermocouple-psychrometer measurement range is reported to be approximately 2 to 50 bars suction (Wiebe et al., 1971). The osmotic-tensiometer measurement range is reported to be 0 to 15 bars suction (Peck and Rubbidge, 1969), although the modified device evaluated in this study is more likely limited to the range of 0 to about 3 bars suction.

3.1.1 Thermocouple Psychrometer

The thermocouple psychrometer is an electronic probe used to measure the relative humidity of the pure air. The water potential is related to the equilibrium vapor pressure by the expression:

(3-1) $\phi_T = R\ T / M_W\ \ell n(P/P_o)$

where

R is the universal gas constant;
T is the absolute temperature;
M_W is the molecular weight of water;
P is the actual vapor pressure; and
P_o is the saturated vapor pressure.

The water potential measured by the psychrometer is the sum of matric and osmotic potentials.

The psychrometer contains a small thermocouple, with a measuring and a reference junction. The measuring junction is moistened while the reference junction remains dry. As water evaporates from the measuring junction it cools the junction and the temperature difference between the measuring and reference junction creates a voltage. This voltage is proportional to the difference between the wet- and dry-bulb temperatures of the vapor being sampled. Cooling at the wet junction is proportional to the product of the evaporation rate and the latent heat of vaporization. The evaporation rate is primarily a function of the relative humidity of the chamber, but also varies with the diffusivity of water in air. The latent heat of vaporization, thermal conductivity and water-vapor diffusivity of air are all functions of temperature.

Errors in psychrometer readings may result from temperature fluctuations, temperature gradients, vapor-pressure gradients and variation in wet-junction size and shape. Two designs for thermocouple psychrometers have been developed to minimize these sources of errors. The two designs, a field thermocouple psychrometer and a thermocouple psychrometer sample changer, utilize two variations of the basic design described above.

The "psychrometric" method (Merrill and Rawlins, 1972; Brown and Johnson, 1976; Briscoe, 1979; and Daniel et al., 1981) involves the measurement of the temperature depression associated with the evaporation of water from wet surface of the measuring thermocouple. The thermocouple surface is initially wetted by inducing condensation through Peltier cooling; i.e., a small current (5 to 8 mA) is passed through the thermocouple for a length of time (6 to 60 seconds) sufficient to cool the thermocouple and completely wet the surface of the thermocouple. The magnitude of the temperature depression, relative to that measured by the reference electrode, is a function of the relative humidity of air surrounding the exposed thermocouple.

The second variation is the "dew point" method (Campbell et al., 1973), which utilizes circuitry within the control unit to maintain the temperature of the wetted measuring thermocouple at the dew point corresponding to the ambient relative humidity. At this temperature, moisture neither condenses on, nor evaporates from, the thermocouple. Typical response curves for the dew point, psychrometric, and combined modes of operation are illustrated in Figure 3.1.

Psychrometer response is a function of ambient temperature and pressure as well as relative humidity. Since response characteristics of individual psychrometers differ slightly, precise field measurements require prior calibration of each instrument in the laboratory. A detailed description of the calibration procedure utilized for this part of the project is outlined in Appendix A. Briefly, the calibration procedure involves a series of measurements made over salt solutions having known osmotic potentials. Measurements are repeated at several temperatures covering the range anticipated in the field. Variations in response of individual psychrometers to ambient pressure changes are insignificant and are not evaluated during the calibration procedure.

An additional aspect of psychrometer-response characteristics evaluated during the present study concerns the rate at which measuring thermocouples cool when a fixed current is applied under moisture-potential extremes. As stated previously, the effective range of the thermocouple psychrometer is about 2 to 50 bars suction. Beyond the extremes of this range, psychrometers do not respond to either dew point or psychrometric measurement methods. At the wet extreme (0 to 2 bars suction), failure is attributable to moisture evaporating from the wet-measuring thermocouple at a rate insufficient to produce a measurable temperature depression after the cooling current is terminated.

At the dry extreme (more than about 50 bars suction), the failure results from the fact that condensation cannot be induced on the measuring thermocouple by Peltier cooling. Because it is of great importance to the hydrologist to ascertain which moisture extreme exists in a given situation, we have attempted to develop a method which differentiates between very wet and very dry conditions utilizing the rate at which the measuring thermocouple cools when a fixed current is applied. The reasoning is a wet thermocouple should cool significantly slower than a dry thermocouple due to the large heat capacity of water films which condense on the thermocouple surface in response to Peltier cooling under wet conditions.

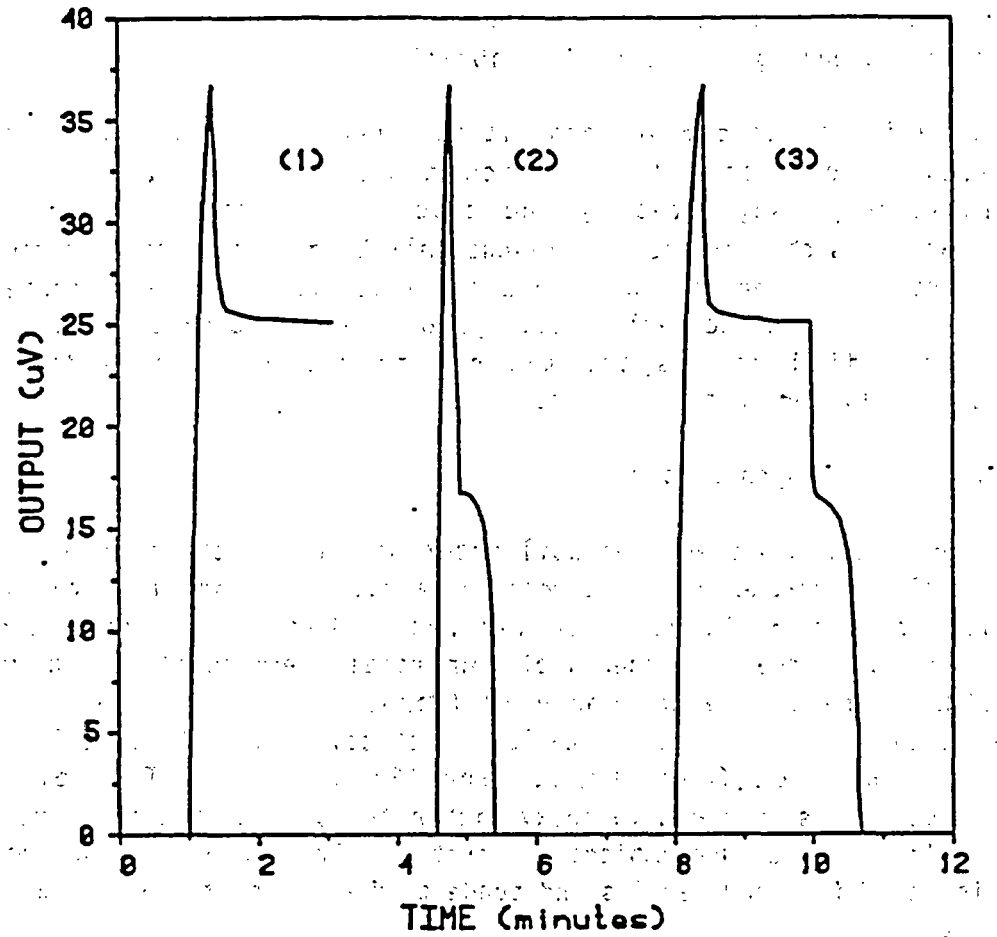

Figure 3.1 Thermocouple psychrometer response curve for dewpoint (1), psychrometric (2), and combined modes (3). Water potential is 25 bars suction. Temperature is 32.8°C.

Laboratory experiments have been conducted to ascertain whether such a distinction between cooling rates under wet and dry conditions could be made. Results obtained for 8 Merrill screen-cage psychrometers which were equilibrated over distilled water (0 bars) and a 1.6 molal NaCl solution (76 bars suction) are presented in Figure 3.2. These results suggest that a distinction can be made either by comparing cooling curves plotted from field data with corresponding laboratory calibration curves or more simply, by comparing the microvolt reading taken at a fixed time after Peltier cooling is initiated (e.g., at t = 30 seconds) with corresponding values from calibration data.

When making these comparisons, it is imperative that all microvolt values be corrected to a common temperature (e.g., 25°C) using relationships suggested by the psychrometer manufacturer. Also imperative is that direct comparisons only be made between psychrometers manufactured by the same company and having the same type of protective shield (ceramic or screen). Ideally, one should compare field results for an individual psychrometer with cooling curves developed specifically for that psychrometer.

3.1.1.1 Field Psychrometer

For in situ measurements of soil water potential, the thermocouple of the field psychrometer is protected by a cup-shaped shield; the shield should permit rapid vapor equilibration between the soil and the chamber. Essential components of commercial thermocouple psychrometers include a reference thermocouple (copper-constantan), a measuring thermocouple (chromel-constantan), a protective shield, a Teflon base, and a length of four-strand wire (Figure 3.3). The reference thermocouple is embedded in epoxy within the base of the instrument and is utilized to measure ambient temperature. This reference thermocouple is isolated from and remains independent of effects of changing moisture conditions.

The measuring thermocouple, supported by the Teflon base and protected by the shield, is exposed to ambient moisture conditions of the rock or soil being measured. The protective shield which surrounds the measuring thermocouple consists of either a wire screen cage or a porous ceramic cup. Ceramic shields provide greater protection, but they also inhibit vapor transport through the shield and thus require longer equilibration times during calibration and field measurement.

Psychrometer measurements are made utilizing control units/meters available from several manufacturers. These units provide the required

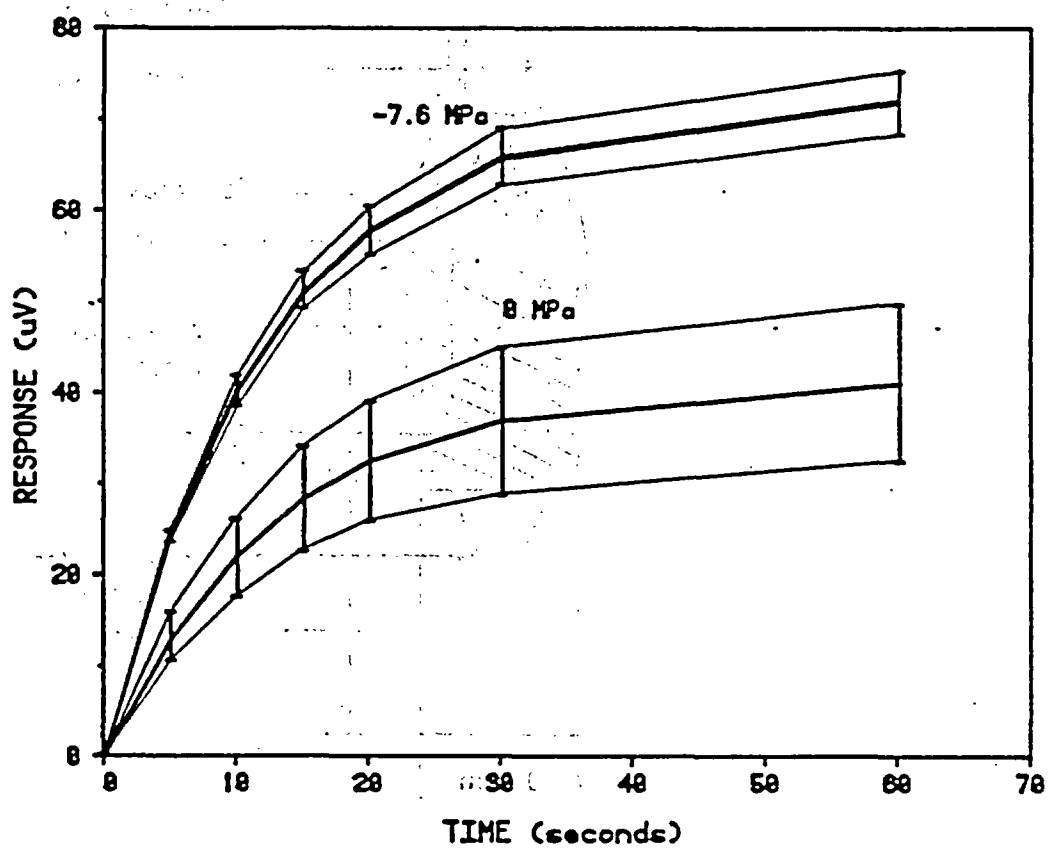

Figure 3.2 Average cooling rate curves for eight screen cage psychrometers under saturated (0 bar) and very dry (76 bar suction) conditions. Vertical bars about the mean values indicate the one standard deviation confidence region.

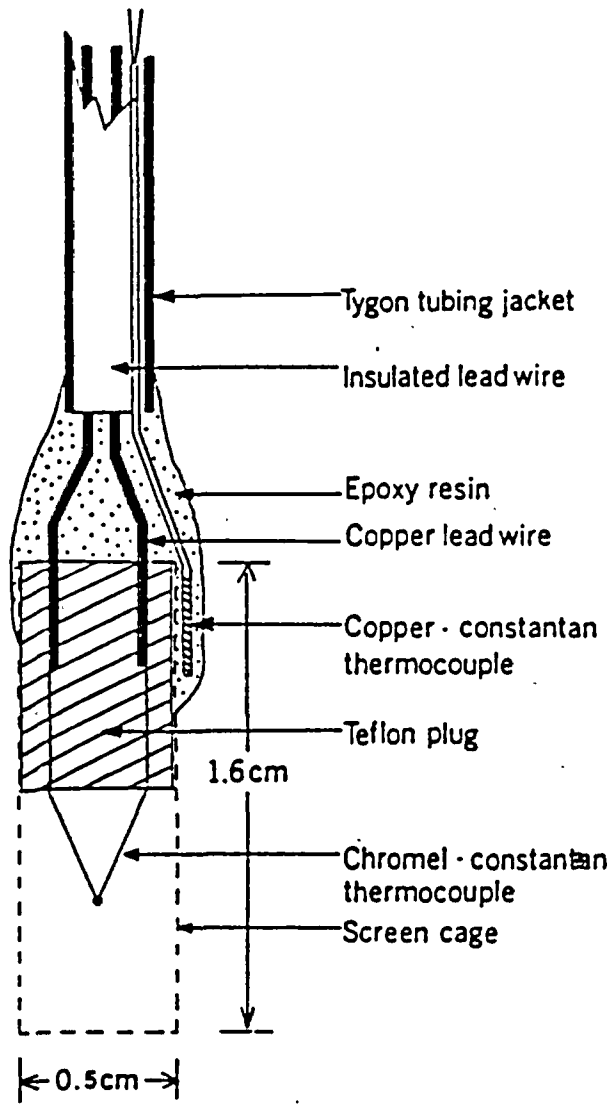

Figure 3.3 Median longitudinal section of a screen-enclosed thermocouple psychrometer (after Meyn and White, 1972).

switching and cooling circuitry and signal amplification and measurement devices. Psychrometer response is read in microvolts using a built-in meter or an auxiliary chart recorder. Available control units range from relatively simple switch boxes to automated scanning/recording devices.

Thermocouple psychrometers have been emplaced for variable periods of time in seven boreholes in the Santo Nino mine, six boreholes in the Pride-of-the-West mine, three boreholes in the Queen Creek road tunnel, and one in the haulage tunnel in the Magma mine. Typically, two psychrometers have been emplaced and sealed in each borehole using inflatable packers. After an initial equilibration period, these psychrometers measure an "average" moisture potential of the rock matrix and of all open fractures which intersect the borehole. Periodic measurements have been made at one to four week intervals in an effort to quantify temporal changes in moisture conditions within each borehole.

Results obtained from the Pride-of-the-West mine and the Santo Nino mine indicate that moisture potentials for all but Borehole 3 of Pride-of-the West are out of the psychrometers' measurement range. Psychrometric measurements obtained at the Pride-of-the-West site are summarized in Table 3.1. Results for Borehole 3, presented graphically in Figure 3.4, indicate a wetting trend (decreasing negative potentials) during the first several weeks after installation followed by essentially constant moisture conditions during the next four months. This pattern suggests that the initial wetting period may have been the result of a gradual re-equilibration of moisture conditions within the borehole after it was sealed with the packer.

Cooling rate data were obtained on several occasions in order to determine whether the psychrometer response failures in Boreholes 1, 4, 5, 6 and 8 were due to excessive moisture or excessive dryness. Microvolt readings (corrected to 25°C) recorded after a 30-second cooling period are presented in the last column of Table 3.1. Laboratory calibration data (Figure 3.5) indicate that if the 30-second reading is less than 45 μV, then moisture conditions are probably too wet; and if the reading is greater than 60 μV, then conditions are probably too dry.

On this basis, Boreholes 5 and 6 appear to be too wet, and Boreholes 4 and 8 appear to be too dry. Substantiation of this interpretation of conditions in Borehole 5 was obtained in July, when the packer was deflated and a significant volume of water poured out of the borehole.

Table 3.1 Summary of thermocouple psychrometer measurements in Pride-of-the-West mine.

Borehole Number	Borehole Length (m)	Date of Measurement	Psychrometer Number	Borehole Temperature (°C)	Psychrometric Response (μV)	Moisture Potential (Mpa)
1	4.4	3/22/82	M73[a]	16.2	NR[f]	
			M152[a]	16.3	NR	
		3/30/82	M73	16.3	NR	
			M152	16.1	NR	
		4/20/82	M73[b]	16.3	NR	
			M152[b]	16.5	NR	
3	>6.1	3/22/82	M150[a]	16.7	13.7 ± 0.15	-4.01
		3/30/82	M150	16.5	13.1 ± 0.1	-3.78
		4/20/82	M150	16.5	12.1 ± 0.1	-3.4[o]
		5/11/82	M150	16.6	12.0 ± 0	-3.4
		5/25/82	M150	16.6	12.0 ± 0	-3.4
		6/08/82	M150	16.4	12.0 ± 0	-3.49
		7/12/82	M150	16.6	12.1 ± 0.2	-3.48
		8/01/82	M150	16.6	12.0 ± 0.05	-3.45
		9/24/82[e]				
						μV at 30 sec
4	4.0	5/11/82	M73[c]	16.8	NR	-
			M152[c]	16.8	NR	-
		5/25/82	M73	16.7	NR	-
			M152	16.7	NR	-
		6/08/82	M73	16.6	NR	64.0
			M152	16.6	NR	67.2
		7/12/82	M73[d]	16.6	NR	64.0
			M152[d]	16.6	NR	67.2

Table 3.1 (continued)

Borehole Number	Borehole Length	Date of Measurement	Psychrometer Number	Borehole Temperature (°C)	Psychrometric Response (μV)	μV at 30 sec
5	>6.1m	4/20/82	M151[g]	16.4	NR	-
		5/11/82	M151	16.9	NR	-
		5/25/82	M151	16.6	NR	-
		6/08/82	M151	16.7	NR	86.4
		7/12/82[d]	M151	16.9	NR	32.9
6	-	8/01/82	M73[h]	-	NR	39.5
			M152	16.5	NR	-
		11/10/82[i]	M73	16.5	NR	30.9
			M152	16.7	NR	28.4
8	>6.1m	5/11/82	M153[c]	16.5	NR	-
		5/25/82	M153	16.6	NR	-
		6/08/82	M153	16.8	NR	66.8
		7/12/82[d]	M153	16.7	NR	68.3

a. Psychrometers installed 3/18/82.
b. Borehole abandoned 4/20/82.
c. Psychrometers installed 4/20/82.
d. Borehole abandoned 7/12/82.
e. Packer found to be completely deflated; borehole abandoned.
f. NR indicates "no response".
g. Psychrometer installed 3/30/82.
h. Psychrometers installed 7/12/82.
i. Borehole abandoned 11/10/82.

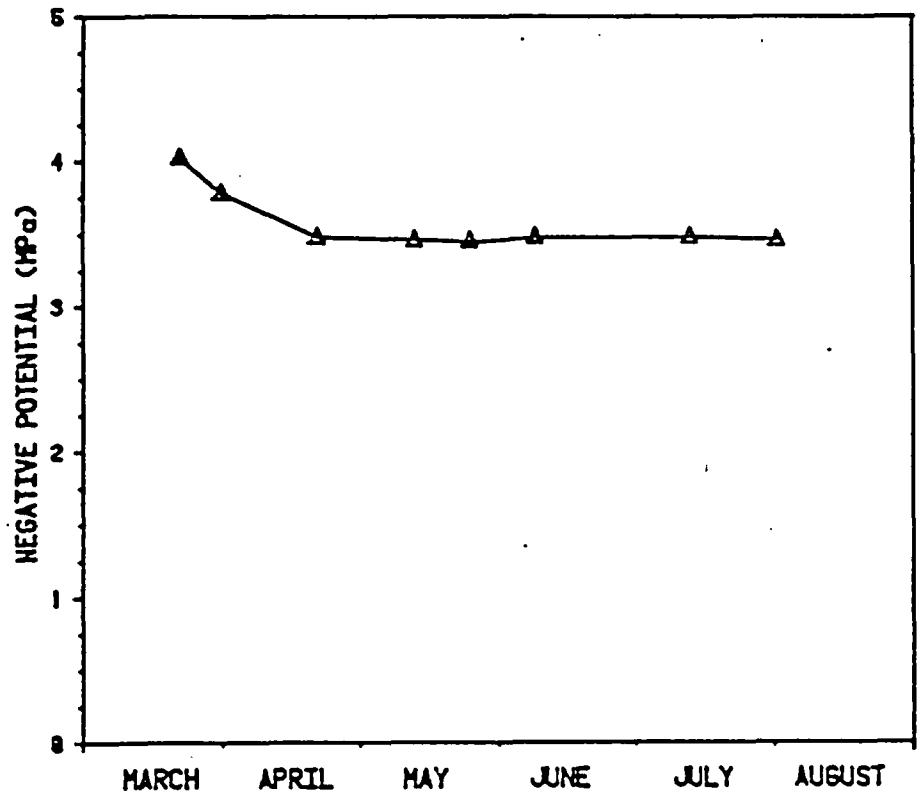

Figure 3.4 Moisture potentials measured in Borehole 3 of the Pride-of-the-West mine using Thermocouple Psychrometer 150.

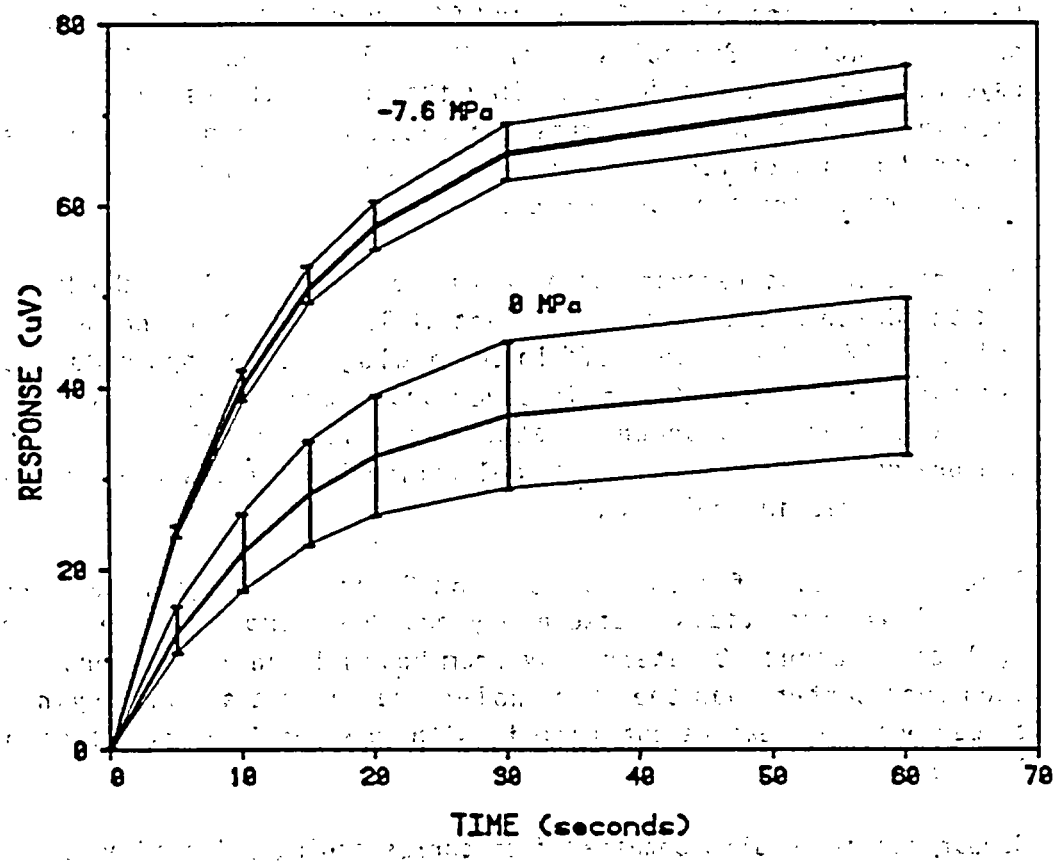

Figure 3.5 Average cooling rate curves for eight screen cage psychrometers under very wet (0 bars suction) and very dry (76 bars suction) conditions. Vertical bars represent a one standard deviation confidence region about the mean.

Indirect support of the hypothesis that Borehole 6 may be too wet is suggested by the presence of some water staining on the mine wall beneath this borehole. Neither staining nor moisture have been evident in Boreholes 4 and 8 during the course of this study.

Moisture conditions at the second field study site, the Santo Nino mine appeared to range from damp to very wet. Seven existing boreholes were instrumented with thermocouple psychrometers. Results are summarized in Table 3.2. All measurements obtained in the Santo Nino mine have been outside the effective range of the psychrometric and dew-point measurement methods. Cooling-rate data (microvolt readings at t = 30 seconds, corrected to 25°C) are presented in the last column of Table 3.2. Using the same criteria as before, Borehole D1 would be judged to be very wet, Boreholes W3, C1, and C2 would be judged to be extremely dry, and data for Boreholes D2 and W4 would be inconclusive. Data for psychrometers having a "W" preceding the numerical designation have not been included in this interpretation because those psychrometers were obtained from a different manufacturer than those which were used during laboratory calibration procedures.

Psychrometer measurements taken in the haulage tunnel at the Magma mine and the Queen Creek road tunnel east of Superior, Arizona, are made in welded tuff. The welded tuff in the haulage tunnel has remained very wet through the period of this study while tuff in the road tunnel is much dryer and has shown greater variation in moisture potential. Measurements made at the road tunnel during the first six months of 1984 are summarized in Table 3.3.

Road tunnel data for Boreholes 1 and 2 indicate significant wetting (i.e., lower potentials) between May and June sampling date. Borehole 3, located about 30 meters away from holes 1 and 2, has consistently been much wetter than the other holes and shows a slight drying trend throughout the measurement period, with the possible exception of the last date.

Comparison of results obtained from corresponding pairs of psychrometers indicates different measured potentials. These discrepancies cast doubt on the precise magnitude of water-potential measurements made using thermocouple psychrometers with the existing procedures. However, the results presented in Table 3.3 do suggest that temporal trends in moisture potential can be readily followed using this method even if the absolute values are subject to uncertainty.

Table 3.2 Summary of thermocouple psychrometer measurements in Santo Nino mine.

Borehole Number	Date of Measurement	Psychrometer Number	Borehole Temperature	Psychrometric Response	μV at 30 sec
D1	3/22/82	M76[a]	10.2	NR	-
	3/30/82	M76	10.2	NR	-
	4/20/82	M76	10.1	NR	-
	5/11/82	M76	10.6	NR	-
	5/25/82	M76	10.6	NR	-
	6/08/82	M76	11.0	NR	49.0
	7/12/82	M76	11.0	NR	51.4
	7/27/82	M76	10.9	NR	40.4
	8/03/82	M5[b]	11.2	NR	51.0
		M76	11.1	NR	37.6
	8/13/82	M5	11.4	NR	46.0
		M76	11.2	NR	35.9
	9/17/82	M5	11.4	NR	38.7
		M76	11.4	NR	34.8
	10/20/82	M5	11.3	NR	32.5
		M76	11.1	NR	33.6
D2	4/20/82	M210[c]	11.0	NR	-
	5/11/82	M210	11.0	NR	-
	5/25/82	M210	11.2	NR	-
	6/08/82	M210	11.3	NR	46.8
	7/12/82	M210	11.3	NR	-
	7/27/82	M210	10.9	NR	56.5
	8/03/82	M20	11.5	NR	54.3
	8/13/82	M20	11.1	NR	56.8
		M210	11.4	NR	55.6
	9/17/82	M20	11.2	NR	55.8
		M210	11.4	NR	48.2
	10/20/82	M20	11.3	NR	56.3
		M210	11.6	NR	43.9

Table 3.2 (continued)

Borehole Number	Date of Measurement	Psychrometer Number	Borehole Temperature °C	Psychrometric Response μV	μV at 30 sec
W1	3/22/82	M209[e]	9.5	NR	-
	3/30/82	M209[f]	9.6	NR	-
W3	5/25/82	M208[g]	9.9	NR	-
	6/8/82	M208	-	NR	49.5
	7/12/82	M208	10.8	NR	64.9
	7/27/82	M208	10.8	NR	63.2
		M6[h]	-	NR	59.5
	8/15/82	M208	11.1	NR	66.0
		M6	10.9	NR	55.0
	9/17/82	M208	11.3	NR	63.2
		M6	10.8	NR	59.2
	10/20/82	M208	10.9	NR	51.7
		M6	11.1	NR	55.6
W4	4/20/82	M210[i]	10.1	NR	-
	5/11/82	M210	10.5	NR	-
	5/25/82	M210	10.4	NR	-
	6/8/82	M210	10.4	NR	52.8
	7/12/82	M210	10.6	NR	46.0
	7/27/82	M210	10.9	NR	63.5
		M2[j]	11.4	NR	44.7
	8/15/82	M210	11.0	NR	57.6
		M2	11.0	NR	45.0
	9/17/82[k]				
C1	7/27/82	M8[l]	10.6	NR	73.6
		W6[l]	10.6	NR	41.7
	8/13/82	M8	11.5	NR	71.0
		W6	12.0	NR	-
	9/17/82	M8	11.1	NR	76.8
		W6	10.9	NR	41.2
	10/20/82	M8	10.5	NR	67.6
		W6	10.3	NR	38.1
C2	7/27/82	M2[l]	10.7	NR	61.9
		M31	10.7	NR	69.2
	8/13/82	M2	11.0	NR	-
		M3	11.1	NR	-
	9/17/82	M2	10.1	NR	58.6
		M3	10.5	NR	61.6
	10/20/82	M2	10.5	NR	48.0
		M3	10.9	NR	58.1

note:

a. Psychrometer installed 3/18/82.
b. Psychrometer installed 7/27/82.
c. Psychrometer installed 3/30/82.
d. Psychrometer installed 7/27/82.
e. Psychrometer installed 3/18/82.
f. Psychrometer removed 3/30/82.
g. Psychrometer installed 5/11/82.
h. Psychrometer installed 7/12/82.
i. Psychrometer installed 3/18/82.
j. Psychrometer installed 7/12/82.
k. Packer had deflated; apparatus removed.
l. Psychrometers installed 7/12/82.

Table 3.3 Moisture potential as measured using thermocouple psychrometers in the dew point (DP) and psychrometric (PS) modes in welded tuff at the Queen Creek road tunnel.

BOREHOLE	PSYCHROMETER	METHOD	1/23/84	3/1/84	3/2/84	3/14/84	4/5/84	5/10/84	6/6/84	6/14/84
#1	M26	DP	-	-	21.5	20.3	19.8	27.5	15.3	15.8
		PS	33.5	29.3	30.0	28.6	27.3	28.0	16.5	17.4
	M27	DP	-	-	21.8	20.9	20.0	24.0	15.5	17.0
		PS	37.5	29.8	29.8	28.5	27.1	29.1	16.8	20.8
#2	M28	DP	-	-	22.9	21.3	24.2	* 21.0	13.6	-
		PS	-	35.5	34.6	32.7	32.4	24.4	12.7	-
	M29	DP	-	-	16.4	18.7	-	* 21.9	20.0	-
		PS	-	25.0	24.5	25.1	-	26.3	22.8	-
#3	M23	DP	-	-	-	<1	<1	4.5	5.7	4.5
		PS	-	<1	-	<1	<1	6.0	8.2	6.8
	M24	DP	-	-	-	2.8	1.5	2.8	5.1	3.8
		PS	-	<1	-	3.5	<1	3.7	5.4	3.5

*Psychrometers M28 and M29 were replaced with psychrometers M22 and M30 following the 4/8/84 readings.

3.1.1.2 Thermocouple Psychrometer Sample Changer

The thermocouple psychrometer sample changer (SC-10A), manufactured by Decagon Devices, Inc., Pullman, Washington, is constructed of a machined and anodized aluminum body 12.7 cm in diameter and 5.4 cm high. (Figure 3.6). The SC-10A consists of a ceramic-bead thermocouple and ten removable chromed-brass sample cups all encased in the massive aluminum housing. Samples are contained within the chromed cups and can be packed with a device which produces a conical depression for the thermocouple.

Just prior to each reading, a special sample cup with distilled water is rotated to the thermocouple, and the ceramic bead is dipped to provide the wet bulb. Voltage and temperature readings are recorded as each sample is rotated and sealed directly below the thermocouple. By sealing the sample directly below the thermocouple in an isothermal chamber, the water potential of the gas phase in the chamber is assumed to be equal to the potential of the water in the liquid phase. The voltage produced becomes stable when equilibrium is attained and is proportional to the wet-bulb temperature depression.

For subsequent calculations of water potential, a psychrometer constant for a particular thermocouple must be determined using salt solutions of known osmotic potentials. Appendix A gives a detailed explanation and the equations necessary for calculating a psychrometer constant. The water potential of a particular sample can be calculated using the equations presented in Appendix A, along with the microvolt and temperature readings of the psychrometer.

The sample cups of the thermocouple psychrometer SC-10A can accommodate samples of soil, rock, filter papers and salt solutions. Rock samples taken from the slightly-welded white unit of the Apache Leap tuff have been used in the SC-10A to calculate a moisture-release curve for the tuff.

3.1.2 Tensiometer

The standard tensiometer consists of a porous, ceramic cup connected by a rigid tube to a device for measuring negative pressures (vacuum gage, manometer, or transducer). The entire apparatus is filled with pure water and sealed before or after insertion at a desired depth within an unsaturated soil. During the subsequent equilibration process, dissolved solutes move through the ceramic cup and water flows out of the cup in response to a matric potential in the surrounding soil.

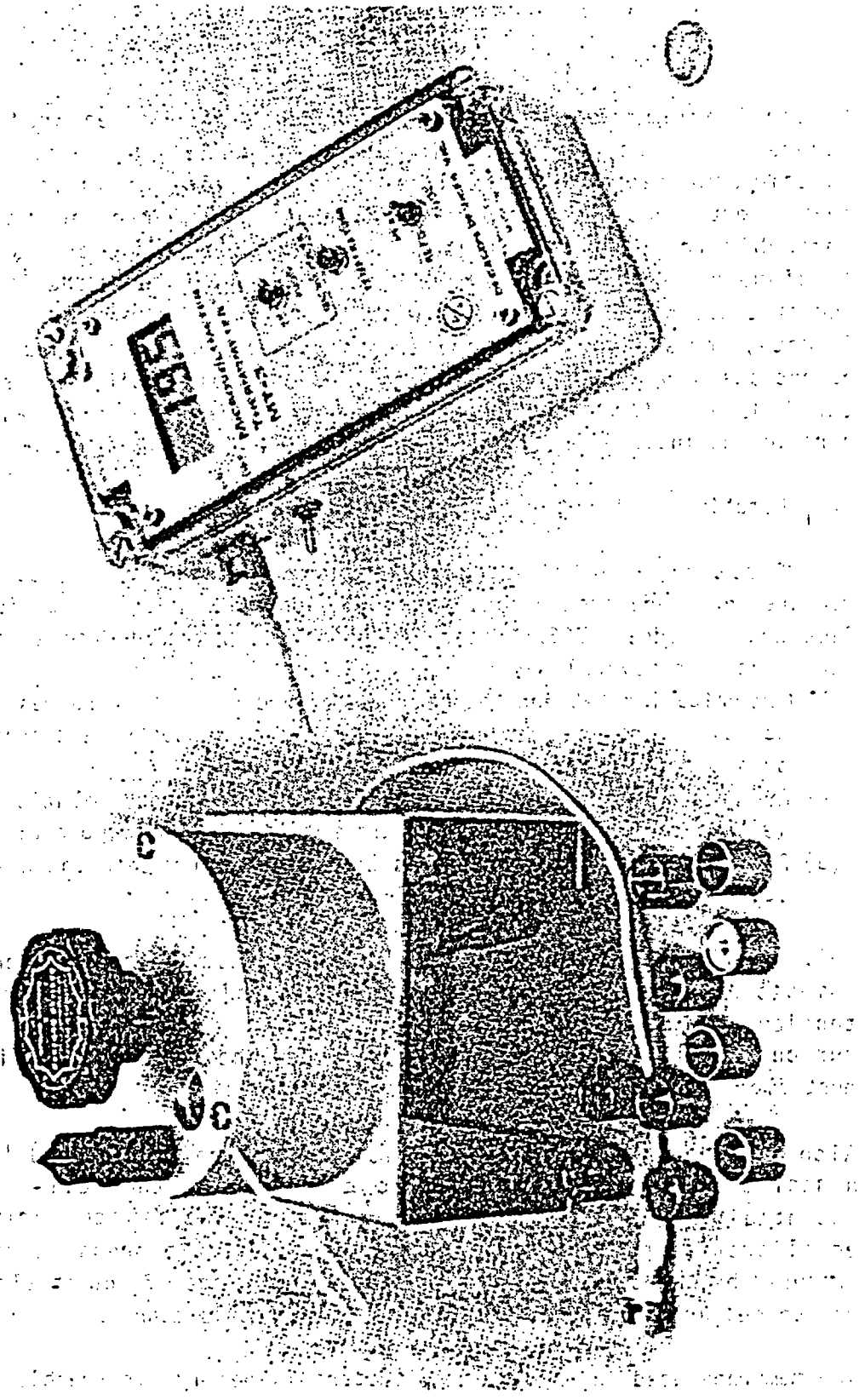

Figure 3.6 Thermocouple psychrometer sample changer, sample cups and microvoltmeter (Decagon Devices, Inc., Pullman, Washington).

At equilibrium, the negative hydrostatic pressure measured by the manometer is equal to the matric potential of the soil moisture. The osmotic component of the total moisture potential is not included in measurements made with standard tensiometers because the ceramic cup is permeable to dissolved solutes. The effective range of a standard tensiometer, 0 to about 0.8 bars suction, is limited by the fact that negative pressures are measured with reference to atmospheric pressure. To date, the standard tensiometer has not been used to measure water potentials of a rock system in boreholes. Possible modifications to the tensiometer which would increase contact between the rock walls and ceramic cup include filling the gap with silica sand or inert material.

3.1.3 Osmotic Tensiometer

Modifications to the standard tensiometer which increased the measurement range from 0 to 15 bars suction were first accomplished by Peck and Rabbidge (1966, 1969). Their device differed from a standard tensiometer in several ways:

(1) Communication between the tensiometer and soil moisture was achieved through a semi-permeable membrane supported and protected by a porous, ceramic disk;
(2) The tensiometer is initially filled with an aqueous solution of large organic molecules which are retained by the membrane; and
(3) Positive hydrostatic pressures are maintained within the device at all times.

This modified tensiometer has been termed the osmotic tensiometer. The osmotic potential created by the organic solute within an osmotic tensiometer serves to partially offset the matric potential of the surrounding soil moisture and thus reduces the amount of liquid that must flow through the membrane during equilibration.

Also, if the total potential inside the device (ϕ_0 and ϕ_p) is more negative than that of the matric component of the soil-moisture potential (ϕ_M), then water will flow into the device during the equilibration process and a positive hydrostatic pressure will be measured by the pressure-sensing device. The range of potentials which can be measured is increased significantly in this manner.

The membrane used in osmotic tensiometers is nearly impermeable to the organic solute but is readily permeable to the smaller inorganic solutes generally found in soil water. Consequently, this instrument, like the standard tensiometer, does not measure the osmotic component of the

total moisture potential if sufficient time is allowed for inorganic solute concentrations to equalize on either side of the membrane.

The osmotic tensiometer developed in this study differs from that utilized by previous workers. The device is intended for use in a fractured rock in which the volumetric moisture content is small. Our design incorporates a tubular membrane to provide contact between the tensiometer fluid and the wall of the borehole in which the device is installed. Hydrostatic pressure within the tensiometer is measured with a 0 to 3.5 bar transducer.

During laboratory testing, the hydrostatic pressure can be adjusted using a piston assembly controlled by a computer/data-acquisition unit. The null-type pressure control system (which may be deleted for field applications) serves to greatly decrease the length of time required for the tensiometer to equilibrate with the surrounding medium and to significantly reduce the volume of water which must be transmitted through the membrane during equilibration.

An illustration of how the prototype osmotic tensiometer appears following insertion in a borehole in fractured rock is presented in Figure 3.7. The core of the prototype (3.8 cm diameter x 91.4 cm stainless steel pipe) contains internal access tubes (0.32 cm diameter) which open to the annular space at each end of the device. A tubular semi-permeable membrane provides contact between moisture in the rock surrounding the borehole and the osmotic solution within the tensiometer. Each end of the membrane is sealed by compressing it between a flat, rubber gasket and an O-ring by bolting a circular end plate to the stainless-steel core. A thin layer of silicone sealant applied between the gasket and membrane assures complete sealing.

The prototype is evacuated prior to insertion in a borehole, and the annular space is filled with the osmotic solution after the device is in place. Filling is accomplished by applying positive pressure to the solution reservoir attached to one of the access tubes. Valves on the vacuum and inlet lines are closed after the device has been filled. During the subsequent measurement procedure, hydrostatic pressure within the tensiometer is monitored using a pressure gauge or pressure transducer attached to the inlet line.

Hydrostatic pressure increases or decreases in response to water flowing through the membrane until such time as the sum of the osmotic and hydrostatic pressures inside the tensiometer is equal to the total water potential in the surrounding rock mass. This equilibration process can

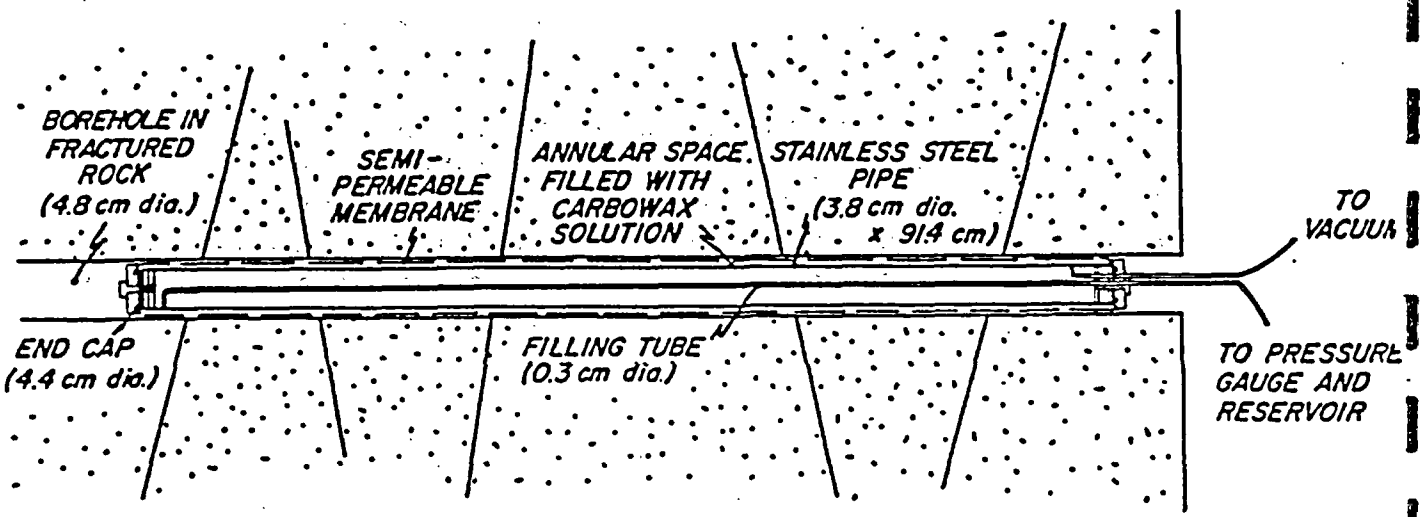

Figure 3.7 Diagram of the prototype osmotic tensiometer in a borehole in fractured rock.

be accelerated by incrementally pressurizing or depressurizing the tensiometer, manually or automatically, when significant increases or decreases in hydrostatic pressure are observed.

Development of the prototype osmotic tensiometer involved lab and field evaluations of several membrane materials and organic solutes. The following properties were considered to be important in the selection of a semi-permeable membrane:

(1) Maintains sufficient strength and flexibility to permit insertion into a borehole without damage and to withstand several bars of hydrostatic pressure from within;
(2) Readily permeable to water at low pressure gradients;
(3) Permeable to inorganic solutes commonly found in water within the fractured host rock;
(4) Completely impermeable to large organic molecules of the type used to create a known osmotic potential within the tensiometer;
(5) Available in tubular form with diameters approximately equal to those of test boreholes; and
(6) Resistant to microbial decomposition.

Detailed descriptions and evaluations of various types of membranes are presented in Appendix B. The solute molecules utilized to generate a known osmotic potential should ideally be:

(1) Large enough to preclude passage through the semi-permeable membrane;
(2) Inert with respect to the membrane material and to metals used in the tensiometer support apparatus;
(3) Chemically stable; and
(4) Resistant to microbial decomposition.

Several organic solutes have been evaluated during this study, including polystyrene sulfonic acid, polyethylene glycol, polyvinyl pyrrolidone, and polyethylene oxide. Results and descriptions for each are also summarized in Appendix B.

3.1.4 Absorber Method

The absorber method uses filter papers to determine rock-water potentials *in situ*. The method assumes the porous materials in liquid or vapor contact with the filter paper will exchange water until the water potential of both are the same. The technique involves placing the filter paper in contact with the soil or rock, allowing it to equilibrate, and determining the water potential of the filter paper with a thermocouple psychrometer sample changer.

Gardner (1937) first proposed the water uptake by filter papers to measure soil-water potential and obtained a calibration curve for a type of filter paper. Fawcett and Collis-George (1967) modified the method, allowing the papers to equilibrate with soil samples for seven days using Whatman No. 42 filter papers treated with 0.005% $HgCl_2$.

McQueen and Miller (1968) noted that when filter paper is placed in direct contact with the soil, only the matric potential is measured, whereas when the filter paper is in a closed chamber on top of the soil, the matric and osmotic potentials are measured. Improving the measurement of matric and osmotic potentials, Al-Khafaf and Hanks (1974) used a modification of the method of McQueen and Miller (1968) by placing the filter paper across a rubber ring to prevent soil contact. Hamblin (1981) used Whatman No. 42 filter papers to construct a calibration curve and, comparing two different batches two years apart, found the calibration curves to be nearly identical.

To estimate in situ rock-water potentials with the filter papers, a device is being designed for use in a borehole. The device will place the filter papers in contact with the borehole wall, the water potential of the filter papers and rock wall will be allowed to equilibrate, and the filter papers will be removed. The filter papers are then quickly placed in the psychrometer cups to determine their water potential. In addition, the water content can be estimated using calibration curves. Appendix C provides additional information about this technique.

3.2 Water Content Measurement

Many parameters in the governing equations for the flow through unsaturated media are functions of water content. The hydraulic conductivity and the fluid potential are examples of such parameters. The objective of this section is to evaluate the ability of two geophysical methods, electrical resistivity and neutron logging, to measure in situ changes in the water content of unsaturated, low-porosity, fractured rocks.

Downhole resistivity and neutron logging are used to detect temporal variations in the water content of a quartz monzonite at the Santo Nino mine and at the Magma mine. The feasibility of using electrical resistivity and neutron logging to measure temporal changes in the water content at the quartz monzonite site is decided by:

(1) Comparing the relative measurements over time;
(2) Comparing the results of both methods; and
(3) Correlating the borehole measurements with surface rainfall data.

These results are then used to evaluate temporal changes in the water content at the dacitic ash-flow tuff site from the wet winter months through the dry summer months. Before this qualitative analysis can be undertaken, the physical parameters which affect each method must be evaluated.

Neutron logging has been used extensively by soil scientists to measure the water content of soils and by geophysicists to measure the saturated porosity of oil-bearing formations. The procedure uses high-energy neutrons which are emitted from a radiation source. The water content within the pore volume is calculated from the number of low-energy neutrons which are reflected by hydrogen atoms in water molecules (or in oil molecules) and counted at a detector.

Three dimensional plots of the neutron data collected at the Santo Nino field site are presented in Figures 3.8 and 3.9. Similarly, three dimensional plots of the neutron and resistivity data collected at the Magma field site are presented in Figures 3.10 and 3.11. The average apparent resistivity values for the two Santo Nino boreholes are plotted versus time in Figures 3.12 and 3.13. The average is used in these plots because only a small interval (less than one meter) was logged in each hole. For comparison, the average neutron data for the Santo Nino boreholes are also plotted in Figures 3.12 and 3.13.

Temporal variations in resistivity data can be attributed to changes in the water content of a rock. An increase or decrease in the water content of the rock can be detected by a corresponding increase or decrease in the number of thermal neutrons detected by the neutron probe. Indeed, by comparing the two dimensional plots for the Santo Nino boreholes (Figures 3.12 and 3.13), the maximum and minimum resistivity values corresponding to the minimum and maximum neutron values, respectively, can be found.

The resistivity profile for the Borehole 5.2 at the Santo Nino field site (shown in Figure 3.12) indicates that the water content of the quartz monzonite gradually decreased from the beginning of October through the end of December; then, responding to winter rain, steadily increased through February. The water content remained at this high level until the end of May. In June the water content decreased slightly, only to rebound upward in July and August.

The normalized neutron profile for Borehole 5.2 shows the same general trends. The major difference is the neutron counts did not level off in

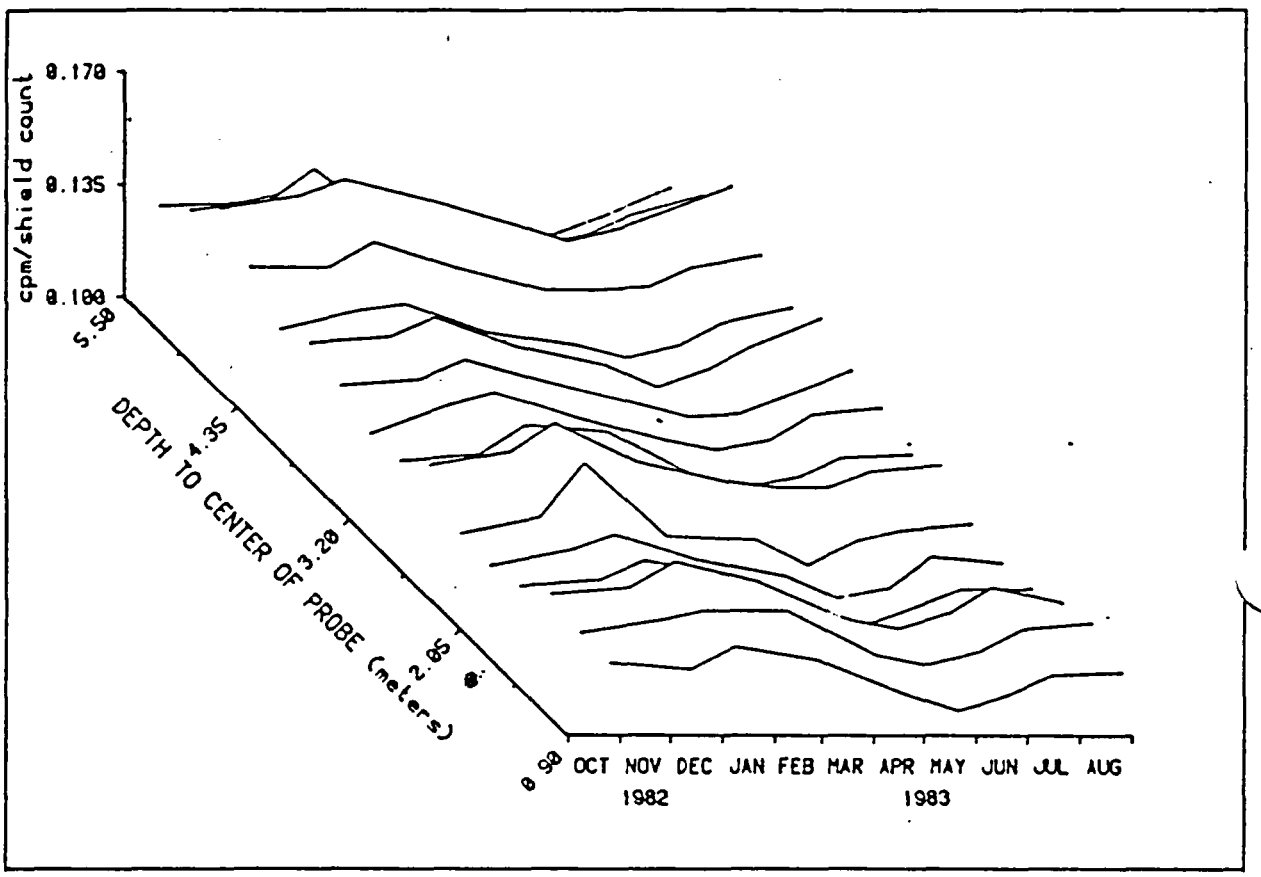

Figure 3.8 Variation in the normalized neutron data with time and space in Borehole 5.2 at the Santo Nino field site.

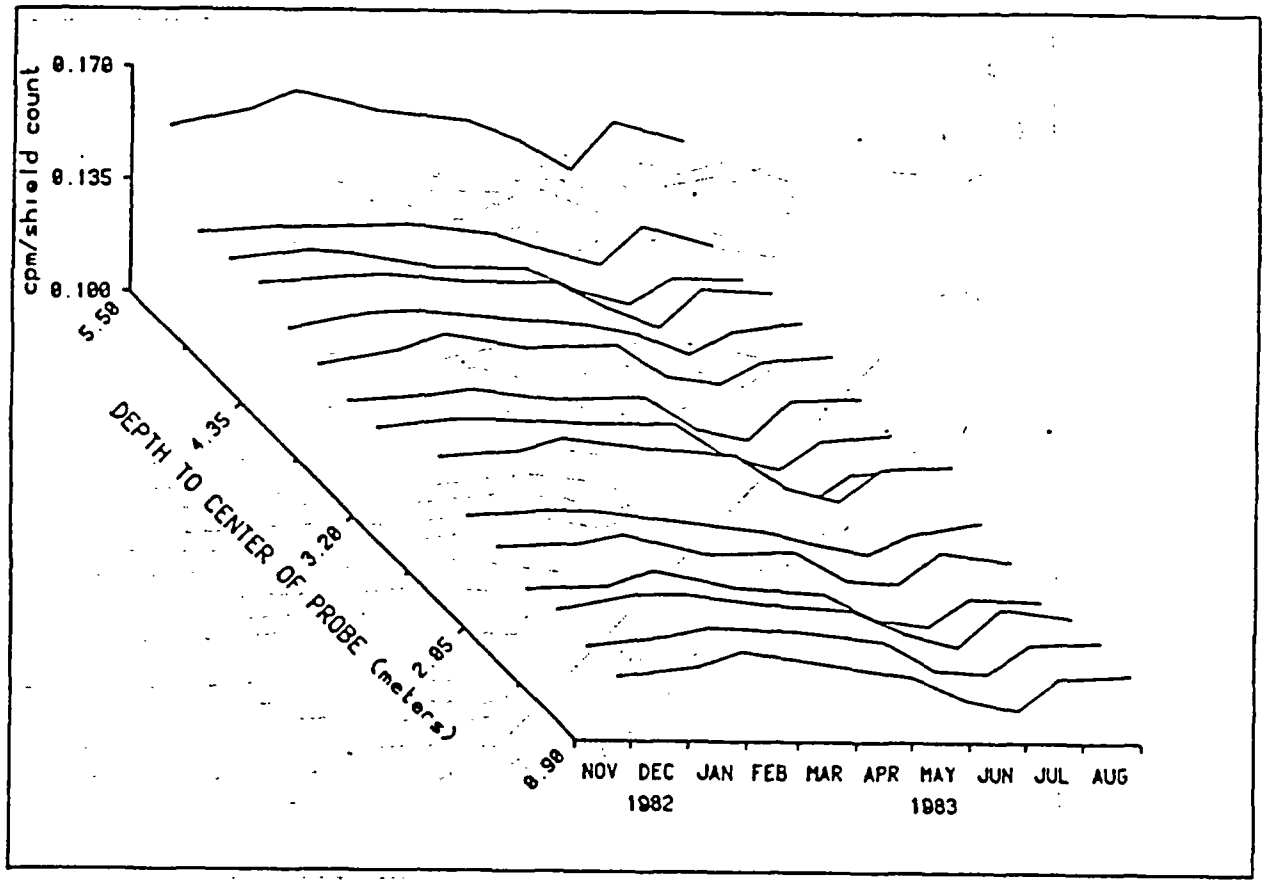

Figure 3.9 Variation in the normalized neutron data with time and space in Borehole 5.8 at the Santo Nino field site.

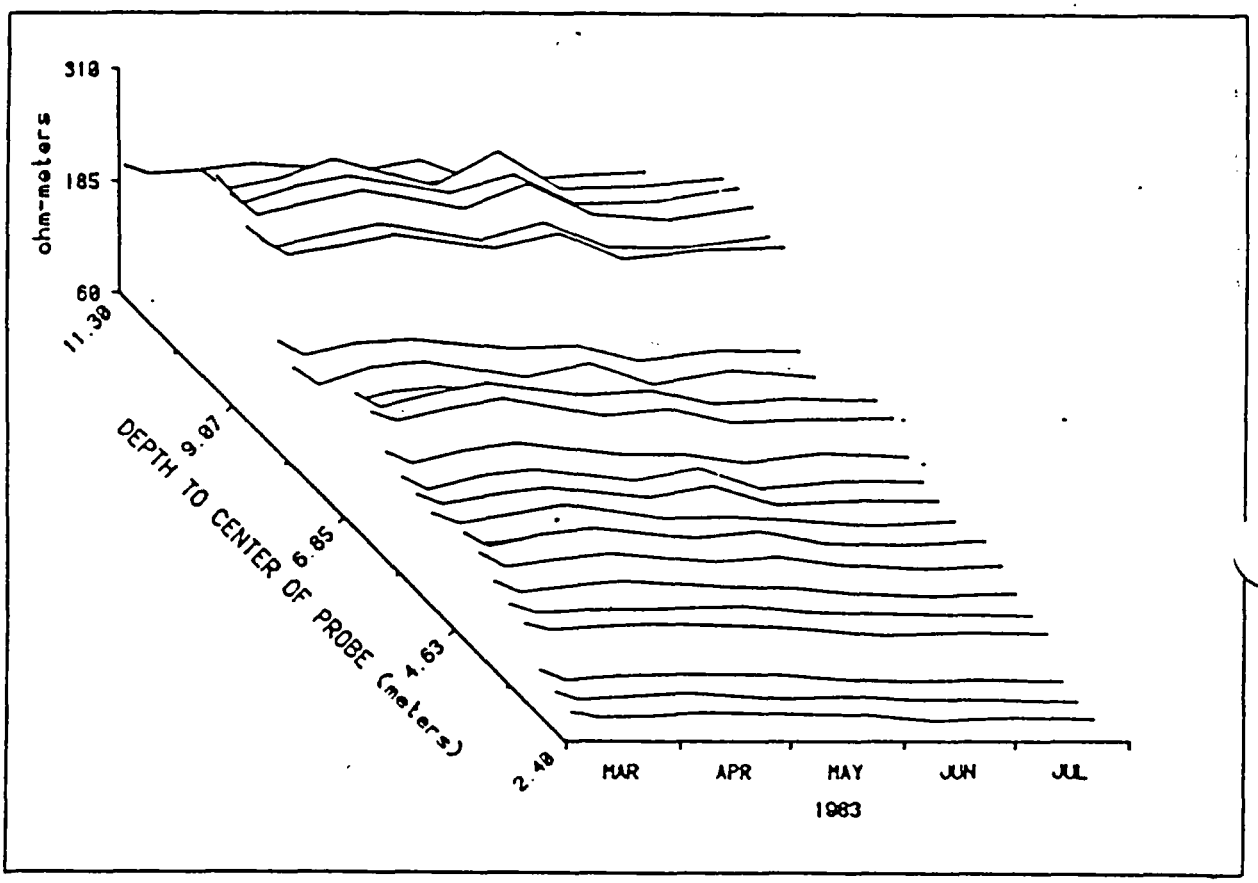

Figure 3.10 Variation in the resitivity data with time and space in upper borehole at the Magma field site.

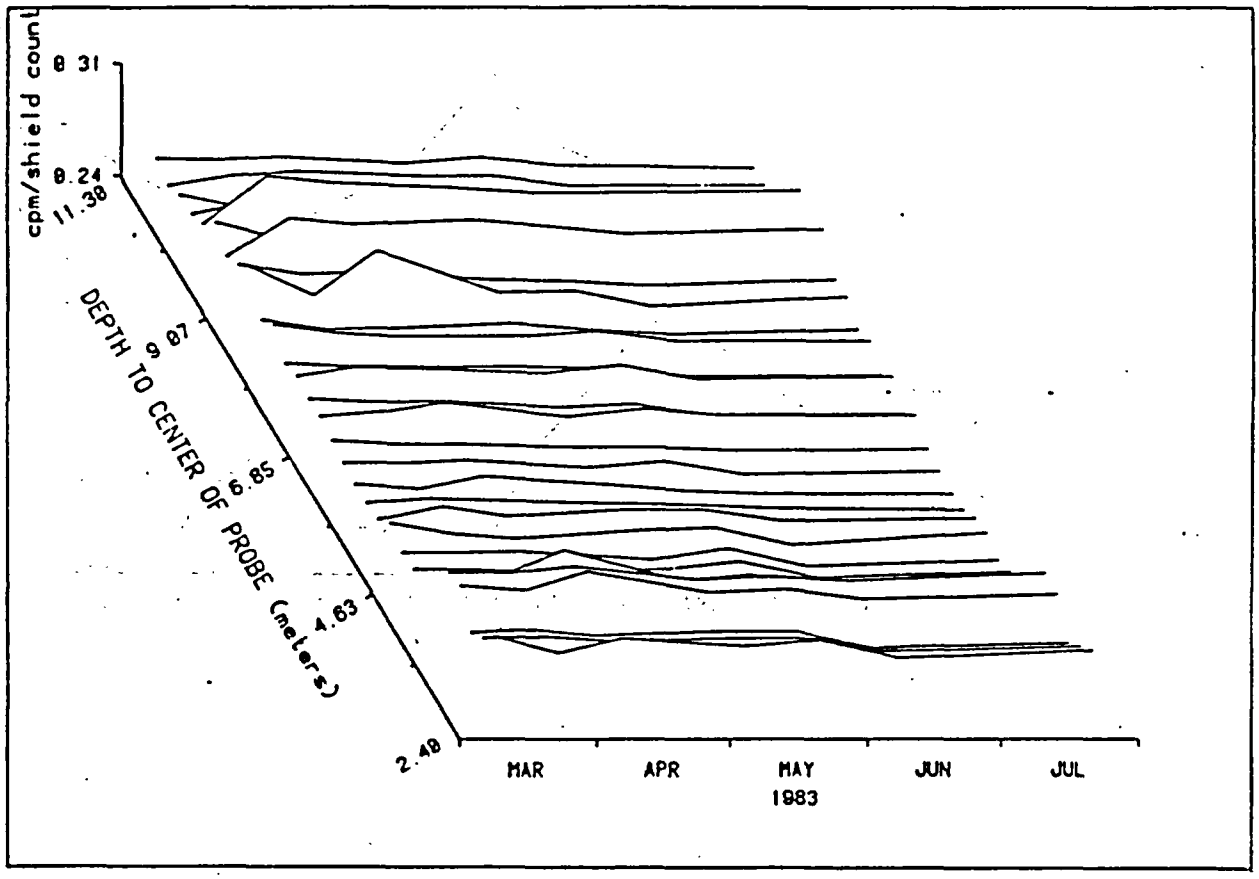

Figure 3.11 Variation in the normalized neutron data with time and space in the upper borehole at the Magma field site.

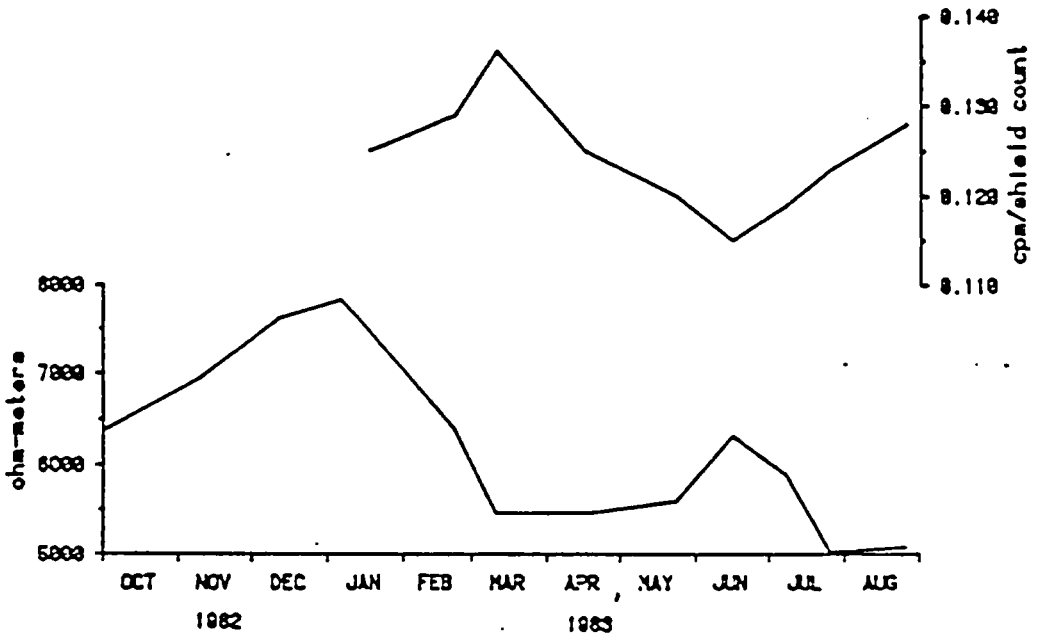

Figure 3.12 Resitivity (lower) profile and normalized neutron (upper) profile for Borehole 5.2 at the Santo Nino field site.

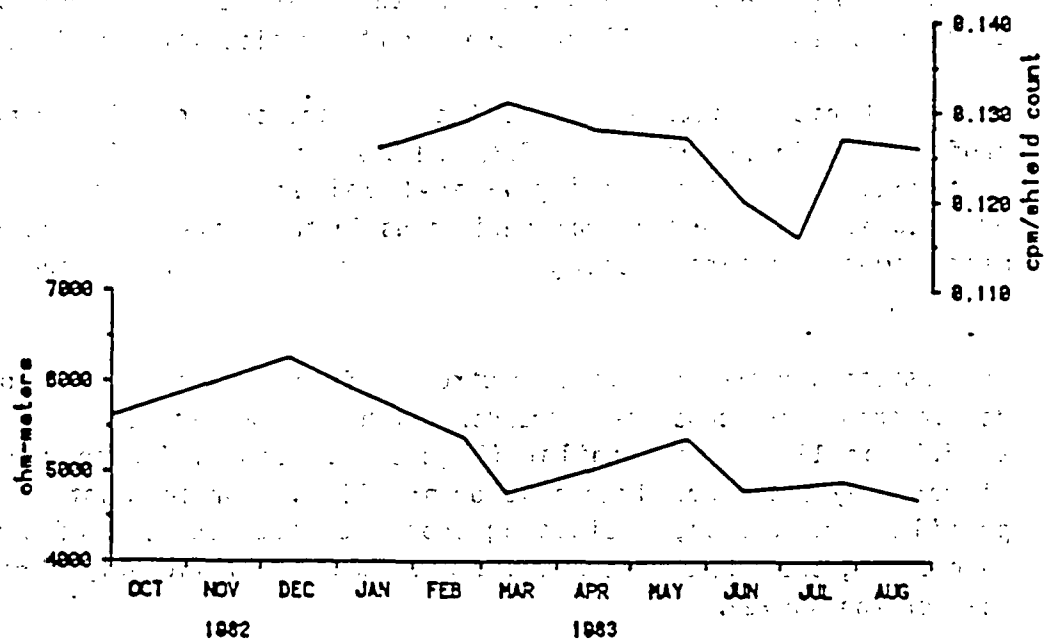

Figure 3.13 Resitivity (lower) profile and normalized neutron (upper) profile for Borehole 5.8 at the Santo Nino field site.

March and April. A possible explanation for this is the standing water in the adit (Figure 3.14) affected the resistivity measurements but not the neutron measurements. Similar trends for Borehole 5.8 at the Santo Nino field site are shown in Figure 3.13. The June resistivity data point in this figure may be in error. On this data, the wire inside a current electrode broke while the hole was being logged. Attempts to remedy the problem in the field were unsuccessful.

Besides responding similarly in time, by overlaying these profiles with the borehole water-level profile presented in Figure 3.15, it appears both methods respond to the same mechanism which controls the water level in Borehole 6.0a. In particular, the borehole water-level profile correlates remarkably well with the inverted resistivity profiles.

The similarities between the resistivity and the normalized neutron profiles for Boreholes 5.2 and 5.8, and the positive correlation between these profiles and the standing water-level profile for the Borehole 6.0a suggest that the temporal variations in the resistivity and neutron measurements recorded changes in the water content of the quartz monzonite.

The resistivity and normalized neutron profiles from the Magma borehole do not show these consistent trends. Although the resistivity profiles at 5.2 and 11.3 m are similar (Figure 3.16 and 3.17), they are not mirrored by the normalized neutron profiles. For the most part, the profiles are smooth, indicating that the water content of the rock surrounding the Magma borehole did not change significantly during the span of the survey.

In summary, two geophysical methods have been evaluated as to their usefulness in measuring the water content of unsaturated, fractured, low- porosity, crystalline rocks. The conclusion is that downhole resistivity and neutron-moisture measurement techniques are able to detect qualitative changes in the water content of these rocks. The evidence supporting this conclusion is that each method responded similarly in time; and precipitation and borehole water-level data corroborated these trends at the Santo Nino field site. Furthermore, the time lag between the surface precipitation data and the borehole data appears to be eight weeks during the dry months and less as the overburden becomes saturated. The distance between the boreholes and the surface is six meters. Similar trends were not observed at the Magma field site, where the distance between the borehole and the surface is 80 m.

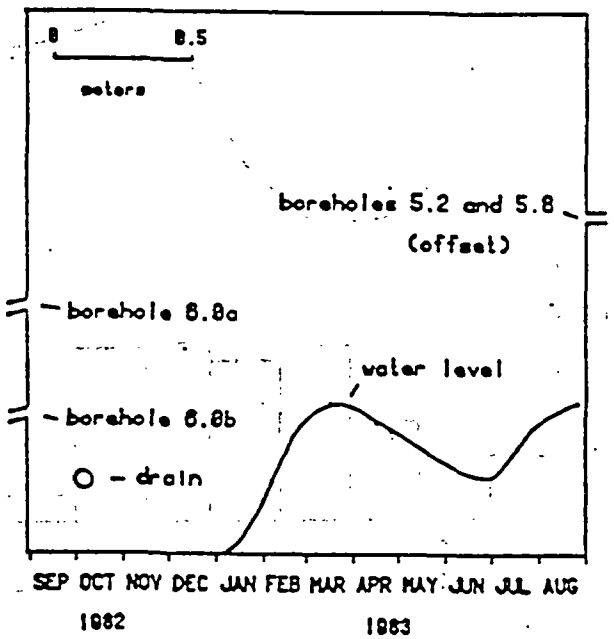

Figure 3.14 Cross-section perpendicular to the Santo Nino mine adit showing the location of boreholes and ponded water levels.

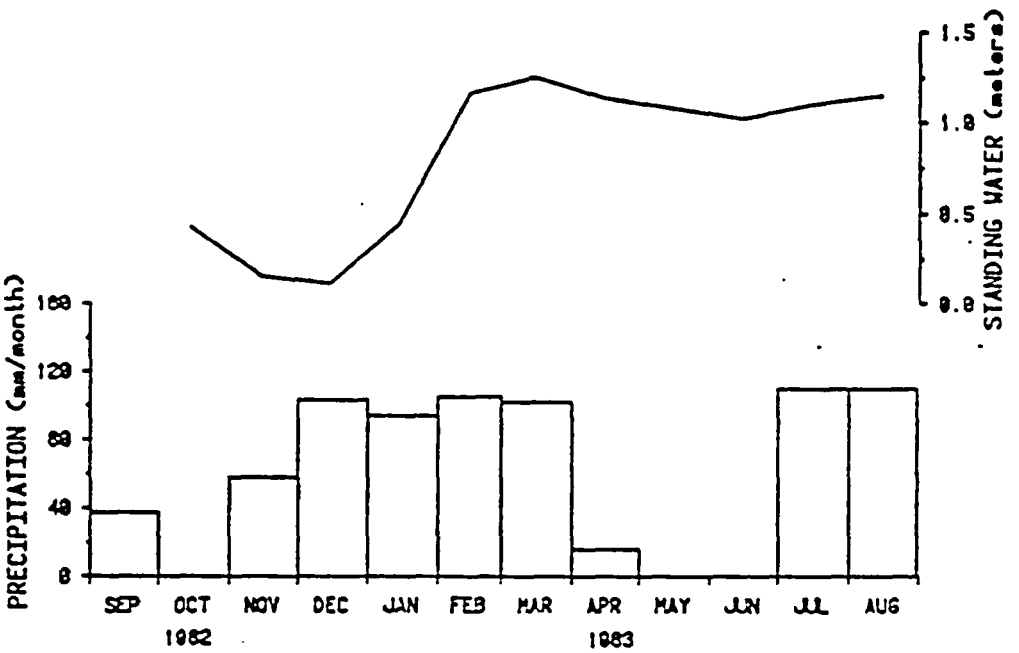

Figure 3.15 Relative water levels in borehole 6.0a.

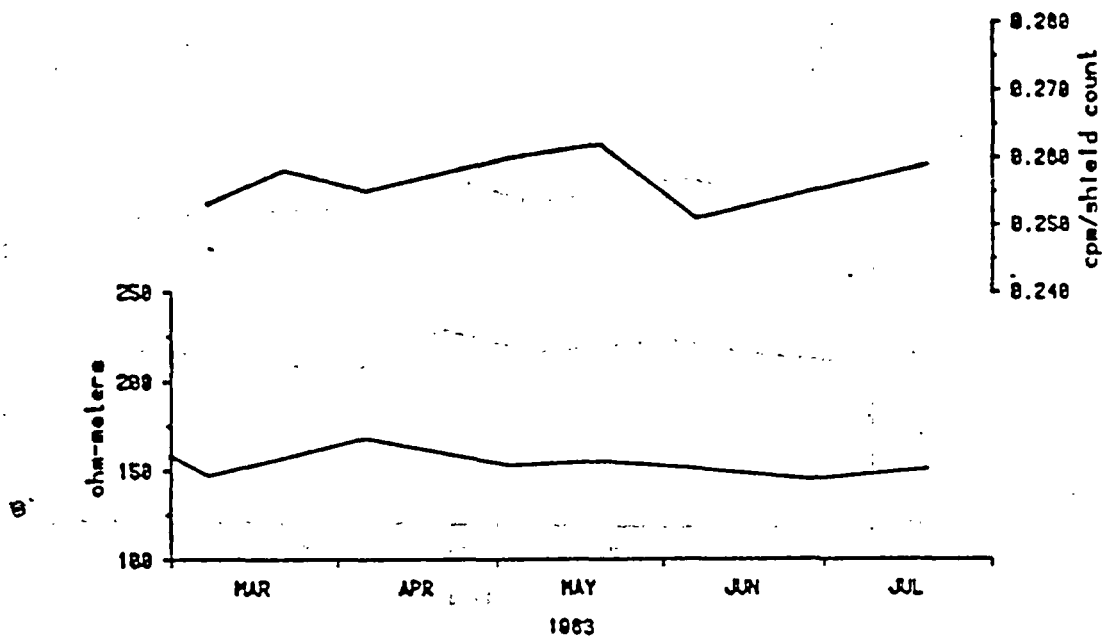

Figure 3.16 Resitivity (lower) profile and normalized neutron (upper) profile at a depth of 5.2 meters in the top borehole at the Magma field site.

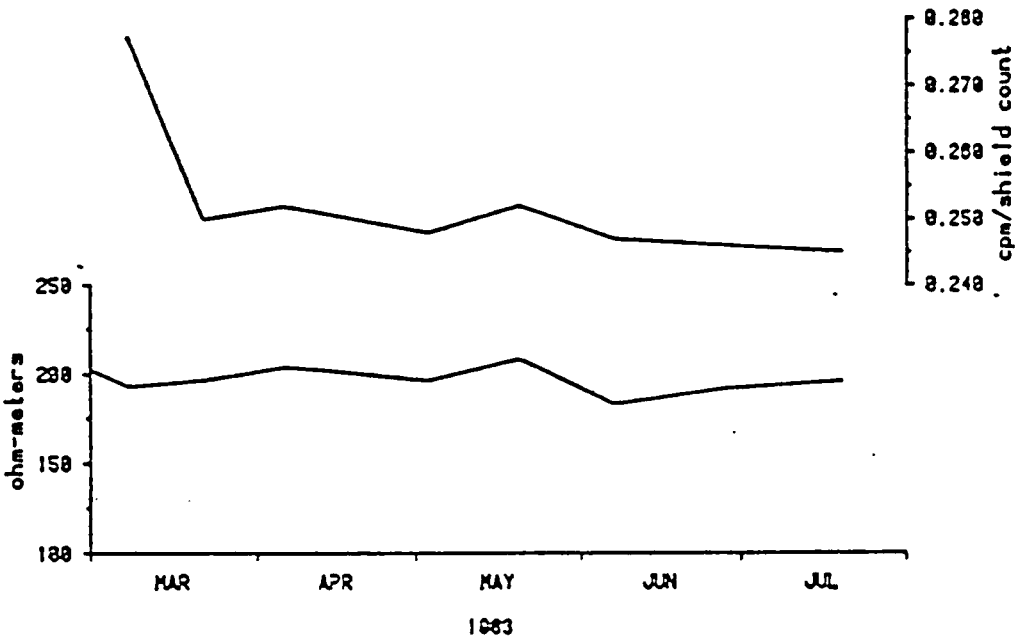

Figure 3.17 Resitivity (lower) profile and normalized neutron (upper) profile at a depth of 11.3 meters in the top borehole at the Magma field site.

How to equate the volume investigated by the resistivity and neutron methods is the most difficult problem in designing a logging program. Decreasing the spacing between the resistivity electrodes increases the effect of fractures, and increasing the spacing between the source and detector in the neutron probe necessitates preliminary calibration before an increasing or decreasing count can be related to an increasing or decreasing water content. A solution to this problem would make these tools more useful in calibrating each other. The current status is that both methods are able to detect qualitative changes in the water content of crystalline rocks.

3.3 Rock Matrix Hydraulic Conductivity

Normally, hydraulic conductivity varies spatially, making it difficult to evaluate by direct measurement in the laboratory or by using *in situ* methods. The unsaturated hydraulic conductivity is a function of the degree of saturation. Computational models are useful for calculating the unsaturated hydraulic conductivity from previously-measured, porous media, water-retention curves, or from moisture-release curves.

The most widely used model for obtaining the unsaturated hydraulic conductivity is that proposed by Mualem (1976), specifically the closed equation given by Van Genuchten (1978 and 1980). This model has been applied to unconsolidated porous media and shows excellent correlation between observed and calculated data (Van Genuchten, 1980; Yates, Van Genuchten and Warrick, 1984; Van Genuchten and Nielson 1985).

Peters et al. (1984) have applied the model to consolidated media (tuffacious material) and have shown a good correlation between the moisture-release curve predicted by the model and the curve found from experimental data. On the negative side, they were unable to reproduce measured hydraulic conductivity values using calculated values, which may have been caused by the use of a psychrometer to define the moisture-retention curve for their samples. As will be shown, the psychrometer method lacks accuracy when defining the retention curve near saturation.

A pressure extractor has been used to define the moisture-release curve for sandstone and tuffacious rock, with emphasis placed on the wet portion of the curve (i.e., from 0 to 1 bar suction). In addition, the measured unsaturated hydraulic conductivity has been compared to the computed value.

3.3.1 Mathematical Development

Two models were used to calculate the hydraulic conductivity, K. The first model, suggested by Burdine (1953), is given by:

$$(3.2) \qquad K(S_e) = K_s\, S_e^2 \int_0^{S_e} h^{-2}(x)dx \;/\; \int_0^1 h^{-2}(x)dx$$

where

K_s is the saturated hydraulic conductivity;
h is the pressure head, a function of reduced water content (S_e); and
S_e is given by:

$$(3.3) \qquad S_e = (\theta - \theta_r)/(\theta_s - \theta_r)$$

where

θ is the water content;
θ_s is the saturated water content; and
θ_r is the residual water content.

Brooks and Corey (1964) adopted an expression relating the moisture content, θ, to the pressure head, h. This expression yields a closed form solution to Equation (3.3):

$$(3.4) \qquad \theta = \begin{cases} \theta_r + (\theta_s - \theta_r)\,(\alpha h)^{-n} & \alpha h > 1 \\ \theta_s & \alpha h < 1 \end{cases}$$

where

a and n are parameters to be determined from the observed moisture-release curve.

The solution for Equation (3.2) using Equation (3.4) is:

$$(3.5) \qquad K(S_e) = K_s\, S_e^{\,(3+2/n)}$$

The second model, presented by Maulem (1976), is an improvement of the statistical model which was developed by Childs and Collis-George (1951). The Maulem equation is of the form:

$$(3.6) \qquad K(S_e) = K_s\, S_e^{1/2} \left[\int_0^{S_e} h^{-1}(x)dx \;/\; \int_0^1 h^{-1}(x)dx\right]^2$$

Van Genuchten (1978, 1980) introduced an empirical equation relating h to θ;

$$(3.7) \qquad S_e = [1 + (\alpha h)^n]^{-m}$$

where

h is positive; and

α, n, and m are determined from the experimental moisture release curve.

Van Genuchten (1978, 1980) substituted Equation (3.7) into Equation (3.6), and gave a closed form solution for the later as:

$$(3.8) \qquad K(S_e) = K_s \, S_e^{0.5} \, [1 - (1-S_e^{1/m})^m]^2$$

where

$m = 1 - 1/n$;

$0 < m < 1$

and $n > 1$

Equations (3.5) and (3.8) show that the unsaturated hydraulic conductivity for a porous media can be estimated from its moisture-retention curve and from the saturated hydraulic conductivity.

3.3.2 Numerical Implementation

A computer code developed by Van Genuchten (1985) is used to produce the best fit to observed data, which consists of a moisture-retention curve and the measured hydraulic conductivity. The program, referred to as RECT, uses least-squares optimization to estimate the parameters. The objective functions, E_1 and E_2, that are to be minimized are of the form:

$$(3.9) \qquad E_1(b) = \sum_{i=1}^{N} [\theta_i - \overset{\circ}{\theta}_i]^2$$

where

θ_i is the observed water content;

$\overset{\circ}{\theta}_i$ is the fitted water content, given by Equation (3.7); and

N is the number of observations.

The second objective function is of the form:

$$(3.10)\quad E_2(b) = \sum_{i=1}^{N} [W_i[\theta_i - \mathring{\theta}_i]]^2 + \sum_{i=N+1}^{M} [W_1 W_2 W_i[K_i - \mathring{K}_i]]^2$$

where

K_i is the observed hydraulic conductivity;
$\mathring{K}_i$ is the fitted hydraulic conductivity;
W_i, W_1, and W_2 are weighting factors designed to give more or less weight to a given set of the observed data; and
M is the total number of the observed points of the retention and conductivity data.

3.3.3 Materials and Methods

Rocks from two different geologic formations in different parts of Arizona have been tested: Coconino sandstone from Strawberry, Arizona, and Apache Leap tuff from Superior, Arizona (Table 3.4). The Coconino sandstone was divided into two samples. The moisture-release curve and hydraulic conductivity were determined for the first sample, while only the moisture-release curve was determined for the second sample.

The moisture-release curve and the hydraulic conductivity were also determined for four Apache Leap tuff samples of which three samples were from the surface and one was collected from borehole cuttings at a depth of eight meters.

All samples were saturated by first placing the oven-dried sample in a vacuum desiccator and evacuating the air for at least two hours. Tap water was introduced into the desiccator until most of the sample was immersed in water. A continuous vacuum was maintained for 4 to 6 hours. The vacuum pump was turned off, but the desiccator was sealed and retained the vacuum for an additional 12 to 24 hours. The samples were then assumed to be fully saturated. Accordingly, the porosity of the sample was assumed to be equal to the saturated water content. Bulk density was calculated by dividing the oven-dry weight of the sample by its volume determined by geometrical measurement. The grain density is calculated from the following relationship:

$$(3.11)\quad \rho_S = \rho_B/(1-\phi)$$

where

ρ_S is the grain density;
ρ_B is the bulk density; and
ϕ is the porosit.

The validity of this calculation relies on the degree of saturation that could be obtained. But it should be a good estimation if we consider the porosity is equal to the effective porosity (i.e., interconnected pores), and by considering the dead-end pores to be part of the solid portion of the rock.

Table 3.4 Selective properties of rock samples.

Sample No.	Rock Type	Diameter (cm)	Length (cm)	Porosity (%)	Bulk Density (gm/cm^3)	Grain Density (gm/cm^3)
S1	Sandstone	5.025	4.88	16.4	2.18	2.60
S2	Sandstone	5.025	1.5	17.5	2.16	2.62
T1	Tuff	7.63	4.84	18.6	2.10	2.57
T2	Tuff	7.63	4.81	17.8	2.11	2.57
T3	Tuff	7.63	4.84	17.8	2.12	2.57
T4	Tuff	6.32	5.04	17.1	2.14	2.58
T5	Tuff	6.32	5.01	17.0	2.15	2.59
TS1A	Tuff	-	-	20.6	1.92	2.42
TS1B	Tuff	-	-	19.8	1.94	2.42
TS2A	Tuff	-	-	19.5	2.03	2.52
TS2B	Tuff	-	-	19.3	2.03	2.52

Three experimental techniques can be used to derive the moisture-release curve for the samples tested. They are the ceramic-plate extractor method, the Tempe pressure-cell method, and the psychrometer method. These methods are described in Appendix D.

The saturated hydraulic conductivity was measured using a modified Tempe Pressure-cell (Figures 3.18 and 3.19). The saturated sample is placed in the cell and confined by O-rings on the top and the bottom. The sides of the sample between the O-rings are sealed to prevent flow along the sides. The cell is filled with water and pressure applied. Outflow from the Tempe cell is collected in a graduated cylinder, and the time to collect 10 cm^3 is recorded. The saturated hydraulic conductivity, K_s, can then be calculated using a form of Darcy's Law.

The unsaturated hydraulic conductivity can be measured by the outflow method as outlined by Gardner (1956), Miller and Elrick (1958), and

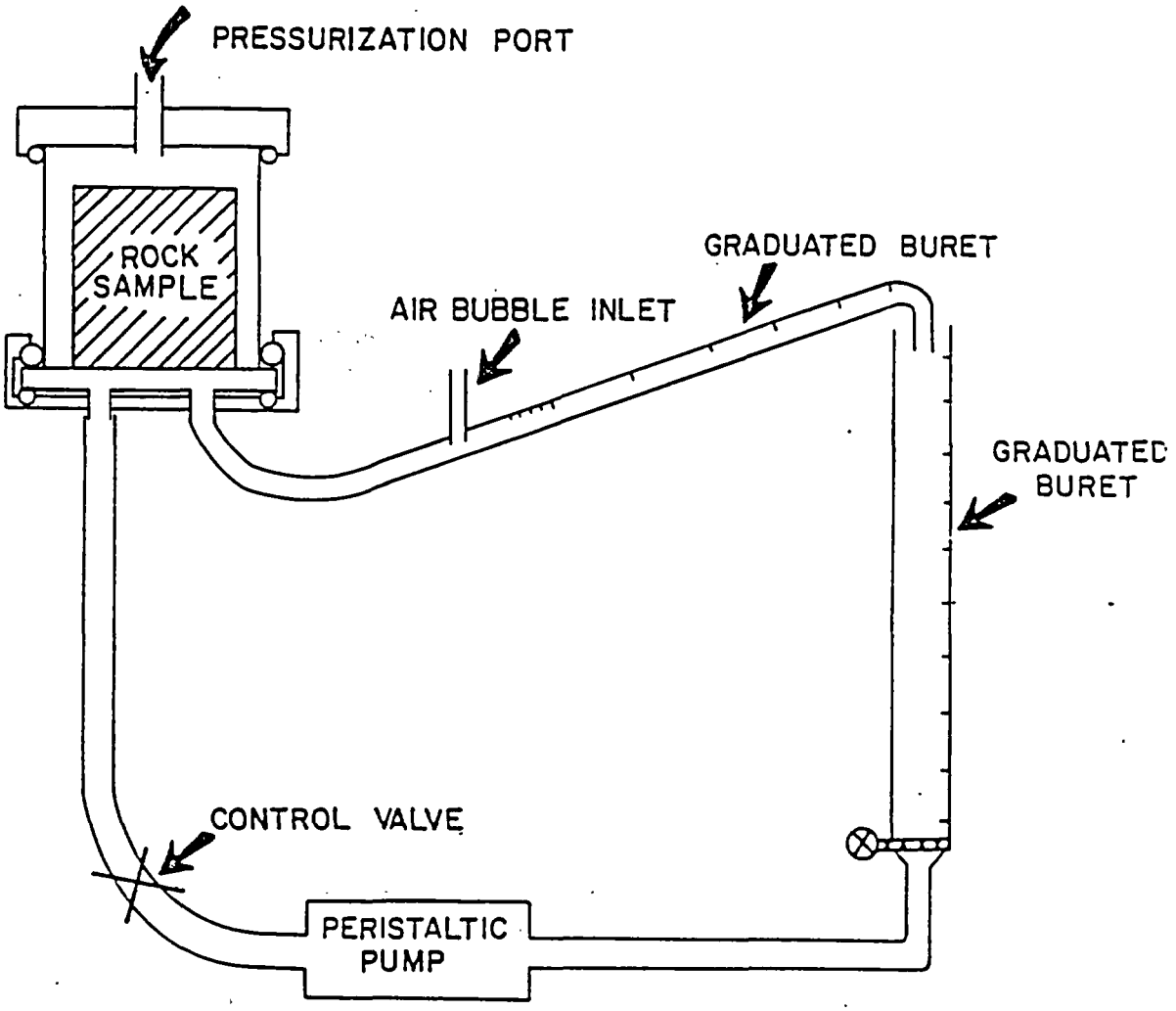

Figure 3.18 Modified Tempe pressure cell for measuring saturated conductivity, K_s. Water is forced through a saturated sample by applying air pressure. Outflow is collected and used to compute K_s by using Darcy's law. Sealant is used to prevent flow along the sides of the sample. Clay and tissue are used to improve the contact between the sample and the porous plate.

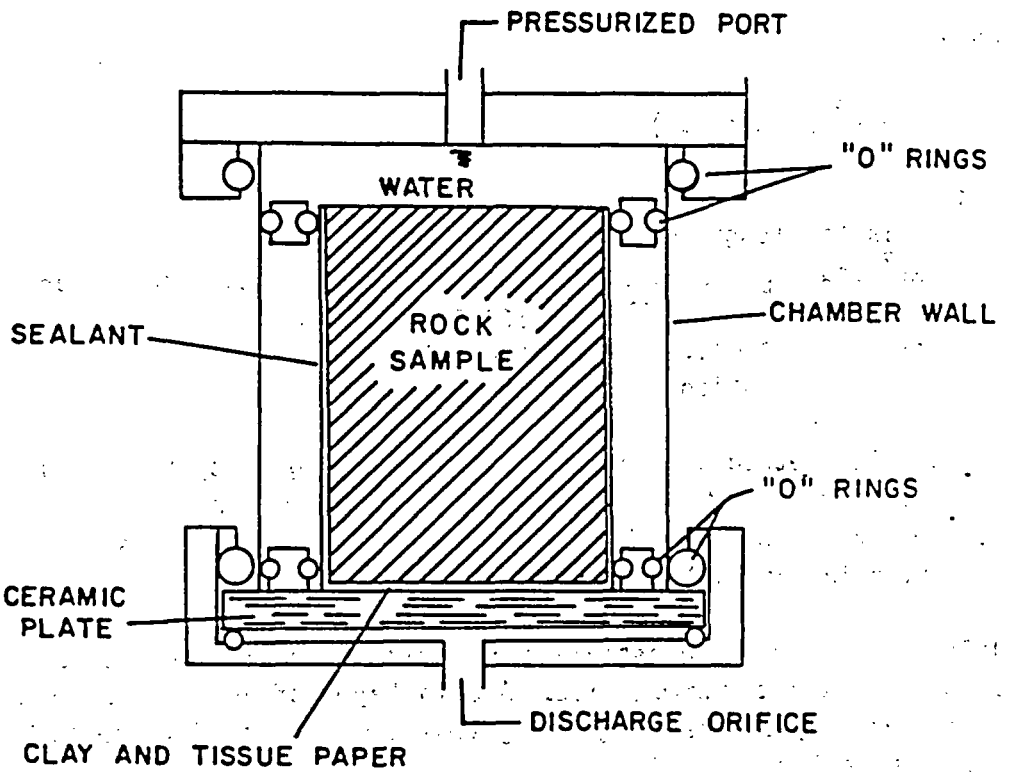

Figure 3.19 Cross-sectional view of Tempe pressure cell used to measure unsaturated hydraulic conductivity, K, by the outflow method. A saturated sample is placed in the cell and, after assuring good contact between the sample and the ceramic plate, a small increment of pressure is applied. Outflow is measured using a graduated tube after an air bubble is introduced into the system. K is calculated by plotting the flow rate against time, and then using a set of type curves.

Kunze and Kirkham (1962). The time dependence of the outflow of water from a rock sample on a porous plate in the Tempe pressure cell (see Figure 3.19) is used to determine rock diffusivity. The unsaturated hydraulic conductivity, can then be determined from the diffusivity using the equation:

(3.12) $K_s = D\ (\Delta\theta/\Delta P)$

where

$$D = L^2 / (\alpha_1^2\ t_{rp})$$

and

L is the length of the sample;
α_1^2 and t_{rp} are parameters determined by fitting the experimental data to a family of type curves; and
$\Delta\theta$ is the change of water content of the sample due to the application of a pressure increment ΔP.

The outflow method assumes that the effect of gravity is negligible, and that the water content is a linear function of pressure head for the applied small pressure increments. Detailed descriptions of the method are given in original papers mentioned above.

Difficulties arise in establishing a good hydraulic contact between the sample and the ceramic plate. A thin layer of bentonite was used for that purpose; the setting being similar to that of Kunze and Kirkham (1962) (see Figure 3.19).

Another contact enhancement material examined was tissue paper. This material gave good results and did not introduce any extra measurable outflow. However, the tissue did not remain saturated for the whole range of pressure used, and weak contact resulted when high pressure was applied (0.6 bar of water or more). The best results were obtained when the tissue and very thin layer of clay were used together.

3.3.4 Results and Discussion

Table 3.5 presents estimates of parameters for the two models examined. The purpose of estimating these parameters is to assess the applicability of methods used to calculate the unsaturated hydraulic conductivity of geologic media. The parameters were estimated by optimization techniques presented as Equations (3.9) and (3.10).

Table 3.5 Computed parameters of rock samples using three models.

Sample No.	θ Model[1]			θ and K Model[2]			Brooks and Corey[3]		
	θ_r	α	n	θ_r	α	n	θ_r	α	n
S1	.0000	.0078	2.09	.00	.0074	2.19	.026	.0108	1.346
S2	.0325	.0034	4.92		-		.031	.0044	2.638
T1	.1092	.0010	2.232	.00	.0018	1.15	.11	.0019	1.005
T2	.0	.0017	1.314	.05	.0019	1.32	.13	.0058	1.005
T3	.0	.0007	1.426	.00	.0060	1.09	.10	.0018	1.005
T4	.0	.0133	1.084	.00	.0046	1.07		-	
TS1A	.0127	.0002	1.775		-			-	
TS1B	.0136	.0002	1.957		-			-	
TS2A	.0001	.0003	1.496		-			-	
TS2B	.0125	.0002	1.730		-			-	

[1] Only moisture content data optimized.
[2] Moisture content and hydraulic conductivity data optimized.
[3] Analytic function proposed by Brooks and Corey.

To verify the computational results, experimental data obtained by the outflow method were compared to the analytic expressions. Before making this comparison, however, a brief discussion of data acquisition limitations is in order. Some difficulties occurred when the outflow method was applied. Establishing good contact between the rock sample and the ceramic plate is one of the problems with this method. An uncertain contact could be overcome by using a relatively large sample and making measurements when the sample is at least 50% saturated.

Other difficulties are related to the equipment used, (i.e., the Tempe pressure cell set-up, Figure 3.18 or 3.19). A volumetric pressure-plate extractor (Soil Moisture Equipment Catalog No. 1250) may be a more suitable device to use because of the greater range of pressures available compared to the Tempe cell. Also, the precision in measuring the outflow rates is better. Problems arise when the moisture-release data are needed for pressure head as high as 15 bars. Without data points at the extremely dry end of the release curve, it is difficult to conclude which of the parameter optimization schemes is more suitable.

The models used to calculate unsaturated hydraulic conductivity were derived mainly for homogeneous, isotropic media, which is rarely encountered in the field. Most consolidated porous media are nonisotropic because the mechanics of sedimentation result in vertical compression of the medium. The assumption of isotropy for small samples, such as the samples used in this study is considered appropriate and accurate (Wyllie and Spangler, 1952). Even though it is generally assumed for this study that the rock being studied is homogeneous and isotropic, some layering of the sandstone samples was noted.

The results of tests of sandstone samples (see Figures 3.20 to 3.23) are in excellent agreement between the computational model and observed data. However, such results would not be expected when evaluating the unsaturated hydraulic conductivity for a large formation, due to heterogeneities and anisotropies.

The parameters used in the solution of the unsaturated hydraulic conductivity equations consist of a residual and saturated water-content parameters, three calibration parameters (α, n, and m) and the saturated hydraulic conductivity. It is generally assumed that the saturated water content and the saturated hydraulic conductivity are known for the computational model. If a value of either parameter is not available, a good estimation can be obtained by the optimization scheme. In this study the saturated water content was assumed to be known because a complete saturation of the rocks' pores is probable. The measured hydraulic conductivity, however, may be incorrect due to experimental error, and so its value was obtained using the optimization scheme. Generally, the optimized value is less than the measured one. For most cases, the difference is not significant and both values fall in the same order of magnitude.

The most ambiguous parameter is the residual water content. By definition, the unsaturated hydraulic conductivity is zero when the water content is equal to the residual water content. This may be true for characterizing soil physics problems such as drainage and irrigation, but for characterizing rock of low permeability, this assumption may be inappropriate.

The present models are not able to define the unsaturated hydraulic conductivity if we assume that the water content may be less than the residual water content. It may be preferable to assume that the residual water content is always zero, and use this value as a known input parameter. In this case, the unsaturated hydraulic conductivity will be zero only if the medium is completely dry.

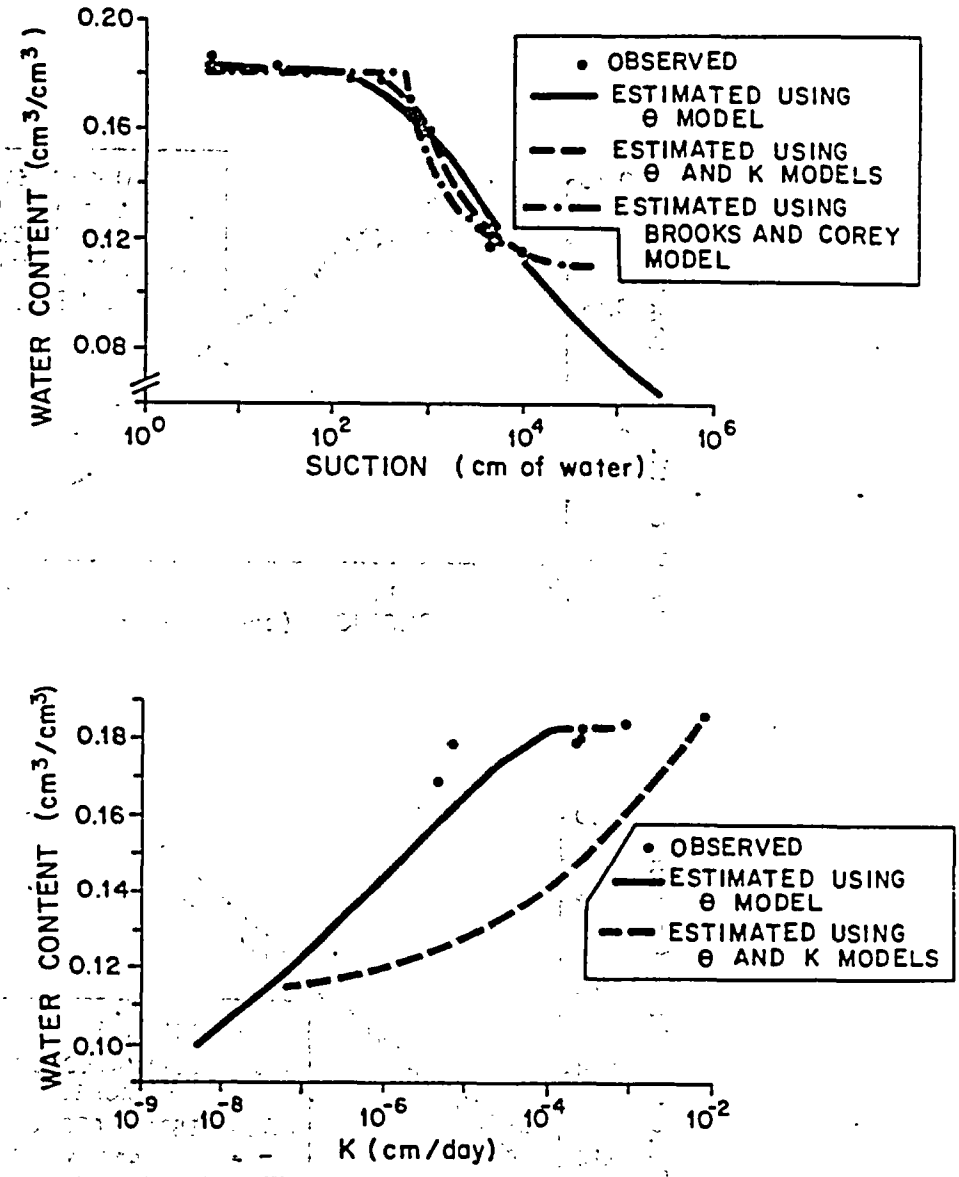

Figure 3.20 Moisture content by volume (θ) versus suction for the Apache Leap Tuff sample T1.

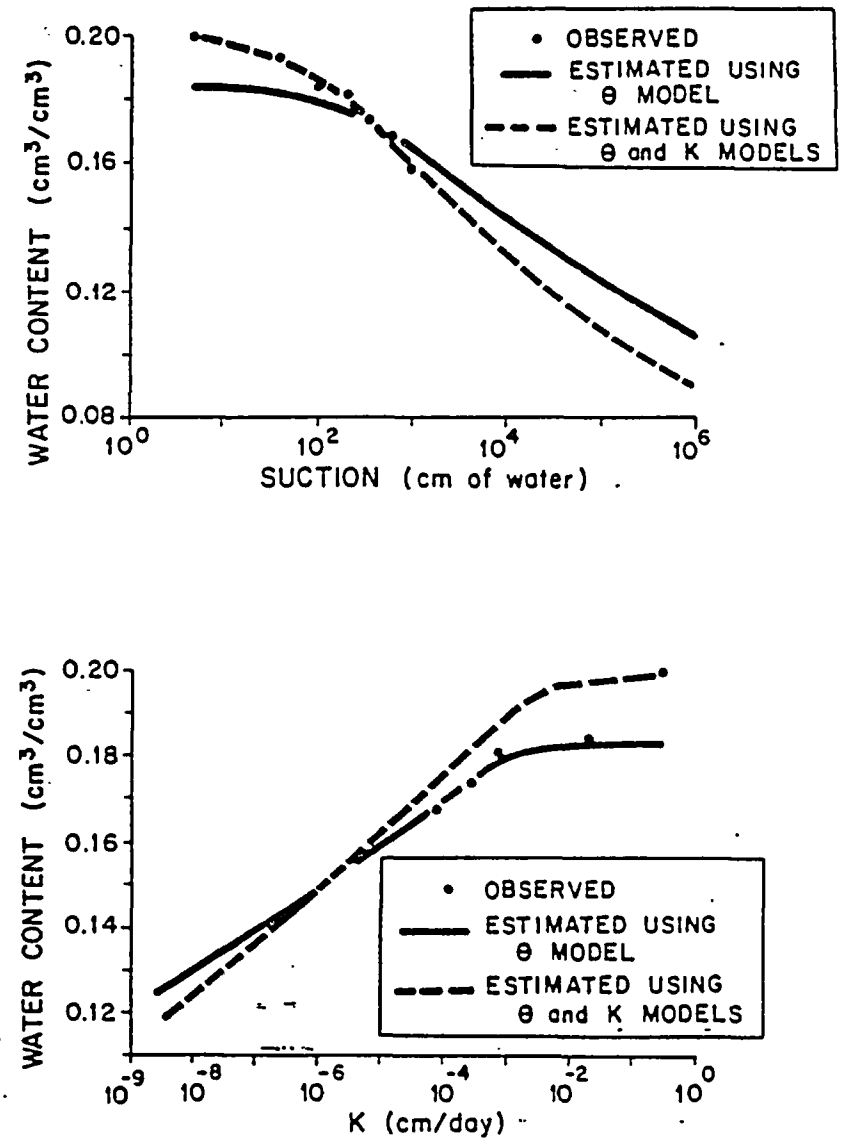

Figure 3.21 Moisture content by volume (θ) versus suction for the Coconino Sandstone sample T4.

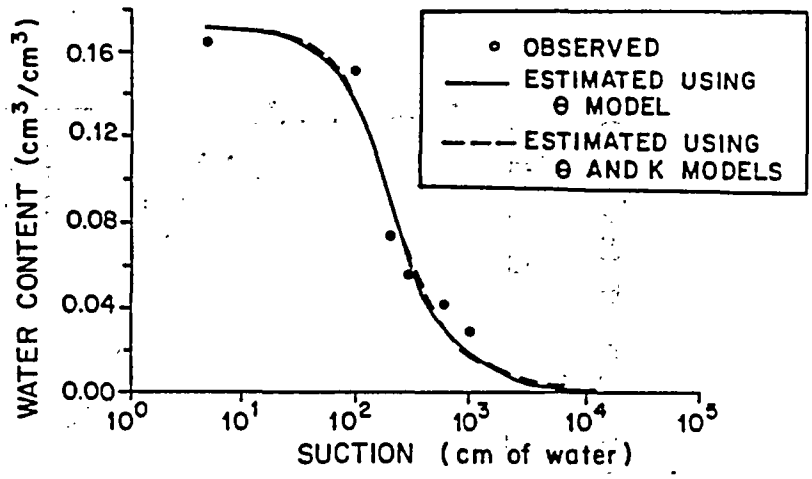

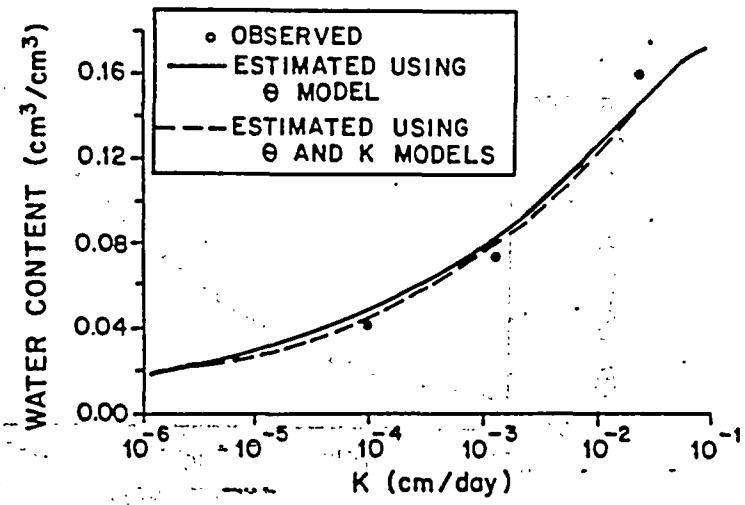

Figure 3.22 Moisture content by volume (θ) versus suction for the Coconino Sandstone sample S1.

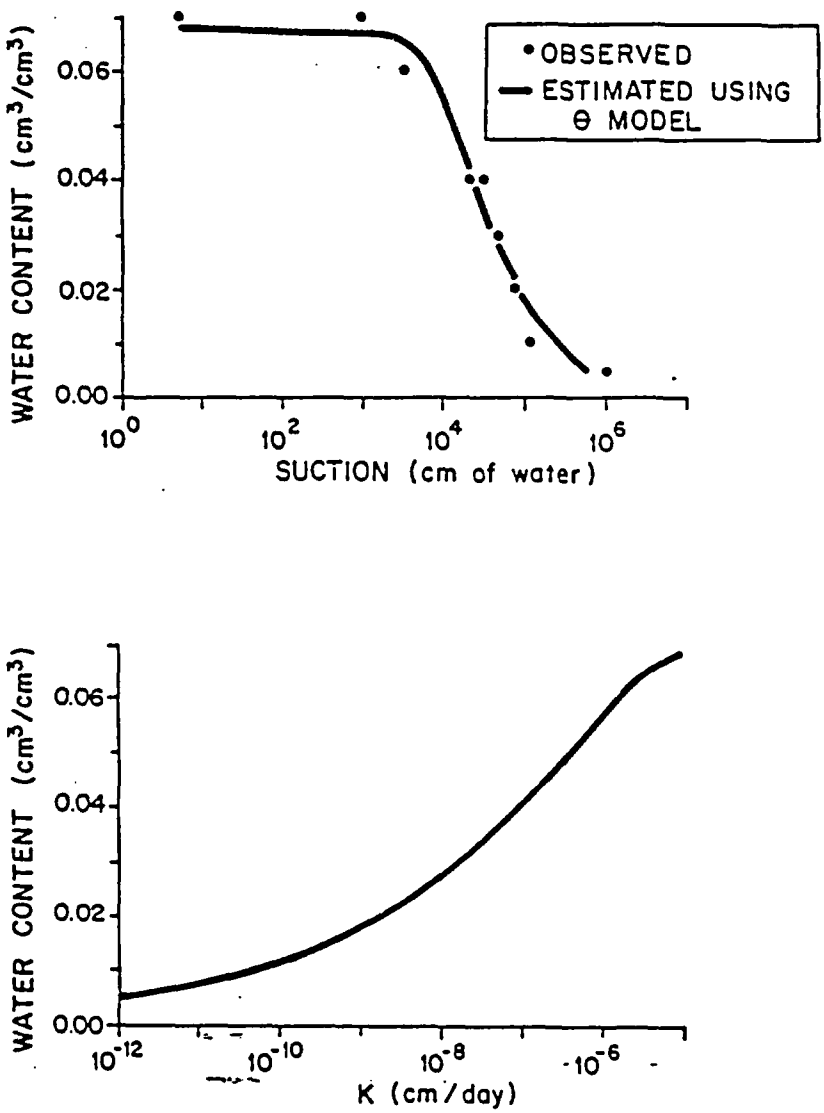

Figure 3.23 Moisture content by volume (θ) versus suction for the tuff sample GU4 (from Peters et al., 1984).

The reliability of the calibration parameters (α, m, and n) depends on the precision by which the experimental data is obtained. A relationship suggested by Van Genuchten (1980) provides a good approximation of the unsaturated hydraulic conductivity and reduces the number of calibration parameters by one.

3.4 Fracture Permeability Investigations Using a Heat-Pulse Flowmeter

The heat-pulse flowmeter is an experimental instrument designed to detect low velocity flows by measuring the travel time of an induced heat pulse. By observing changes in the vertical flow in a borehole it is possible to locate zones of outflow which can be correlated with fractures observed in the drill core. The relative permeabilities of the fractures can be compared by observing the amount of outflow occurring. This information is useful in determining suitable areas for future testing using tracers.

Tracer tests are being used extensively in the analysis of flow in fractured crystalline rock. One of problems associated with this type of testing is the location of permeable zones in a borehole suitable for conducting tracer tests. Drill cores reveal the location and condition of fractures intersected by the borehole and the degree of weathering and mineralization observed along a fracture surface allows some speculation about the fracture permeability.

A borehole flowmeter survey was conducted at the Apache Leap site to locate permeable zones and determine their relative conductivities. By measuring changes in the vertical flow in a borehole, it is possible to identify permeable fractures and observe the amount of flow leaving the borehole. Flow velocities encountered at the Apache Leap site were far below the lower detection limit of conventional flowmeters that measure impeller rate of spin. An experimental heat-pulse flowmeter was used successfully to survey the low velocity flows at the Apache Leap site.

3.4.1 Operation of Heat-Pulse Flowmeter

The flowmeter operates by measuring the travel time of an induced heat pulse that is advected by the borehole flow. The flow sensor consists of a heater grid mounted between two thermistors inside a flow tube (Figure 3.24). A measurement is taken by sending a electric pulse through the heater grid, heating a sheet of water around it. The heated water is advected past one of the two thermistors depending on the direction of flow. The thermistors are wired in a bridge (Figure 3.25)

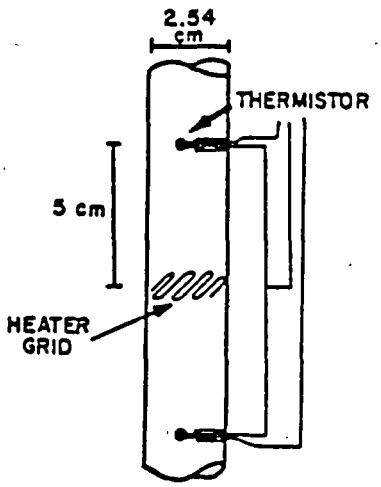

Figure 3.24 View of heater grid and thermistor inside flow tube of heat-pulse flowmeter.

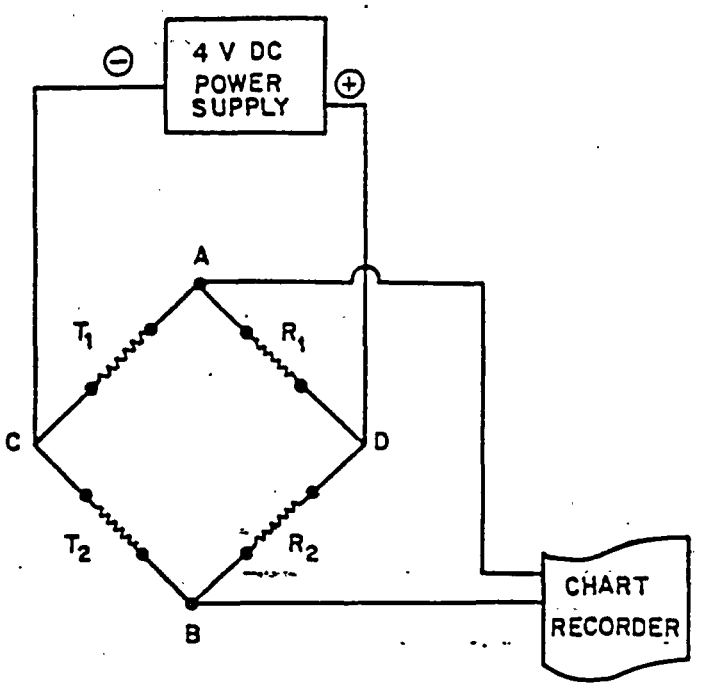

Figure 3.25 Diagram of electronic circuit used for recording temperature pulse in flowmeter.

such that a signal is produced when one thermistor experiences a temperature change not occurring at the other.

The response curve on a chart recorder (Figure 3.26) indicates direction of flow and the temporary thermal imbalance of the two thermistors. The elapsed time between the electrical pulse and the peak of the response curve is compared to a calibration graph (Figure 3.27) to determine the flow rate in the borehole.

The concept of a thermal flowmeter was first developed in 1955 by H.E. Skibitzke of the U.S. Geological Survey (Chapman and Robinson, 1962). Skibitzke used a continuous heat source mounted between two thermistors in a flow tube. The measured difference in temperature is a function of the water velocity. The instrument had a lower limit of 0.5 cm/s.

Flowmeter research is currently being conducted by A.E. Hess and F.L. Paillet of the U.S. Geological Survey, Water Resource Division. Hess (1982) has modified a heat-pulse flowmeter manufactured by Wuidart Engineering and reports an ability to measure flows down to 0.1 cm/s. Paillet has field tested the instrument and increased the sensitivity of the flowmeter by constructing a rubber skirt around the flowmeter that serves to concentrate the flow through the instrument. Laboratory calibrations using a total seal around the flowmeter increased the sensitivity for detecting flows down to 20 cm^3/min. However, Paillet has noted that under field conditions, a significant amount of flow may bypass the instrument producing error in the measurements (unpublished).

Paillet's work demonstrated the need for an effective way of sealing the borehole around the flowmeter. This led to the development of the packer sealed heat-pulse flowmeter used at the Apache Leap site. The packer increased the low range sensitivity and assured a reliable seal around the instrument.

The flow-sensor tube is mounted inside a packer assembly that seals the space around the flowmeter when inflated (Figure 3.28), forcing all flow to pass through the flowtube. The flow remains constant, while the average velocity is inversely proportional to the cross-sectional area. When flow in the 10.16 cm diameter boreholes at the Apache Leap site is forced through the 2.54 cm flowtube of the instrument, the velocity in the flowtube is 16 times that of the borehole velocity. This relationship allows the measurement of very low velocity flows.

The flowmeter was calibrated by comparing known flow rates in a test column to inverse response time (Figure 3.27), i.e., the time from the

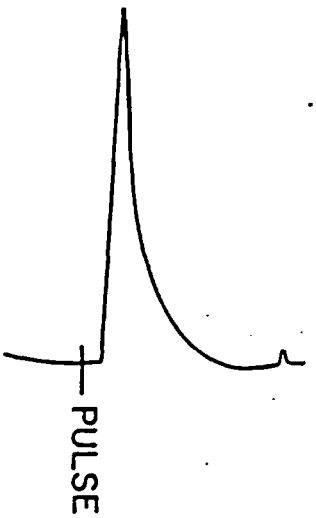

Figure 3.26 Temperature response curve showing electric pulse to heater and peak temperature difference between the two thermistors.

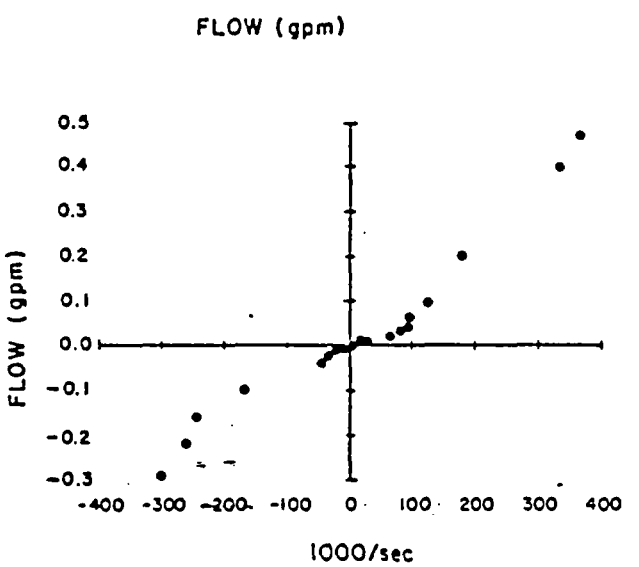

Figure 3.27 Calibration curve for the heat-pulse flowmeter.

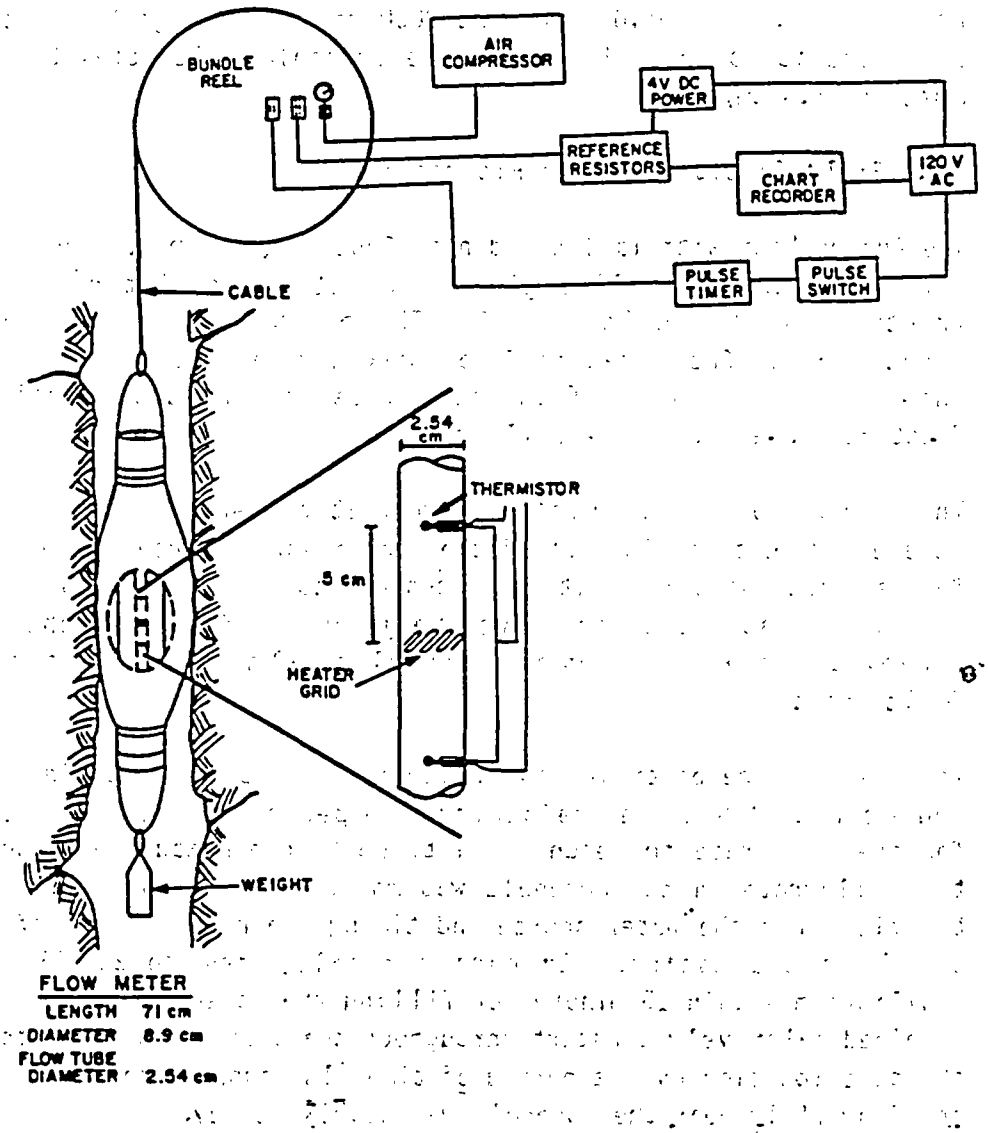

Figure 3.28 View of heat-pulse flowmeter and packer assembly. Wall roughness exagerated.

electrical pulse until the peak temperature response. Inverse time was chosen because it linearizes and spreads the data over the optimum range of the instrument.

The effect of convection caused by the tendency of the heated water to rise, produces a non linear response for low flow rates. It also results in different-shaped curves for upflow and downflow. The effective measurement range of the packer sealed heat-pulse flowmeter is between 40 cm^3/min (0.01 gpm) and 2000 cm^3/min (0.5 gpm). At the Apache Leap site it is possible to measure borehole velocities between 0.008 cm/s and 0.4 cm/s.

3.4.2 Field Investigation of Flowmeter

The Apache Leap site is located near Superior, Arizona. Three boreholes were drilled at a 45° angle in an attempt to intersect vertical fractures in the welded tuff. The boreholes are 10 m apart and penetrate the fractured tuff to a maximum depth of 46 m. Figure 3.29 shows the arrangement of the boreholes and the distribution of the fractures observed in the drill core.

The purpose of the flowmeter survey at the Apache Leap site was to locate and measure flow out of the boreholes. Because the boreholes are in the unsaturated zone, it was necessary to fill them with water to the top of the casing, 30 cm above the ground surface. Borehole X-3 was surveyed in one afternoon and boreholes X-2 and X-3 were surveyed the following day.

In each case the borehole was filled to the top of the casing with water and a constant head was maintained. A period of one hour was allowed for the flow rate to reach equilibrium before measurements began. The total flowrate in the borehole was monitored periodically by stopping the flow from the water source and timing the rate of fall of the water level in the casing. In each borehole, the total flow reached equilibrium within 15 minutes of filling the borehole and the flow rate remained relatively constant throughout the test. Measurements taken at the same location over a period of time also support the conclusion that the flow field near the borehole was nearly steady.

The boreholes were surveyed downhole beginning at the top just below the casing. In some cases, measurements were taken on the return trip uphole. The instrument was moved carefully in the hole to avoid altering fracture permeabilities. Measurement positions were chosen by examining the drill core logs. Measurements were taken above and below

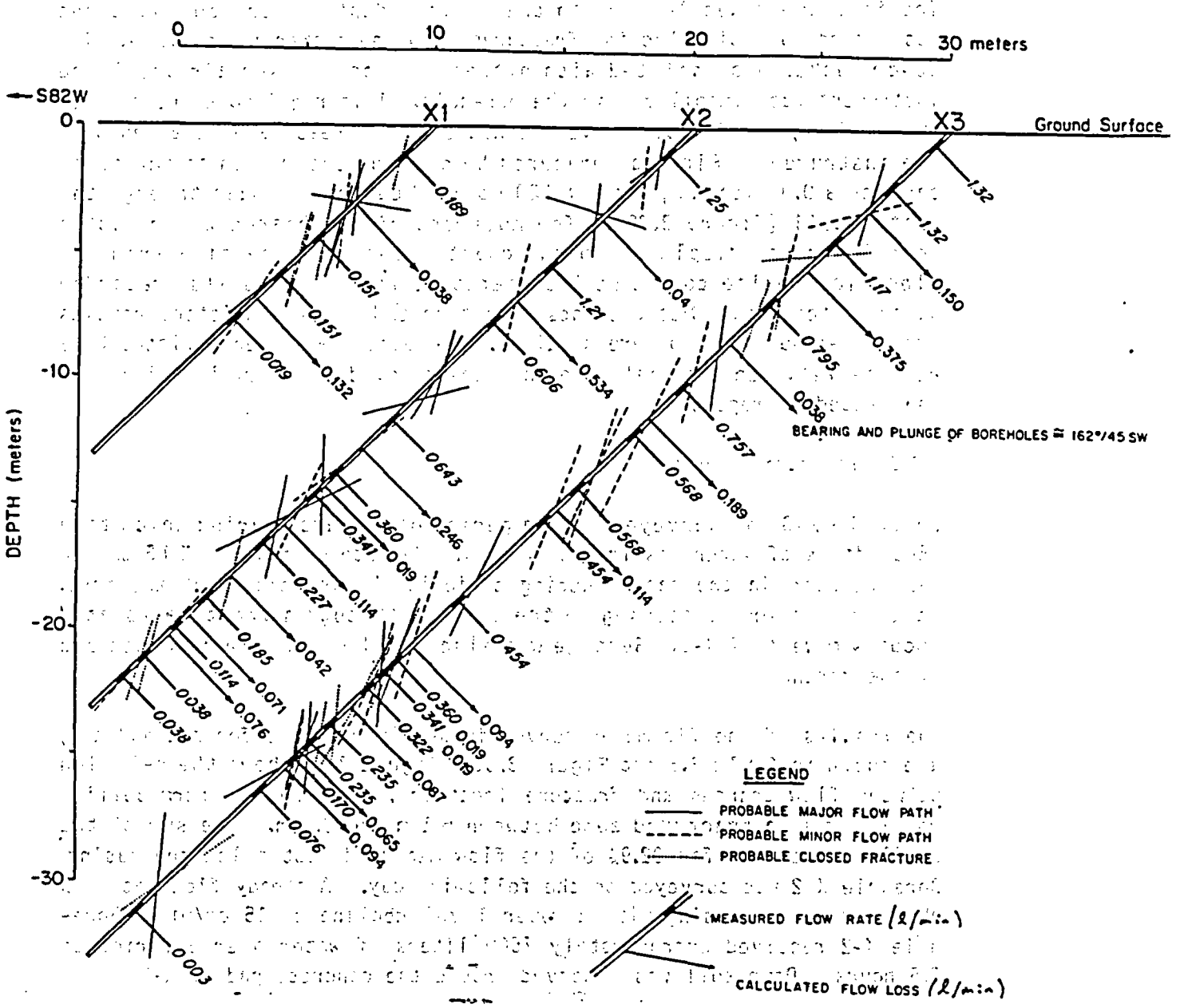

Figure 3.29 Measured flow rates and calculated flow losses for Boreholes X-1, X-2, and X-3 at the Apache Leap site.

all major fracture zones to determine if there was a change in flow. If a flow change was detected, the borehole was surveyed at closer intervals until the fracture conducting the flow was located.

Measurements were taken with the flowmeter by the following procedure. The instrument was lowered to the desired depth in the borehole and positioned to avoid blocking fractures with the packer if possible. The 60-cm packer was inflated with nitrogen or compressed air until the instrument was immobilized in the borehole. This required a pressure of about 0.7 kg/cm^2 (10 psi) above the hydrostatic pressure at the depth of the instrument. Flow was measured by closing the switch to the timer causing a 0.05 second pulse of 120 volt AC current to pass through the heater coil (Figure 3.28). The movement of the heated water past a thermistor was displayed on the chart recorder. The time from the electrical pulse to the peak temperature response was also recorded using a stopwatch. Measurements were repeated until consistent results over a 5-minute period were obtained. The packer was then deflated by a release valve on the reel, the instrument moved to a new location, and the procedure repeated.

3.4.3 Flowmeter Results

Borehole X-3 was surveyed over a period of 5 hours, during which time 1500 liters of water was injected. A steady rate of fall of 30.5 cm/min was observed in the casing during periodic checks throughout the test. Water was observed seeping to the surface through a fracture located about 4 m west of X-3. Seepage was also noted around the concrete pad of the borehole.

The results of the flowmeter survey in X-3 (as well as for X-2 and X-1) are shown in Table 3.6 and Figure 3.30. Figure 3.29 shows the relation between flow changes and fracture locations. The highest permeability was found in a fractured zone between 6.1 m and 9.2 m. The sum of the outflows accounts for 92.9% of the flow measured just below the casing. Borehole X-2 was surveyed on the following day. A steady flow rate was observed in the casing with a water level decline of 15 cm/min. Borehole X-2 received approximately 7500 liters of water over a period of 3.5 hours. Damp soil was observed around the concrete pad of X-2.

Approximately half of the vertical flow in X-2 was seen to exit the borehole between 7.6 m and 10.7 m. There are two fractures recorded in the core log for that interval. Another interval of relatively high permeability was located between 16.2 m and 19.2 m. One fracture was observed in the drill core for that interval at 18.7 m.

Table 3.6 Observed flow rates versus depth of observation for boreholes X-1, X-2, and X-3 at the Apache Leap site.

Borehole X-1		Borehole X-2		Borehole X-3	
Downhole Flow (liters/min)	Depth (m)	Downhole Flow (liters/min)	Depth (m)	Downhole Flow (liters/min)	Depth (m)
0.189	1.52	1.136	1.52	1.320	0.61
0.151	6.10	1.211	7.62	1.320	3.05
0.151	7.92	0.606	10.67	1.170	6.10
0.019	10.67	0.454	14.33	0.795	9.14
		0.825	14.33	0.757	13.72
		0.643	16.15	0.568	16.76
		0.360	19.20	0.568	19.81
		0.341	20.42	0.454	21.34
		0.227	23.60	0.454	25.91
		0.185	25.91	0.360	29.26
		0.114	27.43	0.341	29.87
		0.038	28.80	0.322	30.78
		0.038	29.87	0.235	32.61
				0.235	33.83
				0.170	34.90
				0.076	36.58
				0.030	43.28

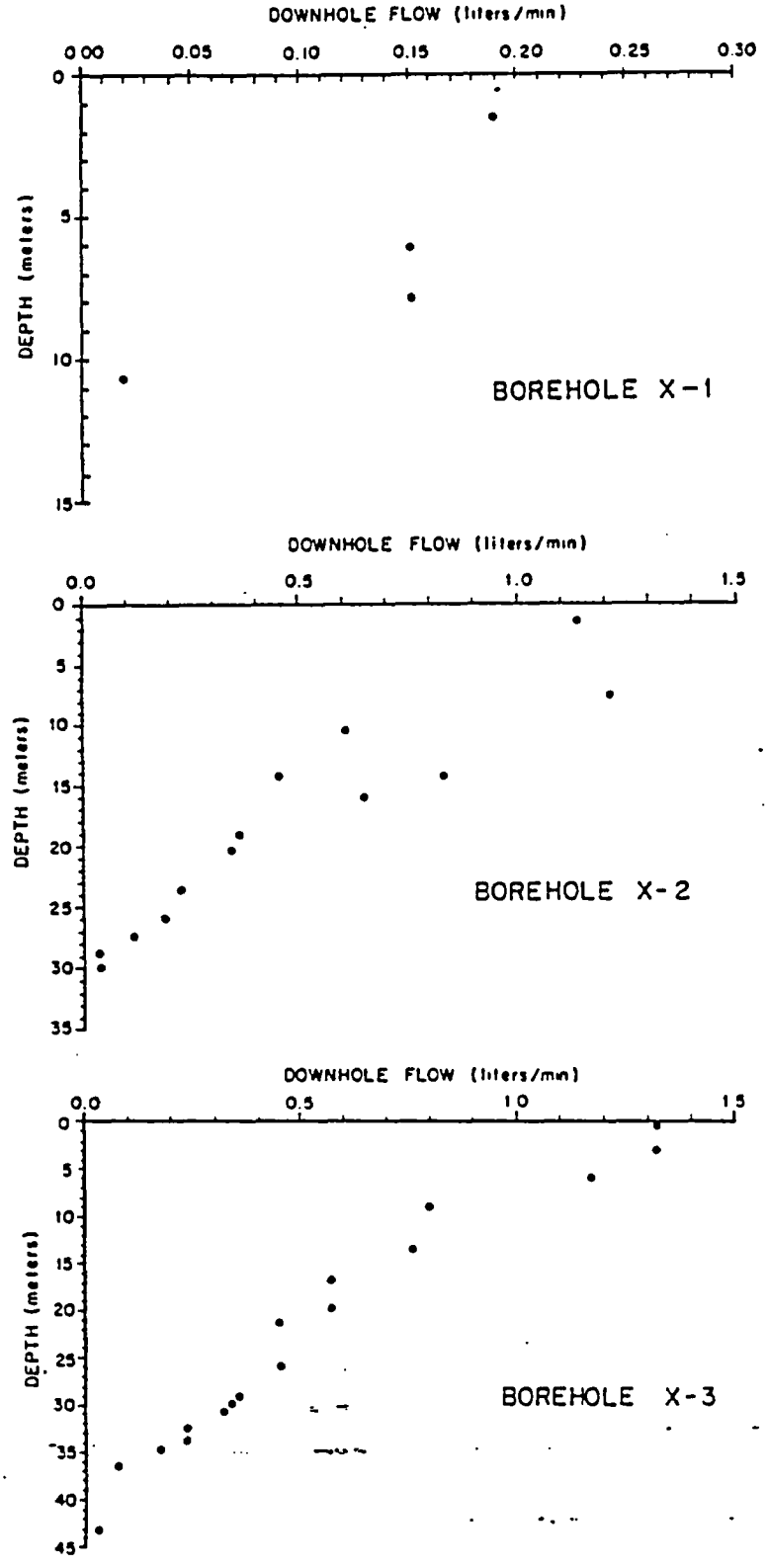

Figure 3.30 Measured downhole flows for Boreholes X-1, X-2, and X-3, plotted against vertical depth.

The rate of flow in X-1 was much lower than in the other boreholes. Water in the casing was observed to fall at the rate of 1.8 cm/min. The zone of highest discharge was between 7.9 m and 10.7 m. Two fractures were observed in the drill core for that interval. No moisture was observed at the surface around the borehole, nor in nearby fractures.

3.4.4 Conclusions from Flowmeter Experiments

The flowmeter survey at the Apache Leap site successfully located permeable fractures in all three boreholes. The results of this test can be used to determine suitable zones for conducting tracer tests in future studies. Time restrictions limited this investigation to a general survey of the three boreholes. Future investigations will be required in some cases to locate the specific fractures responsible for conducting flow in an identified interval of outflow.

A discrepancy exists between the amount of flow measured in the casing by observing water-level decline and the flow rates measured in the borehole with the flowmeter. Flow rates in the casing are double those measured near the top of the borehole. The surface flow observed at X-3 and the damp soil around X-2 suggest that a significant amount of outflow may be occurring where the casing joins the borehole. Further improvements and calibration studies are needed to improve the reliability of the flowmeter at rates greater than 3 l/min (0.5 gpm). In any case, the measurements were consistent and accurately reflect the amount of flow relative to other points in the borehole.

Further analysis of the data may provide more information about the characteristics of the site. If some assumptions can be made about the hydraulic gradient around the borehole, it should be possible to calculate the apparent hydraulic conductivity of a fracture, using Darcy's law. In order to approximate the hydraulic gradient, it is necessary to estimate the borehole pressure at the fracture and the distance to the wetting front. The problem is further complicated by the fracture orientation and the effect of gravity on the shape of the flow field surrounding the borehole. A study has been proposed to model the flow field around similar boreholes in an equivalent porous medium to gain insight into the problem.

One approach to estimating the hydraulic gradient might be achieved by cross-hole testing. First, it would require locating a fracture connection between two boreholes. This could be accomplished by injecting water into a permeable interval of the borehole sealed off by packers. The flowmeter would then be used in an adjacent borehole filled with

water to locate a zone of inflow. If such a connection is found, the hydraulic gradient across the fracture would be equal to the difference in pressure between the injection borehole and the adjacent borehole divided by the estimated fracture length. The flowrate obtained by the flowmeter would then be used in Darcy's Equation to solve for the hydraulic conductivity.

The heat-pulse flowmeter has proven to be a valuable tool for conducting preliminary studies in fractured rock. It can provide information about the permeable zones in a borehole that will be useful in locating equipment in future tracer tests. Further studies hold the promise of providing additional information that will help characterize the hydraulic properties of unsaturated fractured rock.

3.5 Water and Air Intake on Surface-Exposed Rock Fractures

Fractures within lithic units are major contributors to fluid flow, vapor movement, and contaminant transport, particularly when matrix permeability is low. Here, the term "fracture" is defined as any discontinuity within a rock mass characterized by a small but open aperture. Fractures vary in terms of aperture, spatial extent, planar void continuity, tortuosity, and mode of occurrence. The fractures may appear in a rock mass as a result of single or multiple thermal events (i.e., heating/cooling), or geologic structural events. Distinct joint sets are commonly apparent in large rock masses and have a major influence on flow direction and velocity. Rocks of low matrix permeabilities which display high transmissivity are often characterized by spatially-dense fracture networks.

Interest in the flow behavior within unsaturated fractured rock media has been generated by the search for high-level nuclear waste repositories in unsaturated rock and by toxic waste sites located above fractured rock. These sites must provide for the long-term isolation of hazardous wastes. Hydrologic characterization of unsaturated fractured rock media is necessary because liquid phase movement may be the principal mechanism for contaminant transport.

The ability to estimate fluid intake into fractured rock media is an important part of the site characterization process because water intake at the atmosphere-earth boundary may permit or restrict the transport of contaminants at depth. The assumption that matrix flow is negligible compared to fracture flow allows observed fracture intake rates to serve as an estimate of the boundary condition of fluid flow at the atmosphere-earth interface. An accurate estimation of the potential water

input to the geologic medium is a necessary precondition for the reliable simulation of subsurface unsaturated flow systems.

Little or no data have been collected from in situ experiments of water intake into individual rock fractures. Data from in situ experiments are important because previous fluid flow studies of both artificial and natural fractures have shown that the effects of applied stress on fracture conductivity are significant. Sharp (1970) examined one-dimensional flow through a single fracture in a granite porphyry under variable stress. Sharp's findings reveal that flow rate is not strictly a linear function of applied hydraulic gradient, but may vary according to inertial losses and turbulence associated with irregular boundaries along fracture walls. In a laboratory study, Schrauf and Evans (1984) show that the magnitude of fracture plane roughness and waviness is secondary to the effects of contact area between fracture surfaces for fracture apertures under 200 to 300 micrometers (μm). The contact area was found to be a function of applied stress.

The fracture aperture is critical in estimating flow through fractures because of the cubic relation between aperture and flow. Iwai (1976) measured water flow rates as a function of fracture aperture in core samples of basalt, marble, and granite. Iwai's results support the cubic relation between flow rate and fracture aperture; i.e.,

$$q = - e^3 f/12 \, dh/dz \qquad (3.13)$$

where

q is the flow rate per unit length of fracture;
e is the mean fracture aperture;
dh/dz is the hydraulic gradient; and
f is the fluidity of the liquid, computed using:

$$f = \rho g/\mu$$

where

ρ is the fluid density;
g is the gravitational acceleration coefficient; and
μ is the dynamic viscosity of the liquid.

The aperture calculation is useful for characterizing distributions of fracture apertures. Snow (1970) and Bianchi and Snow (1968) found that 256 fracture apertures in the Pike's Peak granite in Colorado are log-normally distributed. They measured fracture apertures by photographing fractures on outcrops treated with a fluorescent dye penetrant.

The cubic law is not free of inadequacies: fracture surface roughness, waviness, and variable contact between fracture surfaces are arguments against the unqualified application of the cubic law when examining flow in natural fractures (Iwai, 1976; Shrauf and Evans, 1984). It is important to state, however, that preliminary models are used in this analysis because of the absence of experimental data which are required to verify a more rigorous formulation.

To investigate the adequacy of the cubic law and to demonstrate field and analytical methods for the measurement of water and air intake into individual natural fractures under ambient stress, a fractured rock infiltrometer (FRI) was designed, built and tested at a site in southern Arizona. Intake rate data collected using both water and air FRI measurements are used to calculate apparent fracture apertures. The analytic techniques used to calculate the apertures based on water and air measurements employ different governing equations and different boundary conditions. Despite the substantial differences in the two analytic techniques, results using the two methods compare favorably.

The methods presented are significant because heretofore there has not existed a technique of sufficient precision for providing estimates of potential intake of water into individual fracture segments under conditions of ambient rock stress. The field and analytic techniques described here are important for estimating water intake for a fractured rock medium of large areal extent. A statistical relation can be used as the basis of an event-based precipitation and/or streamflow model to simulate water intake into a fractured rock medium for extended simulation periods. In this manner, it is possible to vary model inputs (e.g., rainfall) for a particular fractured rock medium, allowing the prediction of intake rates for the rock medium under historical, maximal, or minimal climatic conditions.

3.5.1 Water Intake Method

The fractured rock infiltrometer (FRI), when used to determine water intake rates into individual fracture segments, utilizes a dual-chambered system (Figures 3.31 and 3.32) designed to minimize lateral (i.e., divergent) flow in the plane of the fracture below the interior chamber, identical to the purpose of the exterior ring of a double-ring infiltrometer. This arrangement ensures vertical flow when measuring water intake from the interior chamber.

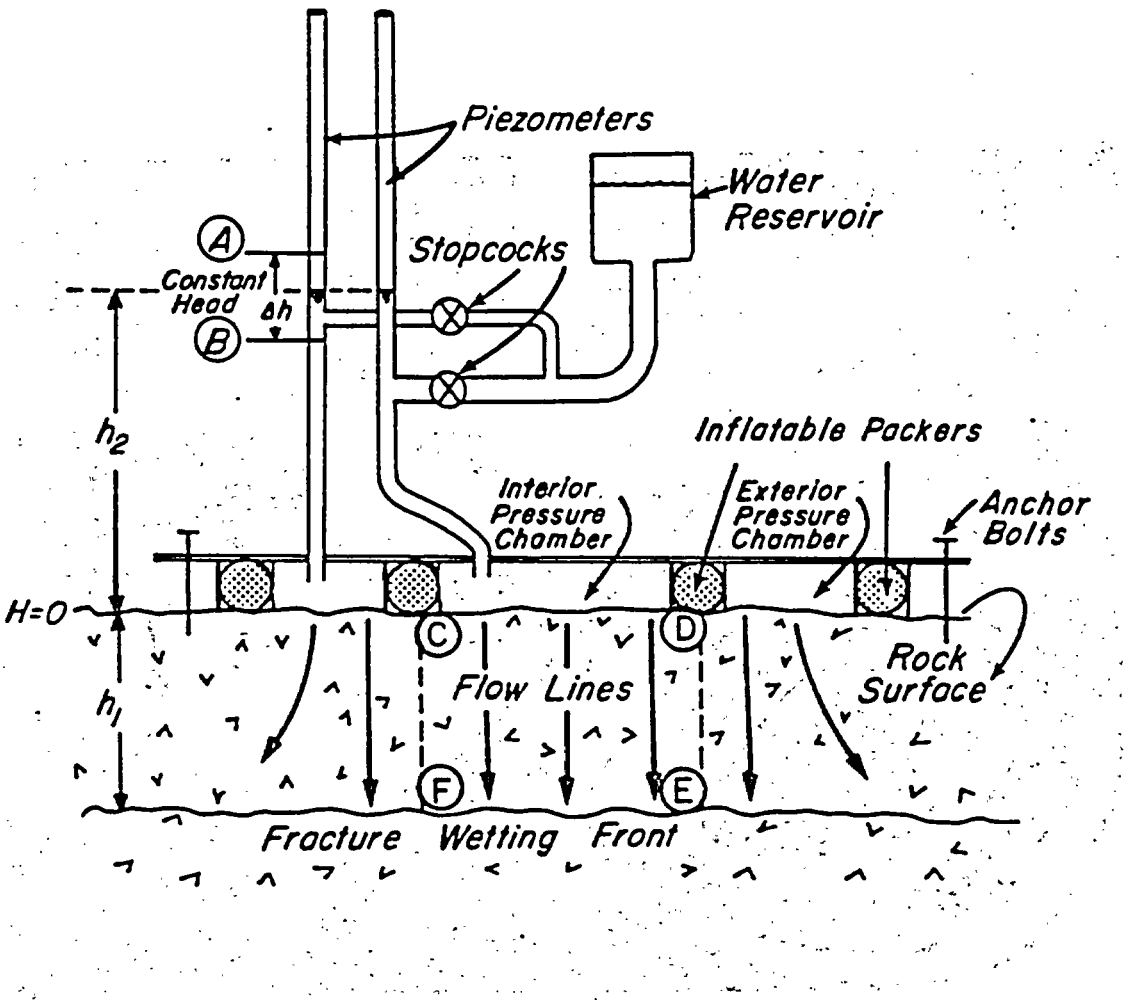

Figure 3.31 Cross-sectional diagram of the FRI, showing the apparatus as used for water intake measurements.

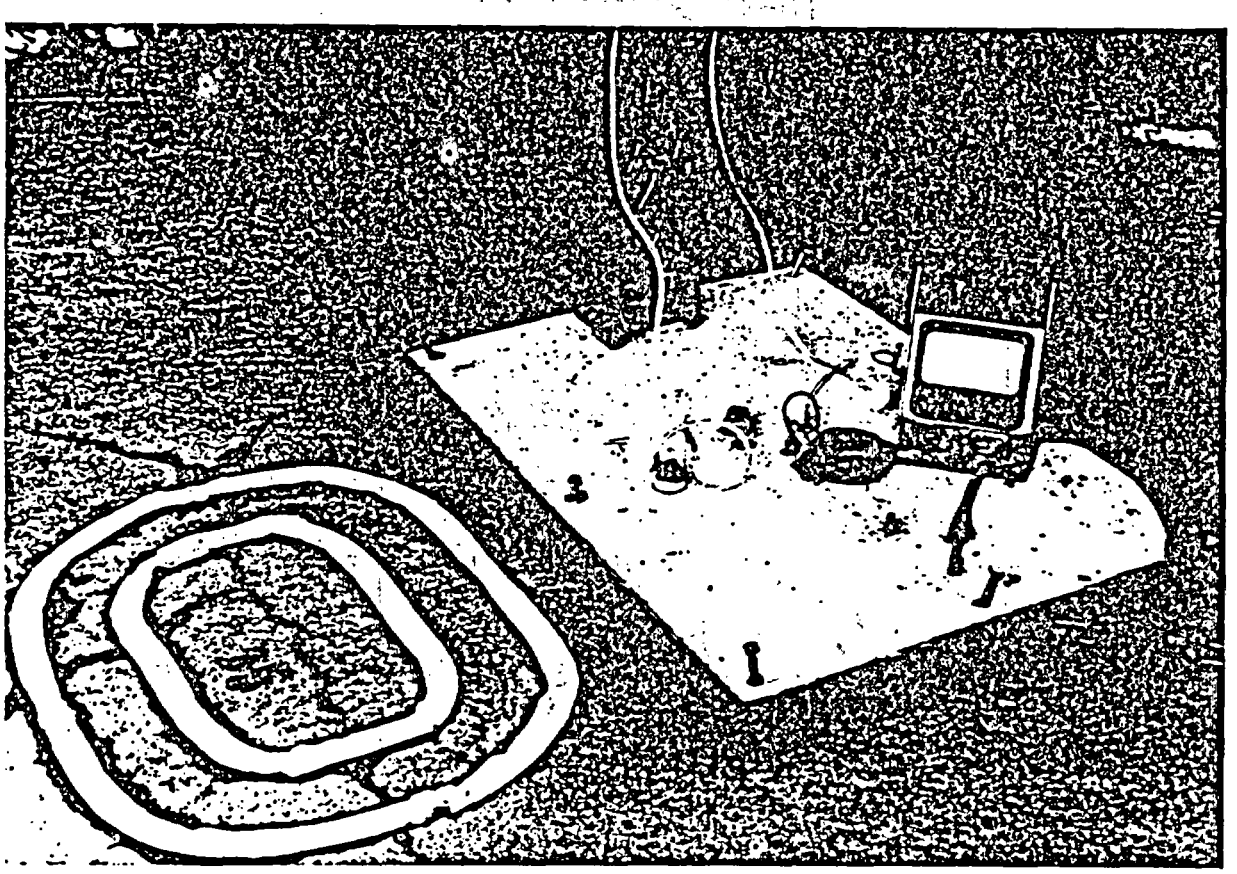

Figure 3.32 Photograph of the FRI set up over a mock fracture.

The top of the FRI is a rectangular 6.35 mm steel plate. Welded onto the underside of the plate are two oval chambers. The two chambers are concentric to each other (one interior to the other) and both are open to the bottom. The interior and exterior chambers are, respectively, 41 and 61 cm in length. A dual piezometer system is used to measure intake from both chambers. A water reservoir is used maintain a constant fluid pressure at the rock surface by replenishing fluid at specific intervals.

The FRI is secured to a rock surface using anchor bolts, with the exposed fracture aligned through the middle of the longitudinal axis of the rectangular plate. Any natural sediment or debris is left undisturbed in the fracture. To ensure a good seal between the rock surface and the FRI, the rock surface is cleaned and holes for anchor bolts are drilled into the rock with an electric hammer drill.

Inflatable packers (consisting of modified bicycle tubes) are used to seal the FRI chambers to the rock surface, and to prevent leakage from one chamber to another or to the atmosphere. During the experiment, the packers are inflated to approximately 240 kPa. Critical to a successful FRI experiment is ensuring that water does not escape from either pressure chamber between the rock surface and the bottom of the packers. A clay caulking material placed under the packers provides an air- and water-tight seal throughout the duration of FRI tests. Each experiment was tested for leaks at the rock-FRI interface by visual inspection. The presence of water exterior to the outer chamber was cause for abandonment of that experiment.

Immediately after the FRI is secured to the rock surface, the packers are pressurized. Both the interior and exterior pressure chambers are quickly filled with water through plugs on the top plate of the FRI. The water reservoir stopcocks are then opened to fill the piezometers to the level labeled A on Figure 3.31. Entrained air is allowed to escape through release valves on the FRI. As water flows into the fracture, the time interval required for the level in the piezometer (connected to the inner chamber) to reach level B is recorded. Water levels in both piezometers are then quickly replenished to level A. This process is repeated until the time interval becomes constant. Because the volume in the piezometer from level A to level B is known, a volumetric flow rate can be computed for each repetition. Water temperature is monitored throughout each FRI test with temperature sensors seated within the chambers.

To provide field tests of the FRI, a site located in undisturbed, unsaturated, relatively flat, exposed rock was required. An outcrop was selected in the Gringo Gulch Volcanics located approximately 3 km southwest of Patagonia, Arizona (Figures 1.11 to 1.14). The outcrop is a flat-topped butte composed of a fractured, densely-welded, ash-flow tuff described by Drewes (1972) as Paleocene in age. Inspection of vertical fractures exposed at the surface reveal no single dominant fracture pattern. It is likely that a combination of fracture-inducing events, such as contraction due to cooling and tectonic events, produced the random fracture strike pattern found at the site.

Boundary conditions for the FRI water experiment below the fractured rock surface and interior chamber are assumed to be (Figure 3.31):

(3.14)

Boundary C - D:	$H = h_2$	$t > 0$
Boundary C - F and D - E:	$\partial H/\partial x = 0$	$t > 0$
Boundary E - F:	$H = h_1$	$t > 0$

where

H is the hydraulic head;
h_2 is the mean applied head;
h_1 is the distance from surface to wetted front;
x is the horizontal direction; and
t is time.

The reference elevation for the hydraulic head is at the rock surface.

In this formulation, the boundary (E - F) is the wetting front which moves downward with time. It is assumed that the pressure head at the wetting front is atmospheric and that the air pressure ahead of the wetting front remains equal to the atmospheric pressure due to the much higher permeability of the fracture to air. In addition, the assumption is made that the fracture is initially dry and there is no air entrapment behind the wetting front.

Figure 3.33 shows a water intake curve resulting from an FRI injection test at the Patagonia field site. For the majority of the 21 FRI tests performed at the site, water intake was high at early time and progressively decayed to a steady-state value. Most of the water intake curves generated at the site are similar in shape to infiltration decay curves characteristic of soils and other porous media. Scatter in the observed water intake is attributed to the presence of silt or clay particles near the fracture entrance which affect intake rates.

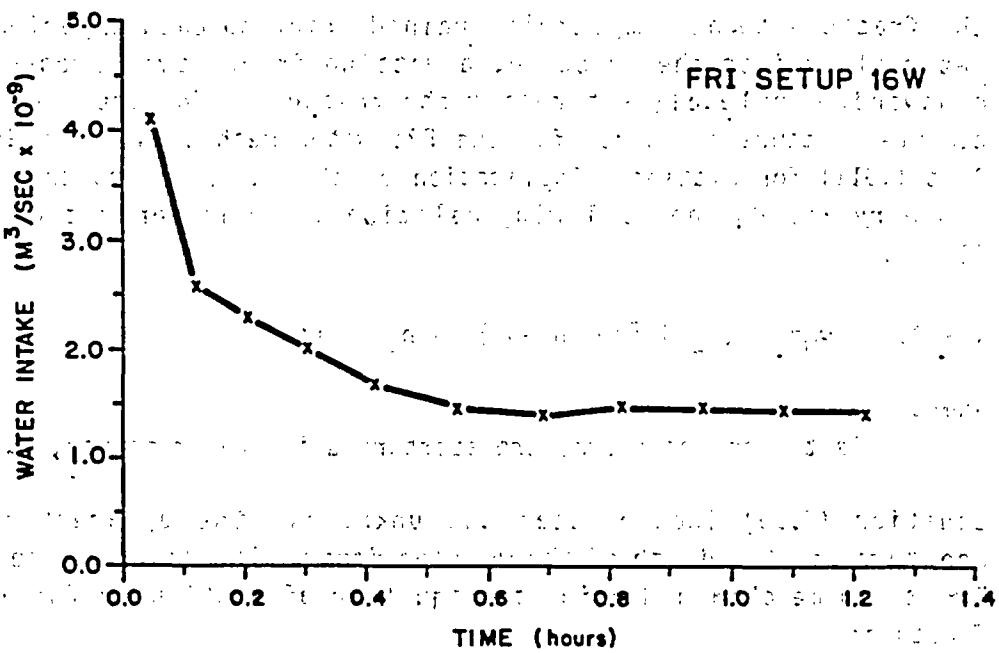

Figure 3.33 Water intake rate vs. time for a representative FRI water experiment (setup 16W).

3.5.2 Fracture Aperture Determination

Once estimates of fracture water intake rates are obtained, a physical model can be formulated which relates the time-dependent intake rate to parameters characteristic of the fractures of interest. One such parameter is the apparent fracture aperture. The ability to characterize a set of fractures by a distribution of apparent fracture apertures allows for the extension of the results obtained at a number of point measurement sites to a regional estimate of water intake.

The mathematical formulation used to compute fracture aperture assumes the fracture to be completely drained prior to each experiment. As water flows into the fracture, a wetting front moves progressively downward, completely saturating the fracture. The equation used to compute fracture apertures for the FRI water method uses the Green and Ampt (1911) formulation. Application of this approach to the FRI flow geometry yields the following relation which is derived in Kilbury (1985):

$$(3.15) \qquad e_w^2 = (h_2 \ln[h_2/(h_2-h_1)] - h_1) / ft$$

where

e_w is the apparent fracture aperture using water method, m.

Equation (3.15) incorporates two unknowns; the apparent fracture aperture and the depth of the wetting front. The depth of the wetting front can be obtained using the equation of continuity for a planar fracture:

$$(3.16) \qquad h_1 = V / (w\, e_w)$$

where

V is the volume of water infiltrated into the fracture; and

w fracture length measured along the fracture in the interior pressure chamber, equal to 41 cm for the apparatus used.

Equations (3.15) and (3.16) can be coupled by assuming that the apparent fracture aperture is equal to the mean fracture aperture. Laboratory evidence (Shrauf and Evans, 1984) supports this assumption for smooth fractures. The equations may be solved using iterative procedures. An algebraic equation solver (e.g., TK Solver, Software Arts, Inc.) can be used to obtain estimates of the fracture aperture and the depth of the wetting front as a function of time.

To estimate the travel time of water in individual fracture segments, the fluid intake velocity and the depth to the wetting front can be determined as a function of time. These functions, plus the cumulative volume versus time, are shown in Figure 3.34 for a representative water experiment. Observed steady-state water intake rates and calculated fracture apertures, depths to wetting front, and fluid velocities are presented in Table 3.7 for 21 test locations at the Patagonia site.

Table 3.7 Steady-state water intake (Q_w), fracture aperture (e_w), final depth to wetting front (h_1), and fluid velocity (v) for 21 FRI experiments.

FRI Setup Number	Steady State Water Intake Q_w (10^{-9} m^3/sec)	Fracture Aperture e_w (μm)	Final Depth to Wetting Front h_1 (m)	Fluid Velocity v (m/hr)
1W	3.25	15.6	-2.62	1.83
2W	5.00	21.7	-7.47	2.02
3W	0.50	7.8	-1.61	0.56
4W	1.80	9.6	-2.29	1.65
5W	0.25	6.9	-1.48	0.32
6W	0.030	1.9	-0.34	0.14
7W	1.00	9.1	-1.05	0.96
8W	0.019	1.5	-0.17	0.11
9W	0.006	1.0	-0.14	0.05
10W	0.60	3.0	-0.43	1.76
11W	3.20	14.1	-1.42	1.99
12W	1.10	8.8	-0.72	1.10
13W	0.65	8.1	-1.14	0.70
14W	4.00	18.4	-2.43	1.91
15W	30.0	33.7	-2.53	7.82
16W	1.50	11.2	-1.44	1.18
17W	1.90	12.4	-1.18	1.35
18W	4.60	14.6	-0.81	3.26
19W	16.0	27.6	-2.73	5.09
20W	3.00	16.0	-3.09	1.65
21W	14.0	26.0	-2.60	4.73

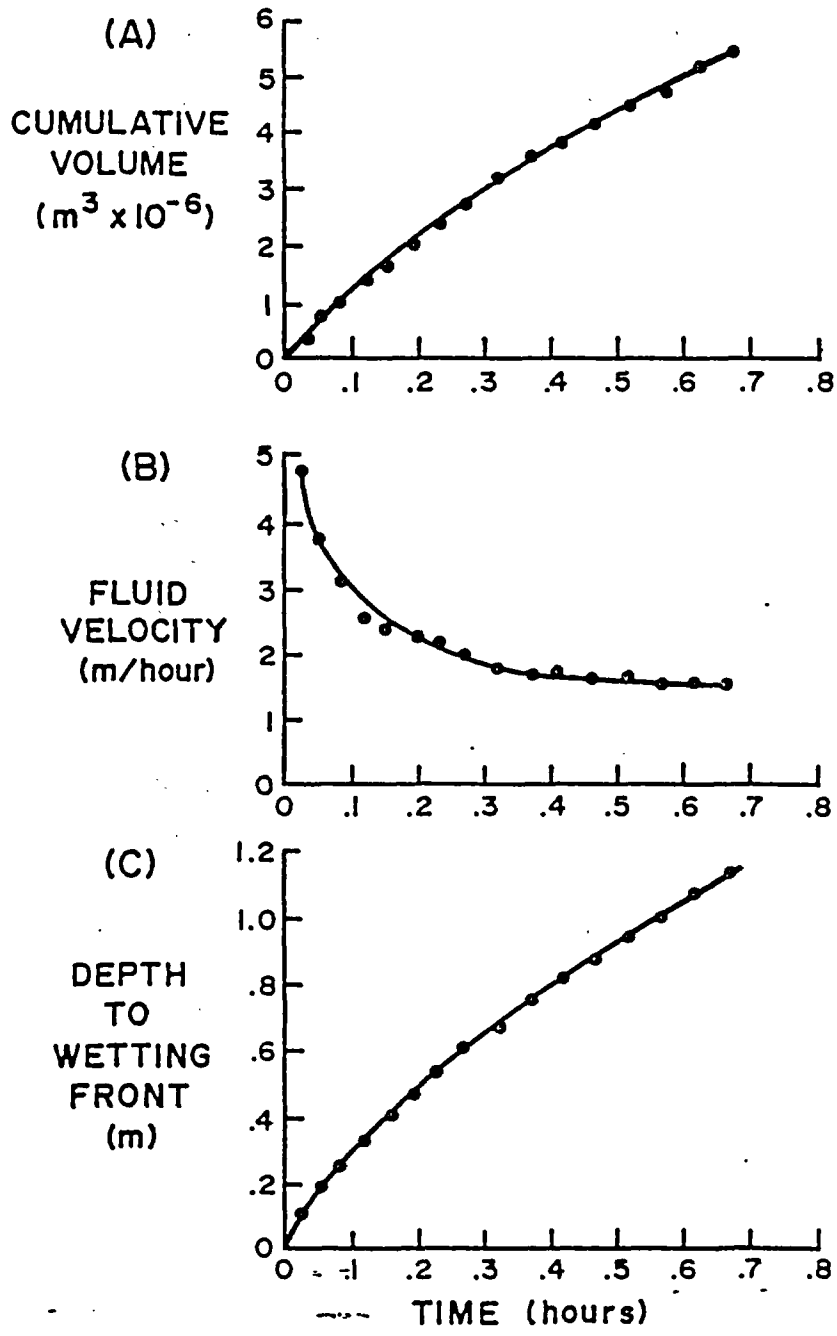

Figure 3.34 Cumulative water intake volume (A), fluid velocity (B), and depth to wetting front (C) vs. time graphs.

A log-probability plot of apparent fracture apertures for the tests reveals a straight line fit for fractures whose computed apertures are greater than 20 μm (Figure 3.35), indicating a log-normal distribution. Fractures with apertures less than 20 μm do not appear to belong to the same distribution. Instead, the computed fracture aperture is smaller than what the log-normal distribution would suggest. This may result because either 1) the smaller fractures are, in fact, less likely to occur, or 2) a heretofore undocumented physical process may cause a reduction in the flow rate and, hence, an under-estimation of the fracture aperture.

A Kolmogorov-Smirnov goodness-of-fit test performed on the larger aperture data failed to reject the hypothesis ($\alpha < 0.05$) that the distribution of apertures is log-normally distributed. The critical test value was 0.8750 with five intervals. Uncertainties which may affect aperture calculation using Equations (3.14) and (3.15) arise from unknown boundary conditions and the validity of applying the cubic law to natural fractures. If the influence of the external pressure chamber introduces a horizontal flow component, the effective fracture length will change as the wetting front advances through the fracture. This situation will affect aperture values computed using Equation (3.15). The variability in the measured constant head level, and the fact that flow continues momentarily while the piezometer system is replenished, are considered to be the main contributors to experimental error.

Another potential error results because the boundary condition along E - F is formulated such that a zero pressure condition is present. If fractures are small, however, there will be an additional negative pressure due to capillary forces acting on the fluid front. This will result in a larger head gradient than when this force is neglected. The capillary head is computed as:

$$h_r = - 2 T / \rho g e_w' \qquad (3.17)$$

where

h_r capillary pressure head;
T surface tension, 0.073 kg/s^2 at 25 °C; and
e_w' computed aperture which includes the capillary effect.

Table 3.8 presents adjusted depths to the wetting front and fracture aperture, along with the original estimates. The magnitude of the influence of the capillary effect is generally minor for the larger fractures, yet substantially affects the estimated fracture aperture for the smaller fractures. Because the effect tends to reduce the estimated

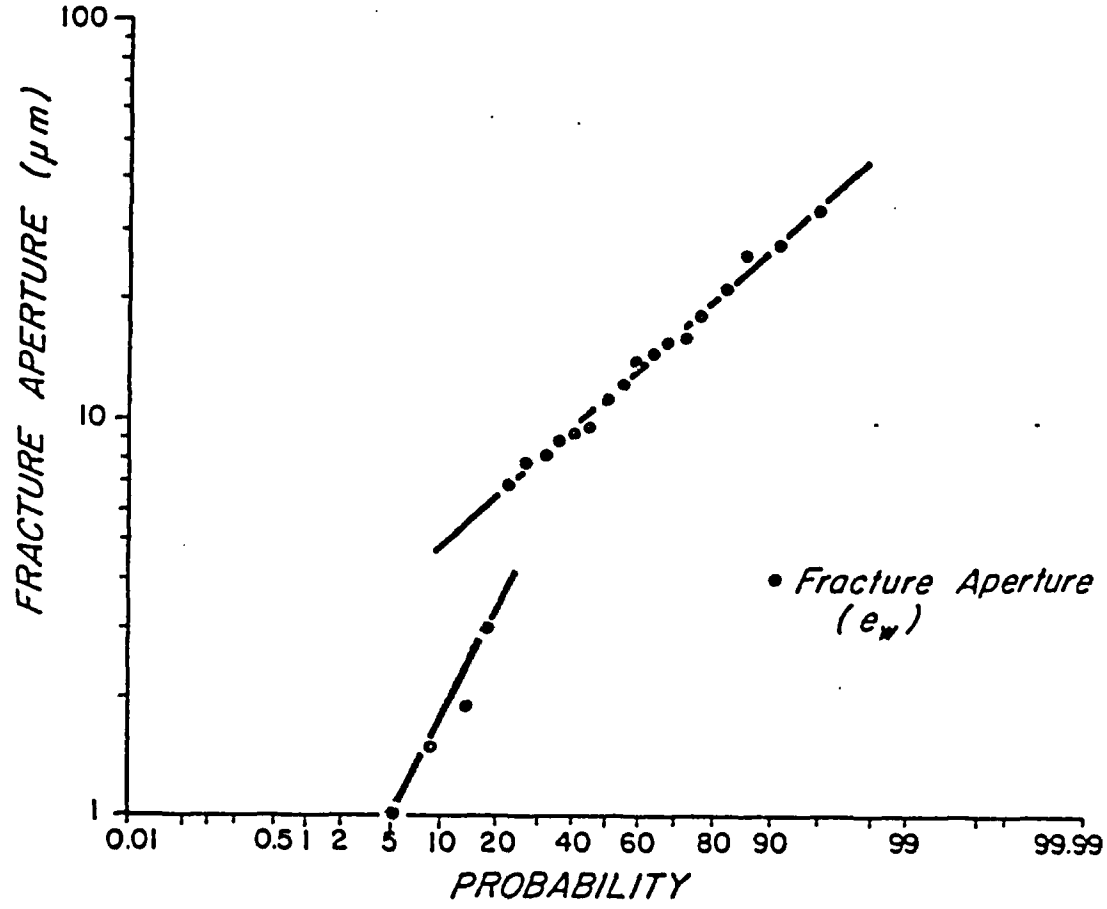

Figure 3.35 Log-probability plot of fracture apertures computed for the FRI water method.

aperture of the smaller fractures, the discontinuity of the probability distribution function (Figure 3.35) is accentuated. The probability distribution function for larger fractures is essentially unchanged.

Table 3.8 Comparison of final depth to wetting front and fracture aperture not considering the capillary effect (h_1 and e_w, respectively) with values computed considering the capillary effect (h_1' and e_w', respectively).

FRI Setup Number	WITHOUT CAPILLARY EFFECT		WITH CAPILLARY EFFECT		Percent Change in Aperture
	Elevation Head at Wetting Front h_1 (m)	Fracture Aperture e_w (μm)	Elevation Head at Wetting Front h_1' (m)	Fracture Aperture e_w' (μm)	
1W	-2.62	15.6	-2.88	14.1	- 9.6
2W	-7.47	21.7	-7.82	20.8	- 4.1
3W	-1.61	7.8	-1.97	6.3	-19.2
4W	-2.29	9.6	-2.69	8.1	-15.6
5W	-1.48	6.9	-1.94	5.3	-23.2
6W	-0.34	1.9	-0.40	1.7	-10.5
7W	-1.05	9.1	-1.29	7.4	-18.7
8W	-0.17	1.5	-1.01	0.3	-80.0
9W	-0.14	1.0	-1.04	0.1	-90.0
10W	-0.43	3.0	-0.71	1.8	-40.0
11W	-1.42	14.1	-1.62	12.3	-12.8
12W	-0.72	8.8	-0.92	6.9	-21.6
13W	-1.14	8.1	-1.43	6.5	-19.8
14W	-2.43	18.4	-2.68	16.8	- 8.7
15W	-2.53	33.7	-2.67	31.9	- 5.3
16W	-1.44	11.2	-1.70	9.4	-14.5
17W	-1.18	12.4	-1.37	10.6	-14.5
18W	-0.81	14.6	-0.94	12.5	-13.0
19W	-2.73	27.6	-2.91	25.8	- 6.5
20W	-3.09	16.0	-3.41	14.5	- 9.4
21W	-2.60	26.0	-2.78	24.3	- 6.5

3.5.3 Air Intake Method

The FRI has also been used to measure air intake rates into fractures subsequently used for water intake experiments. These tests are used to:

(1) Provide information about air permeabilities of fractures in rock masses; and
(2) Augment the water intake investigation by providing a secondary means of determining fracture apertures.

Field and analytic techniques are developed to determine fracture apertures using air. Figure 3.36 shows the FRI configuration and flow geometry for the air experiment. Design for this experiment is comparable to that for water, except that a manometer system is now incorporated to measure air intake into the fracture. Also, an air reservoir (in the form of a 0.121 m^3 drum) is used to provide a volume of air sufficient to reduce the observed pressure changes in the manometer. In addition, the exterior and interior chambers are open to each other and are not separately pressurized.

Experiments using air were completed on individual fractures prior to conducting a water intake experiment. Procedures in this application are similar to those of the water experiment. The clay caulk is again used as a sealant. The packers are inflated to the same pressure used in the water tests. Air temperature within each chamber is recorded throughout each test. Air is pumped into the air reservoir until the manometer level rises to a level marked as level 1 in Figure 3.36(A). As air flows into the fracture, the time required for the manometer to reach level 2 is recorded. The difference between the two levels is Δh, and the corresponding mean head reading is h_c. The process is repeated until several constant time intervals are observed. Boundary conditions for the FRI air experiment below the fractured rock surface and interior chamber are as follows:

(3.18)

Boundary B - C - D:	$p = 2 \rho g (h_c - h_a)$	$t > 0$
Boundary A - B and D - E:	$\partial p / \partial y = 0$	$t > 0$
Boundary A - F' and E - F:	$p = 0$	$t > 0$

where

p gauge pressure, $kg/m\text{-}s^2$.
ρ fluid density at ambient temperature and pressure, kg/m^3.
y vertical direction, m.

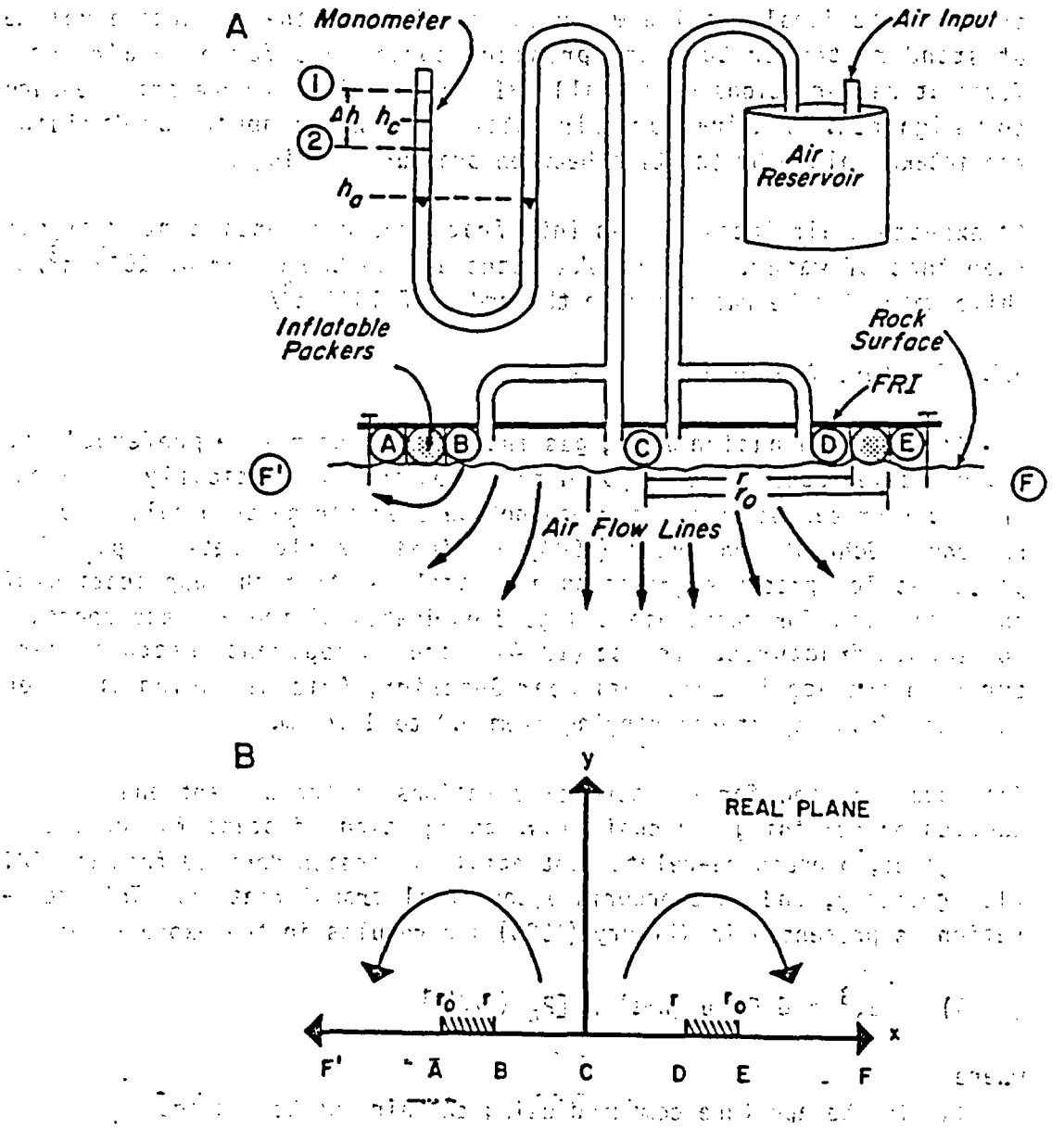

Figure 3.36 Cross-sectional diagram of the FRI as used for air intake measurements (A), and FRI geometry represented in the real plane (B).

Air experiments typically exhibit initial steady-state conditions; i.e., intake rates at early readings are usually similar to those recorded after many repetitions (Figure 3.37).

Each air test was performed using different applied pressures, thus, the air intake rate for each experiment must be standardized. For this problem, the ideal gas law was used to calculate the air intake volume at standard temperature and pressure conditions for each air test. Temperature variations during all FRI air experiments were small enough to be ignored. The fracture air intake rate was computed by dividing the intake volume by the time between pressure readings.

As expected, air intake rates into fractures was consistently higher than that of water. Air intake rates are on the order of 10^{-5} m^3/s, while water intake rates are on the order of 10^{-9} m^3/s.

3.5.4 Fracture Aperture Determination

Aperture determination using gas intake methods may be preferable to water intake methods when exposed fractures are not vertically inclined, or in circumstances when water may not be used for geochemical, or other reasons. Schrauf and Evans (1984) examined gas flow between parallel plates at low pressure gradients and concluded that the application of the cubic law for gases yielded good estimates of the average aperture for smooth fractures. Trautz (1984) measured apparent fracture apertures in the Apache Leap Tuff near Superior, Arizona, using nitrogen gas, and found apertures ranging from 9.0 to 19.7 μm.

The equation used for aperture calculations in the present analysis is derived by combining the cubic law, an equation of state for compressible gases, a pressure-related potential expression derived from the FRI flow geometry, and an appropriate conformal transformation. This derivation is presented in Kilbury (1985) and results in the expression:

$$(3.19) \qquad e_a^3 = 6\, Q_a\, \mu\, (n+1) \,/\, [P_a\, (K/K')] \qquad (5)$$

where

- e_a is the aperture computed using the air intake method;
- Q_a is the volumetric flow rate; and
- μ is the dynamic viscosity;
- n is the ratio of specific heats at constant volume and pressure, C_v/C_p, dimensionless. For an incompressible fluid, $n = 0$; for air, $n = 0.71$; and for isothermal expansion, $n = 1$;

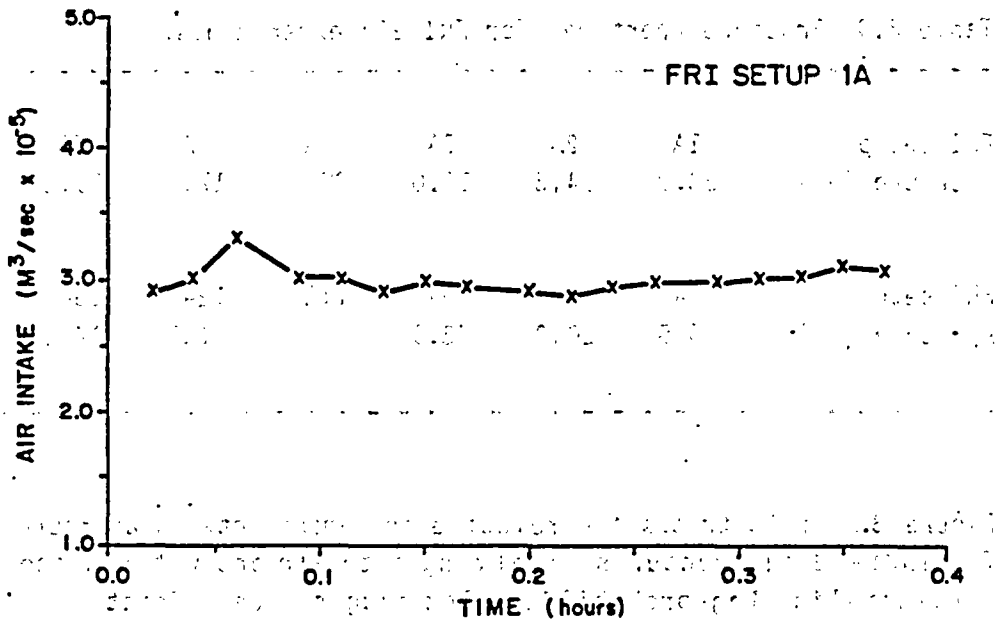

Figure 3.37 Air intake rate vs. time for a representative FRI air experiment (setup 1A).

P_a air pressure at ambient temperature, $kg/m\text{-}s^2$; and
K/K' the ratio of the complete elliptical integral to its complement for a specified modulus (see Kilbury, 1985).

Table 3.9 presents calculated fracture apertures for 14 FRI air tests, which replicated many, but not all, of the water tests. The calculated apertures range from 10.0 to 37.2 μm, a range similar in magnitude to the range (1.0 to 33.7 μm) computed using the FRI water tests.

Table 3.9 Fracture apertures for FRI air experiments.

FRI setup:	1A	2A	3A	4A	5A	6A	7A
Aperture (μm)	28.0	14.3	10.0	32.1	17.8	29.2	37.2

FRI setup:	8A	9A	10A	11A	12A	13A	14A
Aperture (μm)	35.5	20.9	23.3	18.2	26.5	14.1	30.0

Figure 3.38 illustrates the relative agreement between aperture results for individual fractures involving both air and water methods. The straight-line log-probability plot suggests that fracture apertures computed using the air method are log-normally distributed. The paucity of data points, however, prevents the determination of a unique probability density function.

A comparison of fracture apertures calculated by first performing an air test, followed by a water test is presented as Figure 3.39. In this assessment, the fracture is initially assumed to be completely drained and a fracture aperture is calculated using the air method. Once the air experiment is terminated, the same location is retested using water.

It is important to note that calculated fracture apertures were obtained by using different governing equations and boundary conditions. Thus, the general agreement between apertures calculated from air and water experiments provides confidence with regard to both methods of aperture calculation, and to the application of the cubic law for fluid flow in natural fractures.

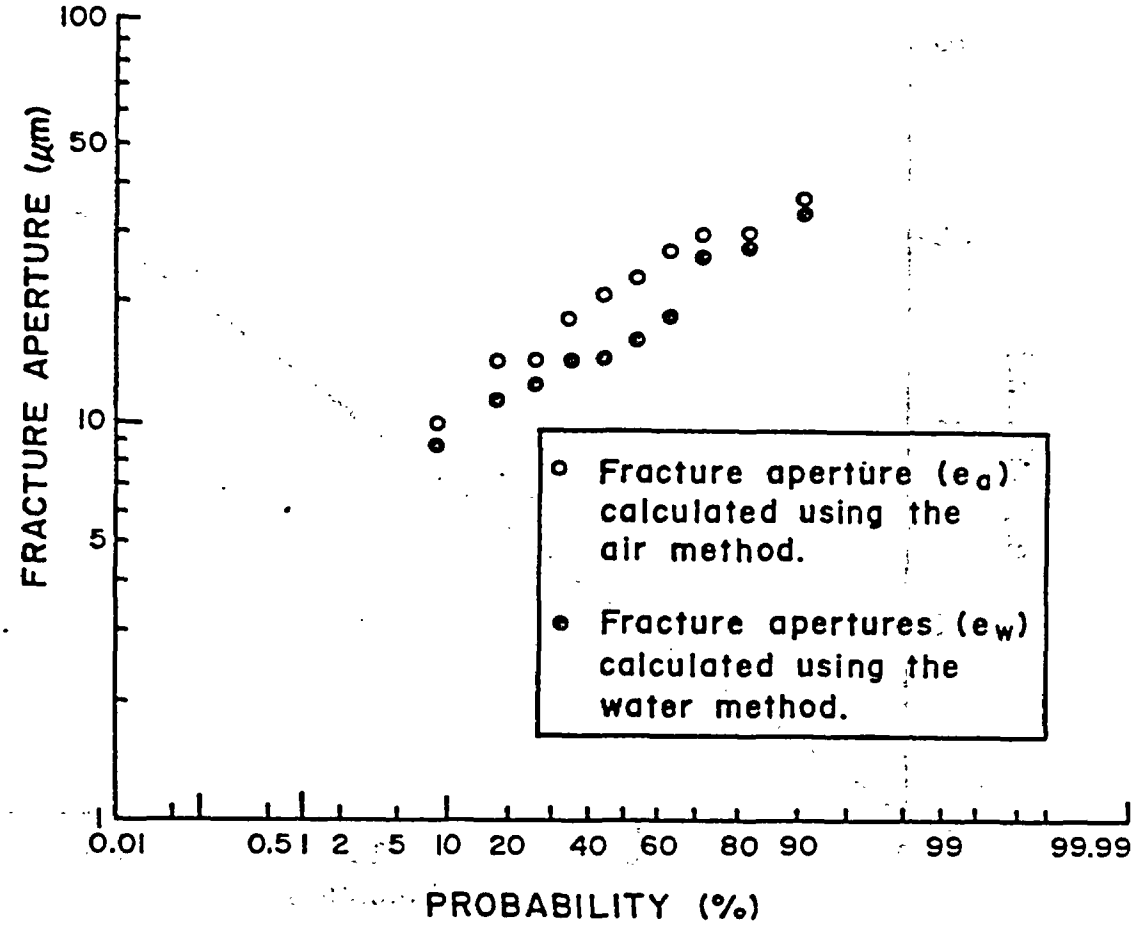

Figure 3.38 Log-probability plot of fracture apertures computed using the air and water methods on the same fractures.

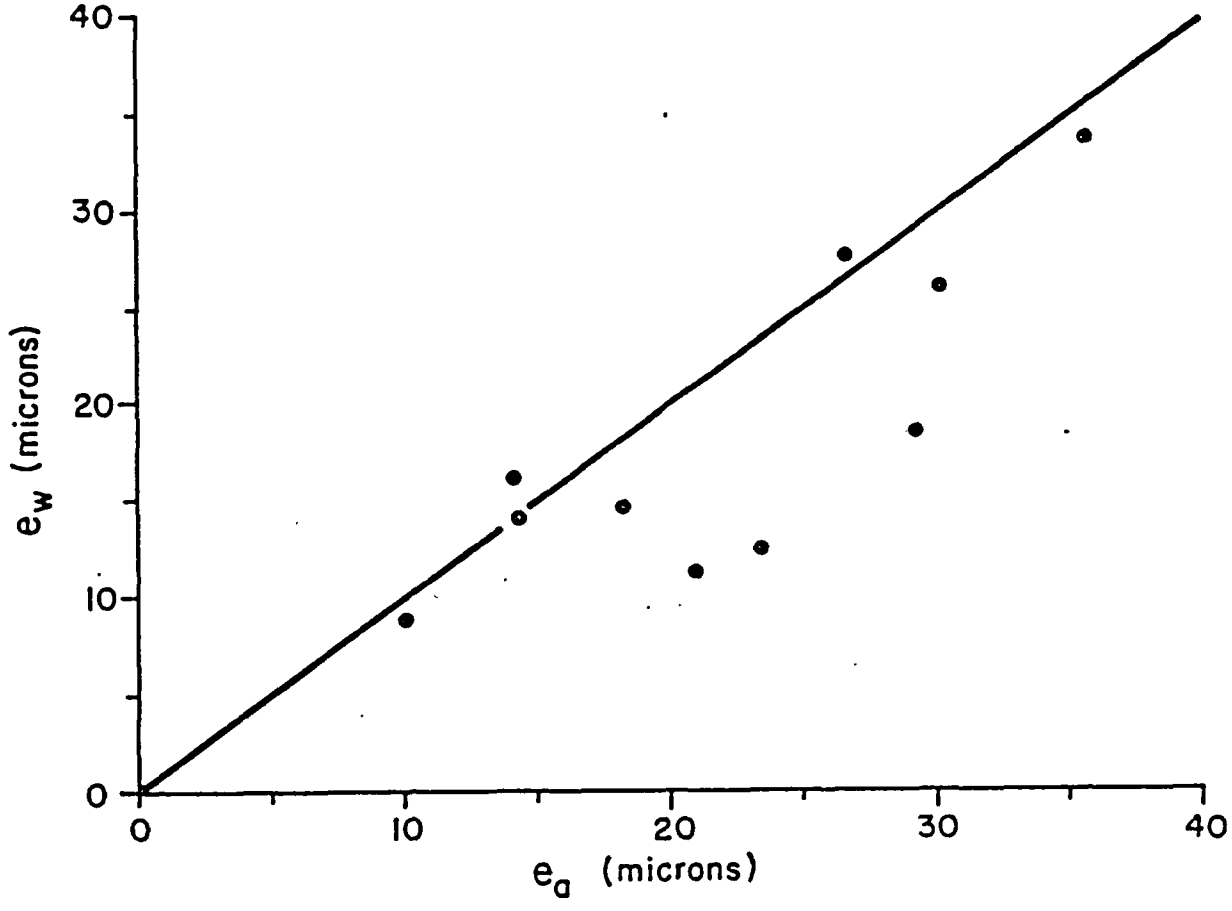

Figure 3.39 Plot of fracture apertures calculated using the water method (e_w) vs. apertures calculated using the air method (e_a) for the same fracture.

To evaluate the assumption that the fracture was initially completely drained, a series of experiments were performed. Figure 3.40(A) displays a plot of the air intake rate of an undisturbed fracture. Figure 3.40(B) displays a plot of the water intake of the same fracture following the completion of the air intake experiment. Finally, Figure 3.40(C) displays a last experiment in which the air experiment is repeated after the completion of the water experiment. The fact that the air intake rate after the termination of the water intake experiment is initially very low, and then rises toward the pre-water intake experiment lends support to the assumption that the fracture was initially completely drained and briefly became relatively impermeable to air following a water intake experiment.

3.5.5 Discussion and Conclusion

The presented analytic solutions provide a description of the transient intake rate over time for prescribed external boundary conditions at fractures which intersect the earth-atmosphere interface. The solutions are for air and water. These solutions require the application of the cubic law and the estimation of fracture aperture. While the validity of the application of the cubic law to flow in natural fractures has not been fully substantiated, especially for fractures smaller than 20 μm, the fact that calculated apertures compare favorably when two independent tests are performed (and also with other studies in similar geologic materials) increases the credibility of the technique and of the underlying assumptions.

The FRI method is an approach potentially capable of serving as an intake measurement device under an assortment of conditions. The analytic solution for the water experiment is limited to a horizontal, relatively flat, exposed rock surface, which also is required for FRI experiment procedures. The solution for air experiments is not limited to horizontal rock surfaces, however, and may be used on any flat, exposed rock surface. The use of air as a surrogate measure of hydraulic conductivity is useful when horizontal surfaces are not available, or when the use of water is contra-indicated.

3.6 Determination of Fracture Aperture Using Air Injection

The flow-test theory is developed for the case where two boreholes intersect a single fracture. One borehole is pressurized, forcing radial flow outward in the plane of the fracture toward the second borehole. Radial flow is a special case of a more general type of flow condition called elliptical flow. Strictly radial flow (i.e., when

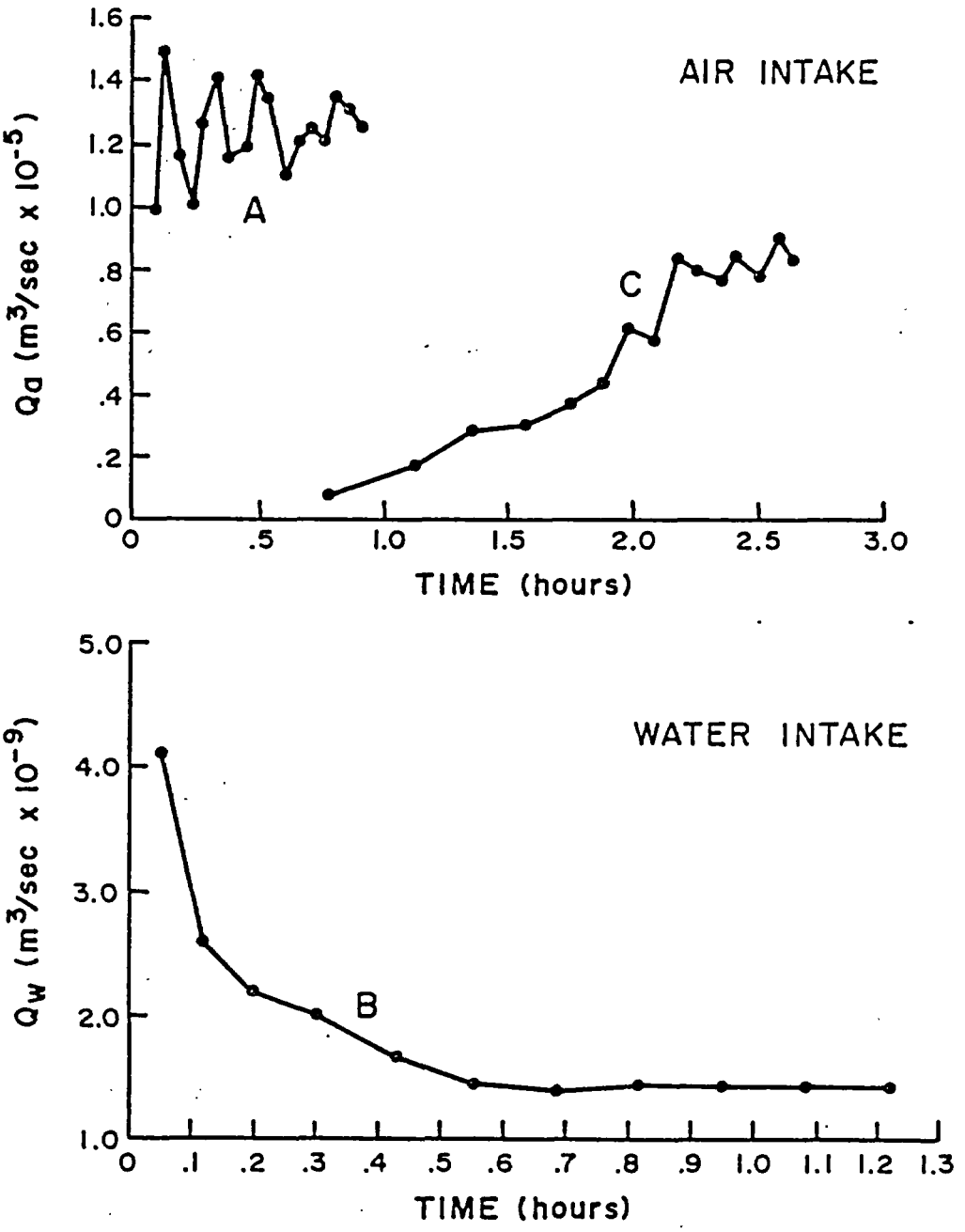

Figure 3.40 Sequential air-intake (A), water-intake (B), and air-intake (C), curves for a single fracture at the Patagonia study area.

equipotential lines form concentric circles) will only occur when the axis of the borehole is oriented perpendicular to the fracture plane. If the borehole intersects the fracture at a nonzero angle ($\alpha \neq 0$), as shown in Figure 3.41, the fracture-borehole intersection trace in the plane of the fracture will be an ellipse.

The ellipse will form a constant-pressure boundary along which flow will take place. Elliptic flow can be described using the cubic law:

$$(3.20) \quad Q_m = -\frac{\pi e^3 \rho_b}{12\mu P_b} \frac{P_2^2 - P_1^2}{\ln [(a_2+b_2)/(a_1+b_1)]}$$

where

Q_m is total mass flow rate, kg/s;
e is fracture aperture, m;
μ is dynamic viscosity, kg/m-s;
ρ_b is density of fluid at reference state b, 1.164 kg/m^3;
P_b is pressure at reference state b, 0.101325 * 10^6 Pa;
P_2 is absolute pressure at observation borehole, Pa;
P_1 is absolute pressure at injection borehole, Pa;
a_1 is semimajor axis of the inner ellipse formed by the borehole-fracture plane interaction, m;
b_1 is semiminor axis of the inner ellipse formed by the borehole-fracture plane interaction, m;
a_2 is semimajor axis of the outer ellipse on which observation borehole lies, m; and
b_2 is semiminor axis of the outer ellipse on which observation borehole lies, m.

The geometry of variables a_1, b_1, a_2, and b_2 are presented in Figure 3.42. It may be observed that for distances far from the inner elliptical boundary a_2 approaches b_2. This implies that at a given radial distance from the injected borehole, radial flow conditions will exist. The radial distance from the injection borehole necessary for this assumption depends upon the borehole-fracture plane intersection angle, α. Figure 3.43 is a plot of a_2/b_2 versus an average radius, r_{ave}, for various angles.

The average radius is defined as:

$$(3.21) \quad r_{ave} = (a_2 + b_2) / 2 r_1$$

where r_1 is the radius of the injection borehole, m.

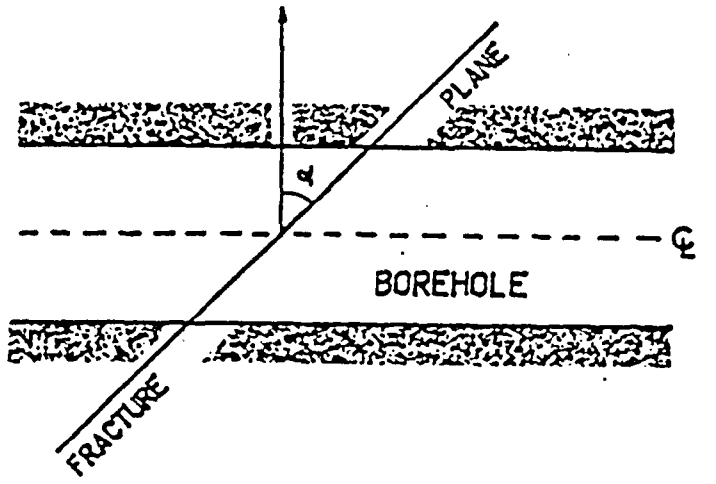

Figure 3.41 Fracture-borehole interaction angle, α.

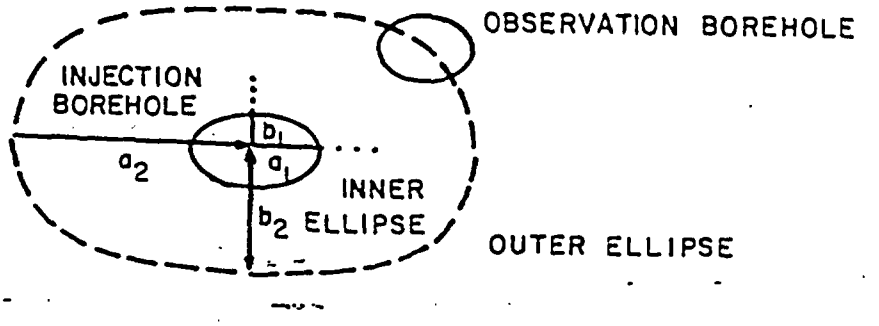

Figure 3.42 Geometric relations between injection and observation boreholes.

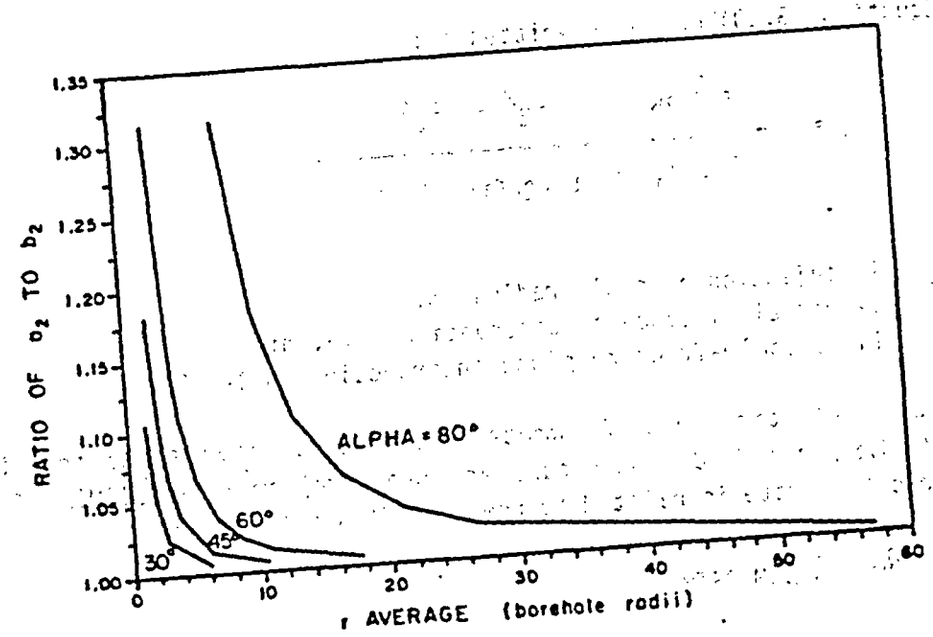

Figure 3.43 r_{ave} versus a_2/b_2 for different borehole-fracture plane interaction angles, α.

This formulation allows the average radius of the outer ellipse (along which the observation borehole lies) to be given in terms of borehole radii instead of dimensional units. It is evident from Figure 3.43 that radial flow exists at distances greater than 57 borehole radii from the origin for all intersection angles less than 80° and a_2 to b_2 ratios less than 1.01. For intersection angles less than 60°, radial flow will occur at distances greater than 18 borehole radii. If the observation borehole is located within this critical radius, then Equation (3.20) can be simplified even further. By noting that a_2, b_2, and r_2 are approximately equal for a distance greater than the critical radius, and realizing:

$$a_1 = r_1 \sec\alpha \qquad \text{and} \qquad b_1 = r_1$$

then Equation (3.20) can be rewritten as:

$$(3.22) \qquad Q_m = -\frac{\pi e^3 \rho_b}{12\mu P_b} \cdot \frac{P_2^2 - P_1^2}{\ln [2r_2/r_1(\sec\alpha + 1)]}$$

where

r_1 is injection borehole radius, m;
r_2 is radial distance to observation hole, m; and
α is borehole-fracture plane intersection angle, °.

The Teledyne-Hastings mass flowmeter was used to provide readings in standard (i.e., standard temperature and pressure) cm^3/min (SCCM). The volumetric flow rate is related to the mass flow rate using:

$$(3.23) \qquad Q_m = Q_{SCCM}\, \rho_{STP}$$

where

ρ_{STP} is the density of the gas; a function of the standard temperature and pressure state for which the flowmeter was calibrated.

3.6.1 Single Hole Flow Test

When a single hole is being utilized to measure fracture aperture, there is no longer an observation borehole where P_2 can be measured or easily defined. To remedy this difficulty, an undisturbed pressure head is assumed to exist at a effective radius, r_e, from the injection borehole. The effective radius corresponds to the rather ill-defined radius of influence. Outside of the effective radius, the pressure distribution

is unaffected by gas injection at the injection well. For a gas flow test, the pressure outside of the effective radius is atmospheric.

The effective radius can be determined using cross-hole flow tests. The test results from the Santo Nino and Superior Road tunnel flow experiments indicate that for fractures with apertures between 100 and 200 μm, the effective radius is approximately 1 m for flow rates less than 500 SCCM. The borehole radius for these experiments was 0.025 m. For a borehole with a radius of 0.05 m, such as boreholes being tested near the Number 9 Magma shaft, the effective radius would be 2 m. In general, for a single-hole test with injection borehole radius equal to r_1, the effective radius r_e would be calculated using:

$$r_e = r_1 \,/\, 0.025 \tag{3.24}$$

The estimate of the effective radius would be for a flow test conducted on a fracture with aperture between 100 and 200 μm and flow rate less than 500 SCCM. The development of Equation (3.24) is given by:

$$\frac{Q_a}{Q_b} = \frac{-\dfrac{\pi e^3}{12\mu}\dfrac{\rho_b}{P_b}\dfrac{(P_2^2 - P_1^2)_a}{\ln [2r_2/r_1(\sec\alpha + 1)]_a}}{-\dfrac{\pi e^3}{12\mu}\dfrac{\rho_b}{P_b}\dfrac{(P_2^2 - P_1^2)_b}{\ln [2r_2/r_1(\sec\alpha + 1)]_b}} \tag{3.24a}$$

where subscripts a and b indicate the cross-hole and single-hole tests, respectively. Simplifying Equation (3.24a) yields:

$$\frac{Q_a}{Q_b} = \frac{\ln [2r_2/r_1(\sec\alpha + 1)]_b \; (P_2^2 - P_1^2)_a}{\ln [2r_2/r_1(\sec\alpha + 1)]_a \; (P_2^2 - P_1^2)_b} \tag{3.24b}$$

To maintain the same pressure drop and flow rate:

$$Q_a = Q_b \qquad \text{and} \qquad (P_2^2 - P_1^2)_a = (P_2^2 - P_1^2)_b$$

Equation (3.24b) can now be reduced to:

$$\ln [2r_2/r_1(\sec\alpha + 1)]_a = \ln [2r_2/r_1(\sec\alpha + 1)]_b \tag{3.24c}$$

or;

(3.24d) $(r_2/r_1)_a = (r_2/r_1)_b$

and finally;

(3.24e) $r_{2b} = r_{1b} * (r_2/r_1)_a$

where

r_{1a} is borehole radius of cross-hole flow test, m;
r_{2a} is known effective radius from cross-hole flow test, m;
r_{1b} is borehole radius of single-hole flow test, m; and
r_{2b} is the unknown effective radius, m.

For the application of interest, r_{2b} is equal to the effective radius, r_e. In addition, r_{2a} is equal to 1 m and r_{1a} is equal to 0.0025 m. Thus, the new effective radius can be computed for variable borehole radii (Figure 3.44).

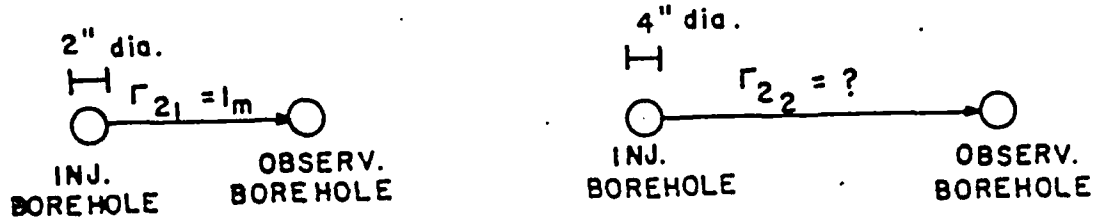

Figure 3.44 Geometric relations between radius of influence for a known case (left) and for an unknown case (right).

The analytical equation used to reduce the field data from a single-borehole flow test would be identical to Equation (3.24), except that the following relationships are utilized:

$$r_2 = r_e \quad \text{and} \quad P_2 = P_{atm} = 0.101325 \text{ mPa}$$

Thus:

$$(3.25) \quad Q_m = - \frac{\pi e^3}{12\mu} \frac{\rho_b}{P_b} \frac{P_{atm}^2 - P_1^2}{\ln [2r_e/r_1(\sec\alpha + 1)]}$$

Figures 3.45 and 3.46 give the pressure drop versus flow rate for fractures with varying aperture and borehole-fracture plane intersection angles of 0° (radial flow) and 60° (elliptical flow), respectively. These figures can be used by field personnel to determine the fracture aperture from a flow test. These figures were developed using Equation (3.25) with an effective radius of 2 m and injection borehole radius of 5 cm. Steady-state flow conditions must exist in order to use these figures. Also, it must be assumed that nonlinear flow conditions (i.e., nonlinear relationship between P_{atm}^2-P_1^2 and Q_m) brought on by turbulence, water blockages or fracture opening are not exhibited.

3.6.2 Procedure of Fracture Aperture Test

There are many direct methods of measuring fracture apertures in situ. However, a hydraulic or pneumatic test can be used to measure fracture apertures indirectly. The results of the hydraulic test are interpreted using the cubic law by relating the mass flow rate, Q_m, to the fracture aperture, e, as follows for a compressible fluid such as a gas;

$$(3.26) \quad Q_m = C\, e^3\, \Delta P^2$$

where

C is a constant dependent upon flow geometry and fluid properties; and

ΔP^2 is the difference between the squared injection borehole-pressure and nearby squared observation borehole-pressure.

When an observation borehole is not being utilized, the pressure is assumed to be atmospheric. Equation (3.26) can be solved for the fracture aperture:

$$(3.27) \quad e^3 = Q_m / (C\, \Delta P^2)$$

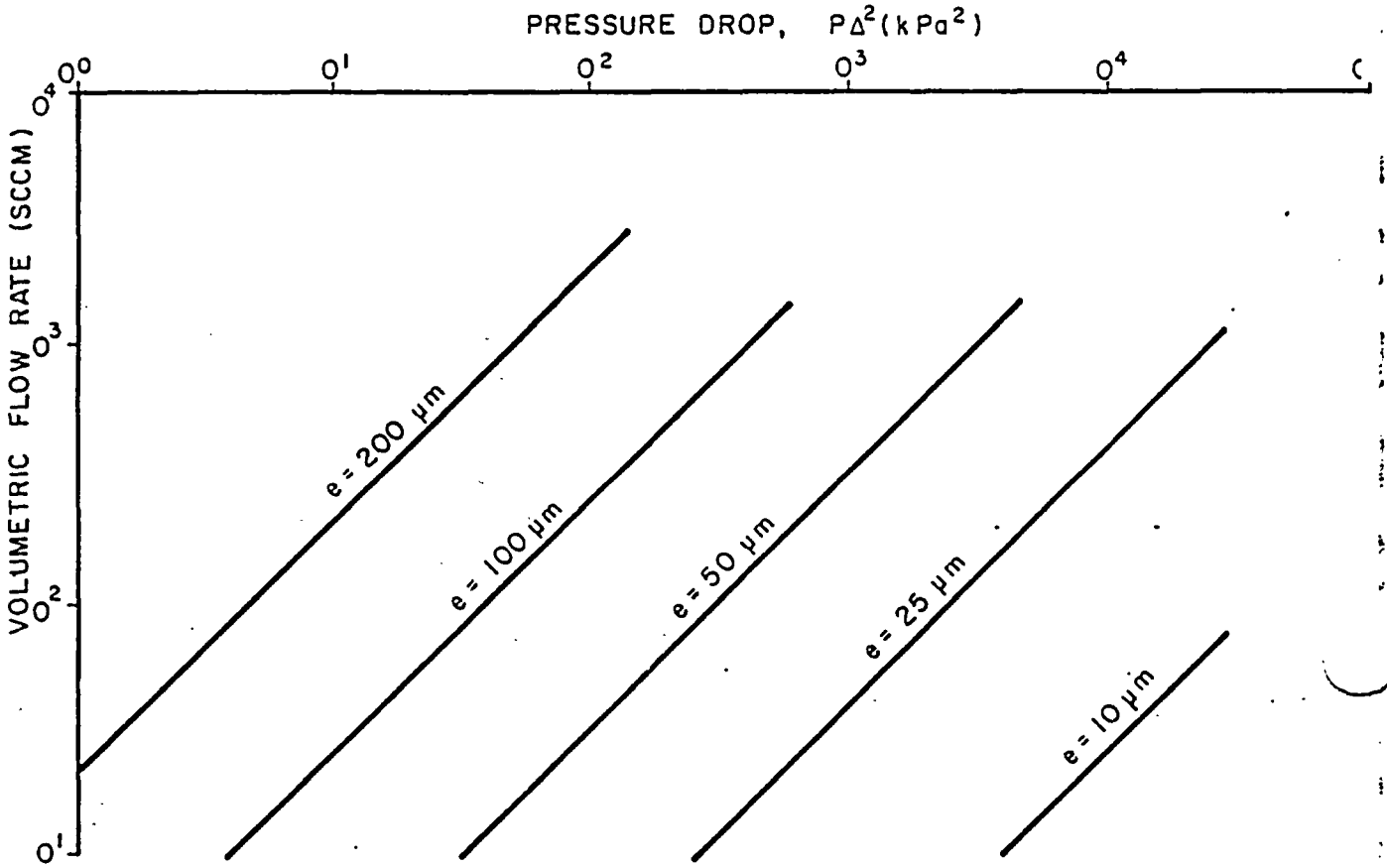

Figure 3.45 Pressure drop versus volumetric flow rate for different apertures, e. Theoretical equations using r_2 = 2 m, r_1 = 0.05 m and α = 0°.

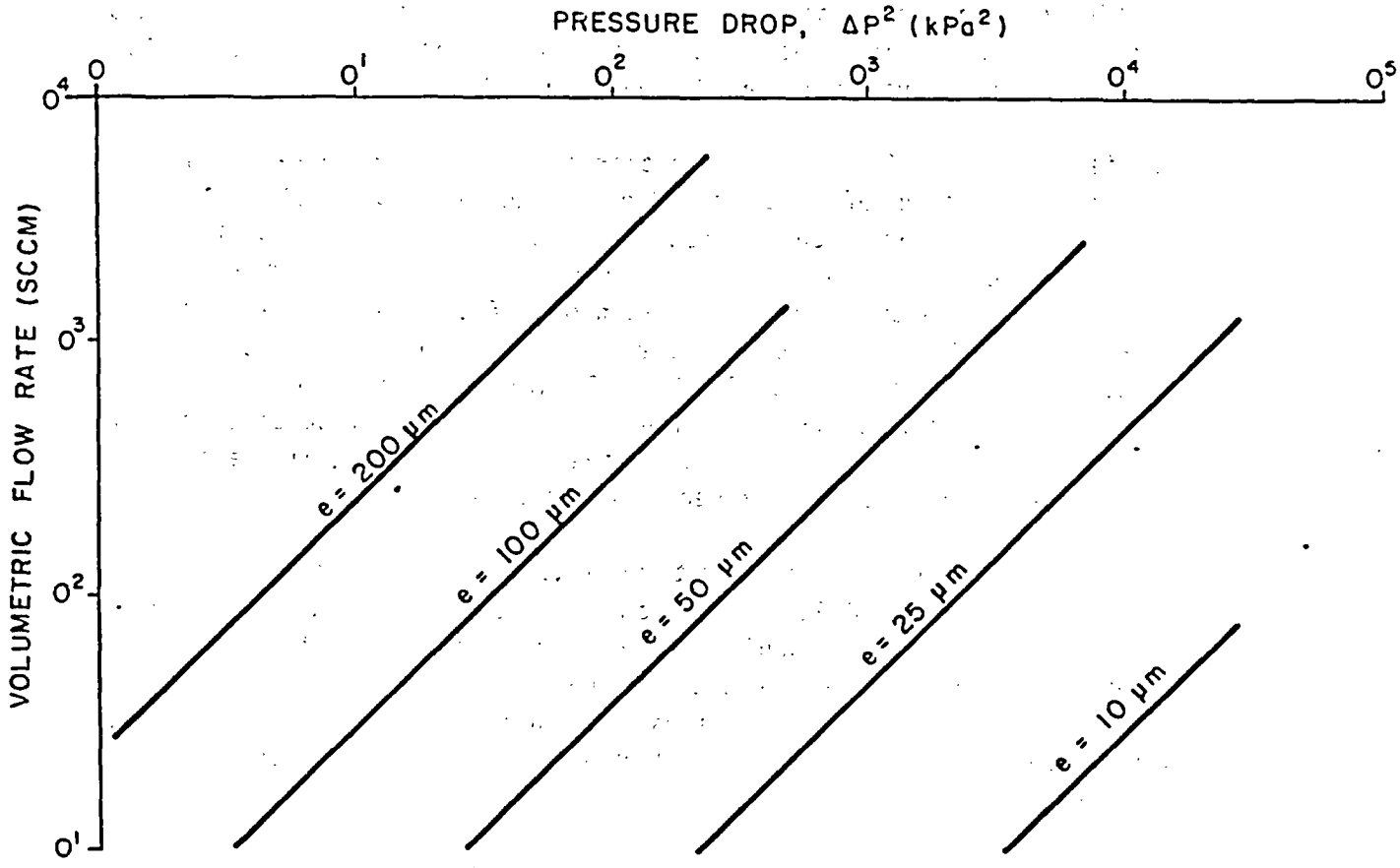

Figure 3.46 Pressure drop versus volumetric flow rate for different apertures, e. Theoretical equations using r_2 = 2 m, r_1 = 0.05 m and α = 60°.

The mass flow rate, Q_m, is measured using mass flowmeters and the pressure drop, ΔP^2, is measured using a mercury-filled manometer. Because the constant, C, is known, Equation (3.27) can be used to calculate the hydraulic aperture, e. The procedure for measuring Q_m and ΔP^2 is described below.

First, the packer system is assembled in a plastic or steel pipe to check the system for leaks. The packers are inflated after placing them inside the pipe which simulated a nonporous, nonfractured section of borehole. The downstream and upstream values on the 10,000 SCCM flowmeter board are then opened (see Figure 3.47).

Gas is allowed to flow into the packer system. The flow rate should be set to the maximum of 5 volts (V) or approximately 10,000 SCCM. The pressure regulator on the nitrogen tank should read between 15 and 20 psi. The regulator should not be set any higher than 20 psi or the mercury in the manometer will be blown out of the top of the glass. If there is a leak in the packer system, the flow rate will become steady or constant after approximately 30 to 50 minutes. If there are no leaks in the packer system, then the flow rate will drop off to zero voltage. Fittings should be tightened if there are leaks and the leak test should be repeated using the same procedure and the 0-100 SCCM flowmeter.

The packer system is said to be tight (i.e., no leaks) when the maximum flow rate using the 0-100 SCCM flowmeter is less than 1 SCCM (0.05 V). A leak-detection test should be performed each time fittings are put together or loosened for transport. Leak-detection tests do not have to be performed if the injection lines and manometer lines are not tampered with when the packers are deflated or inflated during the fracture testing procedure.

Table 3.10 Sample flow test.

TIME	PRESSURE DIFFERENCE (cm Hg)	PRESSURE TRANSDUCER (mV)	FLOW RATE (V)	COMMENTS
14:32	60-40 = 20	19.95	0.95	- flowmeter used - temperature - no flow, flow, etc.

Table 3.10 Sample flow test.

TIME	PRESSURE DIFFERENCE (cm Hg)	PRESSURE TRANSDUCER (mV)	FLOW RATE (V)	COMMENTS
14:32	60-40 = 20	19.95	0.95	- flowmeter used - temperature - no flow, flow, etc.

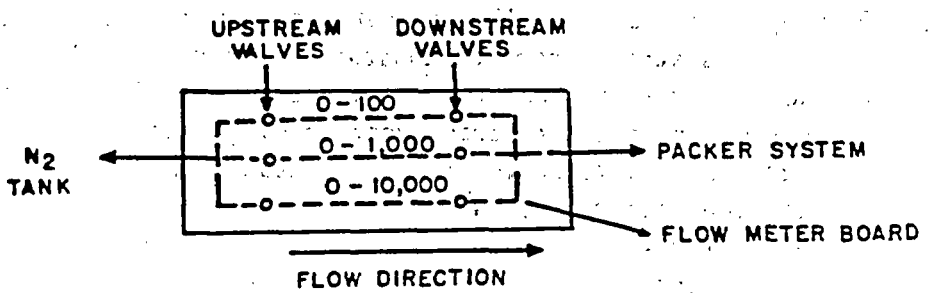

Figure 3.47 Arrangement of valves for packer system.

Table 3.11 Summary of the single-hole pneumatic testing procedure.

I. Leak Detection Test
   A. Place packers in plastic pipe.
   B. Inflate packer.
   C. Inject gas into system using 0-10,000 SCCM flowmeter.
      1. If flow rate becomes constant then leaks exist.
         a. Check fittings and tubing for leaks - repeat C.1.
      2. If flow rate drops off to 0 then no leaks.
   D. Inject gas into system using 0-100 SCCM flowmeter.
      1. If flow rate becomes constant then leaks exist. Repeat C.1.
      2. If flow rate drops off to less than 0.05 V, no leaks exist.

II. Fracture Test
   A. Place packer at desired depth.
      1. Record borehole being used, depth to center of injection zone, injection-zone length, etc.
   B. Zero flowmeter.
   C. Open downstream valve.
   D. Open upstream valve until flow rate is approximately 2 V.
      1. Allow system to come to constant pressure and flow rate.
      2. Record time of day, flow rate, pressure difference from manometer, pressure transducer reading, and any comments.
   E. Open upstream valve again until 4 V output is reached.
      1. If flow rate reaches 4 V:
         a. Allow system to come to steady state; and
         b. Record information under D.1. above.
      2. If flow rate of 4 V cannot be reached without exceeding the range of the manometer:
         a. Drop flow rate below 2 V;
         b. Allow system to come to steady state; and
         c. Record information under D.1.
   F. Deflate packers and move on to next fracture.

CHAPTER 4
NONISOTHERMAL HYDROLOGIC CHARACTERIZATION

Geologic media near HLNW repositories will reach high temperatures as the result of heat generated by the radioactive decay of the waste (Wang et al., 1981). The resulting temperature gradients will alter the ambient-moisture flow field by changing the distribution and physical properties of water residing in the surrounding rock. This could give rise to a liquid-vapor countercurrent flow system in the rock pore space surrounding the subsurface HLNW disposal facility.

Liquid water near the repository will evaporate more readily due to the higher temperature surrounding the repository. Because water vapor density increases with increasing temperature, the thermally-induced temperature gradient will cause water vapor to diffuse away from the repository and condense where the rock is cooler. The creation of a dry zone near the repository and a wetter zone away from the repository will create a potential for flow of liquid water back towards the facility.

Temperature gradients will persist for centuries in rock surrounding a repository. Initially, liquid water will flow more slowly in this system than water vapor, in part because hydraulic conductivity falls very rapidly with decreasing water content, while vapor diffusivity increases as the rock water content decreases. For this reason, net moisture flow will initially be directed away from the repository. The flow could maintain a dry zone near the repository while simultaneously maintaining a moist zone at a greater distance from the repository where the rock is near ambient temperature. The dimensions of the flow system are to a large extent controlled by the thermal properties, the pore-size distribution, and the initial water-content distribution of the rock surrounding the repository, as well as by the intensity and persistence of the radioactive-decay heat source.

Soluble radionuclide migration toward the accessible environment will tend to be contained within the zone of the countercurrent flow system by liquid-water return flow. The high temperature zone will inhibit the release of soluble radionuclides to the accessible environment, provided the countercurrent flow system lies within the confines of the geologic medium selected for the repository.

Experimental work (e.g., Gurr, Marshall and Hutton, 1952) supports the countercurrent phenomenon, showing that a steady thermal gradient can give rise to a liquid-vapor countercurrent in closed systems of unsaturated soil materials. A number of investigations, including those

of Taylor and Cavazza (1954) and Cassel, Nielsen and Biggar (1969), have reported measuring transfer coefficients for water vapor-movement resulting from thermal gradients in various soil types.

While the countercurrent phenomenon has been established for soils, published experimental investigations of countercurrent flow systems operating in unsaturated rock are lacking. Likewise, measurements of vapor and liquid transfer coefficients for unsaturated rock are limited.

The objectives of this chapter are:

(1) To demonstrate the existence of the thermal countercurrent phenomenon in unsaturated rock;
(2) To evaluate the effect of rock type on the formation of the thermal countercurrent; and
(3) To present a method for estimating unsaturated flow parameters from laboratory scale heating experiments.

Axial temperature gradients have been established in sealed, unsaturated sand and rock cores and maintained until steady distributions of temperature and moisture content were observed. The laboratory experiments have been designed to permit the resulting unsaturated flow system to be modeled as a one-dimensional system.

Also, a heat source has been placed in a borehole within a fractured tuff medium. The heat source was used to establish a temperature pulse, and the resulting temperature, water content and water potential have been measured in a nearby observation borehole, as well as in the source borehole following the heating phase.

Finally, a numerical model is presented which incorporates the physical processes. The simulation model is useful for confirming observed distributions of temperature, water content and water potential at various distances from a heat source.

4.1 Laboratory Experiments

Bouyoucos (1915) proposed that soil water can move in response to a temperature gradient. The study by Gurr et al. (1952) of closed unsaturated soil systems subjected to a temperature gradient provided evidence of a liquid-vapor countercurrent system operating under these conditions. These investigators found that liquid water moved towards the heated end of a soil column while water vapor moved towards the cooled end.

The observed vapor flux was far greater at intermediate water contents than that predicted by a Fickian diffusion model modified for porous media. Taylor and Cavazza (1954) found that the movement of water from warm to cool regions occurred mainly in the vapor phase and was accompanied by a liquid water return flow in response to the induced, matric potential gradient.

The heat flux through a porous unsaturated rock is the result of contributions from heat conduction through the rock matrix, the pore water, the pore air, heat convection accompanying movement of pore fluids, and the transfer of latent heat (Philip and deVries, 1957). The transfer of heat by evaporation near a heat source and the subsequent vapor movement and condensation downgradient releasing the latent heat of evaporation is known as heat piping, and can transfer heat rapidly with a small temperature gradient (Grover, Cotter and Erickson, 1964).

Philip and de Vries (1957) tried to reconcile the observed vapor flux rates with the theory of diffusion in unsaturated porous media. Cary and Taylor (1962) developed equations for heat and moisture transfer in unsaturated soil subjected to temperature gradients using the theory of thermodynamics of irreversible processes.

Cassel et al. (1969) measured moisture movement in response to steady temperature gradients in sealed cylinders of uniformly-packed, fine sandy loam at several different initial water contents. They observed countercurrent flow with maximum moisture transfer at intermediate, initial water contents. Their observed vapor fluxes agreed closely with that predicted by the theory of Philip and de Vries, while the Taylor and Cary expression underestimated the vapor flux in all cases.

Another experimental study (Tromble, 1973) concluded that neither the Taylor and Cary model nor the Philip and de Vries physically-based formulation was entirely successful in predicting the observed vapor flux in a closed, heated-soil column.

4.1.1 Experimental Procedure Using Gamma Attenuation Method

Heating experiments have been performed on a sand core and on diamond-drilled, rock core samples. The bulk density and water content of the cores were measured using gamma attenuation equipment originally built (Thames and Evans, 1968) to measure water content of soil columns during infiltration experiments. A core was mounted on a steel carriage, shown in Figure 4.1, which has an aluminum track to carry the cylindrical core sample into the path of the gamma-ray beam.

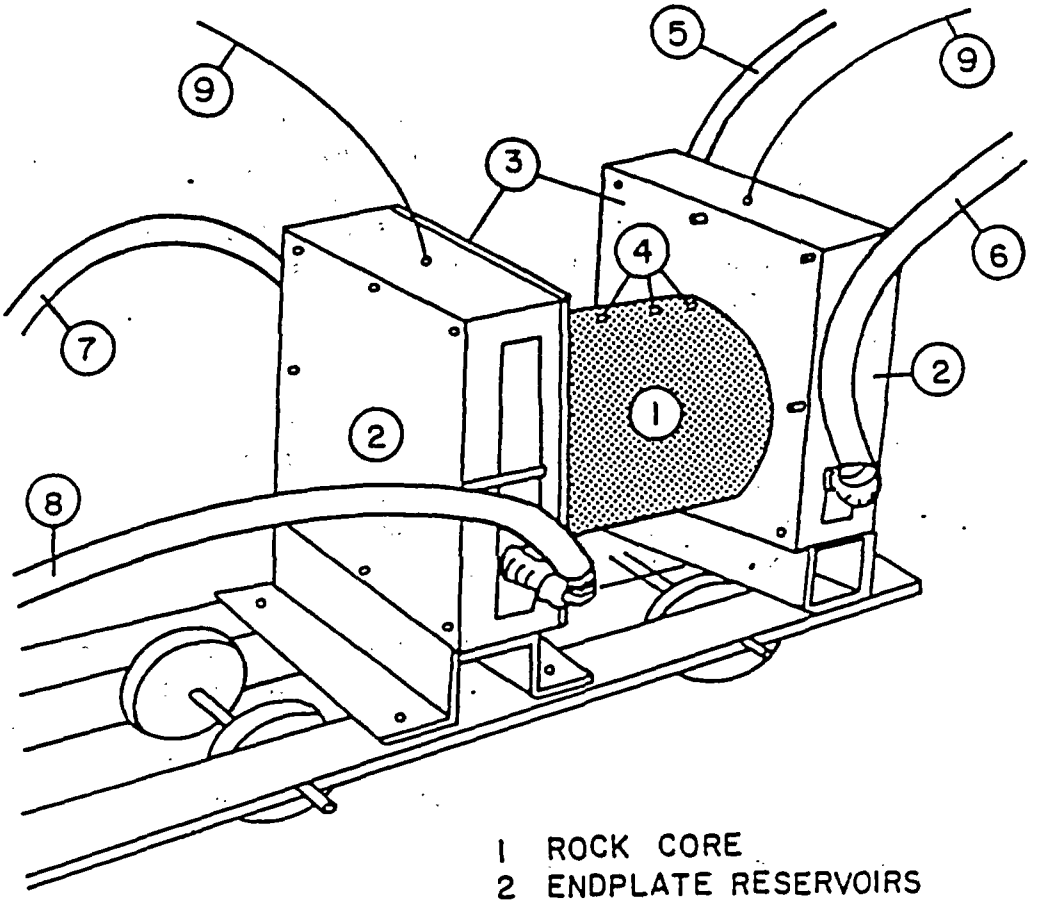

1 ROCK CORE
2 ENDPLATE RESERVOIRS
3 ALUMINUM ENDPLATE
4 THERMOCOUPLE PORTS
(FIVE TOTAL)
5 PRECOOLED WATER INLET
6 PRECOOLED WATER OUTLET
7 PREHEATED WATER INLET
8 PREHEATED WATER OUTLET
9 ENDPLATE RESERVOIR THERMOCOUPLE

Figure 4.1 Heating experimental carriage.

Temperature gradients were established lengthwise along the rock cylinders. Initial, transient, and final temperature distributions in the cores were monitored by a data acquisition system. The rock cylinder in the heating carriage was wrapped with insulating material to reduce radial heat loss. A pinhole in the plastic vapor barrier coating the rock core sample helped maintain atmospheric pressure in the rock.

Gamma attenuation measurements were made periodically during a heating test until no significant gamma attenuation change could be detected. Bulk density and water content were calculated at specific locations along the length of the core using the gamma attenuation data.

4.1.1.1 Theory of Gamma Attenuation

The volumetric water content of a material can be obtained by passing a mono-energetic, gamma radiation beam through the material. The formula is given by Reginato and Van Bavel (1964):

$$(4.1) \qquad \theta = - (\ln(I/I_0) - x\,\mu_r\,\rho_r) / (x\,\mu_w\,\rho_w)$$

where

θ is the volumetric water content of the rock;
I is the measured beam intensity after attenuation by the porous material;
I_0 is the source strength;
x is the thickness of soil material in the path of the gamma beam;
μ_r is the gamma absorption coefficient for the porous material;
ρ_r is the dry bulk density of the porous material;
μ_w is the gamma absorption coefficient for water; and
ρ_w is the density of the pore water.

The intensity of a gamma radiation beam (I and I_0) is defined as the number of gamma photons counted during a given time interval. As the gamma beam from the source passes through matter, a fraction of the incident photons interact with nuclei in the matter. Most of this interaction is Compton scattering where a photon is deflected with a reduction in energy. The reduction in intensity of the gamma beam (reduction in the number of photons with energies near the 0.66 MeV peak for Cs-137) can be related to the water content or bulk density of the material mounted in the carriage using Equation (4.1). The intensity of the Cs-137 source was fixed and assumed constant for the relatively short duration of these experiments.

Radioactive decay is a random process in which the number of disintegrations occurring during a given time interval is normally distributed about a constant mean for a sufficiently intense source (MacIntyre, 1970). This implies that the standard deviation of the number of counts occurring in a given time period is approximately equal to the square root of the mean number of counts.

The number of counts recorded for a given configuration of the experimental setup can only be increased by increasing the counting time. This indicates that if the counting time is increased by a factor of 100, the mean number of counts also increases by a factor of 100. As a consequence, the error associated with variations in the number of gamma radiation counts recorded for a set of repetitive measurements only increases by a factor of ten. The relative error (the standard deviation of a series of measurements divided by the mean number of counts) decreases with increasing mean counts. Therefore, the precision of measurement is improved by increasing the counting time.

4.1.1.2 Gamma Attenuation Equipment

The equipment used for gamma attenuation measurements consists of a 110 millicurie Cs-137 source enclosed in a 5-cm, thick lead shielding unit; a sodium-iodide crystal gamma detector also mounted in a lead shield; and associated electronics to process and record the detector signal. The source and detector are mounted in a heavy steel frame and separated by a 25 cm air gap through which the carriage passes carrying the core sample (Figure 4.2). All of the electronics in the detector system, consisting of an automatic, gain control amplifier; a discriminator unit; a timer; and a six digit counter, were manufactured by Harshaw Electric. The discriminator was operated in integral mode to pass a signal marking the arrival of all gamma photons with energies greater than 0.51 MeV.

4.1.1.3 Sand Column

Initial tests to assist in developing the experimental techniques were conducted with plexiglas columns packed with washed silica sand. A clear plexiglas column, 12.7 cm long with an inside diameter of 8.9 cm, was packed with dry sand. A solution of Schaefer water-soluble black ink in water was slowly added to the sand column until the tracer was visible throughout the column. To obtain a uniform, initial water content, the saturated sand column was placed on a 1-bar porous plate. The plate was then placed in a porous-plate moisture extractor at a pressure of 2/3 bar for a period of five days.

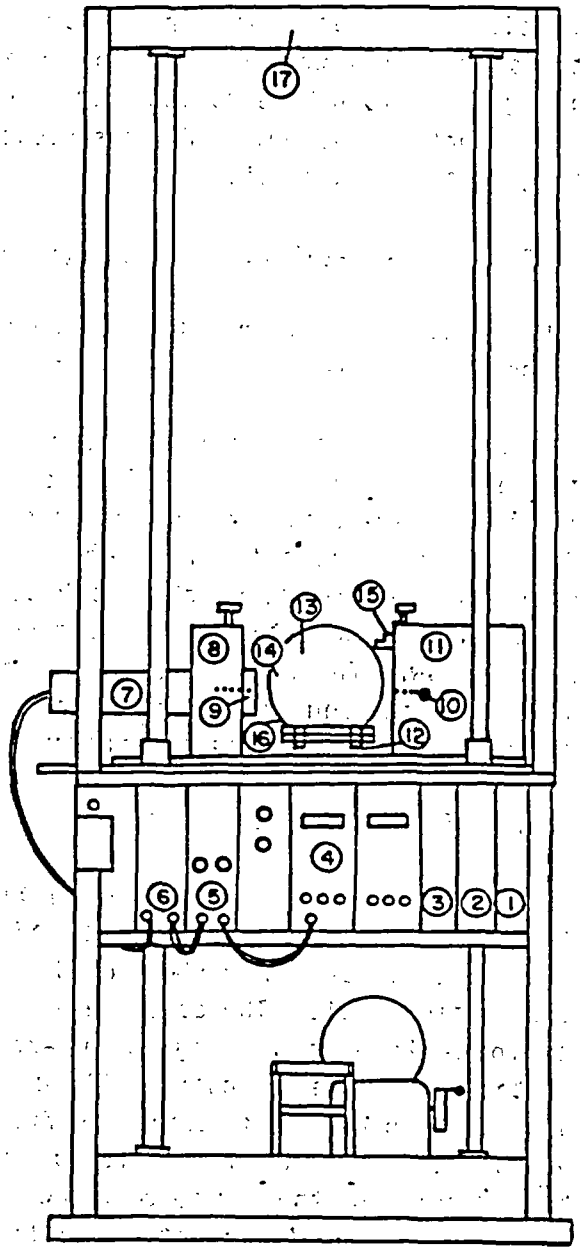

1 Power Supply
2 High Voltage Power Supply
3 Timer
4 Six Digit Counter
5 AGC Amplifier
6 Linear Amplifier
7 Gamma Detector
8 Lead Detector Shield
9 Gamma Beam Collimater
10 Cs-137 Gamma Source
11 Lead Source Shield
12 Aluminum Track
13 Endplate Reservoir
14 Insulation
15 Precooled Water Inlet Port
16 Precooled Water Outlet Port
17 Steel Frame

Figure 4.2 Gamma attenuation equipment.

Upon removal from the moisture extractor, the average water content was determined gravimetrically. Aluminum endplates were fastened to the ends of the sand column with Dow RTV silicone-adhesive sealant compound. This assembly was secured to the carriage and insulation was wrapped around the column.

Initial gamma attenuation measurements under isothermal conditions in the sand column were used to calculate the bulk density distribution along the column by assuming that the initial gravimetrically estimated water content was uniformly distributed. Equation (4.1) was rearranged to give the bulk density:

$$(4.2) \qquad \rho_r = (-\ell n I/I_o - x\rho_w e\mu_w)/(x\mu_r)$$

Subsequent calculations of water content under nonisothermal conditions using Equation (4.1) were made using this bulk density distribution.

The endplate reservoirs at the hot and cold ends were maintained at temperatures of 40 and 20°C respectively for nine days. For this initial experiment, temperature sensors were placed in the sand column. Periodic measurements of water content were made over several days, until the water-content changes became small. The tracer added to the solution used to saturate the sand column was intended to trace liquid-water flow. The final distribution of tracer in the sand column was viewed at the end of the experiment by carefully scooping out half of the sand (lengthwise) in the clear plexiglas column.

4.1.1.4 Rock Core Preparation

Cores were prepared from a fine-grained sandstone, a slightly-welded ash-flow tuff, and a densely-welded ash-flow tuff. The cores (10.2 cm in diameter) were diamond-drilled from each rock sample using water as the cutting fluid. The cores were cut to a length of 12 to 13 cm with a diamond-tipped saw using an oil-based cutting fluid and washed with acetone to remove the cutting fluid. Then the rock cores were placed in a convection oven and heated for five days at 105°C. The dry cores were weighed and wrapped in plastic to prevent moisture entry. The average bulk density of the dry cores was calculated from the measured volume of the cores and their weight after drying. Each rock core cylinder was individually secured in the carriage described above. Bulk density was measured at 1-cm intervals along the length of the core by means of the gamma attenuation method.

4.1.1.5 Sample Wetting Procedure

After the bulk density measurement, individual rock cores were placed in a desiccator vessel and the vessel was evacuated for 24 hours to remove pore air. Deionized water containing 100 ppm fluorescein was released into the chamber to saturate the rock cores. Fluorescein is strongly fluorescent under ultraviolet light and is a simple but effective tracer of liquid-water movement. Vacuum was maintained during water entry so that water could infiltrate the core samples without entrapping air. Heating experiments were not performed on nonwelded ash-flow tuff cores because the samples swelled and cracked on wetting.

4.1.1.6 Sample Desaturation

Previously wetted rock cores were desaturated under controlled conditions similar to those used for the sand column. However, moist bentonite clay spread on a damp filter paper was placed between the porous plate and the rock core. This improved the hydraulic contact between the somewhat curved surface of the porous plate and the flat end of the rock cylinder. A pressure of 2/3 and 1 bar, for the sandstone and the tuff, respectively, was used to reduce the water content. The cores were left for five to seven days in the moisture extractor.

After desaturation, the rock cores were sprayed with a quick-drying varnish and dipped in an air-dry, liquid plastic (PDI, Inc., Plasti-Dip) compound to prevent moisture loss during the heating experiments. Aluminum plates were fastened to each end of the rock cores with heat-conducting, water-resistant epoxy. Three holes (0.3 cm in diameter and 2 cm deep) were drilled at intervals along the length of each rock core. Thermocouple leads were inserted in these ports and sealed in place with Dow RTV silicone-adhesive sealant compound.

Water could be circulated through the endplate reservoirs over a temperature range of 1 to 100°C, measured to a precision of ±0.5°C. Precise control of the cooled water was provided by a Forma Scientific Model 2095 bath and circulator, while the heated water was controlled by a Braun Thermomix Model 1460 heater. Average temperature in the cores was maintained near ambient temperature, 22°C, in order to reduce radial heat losses; therefore, the hot bath could not exceed 45°C.

4.1.1.7 Tracing Liquid-Water Movement

Water containing fluorescein dye was used to saturate the rock cores. The purpose of the dye was to provide evidence of liquid-water flow.

The initial tracer distribution was assumed to be strongly correlated with the initial water-content distribution. The concentration (percent by weight) of tracer in the rock should not change from the initial distribution unless it is altered by liquid water flow moving the soluble tracer.

At the end of an experiment, the rock core was cut in half, lengthwise, to observe the distribution of tracer on the face of the cut. The relative intensity of the fluorescein dye was determined along the axis of the core. In addition, the half core was sectioned and the sections pulverized. Deionized water was added to 40 gm samples of the crushed rock to make 50 ml solutions. The solutions were stirred and then allowed to sit for 24 hours before 10 ml of solution was filtered from the 50 ml samples. The filtrate from each section of the rock cylinder was ranked by the intensity of flourescence under ultraviolet light.

4.1.1.8 Moisture Characteristic Curves

Moisture-release curves were determined for samples of sandstone and tuff using the porous plate apparatus, as discussed by Richards (1969). Rock discs (five cm in diameter and two cm thick) were saturated by means of the vacuum procedure, discussed previously. The saturated discs were placed on moist filter paper and bentonite clay and set on a saturated extractor plate. An overpressure was applied until the water within the rock discs came to equilibrium with the applied pressure. The discs were then removed and their weights determined. The discs were then returned to the extractor and reweighed after two additional pressures were applied. The retained moisture versus pressure curve is the moisture release curve which can be used to find the pore size distribution for the sample.

4.1.2 Experimental Results

Laboratory experiments were performed to determine how an imposed heat field affects the movement of liquid and vapor on three different geologic media. The media ranged from unconsolidated silica sand to a consolidated sandstone core, and finally to a welded tuff. The samples were of variable porosity and homogeneity, with the welded tuff being the least homogeneous. By varying the media, a better understanding was obtained of the physical parameters which affect the movement of fluid and vapor, as well as heat conduction, in geologic media. The extension of these results to *in situ* tests is reserved for Section 4.2.

4.1.2.1 Sand Column Results

The simplified experiment used to develop experimental techniques was run on a plexiglas column uniformly packed with washed silica sand. The average bulk density of the sand column was 1.5 gm/cm^3 (Table 4.1), using a grain density of 2.65 g/cm^3. The average water content for the column was measured as 3.4 percent by volume and was assumed to be uniform throughout.

The experiment was initiated by applying a temperature difference of 20°C across the two ends of the column. Steady state was attained after nine days. A dry zone was created in the sand column extending 2.5 cm from the hot face of the column, while the water content at a point near the cold face of the sand column increased from 3.4 percent to 7.7 percent (Figure 4.3 and Table 4.1). This redistribution was caused by the vaporization and subsequent movement of water vapor from the hot end to the cold end, where the vapor condensed.

Liquid-water return flow (from the cold end to the hot end) deposited tracer in a darkened disk where the liquid flow intersected the dry zone created by vapor movement away from the heat source. The darkened disk was concave towards the cold end, indicating that vapor flux was greater at the central axis of the sand column than along the boundaries. This suggests that radial heat loss may have occurred.

The darkened disk was tilted from a vertical plane, with the lower edge 0.5 cm closer to the hot face. A convection cell operating in the sand column would tend to enhance the axial vapor flux along the top of the horizontal column (and also liquid flow near the bottom), causing the dry zone to extend further from the hot face. This indicates that gravitational effects on moisture movement may not have been negligible.

4.1.2.2 Sandstone Core Results

The bulk density of the sandstone core was found to range from 2.08 to 2.20 gm/cm^3, averaging 2.15 gm/cm^3. The initial water content ranged from 2.4 percent to 9.9 percent (Table 4.2 and Figure 4.4). These variations indicate considerably more heterogeneities within the core than was anticipated from visual inspection. The variability also implies a large variation in hydraulic conductivity and vapor-diffusion coefficients. Because of the variability, one can expect a more complex water-content distribution over time than would develop in a homogeneous medium.

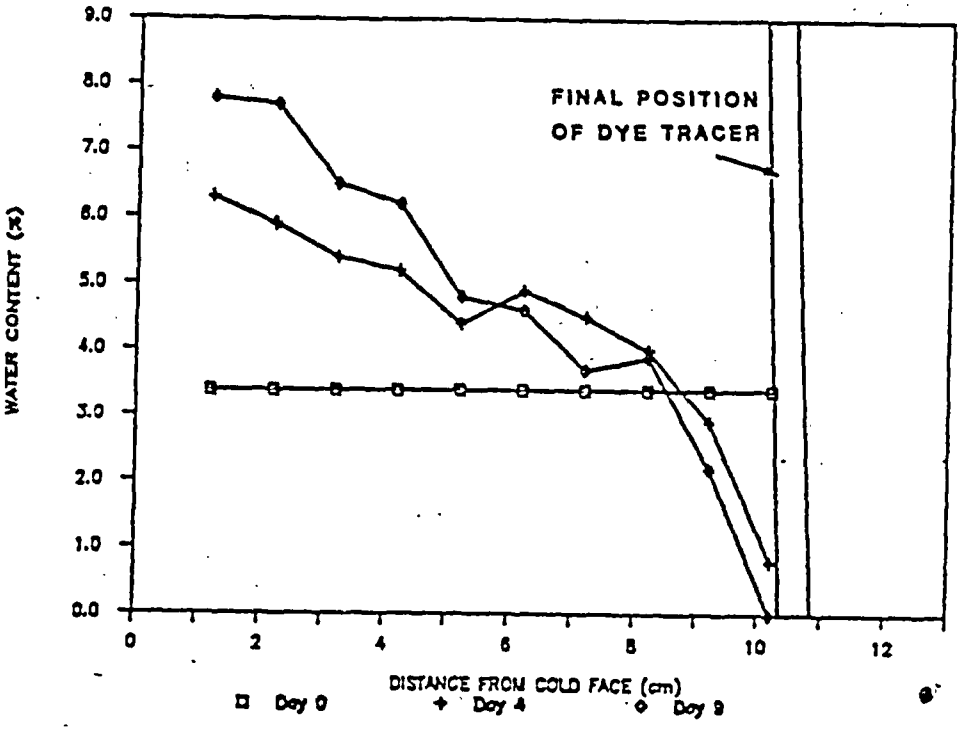

Figure 4.3 Comparison of initial and steady state water content changes for sand column.

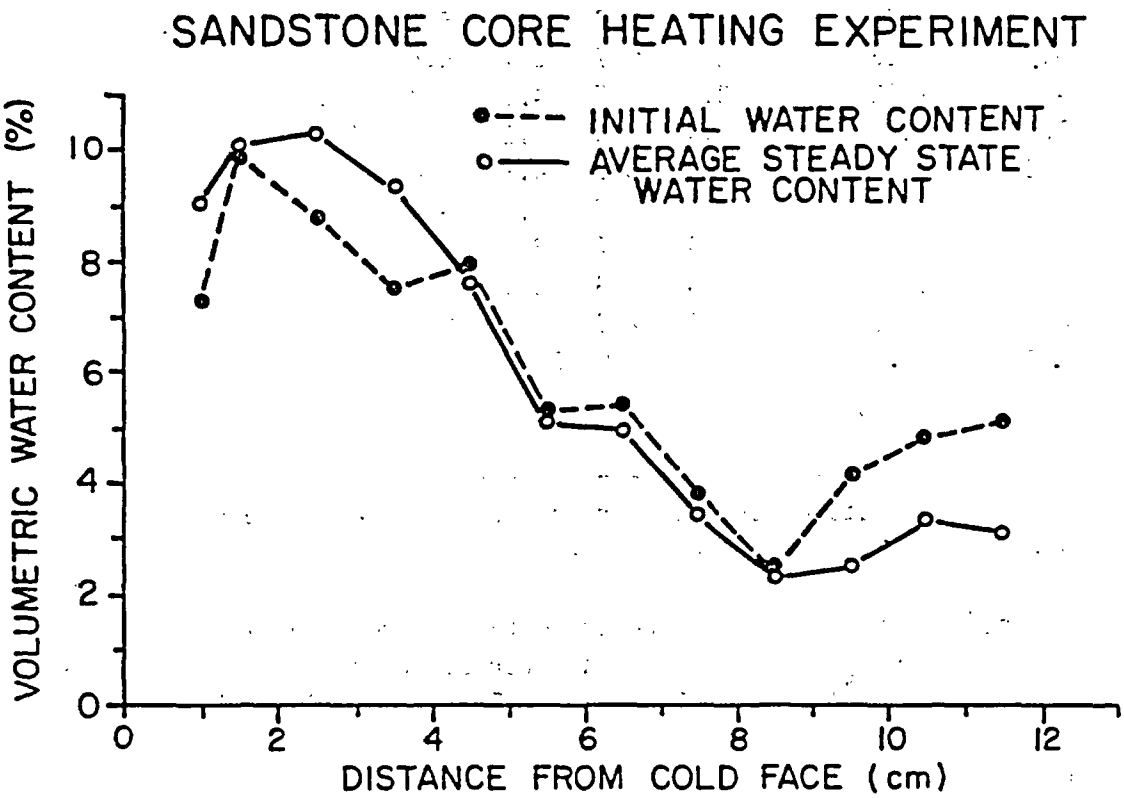

Figure 4.4 Comparison of initial and steady state water content changes for sandstone core.

Table 4.1 Sand column countercurrent experimental results.

Distance (cm)	Dry bulk density (gm/cm^3)	Water content (percent by volume) - Days after start of experiment - 0	2	4	5	9
0.0		- COLD FACE -				
1.2	1.51	3.4	4.4	6.3	6.1	7.8
2.2	1.55	3.4	3.7	5.7	5.6	7.7
3.2	1.56	3.4	3.7	5.7	5.6	7.7
4.2	1.52	3.4	3.5	4.6	5.2	6.2
5.2	1.55	3.4	3.8	5.1	5.3	4.8
6.2	1.55	3.4	3.6	4.7	5.0	4.6
7.2	1.53	3.4	3.6	4.0	4.4	3.7
8.2	1.51	3.4	3.7	3.1	2.9	3.9
9.2	1.56	3.4	2.9	2.9	2.5	2.2
10.2	1.52	3.4	2.3	0.0	0.0	0.0
12.0		- HOT FACE -				

Table 4.2 Sandstone core countercurrent experimental results.

Distance (cm)	Dry bulk density (gm/cm^3)	Water content (percent by volume) - Days after start of experiment - 0	1	3	5	7	9	11	13	16
0.0		- COLD FACE -								
1.2	2.18	7.3	8.8	8.4	8.2	8.4	9.8	8.7	9.1	9.2
1.5	2.12	9.9	9.6	9.7	9.7	9.4	9.7	9.6	10.0	9.9
2.5	2.13	8.8	8.8	9.0	9.6	8.8	9.5	9.0	10.4	9.8
3.5	2.10	7.5	7.6	8.9	9.3	8.1	8.7	8.4	9.2	9.0
4.5	2.08	7.9	7.9	7.9	7.9	7.7	7.6	7.6	7.6	7.3
5.5	2.11	5.3	5.5	5.3	5.4	5.4	5.4	5.4	5.2	5.0
6.5	2.15	5.4	5.1	5.0	4.9	5.0	4.9	4.8	4.6	5.0
7.5	2.20	3.8	3.4	3.3	3.6	3.6	3.3	6.4	3.4	3.4
8.5	2.11	2.4	2.6	2.1	2.4	2.5	2.5	2.4	2.2	2.1
9.5	2.09	4.1	2.8	2.6	2.9	2.8	2.6	2.5	2.5	2.6
10.5	2.09	4.8	3.7	3.2	3.6	3.6	3.4	3.4	3.2	3.3
11.5	2.10	5.1	4.0	3.2	3.7	3.6	3.5	3.3	3.2	3.1
12.0		- HOT FACE -								

An average temperature gradient of 2.2°C/cm was established within the core, with a maximum temperature of about 36°C. The sandstone core reached steady state after twelve days of heating. Water content decreased from 4.7 percent to 2.7 percent at a point near the hot face of the sandstone core while water content increased from 7.3 percent to 9 percent at a point near the cold face. Water content decreased during the experiment at a point 11.5 cm from the cold face, stabilizing after twelve days of heating. Water content increased at a point 1 cm from the cold face, decreasing only between the first and the fifth days and between the ninth and the eleventh days. Water content near the midpoint of the core remained stable throughout the experiment.

Figure 4.5 shows the difference in volumetric water content between the intact core and sections of the core analyzed following the experiment. The intact core retained more water with much more variation in water content than did small slices of that core. This indicates that the saturated rock core was not at a uniform, initial water content.

The initial concentration of fluorescein tracer in the solution used to saturate the sandstone core was 6.0 ppm. When the core was cut in half lengthwise at the end of the experiment, no fluorescein tracer was visible using natural or ultraviolet lighting. The relative amount of tracer found in the filtrate of crushed core sections is shown in Figure 4.6. The initial tracer distribution in the core was assumed to equal the initial water content. The concentration of the tracer in the filtrate was less than 0.1 ppm indicating that the tracer may have been adsorbed by the core.

Figure 4.6 shows that the final tracer concentration was lowest 2 to 5 cm from the cold face and highest in a zone extending from 5 to 8.5 cm from the cold face. The final tracer distribution indicates that liquid- water return flow carried the tracer from cold to warm until an obstruction to flow was encountered 8.5 cm from the cold face. Figure 4.6 also shows that a relatively dry zone existed in the initial water content distribution in this section of the core. This suggests that liquid water flowed from the cold face toward the hot face and that the return flow may have been limited by a low permeability zone resulting from the low, initial water content 8.5 cm from the cold face.

4.1.2.3 Tuff Core Experiment Results

Another heating experiment was conducted on a sealed, slightly-welded tuff cylinder subjected to an average temperature gradient of 2.22°C/cm. The bulk density of the core averaged 2.34 gm/cm^3 (Table 4.3). The

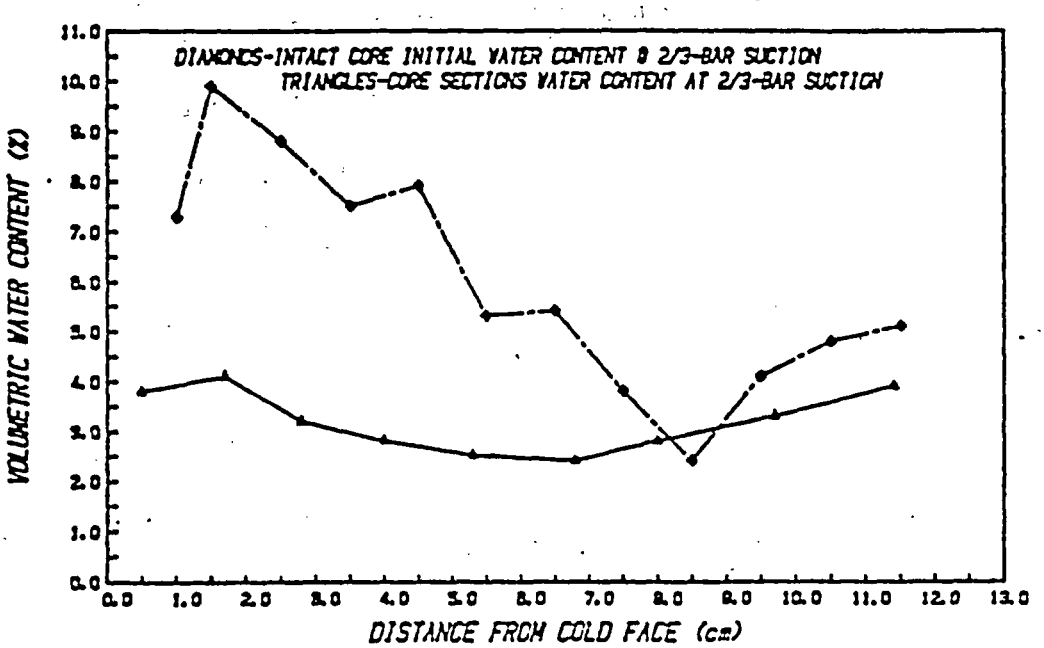

Figure 4.5 Water content of sandstone sample after application of 2/3 bar suction.

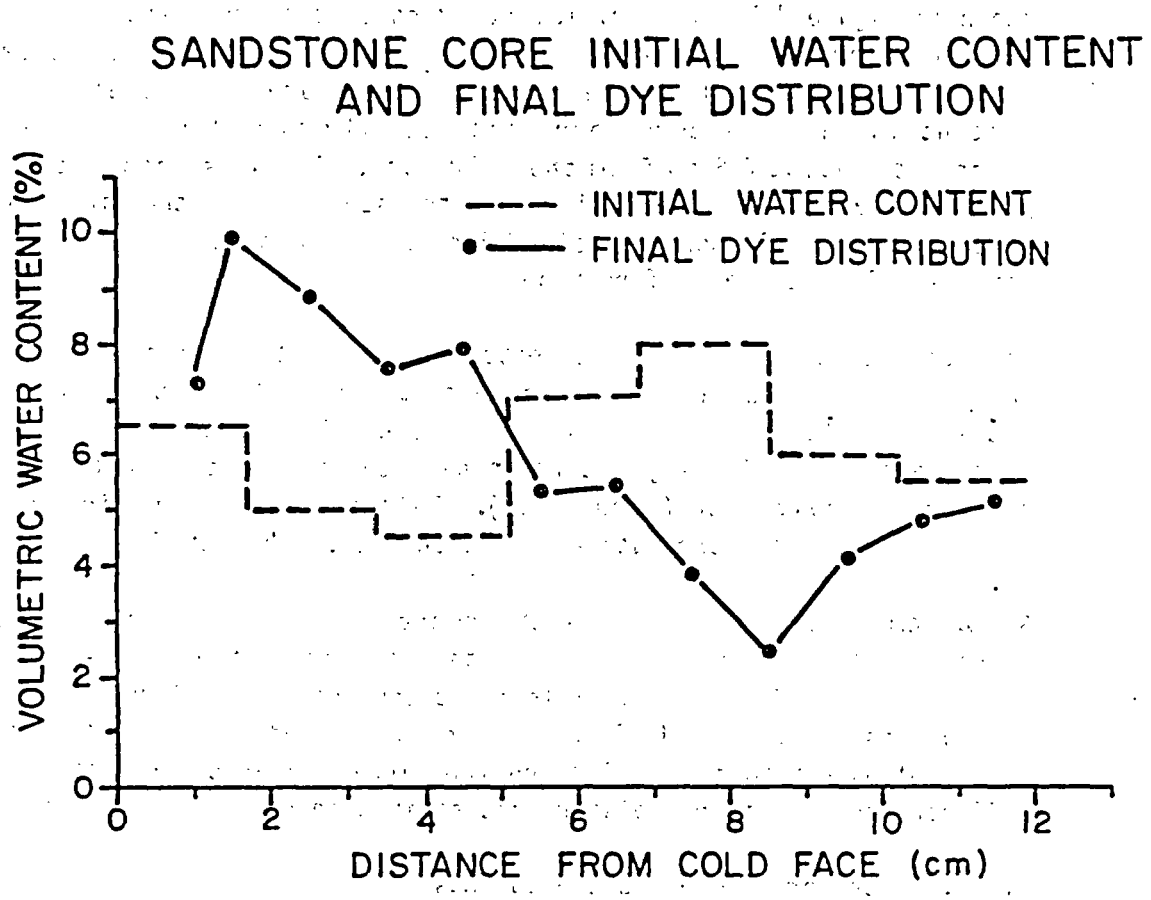

Figure 4.6 Sandstone core tracer distribution.

grain density was estimated to be 2.53 gm/cm^3. The water content of the five small disks cut from the tuff sample after the experiment averaged 10.4 percent with a standard deviation of 0.2 percent water content. The range of the initial water content in the large core was greater than that of the small slices equilibrated at the same pressure, implying that the core may not have had enough time to reach equilibrium when it was removed from the moisture-extractor device.

Initial and final (i.e., after 21 days) water-content distributions are shown in Figure 4.7. The initial water content is substantially larger than the final water content at all points along the core, indicating that water was lost from the system. The figure shows that the water content in the tuff core decreased steadily throughout the experiment except at a point 0.5 cm from the cold face. The water content at that point decreased between the first and the seventh days then increased to a stable value of approximately 9.3 percent. A quasi-steady state was attained after 16 days of heating.

The water-content change is expected to be greatest near the hot face. The calculated decrease in water content during the experiment at the hot end of the core, 12 cm from the cold face, was similar to the decrease of approximately 2 percent near the the middle of the core, 7 cm from the cold face (Figure 4.8). This suggests that liquid-water return flow reduced the water-content change at the hot face.

At 0.5 cm from the cold face the decrease in the water content was approximately 0.5 percent less than that observed at any other location along the axis of the core. This indicates that vapor flow from the hot end towards the cold end of the tuff cylinder reduced the water-content change at the cold face. Data on the final tracer distribution in the tuff core corroborating moisture redistribution could not be obtained.

4.1.2.4 Rock Core Temperature Gradients

The final temperature distributions in the tuff and sandstone cores are shown in Figure 4.9. The thermal conductivity of tuff is greater than that of water and air (Wang et al., 1983). Also the water- and air-filled pore space of this welded tuff core amount to less than 10 percent of the volume of the core suggesting that heat conduction through the solid tuff is likely to be the dominant heat-transport process. The axial temperature data for the tuff core fits a straight line, supporting this premise.

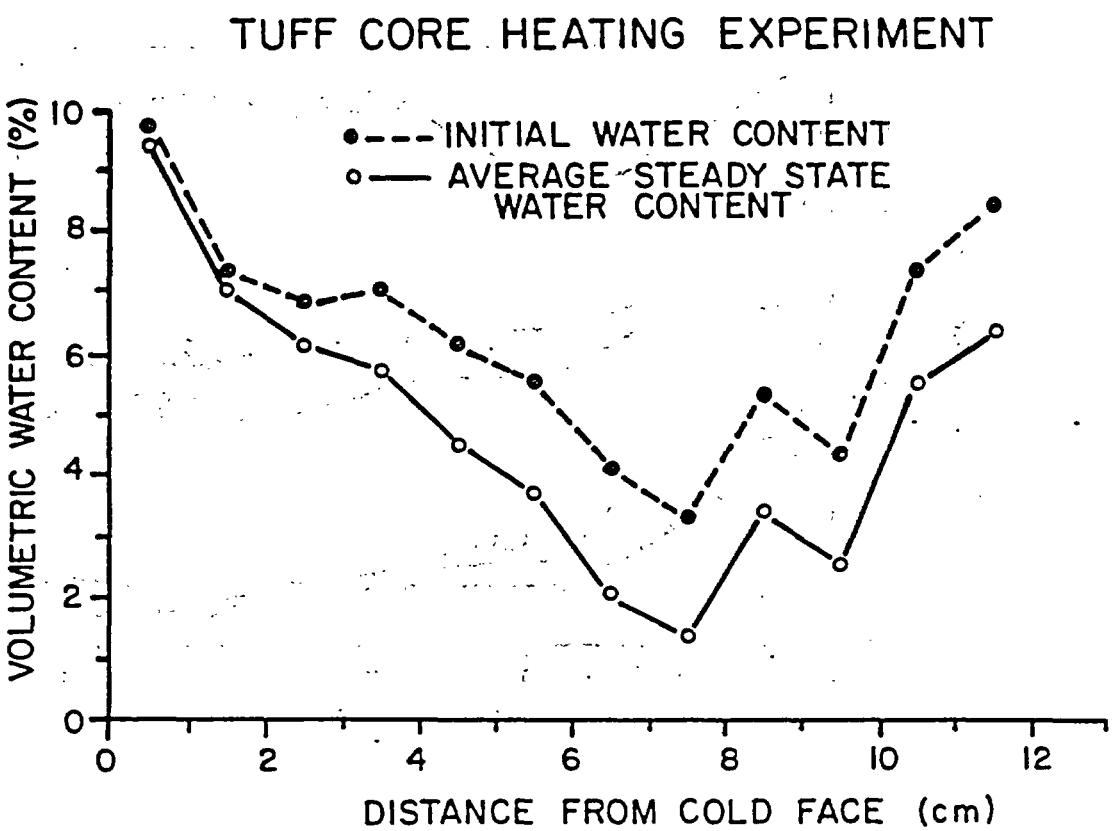

Figure 4.7 Tuff core heating experiment initial and final water content distribution.

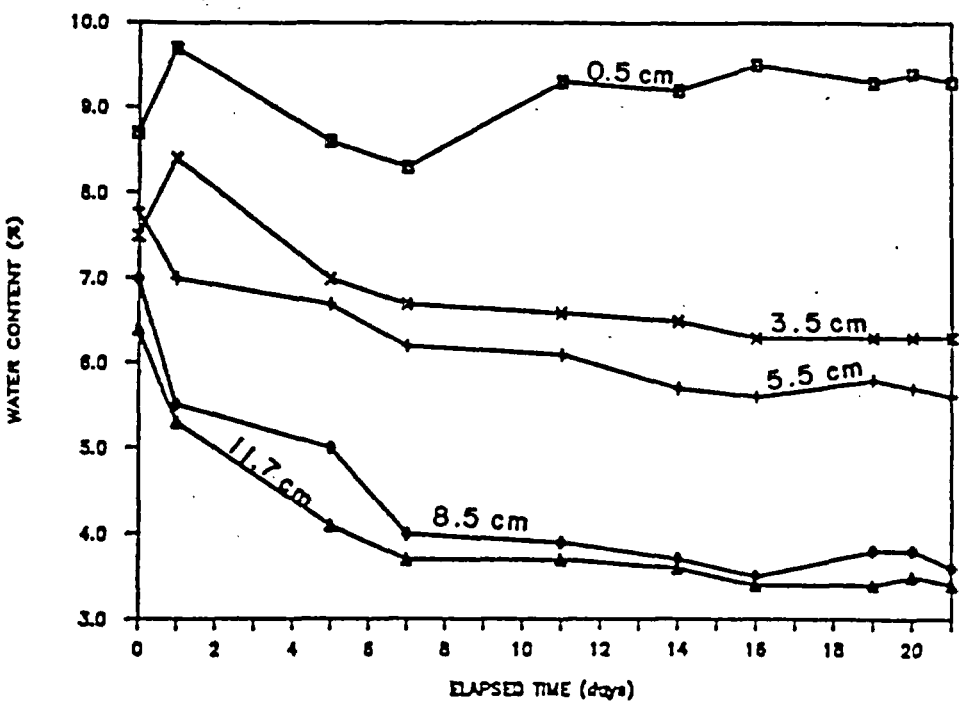

Figure 4.8 Tuff core heating experiment water content changes with time.

Table 4.3 Tuff core countercurrent experimental results.

Distance	Dry bulk density	Water content (percent by volume) - - - - - Days after start of experiment - - - - -								
(cm)	(gm/cm^3)	0	1	5	7	11	14	16	19	21
0.0		- COLD FACE -								
0.5	2.35	8.7	9.7	8.6	8.3	9.3	9.2	9.5	9.3	9.3
1.5	2.34	6.9	7.3	6.6	6.0	6.7	6.5	6.3	7.3	6.9
2.5	2.34	7.1	6.8	6.2	5.7	6.2	5.9	5.9	6.3	5.9
3.5	2.33	7.8	7.0	6.7	6.2	6.1	5.7	5.6	5.8	5.6
4.5	2.33	7.3	6.1	5.1	4.7	4.8	4.5	4.5	4.5	4.4
5.5	2.33	7.0	5.5	5.0	4.0	3.9	3.7	3.5	3.8	3.6
6.5	2.34	5.7	4.1	2.6	2.3	2.0	1.9	1.9	2.0	1.9
7.5	2.35	4.7	3.3	2.3	1.6	1.5	1.4	1.2	1.4	1.2
8.5	2.33	6.4	5.3	4.1	3.7	3.7	3.6	3.4	3.4	3.4
9.5	2.35	6.1	4.3	3.4	2.8	2.7	2.4	2.5	2.3	2.5
10.5	2.35	7.7	7.3	6.2	5.7	5.5	5.5	5.5	5.7	5.5
11.5	2.35	7.5	8.4	7.0	6.7	6.6	6.5	6.3	6.3	6.3
12.0		- HOT FACE -								

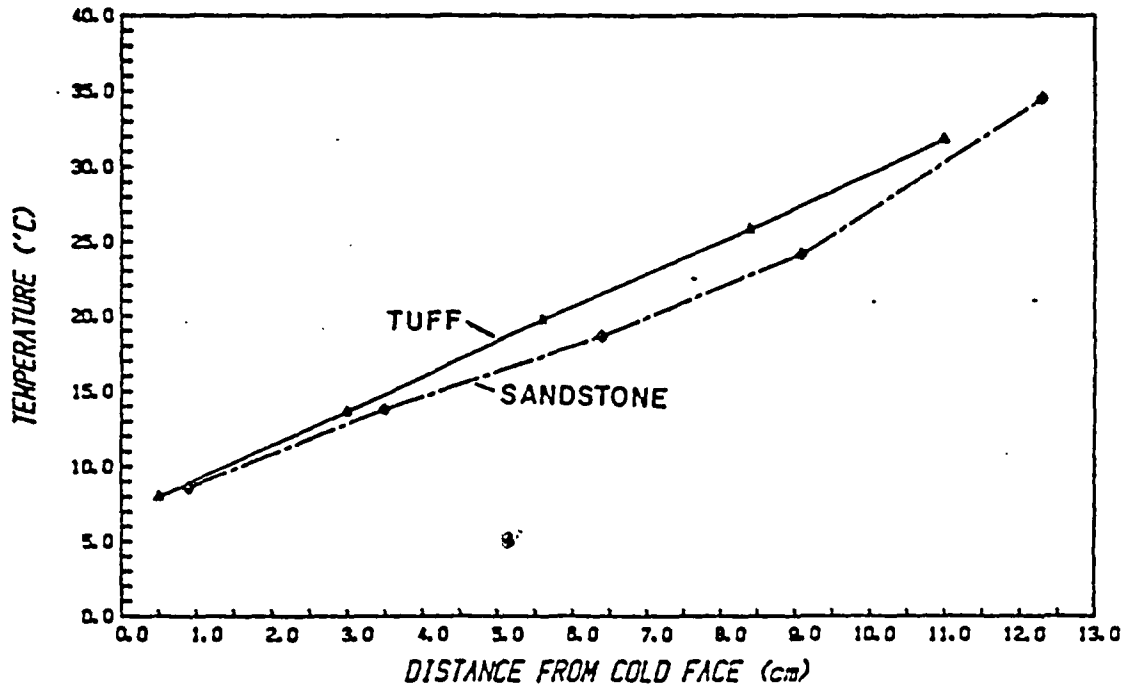

Figure 4.9 Temperature distribution at the end of tuff and sandstone heating experiments.

The plot of temperature versus distance from the cold face for the sandstone core is bowed downward. The temperature gradient was lower near the cold end, indicating that the greater water content at the cold end significantly increased the thermal conductivity of the core. The water content near the hot end had less effect on the thermal conductivity of the core because there was less liquid water. Transfer of heat by convection and latent heat transport would also make the temperature gradient smaller at the hot end.

4.1.3 Conclusions

Countercurrent flow has been demonstrated in heating experiments performed on an unsaturated sand column and with an unsaturated sandstone core. Results of a heating experiment performed on a tuff core also strongly indicates the presence of countercurrent flow phenomenon. The phenomenon was more pronounced in the sand column, followed by the sandstone core, and then by the tuff core.

Heating the sand column results in the creation of a dry zone extending approximately 2.5 cm from the hot face and a sizable water-content gradient with a maximum water content near the cold end. A soluble dye accumulated in a band near the hot end, providing evidence of liquid return flow and a zone of maximum evaporation.

The final distribution of tracer in the sandstone core indicates that liquid-water flow was limited by the presence of a low permeability zone, resulting in a large variation in the water content throughout the experiment. The results for the tuff sample indicates a loss of water from the system during the experiment.

The final temperature distribution observed in the tuff core suggests that conduction is the dominant heat-transport process while the final temperature distribution in the sandstone core indicates that convection and latent heat transfer also contribute to heat transport.

These experiments suggest that countercurrent flow systems might exist in the vicinity of subsurface heat sources in the unsaturated zone. The dimensions of the countercurrent flow system and the rate of moisture movement will depend upon the imposed temperature gradient, on the initial water-content distribution, and on the porosity and pore-size distribution of the surrounding medium.

It is important to note that the rock samples are more variable in water content, porosity, and hydraulic conductivity than sand columns of

identical size. These heterogeneities are not always evident from visual inspections. These differences, however, may not be important for larger samples. For this reason, additional field and simulation studies are required to confirm the existence and nature of the countercurrent phenomenon in natural geologic settings.

4.2 Field Heating Experiment

A small scale heating experiment was conducted in the densely-welded, fractured tuff at the Queen Creek road tunnel site. The objectives of this experiment were to:

(1) Measure the changes in temperature caused by the addition of varied amounts of heat.
(2) Measure the changes in water potential and water content with time.
(3) Determine instrument problems and power requirements for future heating experiments.

Two nearly-parallel, horizontal boreholes (5 cm in diameter, 15 m long and 0.89 m apart), were used in this experiment (Figure 4.10). (For a description of drilling techniques used, see Appendix E.) A heating element was placed six meters into one borehole, while the adjacent hole was packed off at two locations to form an air space approximately the same distance into the borehole. Three thermocouple psychrometers were installed to monitor changes in water potential and temperature in the air space between the packers. A neutron probe was used to determine changes in the water content of the tuff in both boreholes.

4.2.1 Equipment and Procedures

The heating elements used in the experiments are Incoloy 800 sheathed nickel alloy elements manufactured by Dayton. The flange of each element was cut to fit into a combined element and temperature sensor holder (Figure 4.11). The holder is 4.45 cm in diameter and holds the heating element in the borehole, preventing it from coming in contact with the rock. The elements normally use 240 volt current at 60 hertz. While the elements were intended to be used while submersed in a liquid, the application here requires them to be used in air and thus, element burnout was avoided by reducing the voltage to 120 volts. This reduced the heat yield of each element to 1/4 of its potential output.

The two elements used are the 2000 and 6000-watt models, which effectively provide 500 and 1500-watt outputs for the experiments. The element lengths are 23.5 cm and 58.7 cm, respectively. The elements were powered by a field generator and controlled by a thermostat which

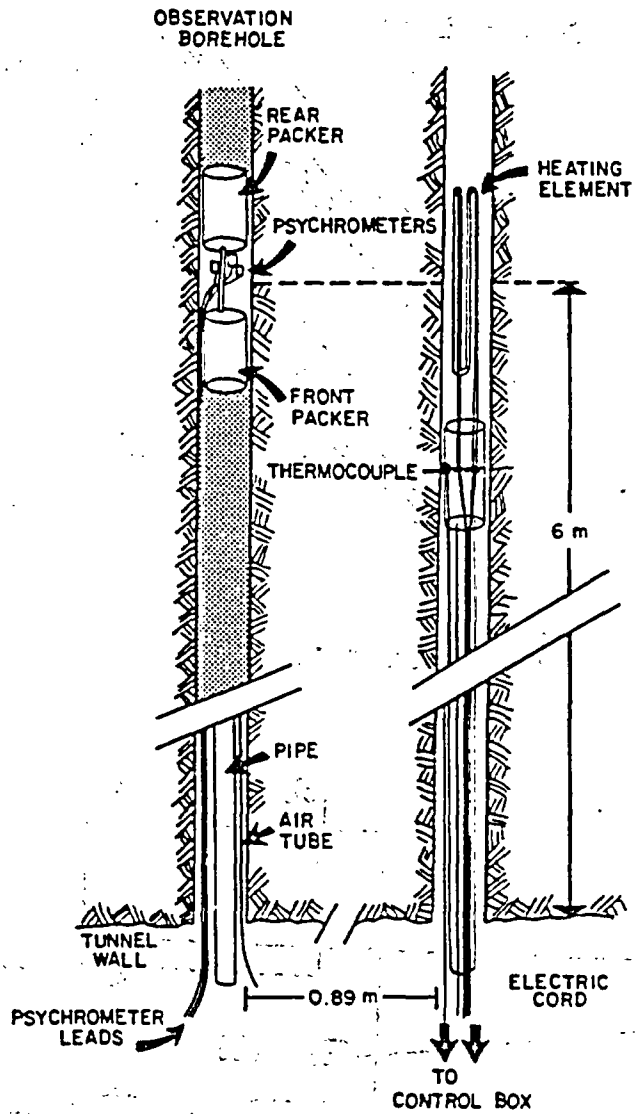

Figure 4.10 Diagram of heating element and thermocouple located behind packer (right borehole), and packers isolating psychrometers (left borehole) at Queen Creek road tunnel site.

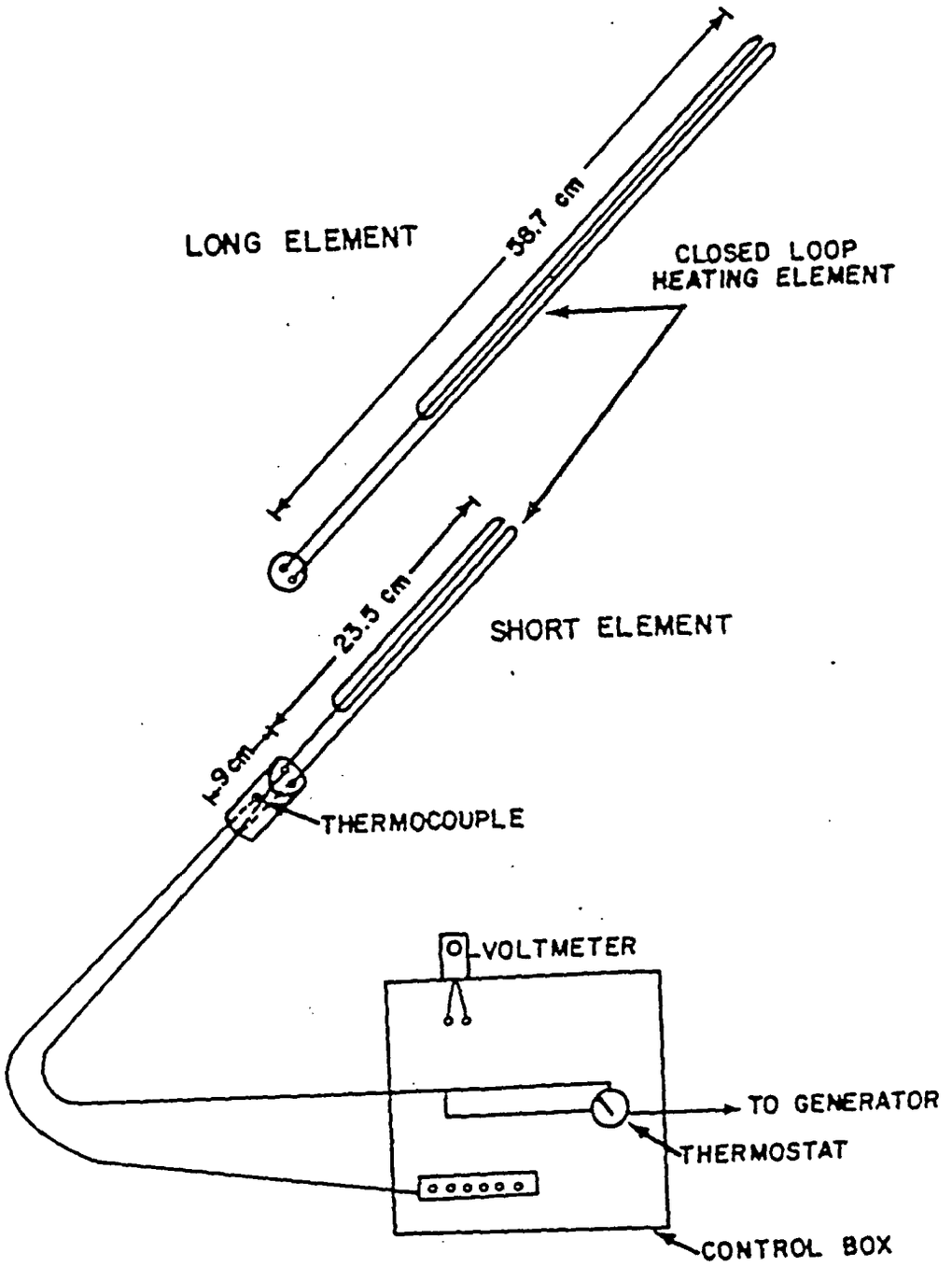

Figure 4.11 Diagram of 500 watt (short element) and 1500 watt (long element) heating units, and wiring to control box.

monitored the temperature of the rock at a point midway along the heating element holder. The thermostat can be adjusted between 100 and 200°C. The thermocouple psychrometers used are manufactured by Wescor and are used in conjunction with a Wescor HR-33T dew point micro-volt meter. Each psychrometer had been calibrated for different temperatures and potentials.

Bulk water content was measured using a neutron probe (Model 503, Hydroprobe, by Campbell Pacific Nuclear). The initial water content of the tuff was determined by taking three neutron probe measurements over one-minute periods at half meter intervals in the two boreholes. The psychrometers were then installed six meters into the borehole between two packers and allowed to equilibrate for four days to determine the initial water potential. The heating element and the element holder was attached to a pipe and placed in the other borehole at a depth of six meters to the middle of the heating element. Power was supplied by an electric cord running through the pipe to the element and connected to the thermostat control box. The thermocouple wire ran from the spring mechanism along the outside of the pipe to the thermostat.

Temperature and potential measurements in the observation borehole were taken hourly while the heater was operating. Heat was applied for approximately three days with the 500-watt element, then no heat was applied for four days. Finally, heat was again applied using the 1500-watt element for another four days. Neutron measurements were taken after heating to determine the change in water content. The thermocouple psychrometers and packers were removed after each heating period, neutron measurements were made, and the packers were replaced for periodic temperature and potential measurements. Periodic neutron measurements were also obtained in the heated borehole.

4.2.2 Results and Discussion from Heating Experiment

In the first part of the experiment, the 500-watt element was emplaced and heated for 65 hours. The water content and water potential in the observation borehole did not change during this period, even though the temperature increased from 21.0 °C to 24.8 °C. In the heated borehole, the water content decreased in the immediate vicinity of the heating element (Figure 4.12). These results indicated that additional heat was required to obtain sizable responses in the observation borehole.

The psychrometers were left in place and a second trial was conducted, starting 103 hours after the first trial ended. During the time between the first and second heating episodes, the temperature in the

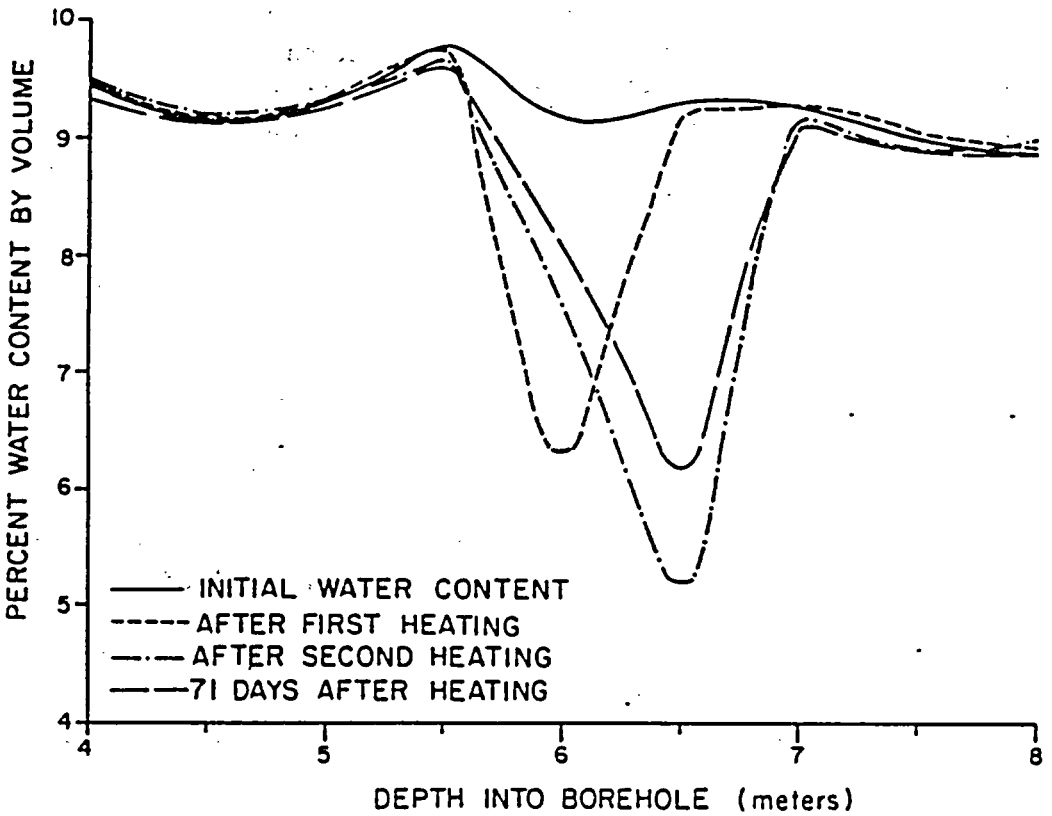

Figure 4.12 Water content against time for heating experiment in the Queen Creek road tunnel.

observation borehole fell from 24.8 °C to 23.5 °C and the water content in the heated borehole remained the same. In the second trial, the 1500-watt element was heated for 94 hours. In the observation borehole, the water suction increased from approximately 0.25 to 9.0 bars. This change, and subsequent changes in suction after the element was turned off, are shown in Figure 4.13.

Data for water potential were obtained using the dew point method and the psychrometric method. The psychrometric method consistently indicated suction readings 0.5 to 1.5 bars above those determined using the dew point method. Data for Figure 4.13 were derived by averaging the values from the two methods. The psychrometer method is not considered accurate above 2 bars suction and, therefore, the initial and final measurements only provide qualitative information about changes in water potential.

The temperature in the observation borehole increased during the time of heating, from 23.5 to 29.5°C (Figure 4.14). The temperature continued to rise for 28 hours after the heating was stopped, and then gradually decreased. Temperature measurements taken in the heated borehole were made by a thermocouple attached to the element holder. At that position, the temperature of the rock increased to 90°C in 48 hours and continued to slowly rise after that to 91.5°C by the end of the heating period. After the heating was stopped, the temperature fell 9.9°C in the first 30 minutes of recovery. The sensor was then pushed further into the hole and allowed to equilibrate. One hour after the heating, the temperature of the rock adjacent to the former heating element position was 132.3°C.

During the second trial, the heating element was mispositioned by 0.36 meters, which resulted in the center of the element being located at 6.36 meters into the borehole instead of 6 meters. The results of this misplacment can be observed in Figure 4.12 which shows the change in water content in the heated borehole after heating with the 1500-watt element. The results show an increase during the second heating period near the 6-meter depth. The neutron method reflects a weighted average water content over a diameter of a few tens of centimeters (the precise diameter has not yet been determined for this site). Therefore, sharp changes in water content cannot be determined.

Seven days after the heating was stopped, the temperature in the observation borehole had dropped to 27.0 °C and the water potential had dropped to near its initial state. Although the suction had increased to approximately 9 bars during this trial no change in water content was

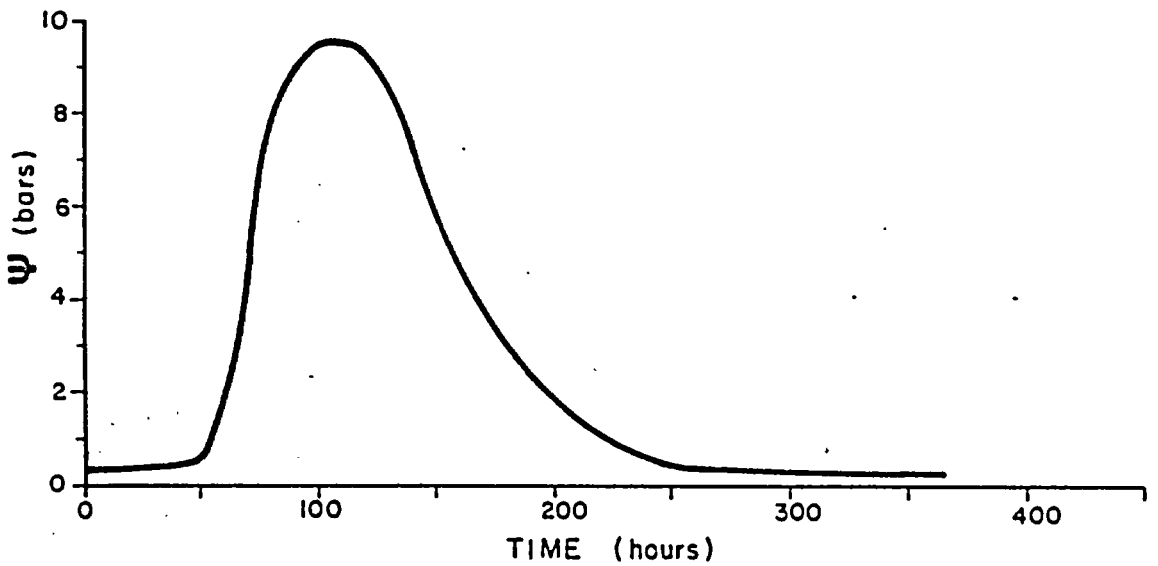

Figure 4.13 Suction against time plot for heater experiment in Queen Creek road tunnel.

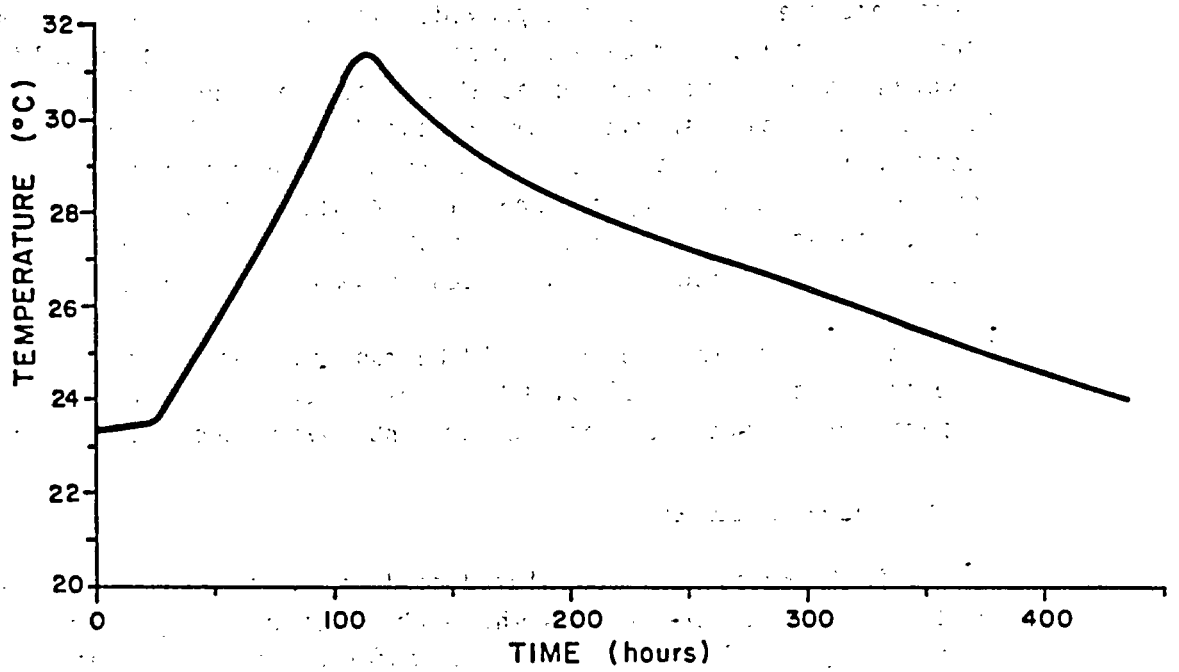

Figure 4.14 Temperature against time plot for heater experiment in Queen Creek road tunnel.

observed. This indicates that a small change in water content can result in a large change in the suction for the range measured.

The recovery of the water content in the heated hole was very slow, as evidenced by the water content distribution after 71 days (Figure 4.12). Because wet and dry zones are located relatively close to each other (thus forming a large hydraulic gradient), the conclusion can be made that the hydraulic conductivity of the rock is low. Another factor in the slow recovery could be that some of the water left the system as a liquid and was unavailable to re-wet the dried area.

These heater experiments have provided valuable data for the design and conduct of more elaborate experiments. Such experiments should include several observation boreholes at varying distances from the heater. Selected boreholes should be instrumented at depth intervals to measure suction and temperature distributions. Other boreholes should be designed to periodically measure water content by the neutron method. The boreholes should be packed off at all times when measurements are not being made to reduce disturbances to vapor and liquid flow.

Finally, future experiments should be run with heating episodes lasting several weeks and then allowed to recover for several months to permit temperature and water content measurements over longer time periods.

4.3 Numerical Simulation

A numerical procedure is developed to demonstrate changes surrounding a heat source under conditions where the host rock may approach 100°C. Such a study involves the coupled transfer of water and heat.

The flow problem investigated is composed of five components; they are:
(1) Heat transfer;
(2) Rock-matrix water flow;
(3) Micro-fracture drainage;
(4) Vapor transfer; and
(5) Evaporation/condensation.

The first three processes are modeled by numerically solving analytic solutions. Vapor transfer is solved by a finite-element method (FEM) which allows temperature dependent properties to be imposed on the fracture system. Finally, evaporation and condensation are approximated by use of a psychrometric table.

The heat- and water-flow domain is illustrated in Figure 4.15. The left boundary (x=o) corresponds to the boundary of a waste repository. At this boundary the temperature rises with time in response to radioactive decay to some peak temperature. This boundary also corresponds to a no-flow boundary for vapor, representing the impermeable repository wall.

The right boundary (x=d) is chosen to be far enough from the repository to have a constant vapor density and temperature. That is, these parameters, at x=d, never change from their initial values. The upper and lower boundaries are symmetrical. In both cases, an imaginary, impermeable plane exists halfway between two main fractures from which liquid, rock- matrix water flows toward the fracture evaporation surface in response to water-content gradients. Finally, gravity drainage through microfractures takes place at specified points throughout the main fracture. For this study, the microfractures were taken to be uniformly distributed.

4.3.1 Assumptions

Given this simplified flow geometry, the nonisothermal flow problem is mathematically formulated based on the following assumptions:

(1) The main fracture (Figure 4.15) is considered to be horizontal, planar, and of uniform aperture. Microfractures are parallel, of equal aperture and spacing, and are normal to the main fracture. Both the main and microfractures are considered smooth. Thus, the fractures are approximated by a parallel-plate analogy.

(2) Vapor transfer takes place solely through the main fracture air space; the air has no velocity. Implicit in this assumption is that no vapor is transported by advection, nor by thermal convection.

(3) The liquid-film flux is negligible. Evans and Huang (1982) state that "an aperture of 1.5 microns will drain at 1-bar potential." Once it is drained, the film thickness on the fracture surface is approximately 30 Å. In this case, the relative cross-sectional area for liquid transport in this particular fracture is 0.004 and the relative flux is 6.4×10^{-8} of that when saturated.

(4) Evaporation and condensation occur instantaneously. This assumption implies that the time span over which the evaporation/condensation process occurs is small when compared to the time step taken in the computer model.

(5) The repository wall (heat source; x=o) can be approximated as an infinite plane in a semi-infinite solid when compared to the intersecting fracture aperture.

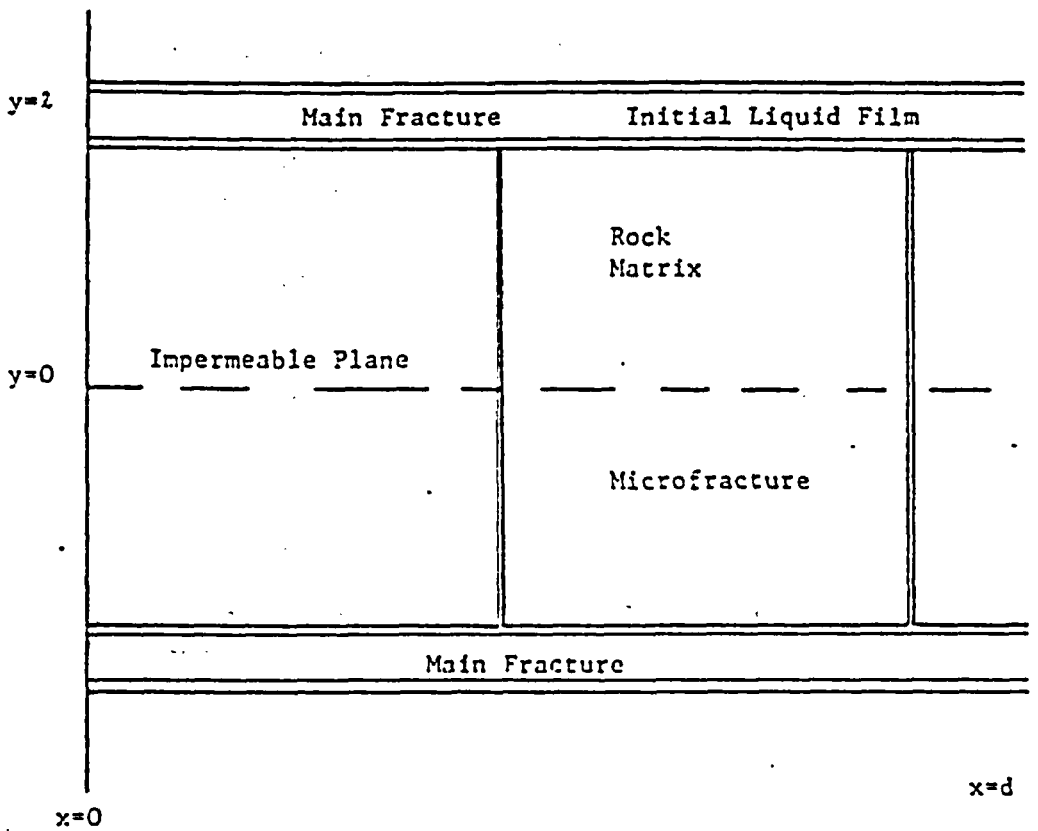

Figure 4.15 The heat and moisture flow domain.

(6) Heat transfer takes place by conduction only, and the air in the fracture is at the same temperature as the adjacent rock. The fracture aperture (millimeters to microns) is small compared to the plane heat source. Because of this difference the distortion on the temperature field resulting from the differing thermal properties of the fracture air/rock matrix is disregarded.

(7) Rock-matrix water flow perpendicular to the main fracture is in response to a water-content gradient. The temperature effect on the host-rock-water diffusivity is disregarded. The effect of the temperature gradient is neglected also because for this study no temperature gradient exists perpendicular to the main fracture. Finally, the rock-water diffusivity value presents a weighted average over the range of water contents expected.

(8) The rock-matrix water reservoir (host rock) is bounded by two main fractures. An impermeable plane exists halfway between the two fractures. Below this plane, water flows to the lower fracture and above this plane, water flows to the upper fracture.

(9) Water contained within the primary porosity of the rock matrix will not exude from the rock into the fracture as the result of thermal expansion.

(10) Water drained from the main fracture by microfractures is considered to leave the system and is no longer accounted for. The fact that the drained water volume is large with respect to the water within the main fracture and small with respect to that within the microfractured rock makes this assumption reasonable.

Given these assumptions, the following mathematical models for heat transfer, water flow in the rock matrix, liquid-water drainage and vapor transfer are combined to demonstrate nonisothermal water flow.

4.3.2 Heat Transfer

The heat-transfer model chosen to simulate the heat produced at the repository wall consists of an infinite plane (with respect to the fracture) in an semi-infinite medium. In addition, the plane heat source has a time varying power density, which in this case decreases with time.

Equation (4.3) accounts for vapor diffusion and the associated evaporation and condensation processes:

$$dc/dt = d\,[D\ dc/dt\ dT/dx]\ /\ dx + Q \qquad (4.3)$$

where

c is vapor density;
t is time;
D is diffusion coefficient for water vapor in air;
T is temperature;
x is a spatial variable; and
Q is a source/sink term.

The net transfer of water is predominantly due to vapor movement, while the vapor source/sink term actually controls flow (Jackson, 1964). For the particular problem studied, Equation (4.3) is solved by the finite-element method with boundary and initial conditions:

$c = w_o$	$t = o$	$o \leq x \leq d$
$dc/dx = o$	$t > o$	$x = o$
$c = w_o$	$t > o$	$x = d$

where

w_o is the initial, saturated vapor density determined by the natural subsurface temperature.

4.3.3 Coupling of Mathematical Models

Each flow component is indirectly coupled through the changing temperature field resulting from radioactive waste decay. Vapor transfer is coupled through the diffusion coefficient for water vapor in air, the vapor density gradient and a source/sink term. Rock matrix water flow is coupled by means of a temperature-dependent boundary condition; namely, the condition that the fracture surface ($y=\ell$) be dry before water flows from the rock to the fracture. That is, the liquid-film-source term for vapor transfer must be zero. Finally, microfracture drainage is coupled through the vapor-transfer-sink term. When enough water has condensed from the vapor phase to the liquid phase to cause gravity drainage, flux through the microfractures is calculated.

4.3.4 Model Discussion

A computer model of a real physical system necessarily simplifies and approximates the actual physical problem. This model is no exception. What follows is a description of the methods used to account for temperature changes, variable vapor-flow parameters, condensation/evaporation, rock-matrix water flow, and microfracture drainage. In addition, the parameters used to assess the water distribution throughout the single fracture at any time are discussed.

Changes in temperature produce changes in water-flow properties. In this investigation thermally introduced changes in vapor-flow parameters were of most interest. The diffusion coefficient for water vapor in air and the saturated vapor density are functions of temperature. New nodal diffusion coefficients and saturated vapor density are calculated by the following two temperature-dependent relationships (Childs and Malstaff, 1982):

$$(4.4) \qquad D = 0.212\ [(T + 273)/273)]^{1.808}$$

where

D is the diffusion coefficient, cm^2/s.

$$(4.5) \qquad w = 1323.0\ [\exp\ 17.17\ T/(237.3 + T)\ (T + 273)]$$

where

w is the saturated vapor density, g/m^3.

While both D and w change with temperature, the saturated vapor density is extremely sensitive. At 50°C, the saturated vapor density is six times its value at 0°C, and at 90°C the increase is 87 times its 0°C value. These increases allow much greater amounts of water vapor in the same volume of air and will, therefore, affect the vapor-transfer process.

As vapor moves away from the repository, the temperature and saturated vapor density decrease, allowing the vapor to condense. In the model, evaporation and condensation are approximated by comparing the calculated vapor density with the existing nodal saturated value (Figure 4.16). If the computed value is greater, condensation occurs until the saturated value is equaled. Likewise, If the computed value is less than saturation, then evaporation occurs assuming there is still water to be evaporated.

The water source for evaporation is composed of two reservoirs. The first reservoir is a liquid film of thickness, h, on the fracture surface which evaporates in the manner discussed above. During this period, actual evaporation equals potential evaporation. When the liquid film is depleted, rock-matrix water moves from the host rock to the fracture evaporation surface. The water source may be supplied initially such that the liquid flux to the surface from within the rock compensates for the rate of evaporation. The duration of this period is short and determined solely by external (i.e., fracture) drying

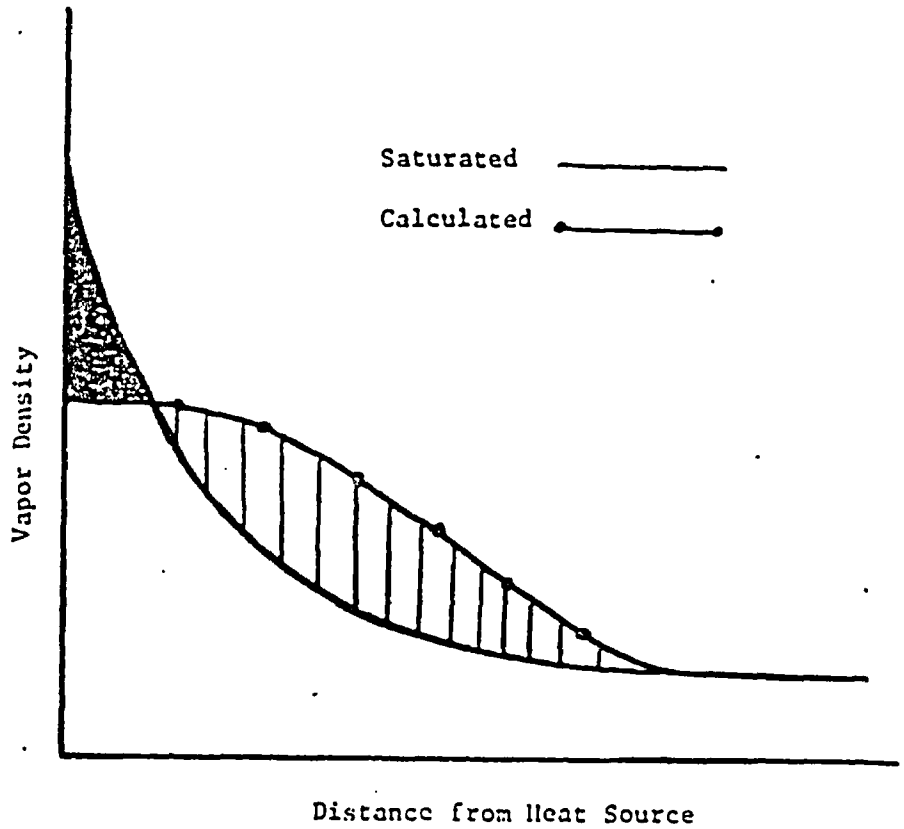

Figure 4.16 Saturated vapor density versus calculated vapor density. The shaded area represents a zone of evaporation and the hashed area a zone of condensation.

conditions. At the end of this drying period the falling-rate, supply period begins (Figure 4.17). Once the drying process has entered the falling-rate period, the external fracture conditions become relatively unimportant compared with rock-water flux parameters. Eventually, the falling-rate period decreases to zero, corresponding to the time at which the rock becomes completely dry (Berger and Pei, 1972).

The temperatures over which the vapor transport process is studied (i.e., less than 100°C, the boiling point of water at 1 atmosphere) ensure that liquid water will still be present in the fracture/rock-matrix flow system. Liquid water flow in the fracture has been disregarded for the reasons discussed earlier in this study (i.e., Assumption 3). Liquid water in the rock matrix flows in response to a water- content gradient. That is, the flux of water (q_w) is assumed to correspond to:

$$(4.6) \qquad q_w = - D_R \, d\theta/dy$$

The lack of data with regard to the temperature and water-content dependence of D_R does, however, limit the use of this flow theory. In zero condensation, Poiseuille drainage may be an important process. In the model, an effective aperture is used for the purpose of fracture drainage at a given node (Figure 4.18). This single drainage fracture takes into account all drainage in the space represented by a node. The amount of water drained at each node is tabulated for mass balance considerations, as it is no longer in the flow domain.

After the evaporation/condensation process has been carried out for a time step, the relative humidity for each node is calculated. The water potential can then be obtained from the relationship:

$$(4.7) \qquad \psi = (R/v_w) \, (T + 273) \, \ln(H_r)$$

where

ψ is water potential;
H_r is relative humidity;
R is universal gas constant; and
v_w is molar volume of water in the fracture air space relative to water-saturated air.

The amount of liquid water on the fractured surface at a given node is assessed by means of a liquid-water ratio (R_L). It is defined as the ratio of liquid water at some time ($t>0$) to the initial amount of liquid water present (S_i) at the node.

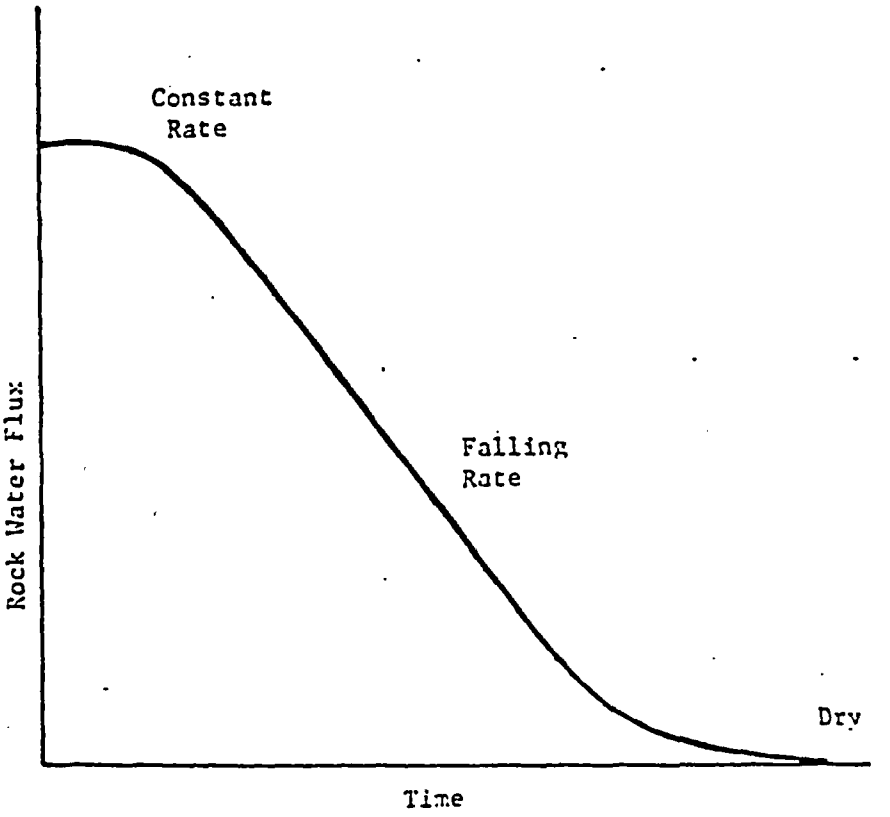

Figure 4.17 Qualitative plot of rock water flux versus time illustrating the drying process.

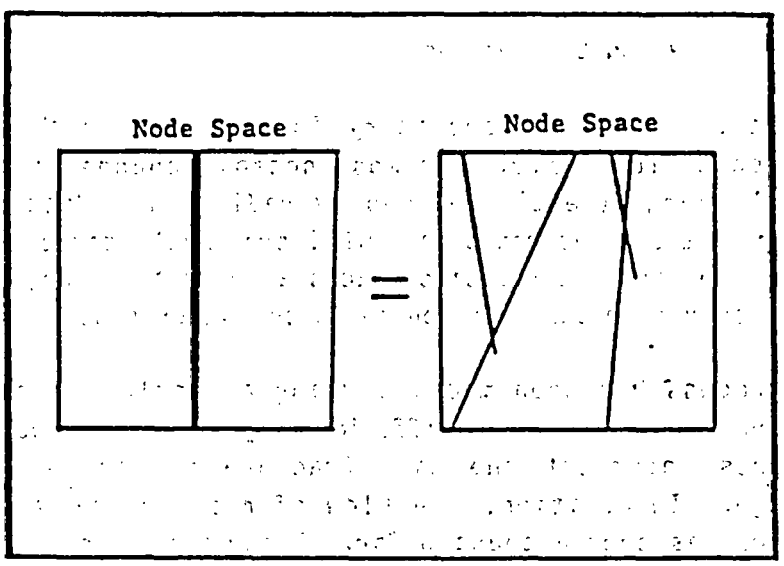

Figure 4.18 Illustration of how a set of natural microfractures is replaced by an effective microfracture. The single fracture takes into account all gravity drainage for a given node space.

$$R_L = S_t/S_i$$

In summary, for each time step (Δt) the temperature distribution is determined. The diffusion coefficients and saturated vapor densities at each node are then calculated. This allows the global matrix to be constructed which is subsequently solved by a direct solution technique for new nodal compared with saturated values to determine whether evaporation/condensation, rock-matrix water flow, or drainage should occur. Finally, the relative humidity and liquid water ratio are calculated in order to assess the drying of the fracture.

4.3.5 Summary and Conclusions

Placement of a HLNW repository in fractured rock will alter the hydrologic flow field. The most notable change will be due to the thermal energy (heat) produced by radioactive decay. A repository located in the unsaturated zone will presumably cause movement of water vapor. That is, the repository acts as a heat source, causing water to diffuse away from the heat source in the vapor phase.

This process has been modeled using a single, main fracture which provides a path for vapor diffusion away from the repository. Smaller fractures intersect the main fracture providing a mechanism for drainage. In addition, the flow of rock-matrix water to the main fracture has been accounted for. These three processes are coupled together with the repository-generated temperature field and the resulting evaporation/condensation process. Thus, using a simple flow geometry, the movement of water away from a HLNW repository was investigated.

Taking all these processes into account required several simplifications. The assumptions that the air is stationary, and that the thermal expansion of water in the rock matrix may be disregarded, are probably most critical. Certainly the effects of air movement on the degree and extent of water movement should be evaluated. The possibility of rock-water flux resulting from thermal expansion is also a flux mechanism which should be investigated further.

From the modeling investigation, one can make several conclusions. First, rising temperatures near the repository will induce vapor diffusion, and over a long enough time-span, significant quantities of water will be transported away from the repository. Model results demonstrate how temperature changes and vapor diffusion have an effect

on the production of wet and dry zones in a fracture. In repository-induced, high-temperature areas, available water is evaporated; this water vapor condenses when it reaches rock near ambient conditions.

Second, the sensitivity analysis indicates that variations in initial film thickness will have only second-order influence on wet- and dry-zone alteration. Aperture and spacing of drainage fractures and the host- rock hydraulic properties will have much greater effects. The greater volume of water within the rock when compared to the fracture is the reason water movement is more sensitive to the water diffusivity. On the other hand, the drainage fractures act as a valve. Even small (micro-range) drainage fractures have the capacity to drain liquid water faster than diffusion away from the heat source. It is this difference in transport rates that makes the water movement sensitive to the drainage mechanism.

Finally, during both heating and cooling phases, the dominant direction of water movement will be away from the repository wall. While temperatures decrease near the repository, the temperature gradient is primarily outward, i.e., away from the repository. This result could be an artifact of the boundary condition specified. In any event, the cooling process must be further evaluated before final conclusions are made with respect to HLNW disposal in the unsaturated zone.